

**STUDY OF THE RADIATIVE PENGUIN $B_s^0 \rightarrow \phi \gamma$
AND $B_s^0 \rightarrow \gamma \gamma$ DECAYS AND THE RESONANT $B^+ \rightarrow K^+ \gamma \gamma$
DECAYS AT BELLE**

THÈSE N° 4057 (2008)

PRÉSENTÉE LE 4 AVRIL 2008

À LA FACULTÉ DES SCIENCES DE BASE
LABORATOIRE DE PHYSIQUE DES HAUTES ÉNERGIES
PROGRAMME DOCTORAL EN PHYSIQUE

ÉCOLE POLYTECHNIQUE FÉDÉRALE DE LAUSANNE

POUR L'OBTENTION DU GRADE DE DOCTEUR ÈS SCIENCES

PAR

Jean WICHT

ingénieur physicien diplômé EPF
de nationalité suisse et originaire du Mouret (FR)

acceptée sur proposition du jury:

Prof. R. Schaller, président du jury
Prof. O. Schneider, directeur de thèse
Dr A. Drutskoy, rapporteur
Dr U. Egede, rapporteur
Dr T. Schietinger, rapporteur



ÉCOLE POLYTECHNIQUE
FÉDÉRALE DE LAUSANNE

Suisse
2008

Abstract

WE present the study of the radiative penguin $B_s^0 \rightarrow \phi\gamma$ and $B_s^0 \rightarrow \gamma\gamma$ decays and the resonant $B^+ \rightarrow K^+h \rightarrow K^+\gamma\gamma$ decays. We use data samples recorded at the $\Upsilon(4S)$ and $\Upsilon(5S)$ resonances with the Belle detector at KEKB, an electron-positron collider located in Tsukuba, Japan. The $\Upsilon(4S)$ sample corresponds to an integrated luminosity of 492 fb^{-1} and contains 535 million $B\bar{B}$ pairs. At the $\Upsilon(5S)$ resonance, we use a sample of 23.6 fb^{-1} containing 2.8 million B_s^0 mesons.

Penguin decays are loop-induced diagrams involving the heaviest particles of the Standard Model, the model describing, successfully so far, all particles and interactions, except the gravitation. Penguin decays are sensitive to physics beyond the Standard Model: particles foreseen by theories extending the Standard Model, whatever their masses are, can enter the loop and modify physics observables away from their Standard Model expectations.

We report the first observation of a radiative penguin decay of the B_s^0 meson in the $B_s^0 \rightarrow \phi\gamma$ mode with a significance of 5.5 standard deviations. We measure

$$\mathcal{B}(B_s^0 \rightarrow \phi\gamma) = (57_{-15}^{+18}(\text{stat})_{-11}^{+12}(\text{syst})) \times 10^{-6}$$

in agreement with the expectation of the Standard Model. We do not observe any significant $B_s^0 \rightarrow \gamma\gamma$ signal and we compute an upper limit at the 90% confidence level on its branching fraction of

$$\mathcal{B}(B_s^0 \rightarrow \gamma\gamma) < 8.7 \times 10^{-6}.$$

This limit is about six times more stringent than the previously published one. However, it is still about one order of magnitude larger than the expectation of the Standard Model and still above expectations of theories beyond the Standard Model.

For the resonant $B^+ \rightarrow K^+h \rightarrow K^+\gamma\gamma$ decays, we search for decays where the h particle can be a η , η' , η_c , $\eta_c(2S)$, χ_{c0} , χ_{c2} or a J/ψ meson, or the $X(3872)$ particle discovered in 2003 by the Belle collaboration. We observe the modes with $h = \eta$ and η' . We obtain an evidence of the mode with $h = \eta_c$; this is the first time that a $B^+ \rightarrow K^+\eta_c$ signal is seen in the $K^+\gamma\gamma$ final state. We measure

$$\begin{aligned}\mathcal{B}(B^+ \rightarrow K^+\eta \rightarrow K^+\gamma\gamma) &= (0.87_{-0.15}^{+0.16}(\text{stat})_{-0.07}^{+0.10}(\text{syst})) \times 10^{-6}, \\ \mathcal{B}(B^+ \rightarrow K^+\eta' \rightarrow K^+\gamma\gamma) &= (1.40_{-0.15}^{+0.16}(\text{stat})_{-0.12}^{+0.15}(\text{syst})) \times 10^{-6}, \\ \mathcal{B}(B^+ \rightarrow K^+\eta_c \rightarrow K^+\gamma\gamma) &= (0.22_{-0.07}^{+0.09}(\text{stat})_{-0.02}^{+0.04}(\text{syst})) \times 10^{-6},\end{aligned}$$

with significances of 7.3, 13.8 and 4.1, respectively. For the other modes, we obtain limits on their branching fractions. We also measure or set limits on the branching fractions of

the $h \rightarrow \gamma\gamma$ decays for the modes where $\mathcal{B}(B^+ \rightarrow K^+ h)$ has been measured elsewhere. We set for the first time an upper limit at the 90% confidence level on the branching fraction of the decay of the $X(3872)$ particle into two photons of

$$\mathcal{B}(X(3872) \rightarrow \gamma\gamma) < 1.1\% .$$

Keywords: high-energy physics, KEK, Belle, Standard Model, New Physics, B physics, penguin decays.

Résumé

NOUS présentons l'étude des désintégrations radiatives pingouin¹ dans les modes $B_s^0 \rightarrow \phi\gamma$ et $B_s^0 \rightarrow \gamma\gamma$ ainsi que l'étude des désintégrations résonantes $B^+ \rightarrow K^+h \rightarrow K^+\gamma\gamma$. Nous employons des échantillons de données produites aux résonances $\Upsilon(4S)$ et $\Upsilon(5S)$ par le collisionneur électron-positron KEKB et récoltées par le détecteur Belle. L'échantillon obtenu à la résonance $\Upsilon(4S)$ correspond à une luminosité intégrée de 492 fb^{-1} et contient 535 millions de paires $B\bar{B}$. A la résonance $\Upsilon(5S)$, nous disposons d'un échantillon de 23.6 fb^{-1} contenant 2.8 millions de mésons B_s^0 .

Les désintégrations pingouin sont des désintégrations en boucle qui font intervenir les particules les plus lourdes du Modèle Standard. Le Modèle Standard est la théorie décrivant avec succès jusqu'à maintenant toutes les particules et interactions sauf la gravitation. Les désintégrations pingouin sont sensibles aux phénomènes physiques au-delà du Modèle Standard: des particules non prévues par le Modèle Standard, quelles que soient leurs masses, peuvent participer à la boucle et, de ce fait, peuvent donner aux observables physiques des valeurs éloignées de celles prévues dans le cadre du Modèle Standard.

Nous rapportons la première observation d'une désintégration radiative pingouin du méson B_s^0 dans le mode $B_s^0 \rightarrow \phi\gamma$ avec une signification statistique de 5.5 déviations standards. Nous mesurons

$$\mathcal{B}(B_s^0 \rightarrow \phi\gamma) = (57_{-15}^{+18}(\text{stat})_{-11}^{+12}(\text{syst})) \times 10^{-6}$$

en accord avec les prévisions du Modèle Standard. Nous n'observons pas de signal significatif dans le mode $B_s^0 \rightarrow \gamma\gamma$ et nous calculons une limite supérieure avec un niveau de confiance de 90% sur son rapport d'embranchement de

$$\mathcal{B}(B_s^0 \rightarrow \gamma\gamma) < 8.7 \times 10^{-6}.$$

Cette limite est environ six fois plus restrictive que celle précédemment publiée. Cependant, elle est environ d'un ordre de magnitude plus élevée que le rapport d'embranchement prévu par le Modèle Standard et encore au-dessus des prévisions des modèles de Nouvelle Physique.

Concernant l'étude des désintégrations résonantes $B^+ \rightarrow K^+h \rightarrow K^+\gamma\gamma$, nous cherchons les désintégrations où la particule h peut être un méson $\eta, \eta', \eta_c, \eta_c(2S), \chi_{c0}, \chi_{c2}$ ou J/ψ , ou la particule $X(3872)$ qui fut découverte en 2003 par la collaboration Belle. Nous observons les modes avec $h = \eta$ and η' . Nous obtenons une évidence du mode où h est η_c ;

¹Le mot anglais "penguin" devrait en fait être traduit en français par "manchot". Manchots et pingouins appartiennent à deux espèces bien distinctes; les manchots vivent dans l'hémisphère sud et les pingouins dans l'hémisphère nord. Pingouin se traduit par "auk" en anglais.

ceci est la première fois qu'un signal de la désintégration $B^+ \rightarrow K^+\eta_c$ est vu dans l'état final $K^+\gamma\gamma$. Nous mesurons

$$\begin{aligned}\mathcal{B}(B^+ \rightarrow K^+\eta \rightarrow K^+\gamma\gamma) &= (0.87_{-0.15}^{+0.16}(\text{stat})_{-0.07}^{+0.10}(\text{syst})) \times 10^{-6}, \\ \mathcal{B}(B^+ \rightarrow K^+\eta' \rightarrow K^+\gamma\gamma) &= (1.40_{-0.15}^{+0.16}(\text{stat})_{-0.12}^{+0.15}(\text{syst})) \times 10^{-6}, \\ \mathcal{B}(B^+ \rightarrow K^+\eta_c \rightarrow K^+\gamma\gamma) &= (0.22_{-0.07}^{+0.09}(\text{stat})_{-0.02}^{+0.04}(\text{syst})) \times 10^{-6},\end{aligned}$$

avec des significations statistiques de 7.3, 13.8 et 4.1, respectivement. Pour les autres modes, nous obtenons des limites sur leur rapports d'embranchement. Nous mesurons aussi les rapports d'embranchement de h en deux photons si le rapport d'embranchement $\mathcal{B}(B^+ \rightarrow K^+h)$ a été mesuré ailleurs. Nous obtenons la première limite sur le rapport d'embranchement $\mathcal{B}(X(3872) \rightarrow \gamma\gamma)$ avec un niveau de confiance de 90% de

$$\mathcal{B}(X(3872) \rightarrow \gamma\gamma) < 1.1\%.$$

Mots-clés: physique des hautes énergies, KEK, Belle, Modèle Standard, Nouvelle Physique, physique du méson B, désintégrations pingouin.

Acknowledgments

ALL the work presented in this document would not have been possible without the help from many people. Particle physics is a world where individual and non concerted efforts usually lead to insignificant results.

I would like to thank my thesis supervisor Olivier Schneider for his incredible patience to answer my numerous questions, as well as Thomas Schietinger for introducing me to the world of penguins.

Belle is a collaboration of more than 300 physicists from 13 countries. I would like to thank the people who internally refereed my analyses: Stefano Villa (chair), Yutaka Ushiroda and Li Jin for the $B^+ \rightarrow K^+ \gamma \gamma$ analysis, and Alexey Drutskoy (chair), Alex Bondar and Gary Varner for the $B_s^0 \rightarrow \phi \gamma$ and $B_s^0 \rightarrow \gamma \gamma$ analysis. Both analyses were refined and presented many times within the DCPV/rare group lead by Mikihiro Nakao, Shohei Nishida and Kai-Feng Chen. The second analysis was also polished during $\Upsilon(5S)$ group meetings convened by Kay Kinoshita, Alexey Drutskoy and Alan Schwartz. I also would like to thank our spokespersons, Tom Browder, Toru Iijima and Masanori Yamauchi, and our physics coordinators, Paoti Chang and Yoshihide Sakai. In addition, Simon Eidelman, Alex Kuzmin, and Bruce Yabsley provided improvements to my work by provoking fruitful discussions. Moreover, many people helped me to survive in a sometimes hostile but always interesting Japanese environment; for this, I would like to thank Frédéric Ronga, Pablo Goldenzweig, Antonio Limosani, Nick Hastings and Ralf Seidl.

Members of the Lausanne Belle group are also accountable for all the results reported in this document. I would like to thank Tagir Aushev, Aurelio Bay, Christian Jacoby, Luc Hinz, Remi Louvot, Olivier Schneider, Kim Vervink, Stefano Villa, Dario Zurcher and Nicolas Zwahlen. Speaking of our laboratory, I would like to thank our secretaries, Erika and Esther, as well as all its members for the good and friendly atmosphere.

I would like to thank the thesis jury president, Robert Schaller, as well as the experts, Ulrik Egede, Alexey Drutskoy and Thomas Schietinger.

Finally, I would like to thank for their support my parents, Henri Joseph and Elisabeth, my brother, Nicolas, and my sister, Laurence. The most significant discovery (at least for me) achieved during this thesis is of course, Satoko, without whom I would not have had the courage to finish this work.

Lausanne, April 2008.

Contents

Abstract	I
Résumé	III
Acknowledgments	V
1 Theoretical framework and motivations	3
1.1 The Standard Model of Particle Physics	3
1.1.1 Consistency test of the Standard Model at LEP and SLC	5
1.1.2 The CP symmetry	7
1.1.3 Flavor dynamics in the SM and measurement of the unitarity triangle	8
1.2 Physics beyond the Standard Model?	12
1.3 New Physics and penguin decays	14
1.3.1 The $B_s^0 \rightarrow \phi\gamma$ decay	16
1.3.2 The $B_s^0 \rightarrow \gamma\gamma$ decay	18
1.4 The resonant $B^+ \rightarrow K^+h \rightarrow K^+\gamma\gamma$ decays	21
2 The Belle experiment at KEKB	23
2.1 The Υ resonances and the B meson factories	23
2.1.1 The KEKB asymmetric electron-positron collider	26
2.2 The Belle detector	30
2.2.1 The beam pipe and the silicon vertex detector (SVD)	31
2.2.2 The central drift chamber (CDC)	34
2.2.3 The aerogel Cherenkov counter (ACC)	37
2.2.4 The time-of-flight counters (TOF)	37
2.2.5 The electromagnetic calorimeter (ECL)	40
2.2.6 The extreme forward calorimeter (EFC)	41
2.2.7 The K_L^0 and muon detector (KLM)	42
2.3 The trigger	42
2.3.1 The Level-1 trigger	43
2.3.2 The Level-3 trigger	46
2.3.3 The Data Acquisition system (DAQ)	46
2.3.4 The Level-4 filter and Data Summary Tapes (DST) production	46
2.4 The detector simulation	48
2.5 The flavor tagging	48
2.6 Number of B meson pairs at the Υ resonances	49

2.6.1	The luminosity measurement	49
2.6.2	The $b\bar{b}$ production cross-section	49
2.7	B_s^0 production at the $\Upsilon(5S)$ resonance	50
2.7.1	The $b\bar{b}$ production cross-section at the $\Upsilon(5S)$ resonance	50
2.7.2	The fraction f_s	50
2.7.3	The fraction $f_{B_s^* \bar{B}_s^*}$	51
3	Reconstruction	53
3.1	Signal reconstruction	53
3.1.1	Charged tracks and kaons	53
3.1.2	Photons	54
3.1.3	Resonances: the h particles and ϕ mesons	54
3.1.4	B meson selections	55
3.1.5	Definition of the signal windows	57
3.2	Background study	57
3.2.1	Continuum suppression variables	57
3.2.2	Optimization of the continuum background suppression	63
3.2.3	Background from B decays	65
3.2.4	The off-time QED background	66
3.3	Summary of all requirements and expectations	68
4	Fitting procedure and results for the $B_s^0 \rightarrow \phi\gamma$ and $B_s^0 \rightarrow \gamma\gamma$ analysis	71
4.1	Fitting procedure	71
4.1.1	Probability density functions for the signal	71
4.1.2	Probability density functions for the background	76
4.1.3	Fit parameters	76
4.2	Systematic uncertainties	77
4.2.1	Uncertainty on the signal reconstruction efficiency	77
4.2.2	Uncertainty on the number of B_s^0 mesons	79
4.3	Fit results	79
4.3.1	$B_s^0 \rightarrow \phi\gamma$	80
4.3.2	$B_s^0 \rightarrow \phi\gamma$ in the $m_{K^+K^-}$ sideband	82
4.3.3	$B_s^0 \rightarrow \gamma\gamma$	82
5	Fitting procedure and results for the $B^+ \rightarrow K^+h \rightarrow K^+\gamma\gamma$ analysis	85
5.1	Fitting procedure	85
5.1.1	Signal probability density functions and efficiencies	85
5.1.2	Background PDFs	87
5.1.3	Fit description	89
5.2	Systematic uncertainties and results	89
5.2.1	Uncertainty on the signal reconstruction efficiency	90
5.2.2	Likelihood including systematic uncertainties	91
5.3	Fit results	92
5.3.1	Fit in bins of the $m_{\gamma\gamma}$ mass	98
5.4	Study of the cross-feeds between the h resonances	99

Conclusion	103
A Continuum suppression figures for $B^+ \rightarrow K^+ h \rightarrow K^+ \gamma \gamma$	105
B Fit Parameters for $B_s^0 \rightarrow \phi \gamma$ and $B_s^0 \rightarrow \gamma \gamma$	109
C Signal probability density functions for $B^+ \rightarrow K^+ h \rightarrow K^+ \gamma \gamma$	111
D Fit Parameters for $B^+ \rightarrow K^+ h \rightarrow K^+ \gamma \gamma$	113
Bibliography	127

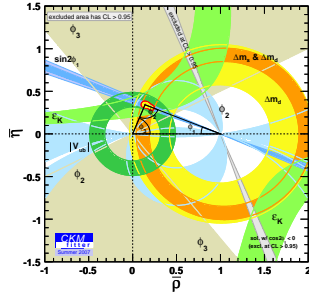
« Much human ingenuity has gone into finding the ultimate Before.
The current state of knowledge can be summarized thus:
In the beginning, there was nothing, which exploded.

Other theories about the ultimate start involve gods creating the universe out of the ribs, entrails and testicles of their father (gods like a joke as much as anyone else). There are quite a lot of these. They are interesting, not for what they tell you about cosmology, but for what they say about people. Hey, kids, which part do you think they made your town out of? »

Terry Pratchett, *Lords and Ladies* (1992).

Chapter 1

Theoretical framework and motivations



This chapter introduces the Standard Model of particle physics. Penguin decays, used to probe physics beyond the Standard Model, are discussed. A detailed motivation for the subjects of this research is presented.

1.1 The Standard Model of Particle Physics

THE Standard Model (SM) is a theory describing all known particles and all known interactions except the gravitation. It was developed by many theorists during the second part of the last century and many Nobel Prizes in Physics are related to its construction. The unification of the electromagnetic and weak interactions and the prediction of the W and Z bosons has awarded the 1979 Nobel Prize to Glashow, Salam and Weinberg. The quantum formulation of the electroweak interaction has awarded 't Hooft and Veltman the 1999 Nobel Prize. The development of quantum chromodynamics (QCD) has awarded Nobel Prizes to Gell-Mann in 1969 and to Gross, Politzer and Wilczek in 2004.

The SM¹ is a gauge theory that describes interactions with the exchange of spin-1 gauge fields. It is based on the symmetry group

$$SU(3)_C \otimes SU(2)_L \otimes U(1)_Y, \quad (1.1)$$

where $SU(3)_C$ describes the strong interaction via the exchange of eight massless gluons (g), $SU(2)_L$ describes the weak interaction which proceeds with the exchange of three massive bosons, the W^\pm and Z , and $U(1)_Y$ describes the electromagnetic interaction proceeding via photon (γ) exchange. C and Y are, respectively, the color and hypercharge

¹The following discussion is mainly based on [1].

Table 1.1: SM bosons. Masses are taken from [2]. The mass interval for the Higgs boson is computed at the 95% CL.

Boson	Mass (GeV/ c^2)	Force carried
Photon	0	electromagnetic interaction
W^\pm	80.403 ± 0.029	weak interaction (charged current)
Z	91.1876 ± 0.0021	weak interaction (neutral current)
8 gluons	0	strong interaction
Higgs	$114.4 < m_H < 144$	–

quantum numbers, and L denotes that weak interactions are left-handed. The SM bosons are listed in Table 1.1.

Fermions are spin- $\frac{1}{2}$ particles. In the SM, they are arranged in three generations and belong to two types, quarks and leptons, with each generation made of two quarks and two leptons, plus corresponding anti-fermions. We have therefore six quarks: u (called up), d (down), c (charm), s (strange), t (top or truth) and b (bottom or beauty). Leptons are composed of the electron (e^-), the muon (μ^-) and the tau (τ^-), and their associated neutrinos (eg. ν_e , the electron neutrino). The fermions are listed in Table 1.2. They are organized in the following structure with three generations

$$\begin{bmatrix} \nu_e & u \\ e^- & d' \end{bmatrix}, \quad \begin{bmatrix} \nu_\mu & c \\ \mu^- & s' \end{bmatrix}, \quad \begin{bmatrix} \nu_\tau & t \\ \tau^- & b' \end{bmatrix}, \quad (1.2)$$

with

$$\begin{bmatrix} \nu_l & q_u \\ l^- & q_d \end{bmatrix} \equiv \begin{pmatrix} \nu_l \\ l^- \end{pmatrix}_L, \quad \begin{pmatrix} q_u \\ q_d \end{pmatrix}_L, \quad l_R^-, \quad q_{uR}, \quad q_{dR}, \quad (1.3)$$

plus the corresponding anti-fermions.

Left-handed fields are therefore $SU(2)_L$ doublets, while right-handed fields are singlets. One can notice that the SM does not contain right-handed neutrinos. The three fermionic families behave identically under gauge interactions. However, they have different masses and flavor quantum numbers.

Quarks cannot act as isolated particles due to the color confinement mechanism [1]. They always appear in quark triplets, called baryons, or in quark-anti-quark pairs, called mesons. Well-known baryons are the proton and the neutron, whose quark compositions are uud and udd , respectively. Mesons appearing in the title of this document are the B_s^0 ($\bar{b}s$), B^+ ($\bar{b}u$), ϕ ($s\bar{s}$) and K^+ ($\bar{s}u$) mesons.

The gauge symmetry is broken by the vacuum in a so-called Spontaneous Symmetry Breaking (SSB) mechanism, where the electromagnetic and weak groups are unified into the electroweak group

$$SU(3)_C \otimes SU(2)_L \otimes U(1)_Y \xrightarrow{\text{SSB}} SU(3)_C \otimes U(1)_{\text{QED}}. \quad (1.4)$$

Table 1.2: SM fermions. Electron and muon masses have been measured with a precision of less than 1 ppm. Anti-particles have the same masses but are oppositely-charged. All values are taken from [2] except the top mass which is taken from [3]. Masses are given in MeV/c^2 and charges (Q) in unit of positron charge (e). Upper limits on the neutrino masses are given at the 90% CL for the muon neutrino and at the 95% CL for the two others. Cosmological evidences indicate that $\sum m_\nu < 0.62 \text{ eV}$ (95% CL) [4].

Generation	Quarks	Q	Mass	Leptons	Q	Mass
1 st	u	$+\frac{2}{3}$	$1.5 - 3.0$	e^-	-1	0.511
	d	$-\frac{1}{3}$	$3 - 7$	ν_e	0	$< 2 \times 10^{-6}$
2 nd	c	$+\frac{2}{3}$	1250 ± 90	μ^-	-1	105.7
	s	$-\frac{1}{3}$	95 ± 25	ν_μ	0	< 0.19
3 rd	t	$+\frac{2}{3}$	170900 ± 1800	τ^-	-1	1776.90 ± 0.20
	b	$-\frac{1}{3}$	$4200 - 4700$	ν_τ	0	< 18.2

The SSB generates the masses of the weak gauge bosons, and creates a scalar particle, the Higgs boson, which is the only fundamental SM particle to remain undiscovered. Fermion masses and flavor mixing are also generated by the SSB.

1.1.1 Consistency test of the Standard Model at LEP and SLC

The gauge sector of the SM was extensively tested at LEP and SLC, e^+e^- colliders which took data at the Z resonance. A summary of these tests is presented in a so-called global electroweak fit [5, 6]. Results are shown in Figure 1.1, where the last column is the pull of each measurement, eg. the difference between the measurement and the SM expectation in units of the measurement uncertainty. All these variables are discussed in [5]. The vast majority of shown pulls are below one standard deviation. Only one measurement, $A_{\text{fb}}^{0,b}$, the forward-backward asymmetry in b productions, has a pull at a dangerous level (2.9σ). This deviation can be viewed as a statistical fluctuation considering the fact that 17 observables were measured. Some physicists had hoped that LEP would have run longer to measure $A_{\text{fb}}^{0,b}$ more precisely; however, the general consensus is that LEP proved that the SM was very successful, beyond the expectations of many physicists.

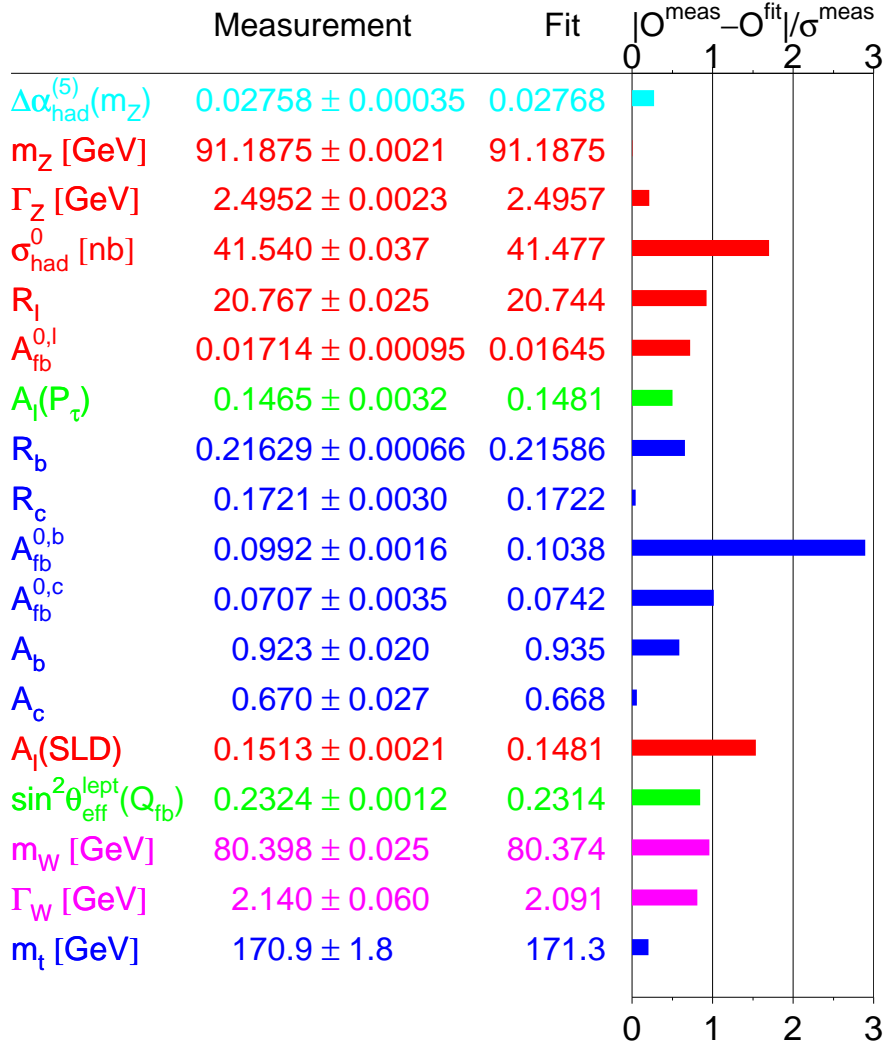


Figure 1.1: Comparison of the combined SM measurements performed at LEP and SLC with the expectation of the SM, obtained from the global electroweak fit [5, 6] (Winter 2007 update). The top mass (m_t) is measured at the Tevatron [3].

1.1.2 The CP symmetry

The CP symmetry denotes the fact that physical processes behave identically for particles and particles converted by the CP transformation. The C operation, the charge conjugation, reverses all additive quantum numbers such as the electric charge, the hypercharge or the strangeness. The P (parity) transformation inverts the coordinate system, ie.

$$\begin{pmatrix} x \\ y \\ z \end{pmatrix} \xrightarrow{P} \begin{pmatrix} -x \\ -y \\ -z \end{pmatrix}. \quad (1.5)$$

The CP operation is the combination of the C and P transformations. For a proton traveling along the x axis with its spin anti-aligned with its momentum (left-handed), P inverts the velocity direction but doesn't change its internal quantum numbers (the spin for instance); the proton helicity becomes right-handed. A left-handed proton becomes, after a CP operation, a right-handed antiproton.

The violation of the P symmetry was discovered in nuclear β decays in 1957 [7]. The P symmetry is now known as being “maximally” violated in the Standard Model: a right-handed neutrino doesn't exist or interact (sterile neutrino), while left-handed neutrinos do. The previous statement arises from the non-observation of right-handed currents in neutrino scattering experiments. C is also “maximally” violated in the SM for the same reason: under a C transformation, a left-handed neutrino becomes a left-handed anti-neutrino.

The CP symmetry was thought to be conserved in Nature: under CP , a left-handed neutrino becomes a right-handed anti-neutrino and both exist and/or interact. However, it was discovered in 1964 that the CP symmetry was slightly broken, at the 0.2% level, in kaon decays [8]. CP violation has been also observed in the B meson system in Summer 2001 by the Belle [9] and *BABAR* [10] experiments with the measurement of $\sin 2\phi_1 \neq 0^2$ in $B^0 \rightarrow J/\psi K_S^{0,3}$ decays. Since then, both Belle and *BABAR* have observed CP violation in many other decay modes of the neutral and charged B mesons.

The violation of the CP symmetry is one of the necessary ingredients to explain the observed absence of anti-matter in our Universe [11]. Indeed, it is thought that the Big Bang created equal quantities of matter and anti-matter. One of the interactions, the weak interaction in the SM, has to violate CP . However, to date, all observed CP violation rates are compatible with the SM predictions and the source of CP violation in the SM is not large enough to explain the observed absence of anti-matter. Hence, new sources of CP violations are needed.

It is to note that the CPT symmetry, where T is the time-reversal operation, is respected in every Lorentz-invariant local quantum field theory with a Hermitian Hamiltonian due to the CPT theorem [12]. To preserve CPT and break CP at the same time means that the T symmetry has to be broken too. In fact, mathematically, CP and T violations are the same phenomena since the CPT symmetry can be derived from theory axioms. The CPT symmetry constrains particles and anti-particles to have the same masses and lifetimes, which is so far always confirmed by experiments. An observation of

²The angle ϕ_1 will be introduced in the next Section.

³If not explicitly written, the inclusion of the charge conjugate mode is implied throughout this document.

CPT violation would put an immediate end to most particle physics theories, including the Standard Model.

1.1.3 Flavor dynamics in the SM and measurement of the unitarity triangle

After the SSB, flavor dynamics in the SM is described with the following Yukawa Lagrangian

$$\mathcal{L}_Y \sim \bar{\mathbf{d}}'_L M'_d \mathbf{d}'_R + \bar{\mathbf{u}}'_L M'_u \mathbf{u}'_R + \bar{\mathbf{l}}'_L M'_l \mathbf{l}'_R + \text{h.c.}, \quad (1.6)$$

where M' are 3×3 matrices containing arbitrary coupling constants and \mathbf{d}' , \mathbf{u}' , \mathbf{l}' are three dimensional vectors in the flavor space defined as

$$\begin{aligned} \mathbf{d}' &\equiv (d', s', b'), \\ \mathbf{u}' &\equiv (u', c', t'), \\ \mathbf{l}' &\equiv ((e^-)', (\mu^-)', (\tau^-)'). \end{aligned} \quad (1.7)$$

Each of the three M' matrices can be decomposed as

$$M' = S^\dagger \mathcal{M} S U, \quad (1.8)$$

where S and U are unitary matrices (ie. $S S^\dagger = S^\dagger S = 1$) and \mathcal{M} is diagonal and contains masses, ie.

$$\mathcal{M}_d = \begin{pmatrix} m_d & 0 & 0 \\ 0 & m_s & 0 \\ 0 & 0 & m_b \end{pmatrix}, \quad \mathcal{M}_u = \begin{pmatrix} m_u & 0 & 0 \\ 0 & m_c & 0 \\ 0 & 0 & m_t \end{pmatrix}, \quad \mathcal{M}_l = \begin{pmatrix} m_e & 0 & 0 \\ 0 & m_\mu & 0 \\ 0 & 0 & m_\tau \end{pmatrix}. \quad (1.9)$$

The Yukawa Lagrangian is now simplified to

$$\mathcal{L}_Y \sim \bar{\mathbf{d}} \mathcal{M}_d \mathbf{d} + \bar{\mathbf{u}} \mathcal{M}_u \mathbf{u} + \bar{\mathbf{l}} \mathcal{M}_l \mathbf{l} + \text{h.c.}, \quad (1.10)$$

where the mass eigenstates are defined by

$$\begin{aligned} \mathbf{d}_L &\equiv S_d \mathbf{d}'_L, \\ \mathbf{u}_L &\equiv S_u \mathbf{u}'_L, \\ \mathbf{l}_L &\equiv S_l \mathbf{l}'_L, \end{aligned} \quad (1.11)$$

and

$$\begin{aligned} \mathbf{d}_R &\equiv S_d U_d \mathbf{d}'_R, \\ \mathbf{u}_R &\equiv S_u U_u \mathbf{u}'_R, \\ \mathbf{l}_R &\equiv S_l U_l \mathbf{l}'_R. \end{aligned} \quad (1.12)$$

Due to the unitarity of S , we have

$$\bar{\mathbf{f}}'_L \mathbf{f}'_L = \bar{\mathbf{f}}_L S S^\dagger \mathbf{f}_L = \bar{\mathbf{f}}_L \mathbf{f}_L, \quad (1.13)$$

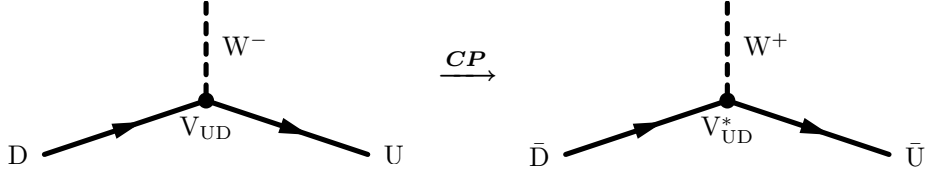


Figure 1.2: Left: D to U charged-current quark transition governed by the V_{UD} matrix element. The D quark can be d , s or b and U can be u , c or t . Right: \bar{D} to \bar{U} transition governed by V_{UD}^* obtained with a CP transformation of the left transition.

and similarly for $\bar{\mathbf{f}}_R \mathbf{f}'_R = \bar{\mathbf{f}}'_R \mathbf{f}_R$. Hence, the $SU(2)_L \otimes U(1)_Y$ Lagrangian responsible for neutral currents is not modified when expressed in terms of mass eigenstates. There are therefore no flavor-changing neutral currents (FCNC) in the SM (eg. $b \rightarrow sZ$). The former affirmation is only valid at the tree level: loop-mediated FCNC (Penguin) decays are possible and will be discussed in Section 1.3. In such diagrams, the flavor is in fact changed twice (eg. $b \rightarrow t \rightarrow s$) by charged currents (W boson). The absence of FCNC at the tree level was explained in 1970 by Glashow, Iliopoulos and Maiani (GIM mechanism) [13] and requires two-fermions families. The existence of a partner to the s quark (the charm quark) was foreseen by this mechanism.

However, charged currents can change flavor since

$$\bar{\mathbf{u}}'_L \mathbf{d}'_L = \bar{\mathbf{u}}_L \mathbf{S}_u \mathbf{S}_d^\dagger \mathbf{d}_L \equiv \bar{\mathbf{u}}_L \mathbf{V} \mathbf{d}_L, \quad (1.14)$$

and \mathbf{S}_u and \mathbf{S}_d are generally different. Flavor-changing currents are shown in Figure 1.2. The \mathbf{V} matrix is a 3×3 unitary matrix coupling up-type (\mathbf{u}) quarks to the down-type (\mathbf{d}) quarks and is called the Cabibbo-Kobayashi-Maskawa (CKM) matrix [14, 15]

$$\begin{pmatrix} d' \\ s' \\ b' \end{pmatrix} = \begin{pmatrix} V_{ud} & V_{us} & V_{ub} \\ V_{cd} & V_{cs} & V_{cb} \\ V_{td} & V_{ts} & V_{tb} \end{pmatrix} \times \begin{pmatrix} d \\ s \\ b \end{pmatrix} = \mathbf{V}_{\text{CKM}} \times \begin{pmatrix} d \\ s \\ b \end{pmatrix}. \quad (1.15)$$

If we consider the general case with N_G fermionic generations, it can be demonstrated that \mathbf{V} can be characterized by $N_G(N_G-1)/2$ (real) mixing angles and $(N_G-1)(N_G-2)/2$ complex phases. Hence, for $N_G = 2$, \mathbf{V} takes the form of the well-known Cabibbo rotation matrix [14]

$$\mathbf{V}_{\text{two gen.}} = \begin{pmatrix} \cos \theta_C & \sin \theta_C \\ -\sin \theta_C & \cos \theta_C \end{pmatrix}, \quad (1.16)$$

where θ_C is the Cabibbo angle. The Lagrangian with $N_G = 2$ does therefore not contain any complex phase and thus cannot accommodate CP violation. A third fermion generation is required and was foreseen by Kobayashi and Maskawa [15] to explain the observed CP violation in the kaon system [8]. Indeed, with $N_G = 3$, the SM contains one complex phase, responsible for the CP violation in the SM, and three real mixing angles.

The CKM-matrix exhibits the following hierarchy in its measured entries: the diagonal elements are very close to unity, the ones connecting the two first generations have a size

$\lambda \equiv \sin \theta_C |V_{us}| \approx 0.22$, the mixing between the second and third families is of the order λ^2 and the mixing between the first and third families of the order λ^3 . The CKM matrix can therefore be expressed in the so-called Wolfenstein parametrization [16]

$$\mathbf{V}_{\text{CKM}} = \begin{pmatrix} 1 - \frac{\lambda^2}{2} & \lambda & A\lambda^3(\rho - i\eta) \\ -\lambda & 1 - \frac{\lambda^2}{2} & A\lambda^2 \\ A\lambda^3(1 - \rho - i\eta) & -A\lambda^2 & 1 \end{pmatrix} + \mathcal{O}(\lambda^4), \quad (1.17)$$

where A , λ , ρ and η owe four real parameters. The η parameter is the complex-phase parameter, hence is responsible of CP violation in the SM.

The unitarity triangle

Due to the unitarity of the CKM matrix, we can write 12 equations given by $\sum_k V_{ki} V_{kj}^* = \delta_{ij}$. Equations with $i \neq j$ can be represented as triangles in the complex plane. The following triangle, called the unitarity triangle, is of particular interest

$$V_{ub}^* V_{ud} + V_{cb}^* V_{cd} + V_{tb}^* V_{td} = 0. \quad (1.18)$$

This triangle is usually rescaled by dividing its sides by $V_{cb} V_{cd} = -A\lambda^3 + \mathcal{O}(\lambda^7)$, which is real to a very good approximation [17, 18]. This aligns one side of the triangle along the real axis and makes its length equal to 1. The coordinates of the 3 vertices are then $(0,0)$, $(1,0)$ and $(\bar{\rho}, \bar{\eta}) \equiv (1 - \lambda^2/2)(\rho, \eta)$. The three angles of this triangle are⁴

$$\phi_1 \equiv \beta \equiv \arg \left(-\frac{V_{cd} V_{cb}^*}{V_{td} V_{tb}^*} \right), \quad (1.19)$$

$$\phi_2 \equiv \alpha \equiv \arg \left(-\frac{V_{td} V_{tb}^*}{V_{ud} V_{ub}^*} \right), \quad (1.20)$$

$$\phi_3 \equiv \gamma \equiv \arg \left(-\frac{V_{ud} V_{ub}^*}{V_{cd} V_{cb}^*} \right), \quad (1.21)$$

and the lengths are

$$R_b \equiv \left| \frac{V_{ud} V_{ub}^*}{V_{cd} V_{cb}^*} \right| = \sqrt{\bar{\rho}^2 + \bar{\eta}^2} = \left(1 - \frac{\lambda^2}{2} \right) \frac{1}{\lambda} \left| \frac{V_{ub}}{V_{cb}} \right|, \quad (1.22)$$

$$R_t \equiv \left| \frac{V_{td} V_{tb}^*}{V_{cd} V_{cb}^*} \right| = \sqrt{(1 - \bar{\rho})^2 + \bar{\eta}^2} = \frac{1}{\lambda} \left| \frac{V_{td}}{V_{cb}} \right| \approx \frac{1}{\lambda} \frac{|V_{td}|}{|V_{ts}|}, \quad (1.23)$$

where R_b is the side opposite to the angle ϕ_1 and R_t is the side opposite to ϕ_3 . The length of the side opposite to ϕ_2 is equal to unity due to the normalization.

Figure 1.3 presents the Summer 2007 status, obtained by the CKMfitter group [19], on the experimental results constraining the unitarity triangle. Every measured observable constrains the upper vertex of the triangle; the agreement between all measurements is very good. The UTfit group provides similar plots [20]. We briefly discuss below how the different parameters are measured.

⁴The denomination $\phi_{1,2,3}$ is used by Belle, while (α, β, γ) is used by BABAR and the rest of the world.

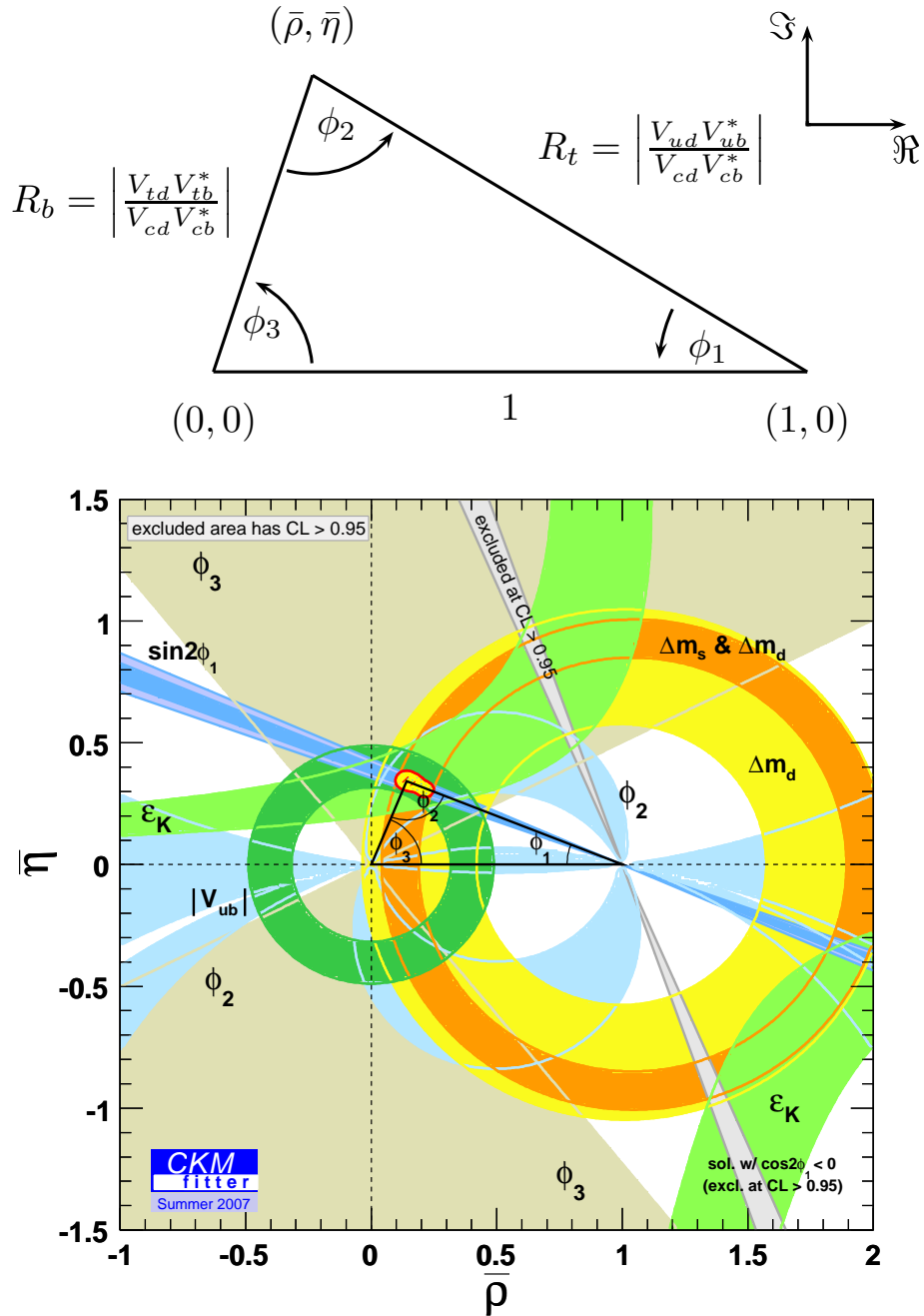


Figure 1.3: Top: the unitarity triangle. Bottom: experimental constraints on the unitarity triangle, as compiled by the CKMfitter group presented at the time of the summer 2007 conferences [19].

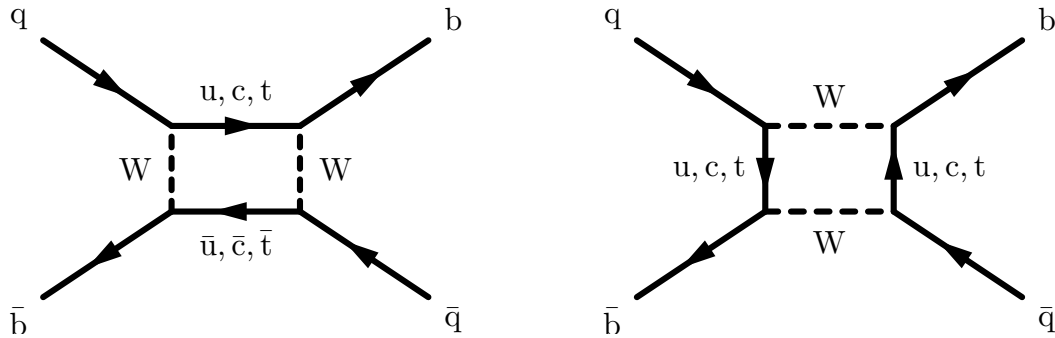


Figure 1.4: Feynman diagrams for the mixing in the neutral B meson systems ($q = d, s$). The mixing amplitude is proportional to the square of the quark mass involved in the box, hence the top contribution dominates entirely.

R_b involves the ratio $|V_{ub}/V_{cb}|$ and is therefore measured by studying $b \rightarrow u$ and $b \rightarrow c$ transitions. Equation 1.22 indicates that its constraint in the $(\bar{\rho}, \bar{\eta})$ plane is a circle centered at $(0, 0)$.

R_t involves the ratio $|V_{td}/V_{cb}|$. $|V_{tb}|$ is obtained from the measured mass difference between the mass eigenstates of the $B^0-\bar{B}^0$ system, $\Delta m_d = (0.507 \pm 0.005) \text{ ps}^{-1}$ [2], which governs the $B^0-\bar{B}^0$ mixing transition, shown in Figure 1.4. The observation of $B_s^0-\bar{B}_s^0$ mixing with the measurement of $\Delta m_s = (17.77 \pm 0.12) \text{ ps}^{-1}$ [21] provides information on R_t since the ratio $\Delta m_d/\Delta m_s$ gives $|V_{td}|/|V_{ts}|$. Constraints on R_t are circles centered at $(1, 0)$ in the $(\bar{\rho}, \bar{\eta})$ plane.

Angles of the Unitarity Triangle can be probed by studying B decays into CP (self-conjugated) final states [22, 23, 24]. $B^0(\bar{B}^0) \rightarrow J/\psi K_S^0$, a $b \rightarrow c\bar{c}s$ transition, is the golden mode to probe ϕ_1 . From the latter and other modes, one obtains $\sin 2\phi_1 = 0.673 \pm 0.028$ [2], which is the strongest constraint on the CKM picture. ϕ_2 can be measured with $b \rightarrow u\bar{u}d$ transitions. The most sensitive mode to determine ϕ_2 is $B^0 \rightarrow \rho^+\rho^-$: we obtain $\phi_2 = (96 \pm 10)^\circ$ [2]. The angle ϕ_3 is the most challenging angle to measure. It is studied with the interference of the $b \rightarrow c$ and $b \rightarrow u$ transitions in $B \rightarrow DK$ decays. To date, the only method returning a significant result on ϕ_3 is the so-called GGSZ method proposed at the same time by the Belle collaboration [25] and Giri, Grossman, Soffer and Zupan [26]. ϕ_3 can also be measured in $B \rightarrow DK$ decays with the ADS method [27] and the GLW method [28]. A combination of all results gives $\phi_3 = (77 \pm 31)^\circ$ [19].

The parameter ϵ_K , related to CP violation in the kaon sector, gives a hyperbolic constraint in the $(\bar{\rho}, \bar{\eta})$ plane.

1.2 Physics beyond the Standard Model?

The SM is a very successful story. The SM, for example, predicted the Z and W boson masses, the existence of the charm quark, and that of the third fermion generation. The SM is compatible with more than 1000 pages of measurements centralized by the Particle Data Group [2]. The gauge part of the SM has been extensively tested at LEP and has proved to be well described. Flavor physics has been extensively tested mainly by the B -factories and has also proved to be well understood. However, the link between gauge

physics and flavor physics, the Higgs boson is still missing. The SM will only be considered a complete theory when the Higgs boson will be discovered, which is expected to happen in the next decade at the Large Hadron Collider (LHC) at CERN.

Although SM Lagrangians can be derived only from the gauge principle [1], the SM looks like a phenomenological model due to the large number of arbitrary parameters. For example, all fermion masses are not predicted by the theory and have therefore to be measured before the SM can be of any use to describe the flavor sector. The SM fails to answer many fundamental questions. Why are there three and only three fermion families? Why are the masses so different between the families? For instance, the top quark is more than 40'000 times heavier than the up quark. The SM can so far describe all measurements of CP violation; however, the SM source of CP violation is not sufficient to explain the matter - anti-matter asymmetry in our Universe. Moreover, the SM cannot accommodate gravitation. Particle physicists can live without gravitation since it is a very weak force at the scale where particle physics occur. However, gravitation is still a fundamental force of Nature, which is quite important at human scale.

Neutrinos in the SM are considered to be massless. However, the observation of flavor mixing in the neutrino sector [29, 30, 31] implies by quantum theory arguments that they are massive. This is an explicit sign of New Physics (NP). However, the SM can be modified quite easily to incorporate neutrino masses and mixing [1]. Consequences are that lepton numbers can be violated⁵ (eg. $\tau^- \rightarrow e^- \gamma$) and the CP symmetry in the leptonic sector may be broken. This new source of CP violation could help understand the anti-matter disappearance in our Universe.

Another hint for NP is the Dark Matter (DM). DM was hypothesized to explain the so-called galaxy rotation problem: for many galaxies, the rotation velocity as a function of the distance to the galactic center doesn't seem to follow Newtonian dynamics, assuming that it is governed by the observed mass distribution of the galaxy [32]. Some invisible mass has to be present. To date, the best evidence for the DM existence is the Bullet Cluster [33], shown in Figure 1.5. Two clusters of galaxies collided about 150 millions years ago. One can notice that the different types of matter had their own behaviour. Stars were only slightly slowed down due to gravitational interaction. Gas, observed in X-rays, was much more slowed down and scattered than the stars due to electromagnetic interactions. However, the mass distribution, observed through gravitational lensing, didn't correspond to the gas distribution as expected but lie ahead. Clowe et al. conclude that most of the matter in the colliding clusters is collisionless and can only be explained by weakly interacting matter, the DM. The galaxy rotation problem relies on Newtonian dynamics, hence it can be solved by modifying this dynamics. The Bullet cluster provides evidence that is difficult to revoke with modified dynamics or gravitation theories. DM seems also to be necessary for the structure formation in our Universe. Just after the Big Bang, the Universe was in a very hot, dense and almost uniform state [34]. However, we observe now structures at all scales: from stars to galaxies and even clusters of galaxies with large voids between them. DM acts as a compactor of structures [35]. Weakly interacting massive particles (WIMP) are currently searched by many experiments; to date, no conclusive evidence has been found. Section 1.3.2 will show that the supersymmetry theory provides a good candidate for DM.

⁵However, this violation is very suppressed due to the very small neutrino masses.

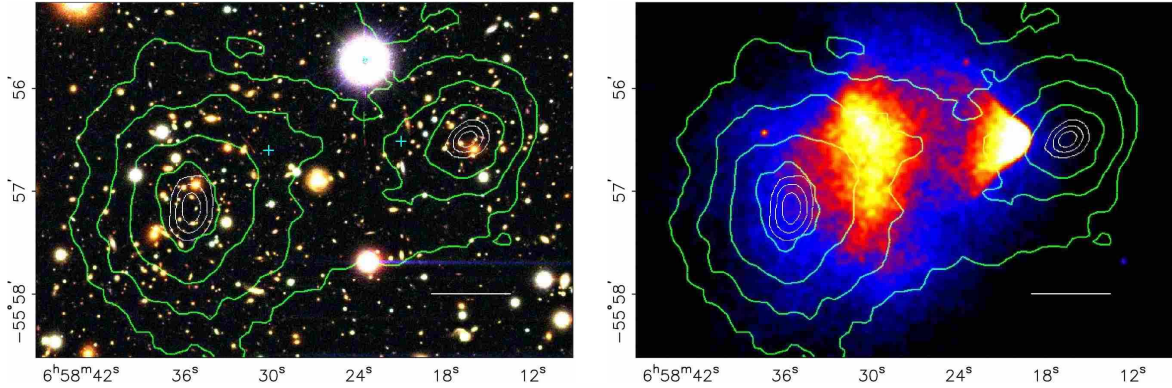


Figure 1.5: Images of the Bullet cluster [33] obtained from optical (left) and X-ray (right) observations. Mass density contours obtained from gravitational lensing are superimposed on both images, showing a clear discrepancy with the distribution of visible matter.

1.3 New Physics and penguin decays

As mentioned in Section 1.1.3, flavor changing neutral currents (FCNC) are absent at the tree level in the SM. However, loop-induced FCNC are possible and are called penguin decays. The “penguin” term takes its origin in a game of darts in the summer of 1977, involving John Ellis and other physicists, where a joke about penguins gave rise to the decision that the dart game loser would have to use the word “penguin” in his next paper. Ellis lost and named loop diagrams in B decays as “penguin decays” in [36], without any further explanation. Since then, “penguin” has de facto become the term to describe all loop diagrams. However, loop diagrams were not invented by Ellis but were first introduced to explain certain kaon properties [37].

For B mesons, two penguin transitions are possible, $b \rightarrow d$ and $b \rightarrow s$, proceeding with a loop where a W boson and an up-type quark are involved. To conserve energy and momentum, a particle has to be emitted in the process. This particle defines the type of penguin transition and can be:

- one or more real photons (electromagnetic penguin),
- a virtual Z boson or virtual photon producing two leptons (electroweak penguin),
- a gluon (gluonic penguin).

One also speaks about annihilation (or vertical) electroweak penguin, when the two quarks of the B meson annihilate into each other in the loop. Example of electromagnetic and annihilation electromagnetic penguin decays are, respectively, the $B_s^0 \rightarrow \phi\gamma$ and $B_s^0 \rightarrow \gamma\gamma$ decays studied in this thesis. Examples of electroweak and gluonic penguin decays are, respectively, the $B^0 \rightarrow K^*(892)^0 l^+ l^-$ decay and the $B_s^0 \rightarrow \phi\eta$ decays. Dominant Feynman diagrams for these decays are shown in Figure 1.6. A review of penguin B decays is available in [38].

Penguin transitions are sensitive to physics beyond the Standard Model: new particles, as long as they can couple to quarks, provide some contribution to the loop and could

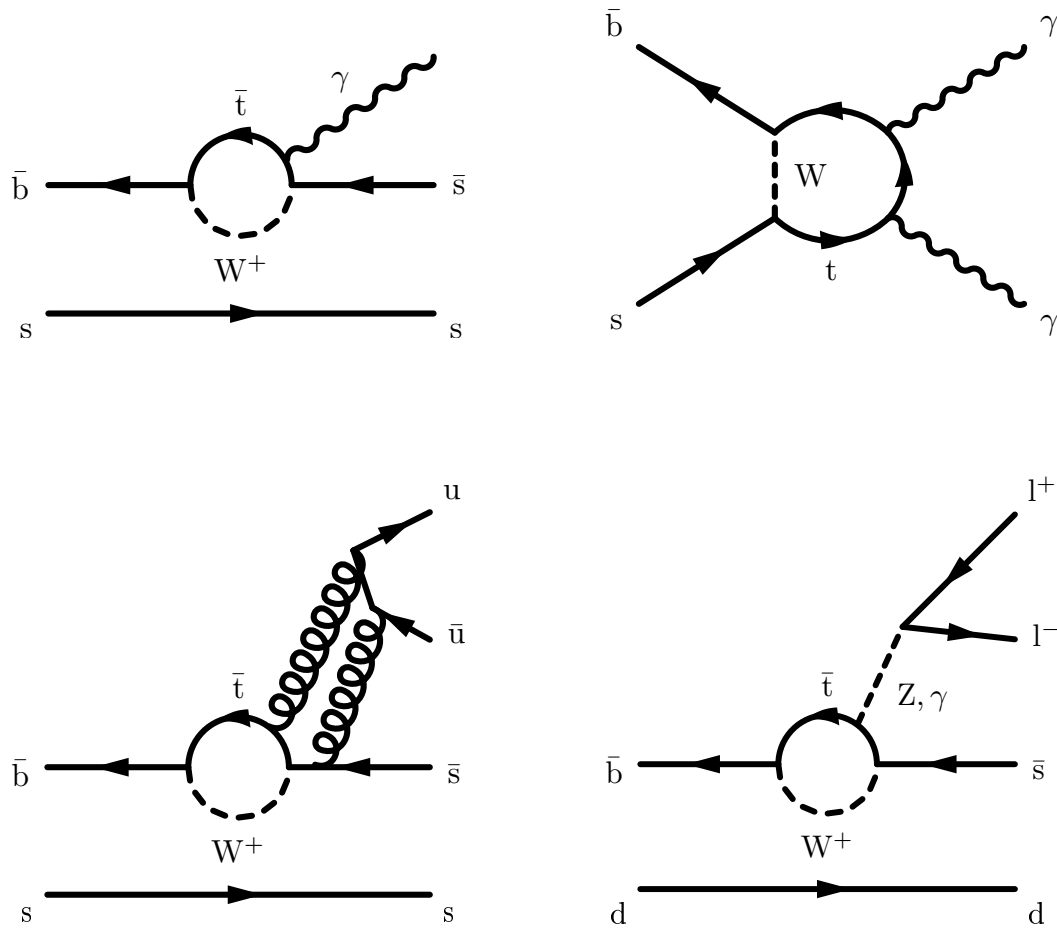


Figure 1.6: Diagrams describing the dominant processes for the $B_s^0 \rightarrow \phi \gamma$ (top left), $B_s^0 \rightarrow \gamma \gamma$ (top right), $B_s^0 \rightarrow \phi \eta$ (bottom left) and $B^0 \rightarrow K^{*0} l^+ l^-$ (bottom right) decays. In the $B_s^0 \rightarrow \phi \eta$ diagram, two gluons need to be emitted to preserve color.

modify physics observables away from their SM expectations. Observables are, for example, branching fractions, CP asymmetries, angular distributions or photon polarization.

We study in this thesis two radiative penguin decays, $B_s^0 \rightarrow \phi\gamma$ and $B_s^0 \rightarrow \gamma\gamma$. Both decays are searched in a data sample with an integrated luminosity of 23.6 fb^{-1} collected with the Belle detector at the KEKB e^+e^- (3.6 on 8.2 GeV) asymmetric-energy collider [39] operating at the $\Upsilon(5S)$ resonance (10.87 GeV). This study has been accepted for publication in Physics Review Letters [40]. Preliminary results were shown at the International Europhysics Conference on High Energy Physics (EPS-HEP2007) held in Manchester, England [41]. This study is also described in an internal Belle document, the Belle note 1009 [42]. Detailed motivations for these two decays are presented in the sections below.

1.3.1 The $B_s^0 \rightarrow \phi\gamma$ decay

The $B_s^0 \rightarrow \phi\gamma$ mode is a radiative process described within the SM by a $\bar{b} \rightarrow \bar{s}\gamma$ penguin diagram (Figure 1.6); it is the strange counterpart of the $B \rightarrow K^*(892)\gamma$ decay, whose observation by the CLEO collaboration in 1993 [43] unambiguously demonstrated the existence of penguin processes. In the SM, the $B_s^0 \rightarrow \phi\gamma$ branching fraction has been computed with $\sim 30\%$ uncertainty to be

$$\mathcal{B}_{\text{SM}}(B_s^0 \rightarrow \phi\gamma) = (43 \pm 14) \times 10^{-6}, \quad (1.24)$$

$$\mathcal{B}_{\text{SM}}(B_s^0 \rightarrow \phi\gamma) = (39.4 \pm 11.9) \times 10^{-6}, \quad (1.25)$$

where the first prediction is taken from [44] and the second from [45].

The $B_s^0 \rightarrow \phi\gamma$ decay has not yet been observed, and the upper limit at the 90% confidence level (CL) on its branching fraction has been set at 120×10^{-6} , hence about three times larger than the SM expectation, by the CDF collaboration [46].

A strong theoretical constraint on the $B_s^0 \rightarrow \phi\gamma$ branching fraction is generally assumed due to good agreement between SM expectations and experimental results for $b \rightarrow s\gamma$ rates. For example, in the $B^+ \rightarrow K^*(892)^+\gamma$ and $B^0 \rightarrow K^*(892)^0\gamma$ decays, the $SU(3)$ companions of the $B_s^0 \rightarrow \phi\gamma$ decay, we have

$$\mathcal{B}_{\text{exp.}}(B^+ \rightarrow K^*(892)^+\gamma) = (40.3 \pm 2.6) \times 10^{-6}, \quad (1.26)$$

$$\mathcal{B}_{\text{SM}}(B^+ \rightarrow K^*(892)^+\gamma) = (46 \pm 14) \times 10^{-6}, \quad (1.27)$$

$$\mathcal{B}_{\text{exp.}}(B^0 \rightarrow K^*(892)^0\gamma) = (40.1 \pm 2.0) \times 10^{-6}, \quad (1.28)$$

$$\mathcal{B}_{\text{SM}}(B^0 \rightarrow K^*(892)^0\gamma) = (43 \pm 14) \times 10^{-6}, \quad (1.29)$$

where the experimentally measured branching fractions are taken from [2] and the branching fractions evaluated in the SM from [45]. Other computations of $\mathcal{B}(B \rightarrow K^*(892)\gamma)$ in the SM can be found in [44, 47]; all predict similar rates.

The good agreement in the inclusive $B \rightarrow X_s\gamma$ decays constrains the $B_s^0 \rightarrow \phi\gamma$ decay too

$$\mathcal{B}_{\text{exp.}}(B \rightarrow X_s\gamma) = (3.54 \pm 0.26) \times 10^{-4}, \quad (1.30)$$

$$\mathcal{B}_{\text{th.}}(B \rightarrow X_s\gamma) = (3.15 \pm 0.23) \times 10^{-4}, \quad (1.31)$$

where the experimental branching fraction is taken from [2] and the theoretical one from [48].

Belle has a sample containing about 2.8 million B_s^0 mesons (it will be discussed in Chapter 2). Using the formula below, we can expect to reconstruct 14 signal events in the clean $\phi \rightarrow K^+K^-$ decay mode ($\mathcal{B}(\phi \rightarrow K^+K^-) \approx 50\%$) assuming a reconstruction efficiency (ϵ) of 25%

$$N_{B_s^0 \rightarrow \phi\gamma} = \mathcal{B}_{\text{SM}}(B_s^0 \rightarrow \phi\gamma) \times \mathcal{B}(\phi \rightarrow K^+K^-) \times N_{B_s^0} \times \epsilon. \quad (1.32)$$

A first observation is possible if we can keep the background low and still maintain this relatively high efficiency.

The goal is therefore to observe $B_s^0 \rightarrow \phi\gamma$ for the first time and to measure and compare its branching fraction with the SM expectation.

With a much larger data sample, the physics objectives could be extended. Time-dependent analyses can probe CP violation effects as well as the photon polarization. Because a ϕ meson is a CP -eigenstate, the time-dependent rate of a $B_s^0(\bar{B}_s^0)$ meson decaying to the $\phi\gamma$ final state is given by

$$\begin{aligned} \Gamma(B_s^0(\bar{B}_s^0) \rightarrow \phi\gamma) \sim & e^{-\Gamma_s|\Delta t|} \left(\cosh \frac{\Delta\Gamma_s}{2} \Delta t - \mathcal{A}^{\Delta\Gamma_s} \sinh \frac{\Delta\Gamma_s}{2} \Delta t \right. \\ & \left. \mp \mathcal{A}^{\text{dir}} \cos \Delta m_s \Delta t \mp \mathcal{A}^{\text{mix}} \sin \Delta m_s \Delta t \right), \end{aligned} \quad (1.33)$$

where \mathcal{A}^{dir} describes direct CP violation, while \mathcal{A}^{mix} and $\mathcal{A}^{\Delta\Gamma_s}$ describe mixing-induced CP violation. The direct CP asymmetry in $b \rightarrow s\gamma$ transitions is expected to be very small in the SM, $< 1\%$ according to [49]. Furthermore, the photon in the $b \rightarrow s\gamma$ transition is expected to be predominantly left-handed (right-handed for $\bar{b} \rightarrow \bar{s}\gamma$), so mixing-induced CP asymmetries are also very small [50]. The SM predicts

$$\mathcal{A}^{\text{dir}} < 1\%, \quad (1.34)$$

$$\mathcal{A}^{\text{mix}} = \sin 2\psi \sin \phi, \quad (1.35)$$

$$\mathcal{A}^{\Delta\Gamma_s} = \sin 2\psi \cos \phi, \quad (1.36)$$

where $\phi \approx 0$ is a combination of B_s^0 -mixing and decay-amplitude weak phases [50], and

$$\tan \psi \equiv \left| \frac{A(\bar{B}_s^0 \rightarrow \phi \gamma_{\text{right}})}{A(\bar{B}_s^0 \rightarrow \phi \gamma_{\text{left}})} \right| \approx \frac{m_s}{m_b} \approx \frac{1}{45}, \quad (1.37)$$

is the fraction of “wrongly”-polarized photons. This helicity fraction can be enhanced up to 40% in some NP scenarios allowing for sizeable CP mixing-induced asymmetries [50, 51]. The direct CP asymmetry could also be enhanced up to 10% to 40% in some SM extensions [52].

At B -factories running at the $\Upsilon(5S)$ resonance, due to the insufficient boost of the B_s^0 mesons, vertex detectors based on currently available technologies cannot resolve the fast B_s^0 - \bar{B}_s^0 oscillations, preventing access to \mathcal{A}^{dir} and \mathcal{A}^{mix} . It is also hopeless to measure these parameters with a tagged time-integrated analysis because B_s^0 mixing occurs with $\approx 50\%$ probability. However, an untagged analysis could in principle take advantage of the large decay width difference ($\Delta\Gamma_s/\Gamma_s \approx 15\%$ [53]) and measure $\mathcal{A}^{\Delta\Gamma_s}$, thus extracting information on the photon polarization, from the following time-dependent rate

$$\Gamma(\{B_s^0, \bar{B}_s^0\} \rightarrow \phi\gamma) \sim e^{-\Gamma_s|\Delta t|} \left(\cosh \frac{\Delta\Gamma_s}{2} \Delta t - \mathcal{A}^{\Delta\Gamma_s} \sinh \frac{\Delta\Gamma_s}{2} \Delta t \right). \quad (1.38)$$

At LHCb, thanks to a much larger boost, B_s^0 - \bar{B}_s^0 oscillations can be resolved and a tagged time-dependent analysis can simultaneously measure $\mathcal{A}^{\Delta\Gamma_s}$, \mathcal{A}^{mix} and \mathcal{A}^{dir} [54].

1.3.2 The $B_s^0 \rightarrow \gamma\gamma$ decay

The $B_s^0 \rightarrow \gamma\gamma$ mode is usually described in the SM by a penguin annihilation diagram (Figure 1.6), and its branching fraction has been calculated in the SM to be in the range [55, 56, 57]

$$\mathcal{B}_{\text{SM}}(B_s^0 \rightarrow \gamma\gamma) = (0.5 - 1.0) \times 10^{-6}. \quad (1.39)$$

$B_s^0 \rightarrow \gamma\gamma$ has not yet been observed, and the upper limit at the 90% CL on its branching fraction is 53×10^{-6} [58], set by the Belle experiment using the first sample (1.86 fb^{-1}) collected at the $\Upsilon(5S)$ resonance.

With about 2.8 million B_s^0 mesons and assuming the same reconstruction efficiency as in [58] ($\epsilon = 20\%$), we expect to reconstruct less than one signal event if the SM prevails:

$$N_{B_s^0 \rightarrow \gamma\gamma} = \mathcal{B}_{\text{SM}}(B_s^0 \rightarrow \gamma\gamma) \times N_{B_s^0} \times \epsilon \approx (0.3 - 0.6). \quad (1.40)$$

The $B_s^0 \rightarrow \gamma\gamma$ decay rate is also constrained by the good agreement between the SM and the measurements in the $B \rightarrow X_s \gamma$ decays [59]. However, various NP scenarios such as supersymmetry with broken R -parity [60], a fourth fermion generation [61] or a two Higgs doublet model with flavor changing neutral currents [62], can increase the $B_s^0 \rightarrow \gamma\gamma$ branching fraction by up to an order of magnitude without violating constraints on the $B \rightarrow X_s \gamma$ branching fraction. We present below the implications of the supersymmetry theory and the fourth fermion generation model for the $B_s^0 \rightarrow \gamma\gamma$ decay.

Supersymmetry

Supersymmetry (SUSY) introduces an operator Q that transforms fermions into bosons and vice versa. Each SM particle has a superpartner. Fermion superpartners are named with the “s” prefix (eg. stop, sneutrino) and boson superpartners are named with the “ino” suffix (eg. gluino, photino). The number of particles is therefore doubled. SUSY does not conserve the baryon (B) and lepton (L) numbers. However, $B - L$ conservation has been tested very precisely, thus, an R -parity is introduced, defined as

$$R = (-1)^{3(B-L)-2S}, \quad (1.41)$$

where S is the particle spin. SM particles have $R = +1$ and SUSY partners have $R = -1$. If R -parity is conserved, SUSY particles must be produced in pairs. Under the same assumption, the lightest SUSY particle must be stable, massive, neutral and colorless, thus a perfect candidate for DM since it cannot decay and it is only sensitive to weak and gravitational interactions.

SUSY does not solve SM questions such as the number of arbitrary parameters or the fermion family number. SUSY is not a more fundamental theory than SM. However, SUSY is thought to be a very promising extension to the SM because it solves the so-called hierarchy problem. In the SM, the Higgs mass diverges quadratically due to radiative correction

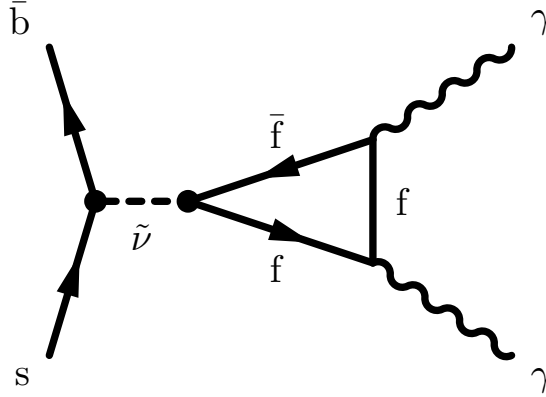


Figure 1.7: λ -irreducible diagram responsible for the large enhancement of the $B_s^0 \rightarrow \gamma\gamma$ branching fraction within the supersymmetry theory with R -parity violation. The $\tilde{\nu}$ is a sneutrino and f are fermions with $-\frac{1}{2}$ weak isospin.

from top loops. An energy cut-off at $\Lambda = 1$ TeV has to be introduced to avoid this phenomenon. In SUSY, the Higgs mass is naturally protected with stop loops. SUSY also helps the Grand Unification Theory (GUT), the theory supposed to unify the electromagnetic, weak and strong interactions at very high energy ($> 10^{14}$ TeV). In the SM, the three coupling constants (α_{EM} , α_W , α_s) run with the energy but they do not seem to converge to a common value at very high energy, thus GUT appears to be impossible within the SM. SUSY is built to allow GUT, ie. the three coupling constants intersect at very high energy.

The authors of Ref. [60] have studied the inclusive $B \rightarrow X_s \gamma\gamma$ and the $B_s^0 \rightarrow \gamma\gamma$ decays in the SUSY framework with broken R -parity. They found that a particular R -parity violating (RPV) diagram, called λ -irreducible and shown in Figure 1.7, can provide a large enhancement, up to one order of magnitude to the $B_s^0 \rightarrow \gamma\gamma$ branching fraction. This diagram is irrelevant for the $b \rightarrow s\gamma$ amplitude and therefore, the good agreement in the latter rate does not introduce any constraint. However, if R -parity is conserved, the $b \rightarrow s\gamma\gamma$ amplitude is highly correlated to $b \rightarrow s\gamma$ [59].

Information on the RPV couplings, shown as dots in Figure 1.7, is obtained from B decays generated at one-loop level in the SM but at tree level in RPV SUSY. Such decays include $b \rightarrow sl^+l^-$, $B \rightarrow hh$ with $h = K, \pi$, $B \rightarrow \phi K_S^0$, $B \rightarrow \phi\phi$ and $B \rightarrow \phi\pi$. Some of these decays, eg. $b \rightarrow sl^+l^-$ and $B \rightarrow \phi K_S^0$, have been measured since [60] was published. The allowed enhancement may be weakened. However, all $B \rightarrow hh$ modes were already measured with good accuracy by Belle, *BABAR* and CLEO.

The fourth fermion generation

The SM can be extended with a fourth fermion generation denoted t', b', τ', ν' . This new SM is usually called SM4. The existence of this new generation is constrained in many ways. Direct searches for the t' and b' quarks at the Tevatron indicate that their masses are larger than $190 \text{ GeV}/c^2$ [2]. The invisible decay width of the Z boson is proportional to the number of neutrino species. A combination of the measurements performed by the

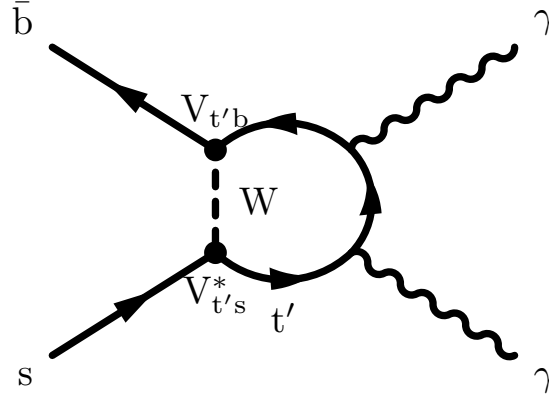


Figure 1.8: Feynman diagram for $B_s^0 \rightarrow \gamma\gamma$ with a fourth fermion generation.

LEP experiments indicates that the number of neutrino is [2]

$$N_\nu = 2.984 \pm 0.008, \quad (1.42)$$

thus in very good agreement with three. The fourth generation neutrino therefore has to be very massive ($m_{\nu'} > m_Z/2 \approx 46 \text{ GeV}/c^2$) or sterile so that it does not contribute to the invisible decay width of the Z . Theory and current observations seem to be able to accomodate such a neutrino [61]. The CKM matrix elements associated with the fourth generation, $V_{t'D}$, also have to be tiny in order not to violate constraints on measurements involving penguin or box diagrams, which are very sensitive to the heaviest quark (up-type quark in B decays). The paper [61] predicts branching fractions for the $B^0 \rightarrow \gamma\gamma$ and $B_s^0 \rightarrow \gamma\gamma$ decay modes in the SM4 framework. Allowed ranges for the relevant CKM matrix element products ($|V_{t'q}V_{t'b}|$) are obtained from the measurement of B^0 - \bar{B}^0 mixing for $B^0 \rightarrow \gamma\gamma$ and from the $B \rightarrow X_s\gamma$ rate for $B_s^0 \rightarrow \gamma\gamma$. Figure 1.8 shows a $B_s^0 \rightarrow \gamma\gamma$ diagram involving the t' quark. The allowed range is computed to be $\mathcal{O}(10^{-4})$ for $|V_{t'd}V_{t'b}|$ ($B^0 \rightarrow \gamma\gamma$) and $\mathcal{O}(10^{-3})$ for $|V_{t's}V_{t'b}|$ ($B_s^0 \rightarrow \gamma\gamma$). The $B_s^0 \rightarrow \gamma\gamma$ branching fraction is allowed to be enhanced up to one order of magnitude above the SM prediction without breaking constraints on $B \rightarrow X_s\gamma$. However, the $B^0 \rightarrow \gamma\gamma$ rate is mostly constrained at its SM value due to the the tiny allowed values for $|V_{t'd}V_{t'b}|$. It is very important to notice that [61] was published prior to the B_s^0 - \bar{B}_s^0 mixing measurement by CDF [21] and that the constraint due to $B \rightarrow X_s\gamma$ was based on the ALEPH measurement, $\mathcal{B}(B \rightarrow X_s\gamma) = (3.1 \pm 1.1) \times 10^{-4}$ [63]; since then, the latter branching fraction has been measured about four times more precisely by CLEO, Belle and BABAR (Equation 1.30 on page 16). The SM prediction was also probably enhanced by a similar factor since then. The allowed enhancement of the $B_s^0 \rightarrow \gamma\gamma$ branching fraction by up to one order of magnitude therefore has to be taken with a grain of salt.

1.4 The resonant $B^+ \rightarrow K^+ h \rightarrow K^+ \gamma\gamma$ decays

The first aim in this study was to search for the double radiative penguin decay $B^+ \rightarrow K^+ \gamma\gamma$. This decay has mostly the same phenomenology as the $B_s^0 \rightarrow \gamma\gamma$ decay and was therefore searched for the same physical interests detailed in Section 1.3.2. The $B^+ \rightarrow K^+ \gamma\gamma$ branching fraction was calculated in the SM to be about 10^{-6} [64]. Such branching fraction is generally accessible at Belle and a preliminary study [65] confirmed it, although Belle's statistics at that time was not sufficient. However, a master student from Lausanne, when trying to reproduce results from [64] with the EvtGen generator [66], discovered inconsistencies between formulae and displayed figures [67]. The authors soon acknowledged mistakes in their paper and published an erratum [68] in which the predicted $B^+ \rightarrow K^+ \gamma\gamma$ branching fraction was lowered by about three orders of magnitude and therefore dropped out of reach at Belle. This new prediction was also confirmed by other theorists [69]. Moreover, it was later discovered that the $B^+ \rightarrow K^+ \gamma\gamma$ decay is hidden by an irreducible background over the whole $m_{\gamma\gamma}$ phase-space from the resonant $B^+ \rightarrow K^{*+} \gamma \rightarrow K^+ \gamma\gamma$ channel [70]. We therefore decided to search for $B^+ \rightarrow K^+ \gamma\gamma$ decays where the two photons originate from a number of specific resonances h , where h can be one of the following mesons: η , η' , η_c , $\eta_c(2S)$, χ_{c0} , χ_{c2} , J/ψ or the mysterious $X(3872)$ particle, discovered by Belle [71] and confirmed by CDF [72], $D\bar{D}$ [73] and *BABAR* [74].

Many of the $B^+ \rightarrow K^+ h$ and $h \rightarrow \gamma\gamma$ branching fractions involved in these decay chains have been measured already, as shown in Table 1.3. The $B^+ \rightarrow K^+ \eta$ and $B^+ \rightarrow K^+ \eta'$ modes are well established [2] and can be used as calibrations in the search for other $B^+ \rightarrow K^+ h \rightarrow K^+ \gamma\gamma$ channels that have smaller or unknown branching fractions. The $B^+ \rightarrow K^+ J/\psi$ channel can also serve as a control mode, since the decay of a spin 1 particle (here the J/ψ) into two photons is forbidden by gauge invariance and Bose-Einstein statistics [75].

The nature and quantum numbers of the $X(3872)$ particle are still being debated; based on analyses of the dipion mass spectrum [76, 77] and angular distributions [76, 78] of $X(3872) \rightarrow \pi^+ \pi^- J/\psi$ decays, $J^{PC} = 1^{++}$ and 2^{-+} are allowed. The 1^{++} assignment is also supported by signals observed in the $B \rightarrow (D^0 \bar{D}^0 \pi^0) K$ [77] and $B \rightarrow (D^{*0} \bar{D}^0) K$ [79] modes under the assumption that they are indeed due to the $X(3872)$ particle. The observation of $X(3872) \rightarrow J/\psi \rho$ [80] and $X(3872) \rightarrow J/\psi \gamma$ [81, 82] indicates that $C = +1$. Evidence of a signal in the $B^+ \rightarrow K^+ X(3872) \rightarrow K^+ \gamma\gamma$ channel would rule out $J = 1$.

The interference of $B^+ \rightarrow K^+ \eta_c \rightarrow K^+ \gamma\gamma$ or $B^+ \rightarrow K^+ \chi_{c0} \rightarrow K^+ \gamma\gamma$ with the radiative decay chain $B^+ \rightarrow K^{*+} \gamma \rightarrow K^+ \gamma\gamma$ can be used to measure the photon polarization in the $b \rightarrow s\gamma$ quark transition [70]. Such measurement would provide a test of the Standard Model, which predicts the photon to be predominantly left-handed in $b \rightarrow s\gamma$ decays and right-handed in $\bar{b} \rightarrow \bar{s}\gamma$ decays. The observation of the $B^+ \rightarrow K^+ \eta_c \rightarrow K^+ \gamma\gamma$ or $B^+ \rightarrow K^+ \chi_{c0} \rightarrow K^+ \gamma\gamma$ decay chain is the first step in this search for new physics, which could be achieved with about 10 ab^{-1} of data (thus requiring a Super B factory [83, 84, 85]).

In this study, we use a data sample of 492 fb^{-1} containing 535×10^6 $B\bar{B}$ pairs that were collected with the Belle detector at the KEKB asymmetric-energy e^+e^- (3.5 on 8 GeV) collider [39] operating at the $\Upsilon(4S)$ resonance. This study has been accepted for publication in Physics Letters B [86] and is also described in the Belle note 936 [87].

Table 1.3: Current status of the measured branching fractions or 90% confidence level upper limits for $B^+ \rightarrow K^+ h$ and $h \rightarrow \gamma\gamma$ (all values are taken from Ref. [2], unless otherwise indicated). The values in the last column are the expectations computed as the products $\mathcal{B}(B^+ \rightarrow K^+ h) \times \mathcal{B}(h \rightarrow \gamma\gamma)$. The decay chain $B^+ \rightarrow K^+ h \rightarrow K^+ \gamma\gamma$ has only been observed for $h = \eta$.

h	$\mathcal{B}(B^\pm \rightarrow K^\pm h)$	$\mathcal{B}(h \rightarrow \gamma\gamma)$	$\mathcal{B}(B^\pm \rightarrow K^\pm h \rightarrow K^\pm \gamma\gamma)$
η	$(2.6 \pm 0.6) \times 10^{-6}$	$(39.39 \pm 0.24)\%$	$(1.02 \pm 0.24) \times 10^{-6}$
η'	$(69.7 \pm 2.8) \times 10^{-6}$	$(2.12 \pm 0.14)\%$	$(1.48 \pm 0.11) \times 10^{-6}$
η_c	$(9.1 \pm 1.3) \times 10^{-4}$	$(2.7 \pm 0.9) \times 10^{-4}$	$(0.25 \pm 0.09) \times 10^{-6}$
$\eta_c(2S)$	$(3.4 \pm 1.8) \times 10^{-4}$	seen	
χ_{c0}	$(1.40_{-0.19}^{+0.23}) \times 10^{-4}$	$(2.76 \pm 0.33) \times 10^{-4}$	$(0.39 \pm 0.08) \times 10^{-7}$
χ_{c2}	$< 2.9 \times 10^{-5}$	$(2.58 \pm 0.19) \times 10^{-4}$	$< 7.5 \times 10^{-9}$
J/ψ	$(10.07 \pm 0.35) \times 10^{-4}$	$< 9.3 \times 10^{-5}$ [88]	$< 9.4 \times 10^{-8}$
$X(3872)$	seen [71]		

Chapter 2

The Belle experiment at KEKB



We present the Belle detector taking data at the KEKB collider in Tsukuba, Japan. The determination of the number of B meson pairs at the $\Upsilon(4S)$ and $\Upsilon(5S)$ resonances and of the number of B_s^0 mesons at the $\Upsilon(5S)$ are also discussed.

2.1 The Υ resonances and the B meson factories

THE Υ resonances are $b\bar{b}$ resonances with masses in the range $9 \text{ GeV}/c^2 - 11 \text{ GeV}/c^2$. The lightest Υ , the $\Upsilon(9460)$ or $\Upsilon(1S)$, was observed for the first time in 1977 by the CFS Collaboration at Fermilab [89]. The Υ resonances can be seen in Figure 2.1, where the hadronic cross-section in e^+e^- collisions is plotted as a function of the e^+e^- center-of-mass energy. Table 2.1 lists their main properties. The mass of the $\Upsilon(4S)$ resonance is $\sim 20 \text{ MeV}/c^2$ above the mass of two B^+ or B^0 mesons, therefore, it is the lightest Υ resonance to be able to decay into a $B\bar{B}$ meson pair. In fact, it decays almost exclusively, $>96\%$ according to [90], to B^+B^- and $B^0\bar{B}^0$ pairs. The $\Upsilon(4S)$ decay rate to B^+B^- is measured to be very consistent with the rate to $B^0\bar{B}^0$ [91]. Generally and further in this report, these rates are assumed to be each equal to 50%, although a few non- BB decay modes of the $\Upsilon(4S)$ have been observed with branching fractions of the order of 10^{-4} . The $b\bar{b}$ production cross-section at the $\Upsilon(4S)$ resonance is about 1.1 nb and e^+e^- storage rings operating at the $\Upsilon(4S)$ resonance are called B -factories. The Υ resonances stand on top of a large continuum background coming from light-quark pair production ($e^+e^- \rightarrow q\bar{q}$ with $q \in \{u, d, s, c\}$) as shown in Figure 2.1. At the $\Upsilon(4S)$ resonance, the continuum production cross-section is about three times larger than the $B\bar{B}$ cross-section.

The $\Upsilon(5S)$ resonance was discovered by the CLEO collaboration in 1985 [92]. The production of B_s^0 mesons at this resonance was established by the same collaboration in 2005 [93]. After 6 years of data taking at the $\Upsilon(4S)$ resonance, Belle took a test run at the $\Upsilon(5S)$ during three days in June 2005. A scan of the resonance, shown on the right of Figure 2.1, was first performed to find the maximum of the hadronic cross-section, estimated at $E_{\text{CM}} = 10869 \text{ MeV}$. A sample with an integrated luminosity of 1.86 fb^{-1} was

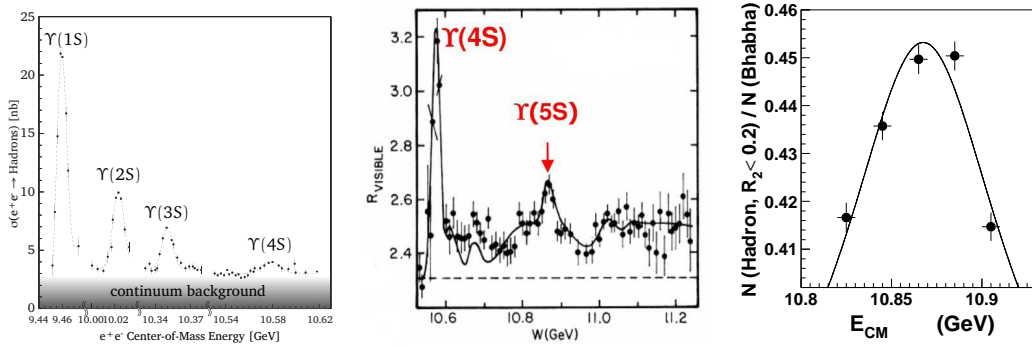


Figure 2.1: Hadronic cross-section in e^+e^- collisions as a function of the e^+e^- center-of-mass energy. Left figure shows it in nb, middle figure shows it normalized to the theoretical muon-pair cross section and right figure normalized to the Bhabha cross-section. Right figure was obtained with the Belle detector near the $\Upsilon(5S)$ resonance. Left figure is taken from [94], middle figure from [92] and right figure from [95].

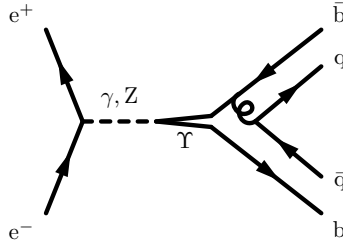


Figure 2.2: Feynman diagram for the $e^+e^- \rightarrow \{\Upsilon(4S), \Upsilon(5S)\} \rightarrow B\bar{B}$ process. At the $\Upsilon(4S)$ and $\Upsilon(5S)$ resonances, the B meson can be a $B^0 \equiv \bar{b}d$ or a $B^+ \equiv \bar{b}u$. At the $\Upsilon(5S)$, it can also be a $B_s^*(B_s^0) \equiv \bar{b}s$, or an excited B meson.

then collected at this energy. In June 2006, during twenty days this time, Belle took a supplementary 21.7 fb^{-1} data sample at the same energy. The total sample at the $\Upsilon(5S)$, 23.6 fb^{-1} , is about 40 times larger than the CLEO sample.

The variety of hadronic events at the $\Upsilon(5S)$ resonance is richer than at the $\Upsilon(4S)$. B^+ , B^0 and B_s^0 mesons are produced in $\Upsilon(5S)$ decays. Unlike the $\Upsilon(4S)$ resonance, the $\Upsilon(5S)$ resonance does not stand just above a $B\bar{B}$ threshold. B mesons are mostly produced through excited states B^* with subsequent low energy photon de-excitation. The $b\bar{b}$ production at the $\Upsilon(5S)$ resonance is about 0.3 nb , hence more than three times smaller than at the $\Upsilon(4S)$ resonance. The production fraction of $B_s^{(*)}\bar{B}_s^{(*)}$ events at the $\Upsilon(5S)$ resonance is about 20%, and, out of these $B_s^{(*)}\bar{B}_s^{(*)}$ events, the vast majority, about 90% of them, are $B_s^*\bar{B}_s^*$ events. These quantities are discussed in more detail in Section 2.7. Figure 2.2 shows a possible Feynman diagram for the $e^+e^- \rightarrow \{\Upsilon(4S), \Upsilon(5S)\} \rightarrow B\bar{B}$ transition. Table 2.1 lists the main B mesons; the B_c^+ meson is the only weakly-decaying B meson not being produced at the $\Upsilon(5S)$ resonance.

The first generation of B -factories, DORIS II at DESY in Germany with the ARGUS

Table 2.1: Masses, widths and quantum numbers of the Υ resonances and the B mesons. Higher excitations (B^{**}) are omitted. All values are taken from [2].

Particle	Mass (MeV/ c^2)	Width (MeV/ c^2)	$I^G(J^{PC})$ or $I(J^P)$
$\Upsilon(1S)$	9460.30 ± 0.26	0.054 ± 0.001	$0^-(1^{--})$
$\Upsilon(2S)$	10023.26 ± 0.31	0.032 ± 0.003	$0^-(1^{--})$
$\Upsilon(3S)$	10355.2 ± 0.5	0.020 ± 0.002	$0^-(1^{--})$
$\Upsilon(4S)$	10579.4 ± 1.2	20.5 ± 2.5	$0^-(1^{--})$
$\Upsilon(5S)$	10865 ± 8	110 ± 13	$0^-(1^{--})$
$\Upsilon(6S)$	11019 ± 8	79 ± 16	$0^-(1^{--})$
B^0	5279.50 ± 0.33	–	$\frac{1}{2}(0^-)$
B^+	5279.13 ± 0.31	–	$\frac{1}{2}(0^-)$
B^{*+}, B^{*0}	5325.1 ± 0.5	?	$\frac{1}{2}(1^-)$
B_s^0	5366.1 ± 0.6	–	$0(0^-)$
B_s^*	5412.0 ± 1.2	?	$0(1^-)$
B_c^+	6286 ± 5	–	$0(0^-)$

experiment and CESR in Cornell, USA with the CLEO detector, were¹ symmetric colliders, where the electron and positron beams have the same energy, corresponding to one half of the $\Upsilon(4S)$ mass. The second generation of B -factories, KEKB at KEK in Tsukuba, Japan with the Belle experiment and PEP-II at SLAC in Stanford, USA with the *BABAR* experiment are asymmetric colliders. At KEKB, electrons are stored in the “High Energy Ring” (HER) with an energy of $E_{\text{HER}} = 8$ GeV, while positrons are stored in the “Low Energy Ring” with $E_{\text{LER}} = 3.5$ GeV. The center-of-mass energy, of course, still equals the mass of the $\Upsilon(4S)$ resonance:

$$E_{\text{CM}} = 2 \times \sqrt{E_{\text{HER}} \times E_{\text{LER}}} = 10.58 \text{ GeV}. \quad (2.1)$$

Due to the beam asymmetry, the $\Upsilon(4S)$ particle is produced with a boost, with respect to the laboratory frame, of

$$\beta\gamma = \frac{E_{\text{HER}} - E_{\text{LER}}}{E_{\text{CM}}} = 0.425 \quad (2.2)$$

along the electron beam direction (z axis). Since the B mesons from the $\Upsilon(4S)$ decay have very little kinetic energy in the center-of-mass, they have approximately the same boost $\beta\gamma$ in the laboratory.

This boost provides the opportunity to perform time-dependent analyses. B mesons fly generally 0.2 mm before decaying and the decay-length difference between the two B mesons along the z axis (Δz) can be measured with a vertex detector. The B mesons

¹In fact, CLEO is still running as a charm factory with $\sqrt{s} \approx 4$ GeV.

decay-time difference (Δt) can then be estimated as

$$\Delta t \approx \frac{\Delta z}{\beta\gamma c}. \quad (2.3)$$

The physics of B mesons is also investigated at hadron colliders, such as the Tevatron, a $p\bar{p}$ collider with $\sqrt{s} = 1.96$ TeV, located at Fermilab near Chicago (USA), with the DØ and CDF experiments. The ATLAS and CMS experiments, and especially the b -devoted LHCb experiment will also study B mesons when the Large Hadron Collider (LHC), a pp collider with $\sqrt{s} = 14$ TeV, located at CERN near Geneva (Switzerland), will produce its first collisions, planned for Summer 2008.

2.1.1 The KEKB asymmetric electron-positron collider

The KEKB collider is installed in a 3 km long tunnel, that was previously used by the TRISTAN experiments in the search of the top quark [96]. The KEKB construction began in April 1994 and was completed in November 1998. KEKB consists of two rings, one for electrons and one for positrons. It has a single interaction point, called Tsukuba, where the Belle detector is installed. Currently, the LER current is about 1.58 A, the HER current is about 0.84 A, and 1584 bunches of particles are simultaneously kept in the rings. The two rings are fed by a linear accelerator (linac).

The main KEKB parameters are listed in Table 2.2 and a schematic layout of the accelerator can be seen in Figure 2.3. KEKB is described in details in [39]. Since January 2004, the injection is performed “continuously”, ie. without stopping the data taking. The collider has achieved its design luminosity of $1.0 \times 10^{34} \text{ cm}^{-2}\text{s}^{-1}$ in May 2003. Since then, the luminosity has continuously increased and reached a peak value of $1.712 \times 10^{34} \text{ cm}^{-2}\text{s}^{-1}$ in November 2006. It is also important to notice that the two beams do not collide head-on but with a small crossing angle of 22 mrad. This has the advantage, at some cost on the luminosity, to simplify the design of the interaction region and to reduce the background in the detector. To cope with this luminosity loss, the bunches are tilted, since January 2007, by two crab cavities installed in each ring: the goal is to collide the bunches with a maximum overlap as shown in Figure 2.4. Although the specific luminosity per bunch has increased (Figure 2.4 right), the peak luminosity in this new crossing scheme has not yet reached its 2006 value.

So far KEKB has provided Belle with $\sim 760 \text{ fb}^{-1}$ of data, out of which $\sim 653 \text{ fb}^{-1}$ were recorded at the $\Upsilon(4S)$ resonance (corresponding to about 718 millions $B\bar{B}$ pairs), $\sim 80 \text{ fb}^{-1}$ recorded 60 MeV below the $\Upsilon(4S)$ resonance, 23.6 fb^{-1} at the $\Upsilon(5S)$ resonance and 2.9 fb^{-1} at the $\Upsilon(3S)$ [97]. Figure 2.5 shows how the luminosity progressed over the nine years of Belle operation.

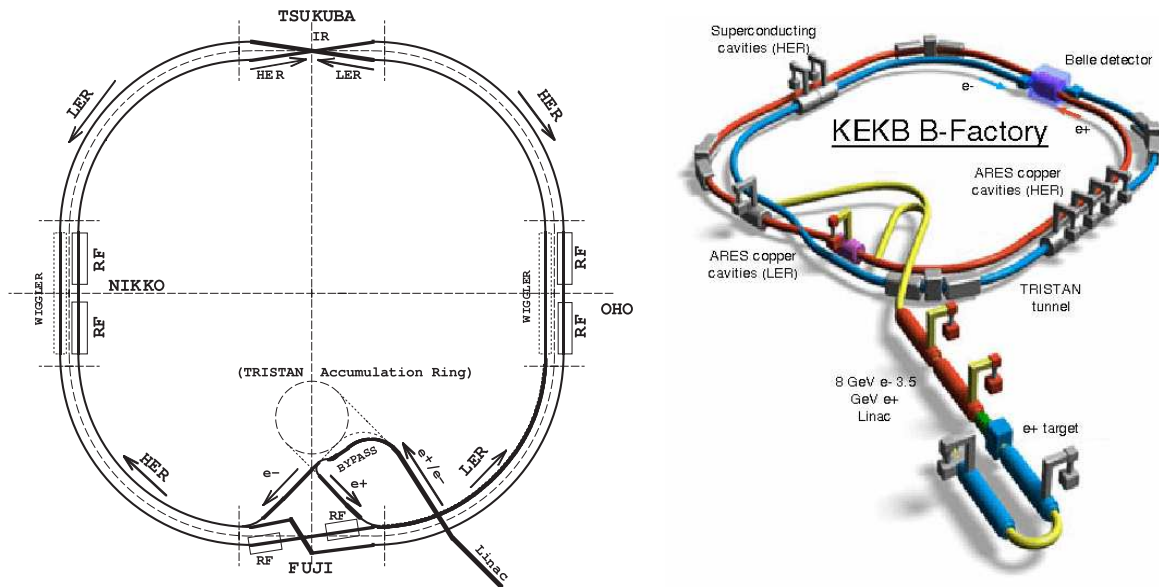


Figure 2.3: The KEKB accelerator.

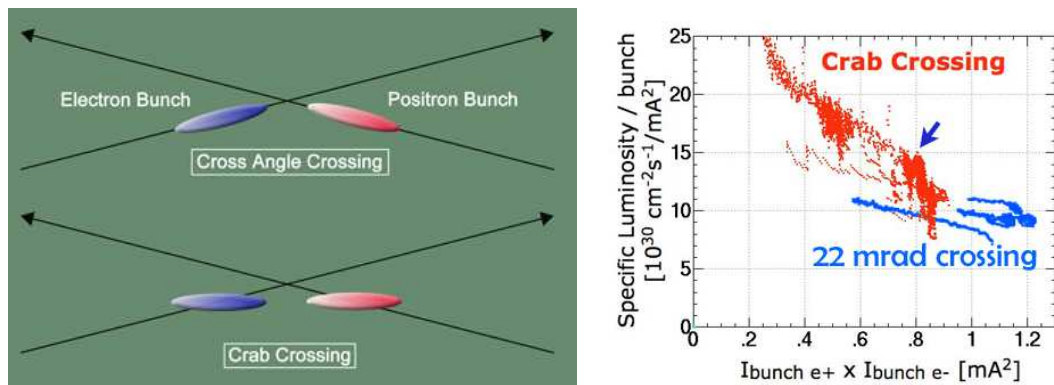


Figure 2.4: Left: bunch crossing schemes without (top) and with (bottom) use of crab cavities. Right: luminosity per bunch divided by the product of bunch currents as a function of this product. The crab crossing scheme allows for an increased specific luminosity.

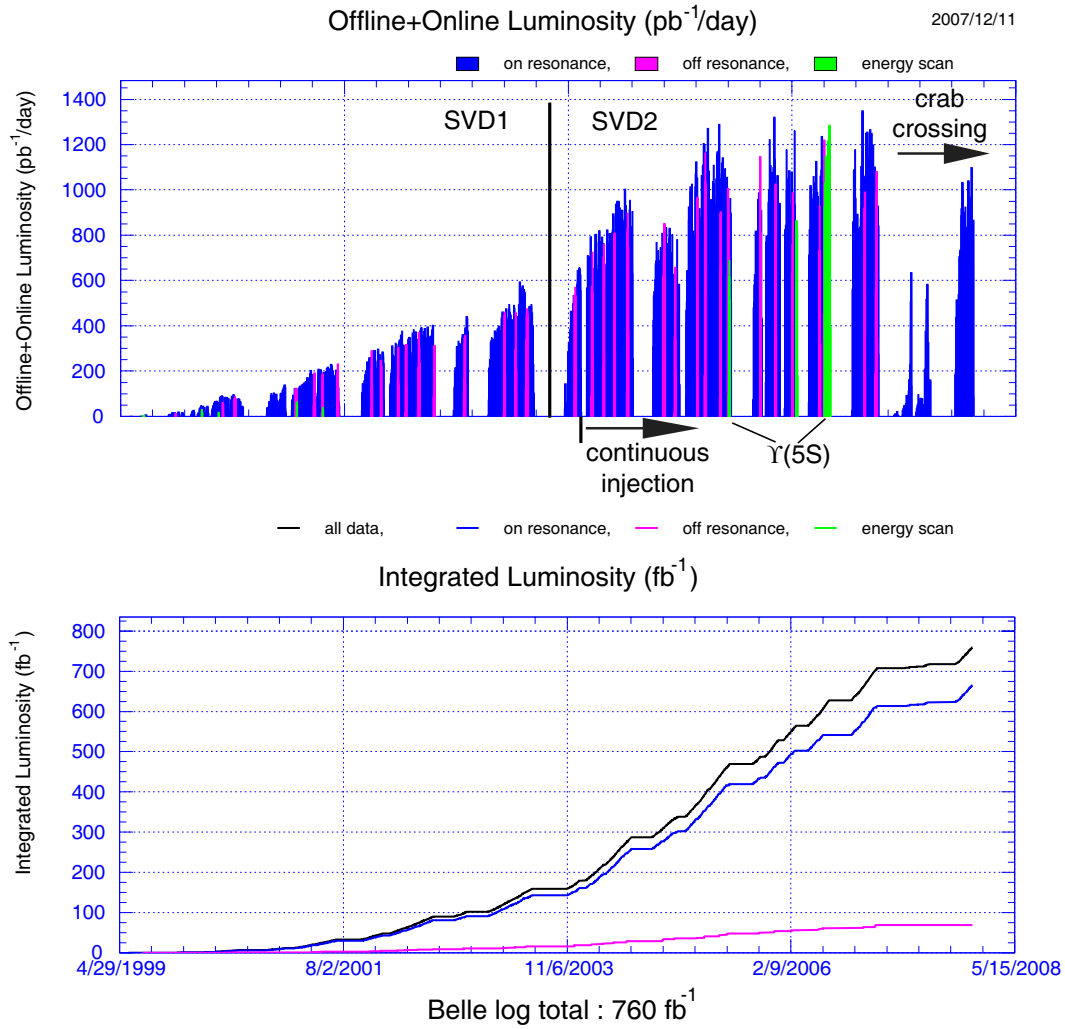


Figure 2.5: Top: luminosity (pb⁻¹/day) as a function of time with main detector or accelerator modifications indicated. Bottom: integrated luminosity (fb⁻¹) as a function of time.

Table 2.2: KEKB machine parameters.

	Design		Nov. 28 2007		unit
	LER	HER	LER	HER	
Circumference	3016				m
RF frequency	508.88				MHz
Current	2.6	1.1	1.58	0.84	A
Crossing angle	22				mrad
Bunches	5000		1584		
Bunch current	0.52	0.22	1.00	0.53	mA
Bunch spacing	0.5		2.1		m
Horiz. emittance	18	18	18	24	nm
Horiz. β_x^*	33	33	90	90	cm
Vert. β_y^*	1.0	1.0	0.59	0.59	cm
Vert. size at IP	1.9	1.9	1.1	1.1	μm
Beam-beam ξ_x	0.039	0.039	0.089	0.098	
Beam-beam ξ_y	0.052	0.052	0.039	0.088	
	Design		Record		
Luminosity	1.0		1.712		$10^{34} \text{ cm}^{-2}\text{s}^{-1}$
\int Lum. / day	~0.6		1.232		fb^{-1}
\int Lum. / 7 days	-		7.82		fb^{-1}
\int Lum. / 30 days	-		30.21		fb^{-1}

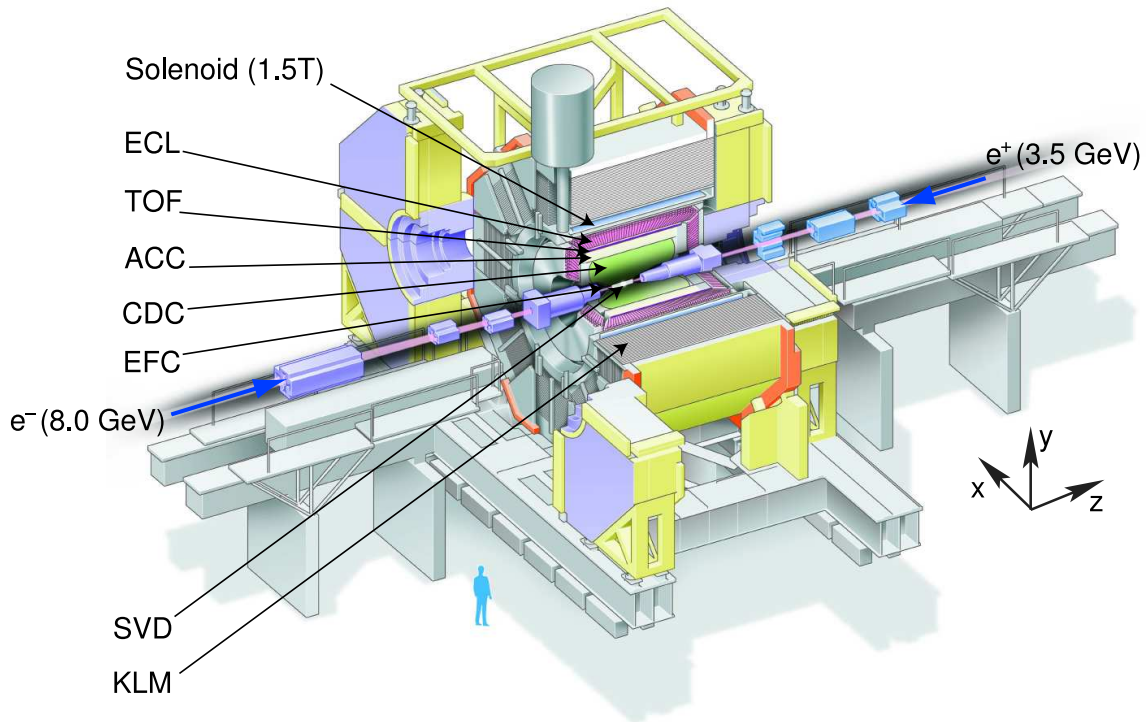


Figure 2.6: Overview of the Belle detector.

2.2 The Belle detector

The “Belle” name is formed from **B** for *B* meson and from **elle** for **e**lectron and anti-electron (**le**). Belle also means “beautiful” in French, which is perfectly suited for an experiment studying the beauty quark. The experiment is also illustrated in its logo, shown on page 23, where the **B** character is formed from two face-to-face **e** characters, symbolizing the electron and the positron, with different sizes to indicate the energy asymmetry.

The Belle detector, shown in Figure 2.6, is a multi-layered full-featured detector covering about 93% of the solid angle. It is immersed in a 1.5 T magnetic field provided by a superconducting solenoid coil. Charged-track momenta (p) are measured with a silicon vertex detector (SVD) and a central drift chamber (CDC). Photons are measured with an electromagnetic calorimeter (ECL) and K_L^0 and muons with an instrumented iron flux-return located outside the coil (KLM).

Charged tracks are then identified by detectors sensitive to the mass or the nature of the underlying particles:

- the CDC measures the energy loss (dE/dx) of particles traveling through it,
- an array of aerogel threshold Cherenkov counters (ACC), based on the Cherenkov effect, can distinguish pions from kaons,
- time-of-flight counters (TOF) measure the time of flight of a particle from the interaction point to a TOF module,

- the ECL can distinguish electrons from other charged particles, and
- the KLM detects muons.

The energy (E) of a charged particle, once identified and therefore its mass (m) chosen, is computed with

$$E^2 = (pc)^2 + (mc^2)^2. \quad (2.4)$$

The following coordinate system is used:

- the z axis is aligned with the LER but is opposite to the positron momentum,
- the y axis is vertical,
- the x axis is horizontal and points to the outside of the ring.

The polar angle θ is defined with respect to the z axis. ϕ is the azimuthal angle with respect to the x axis. The radial distance is defined with $r = \sqrt{x^2 + y^2}$.

The Belle detector is timed with the KEKB Radio Frequency (RF), which governs the bunch crossing rate (~ 509 MHz, ~ 2 ns interval)

The following sections provide a more detailed description of every subdetector based on [98, 99, 100].

2.2.1 The beam pipe and the silicon vertex detector (SVD)

The beam pipe maintains the accelerator vacuum. KEKB has two beam pipes, one for LER and one for HER, which merge at the interaction region. It is here made of a double-wall beryllium cylinder as shown in Figure 2.7. Both walls are only 0.5 mm thick to reduce Coulomb scattering which is the main limiting factor on the z vertex-position resolution. A 2.5 mm gap between the two walls provides a helium-gas cooling channel for removing the heat, a few hundred Watts, produced by the beams. This cooling is particularly important to operate the silicon vertex detector located just around the beam pipe, hence as close as possible to the interaction point to improve the vertex resolution.

The SVD has been designed to precisely measure the B -decay vertices. It also helps with tracking. Two different SVDs have been used so far: a first version (SVD1) has been used from 1999 to July 2003 and a second version (SVD2) is used since October 2003. Both SVDs use double-sided silicon strip detectors (DSSD). A DSSD is essentially a depleted pn junction. A charged particle passing through the junction liberates electrons from the valence band into the conduction band creating electron-hole (e^-h^+) pairs. These pairs create currents in the p^+ and n^+ strips located on the surface of the DSSD. For both SVDs, the p^+ strips are aligned along the beam axis and therefore measure the azimuthal angle ϕ . The n^+ strips are aligned perpendicularly to the beam axis and measure z . Both SVDs use DSSDs originally designed for the DELPHI microvertex detector and fabricated by Hamamatsu Photonics. Each DSSD has 1280 sense strips and 640 read-out pads on each side. The sensor size is 57.5×33.5 mm².

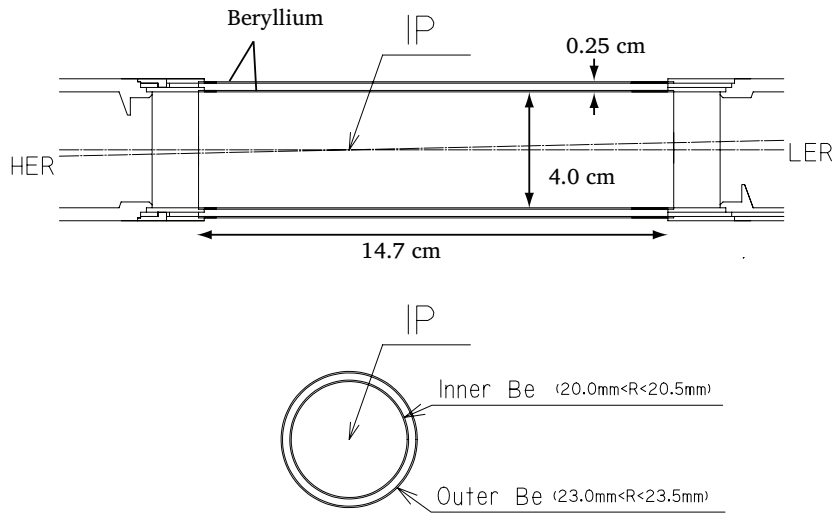


Figure 2.7: The beam pipe at the interaction region used with SVD1. The beam pipe for SVD2 has a smaller diameter of 3 cm.

SVD1

The configuration of SVD1 is shown in Figure 2.8. It consists of three concentric layers arranged on a cylindrical structure at radii of 30 mm, 45.5 mm and 60.5 mm from the interaction point. It covers the region $23^\circ < \theta < 139^\circ$ (86% of the total solid angle). Layers are made of 8, 10 and 14 ladders, respectively, each ladder having two to four DSSDs. SVD1 consists of 102 DSSDs and the total number of readout channels is 81920. SVD1 is described in more detail in [101].

SVD2

The configuration of SVD2 is shown in Figure 2.9. For SVD2, the radius of the beam pipe is reduced from 20 mm to 15 mm in order to put the silicon closer to the interaction point. A fourth layer is also introduced and permits to reconstruct charged tracks from SVD hits only. These four layers are at radii of 20 mm, 43.5 mm, 70 mm and 88 mm from the interaction point. The angular coverage is also extended up to $17^\circ < \theta < 150^\circ$ and is now similar to the coverage of the CDC (92% of the total solid angle). The vertex position resolution is improved by $\sim 25\%$ compared to SVD1. SVD2 consists of 138 DSSDs and the total number of readout channels is increased to 110592. SVD2 is described in more detail in [102].

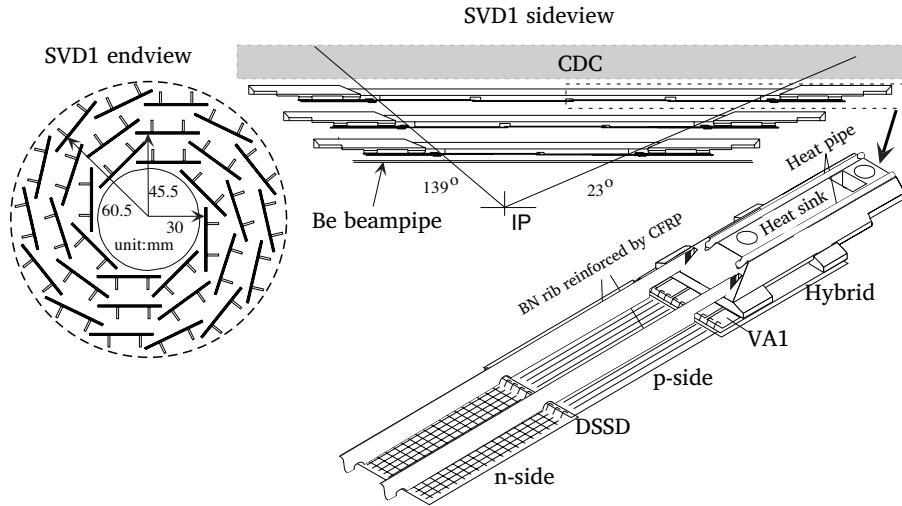


Figure 2.8: Configuration of the first version of the vertex detector (SVD1) shown in a cross-section (left) and in a side view (right).

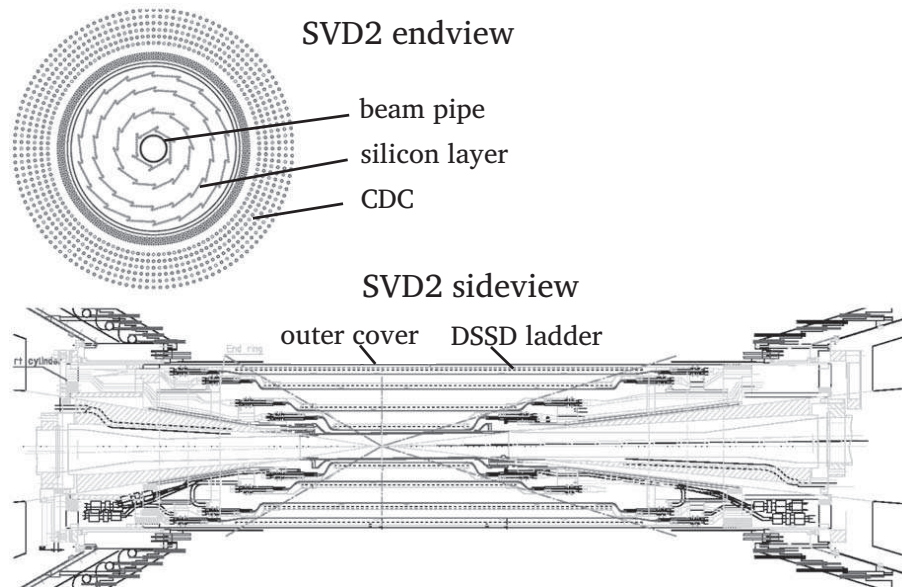


Figure 2.9: Configuration of the second version of the vertex detector (SVD2) shown in a cross-section (top) and in a side view (bottom).

2.2.2 The central drift chamber (CDC)

The CDC is one of the most important subdetectors and is the core part of the tracking system. The CDC has three objectives: it reconstructs effectively the charged particle tracks, it measures precisely their momenta and it helps with particle identification by measuring the energy loss (dE/dx). The CDC is immersed in a 1.5 T magnetic field produced by the solenoidal coil: a charge track will follow a helicoidal trajectory through the CDC.

Figure 2.10 shows the CDC structure. It is asymmetric in the z direction, with an angular coverage of $17^\circ < \theta < 150^\circ$, to cope with the center-of-mass boost. The CDC is composed of three cathode strip layers and 50 cylindrical layers, each containing between three and six axial or small-angle-stereo wire layers. The CDC has a total of 8400 drift cells, each being made of eight field wires and one sense wire. The CDC is filled with a mixture of helium and ethane gas. When a particle travels through a drift cell, electrons are kicked out of gas atoms. These electrons drift with a certain velocity to the sense wire, releasing on their way more and more electrons. The electrons are collected by the sense wire and a hit is recorded by the CDC electronics. The axial wires provide transverse momentum (p_t) information while the small-angle-stereo layers give information on the helix pitch (z information).

A helix track can be defined with five independent parameters which are measured by the CDC [103]:

- the signed curvature of the helix,
- the slope of the helix, and
- the three-dimensional coordinates of the pivot, the helix reference point.

The curvature radius is proportional to p_t , the slope proportional to p_z and the sign of the curvature provides the particle charge. The pivot is chosen as the wire position of the innermost hit in the CDC.

Track parameters are then improved by matching the track to the SVD. Using both tracking detectors, we obtain the following performance

$$\frac{\sigma_{p_t}}{p_t} = (0.19 p_t \oplus 0.34)\%, \quad (2.5)$$

$$\sigma_{xy} = \left(19 \oplus \frac{50}{p\beta \sin^{3/2} \theta} \right) \mu\text{m}, \quad (2.6)$$

$$\sigma_z = \left(36 \oplus \frac{42}{p\beta \sin^{5/2} \theta} \right) \mu\text{m}, \quad (2.7)$$

where p is in GeV/ c and \oplus indicates a quadratic sum.

In addition to track reconstruction, each hit in the CDC provides information on the energy deposited in the gas by the charged particle. Since dE/dx , described by the Bethe-Bloch formula, mainly depends on β , particles with equal momenta but different masses can be distinguished by measuring dE/dx , as shown in Figure 2.11. A clear 3σ separation of pions and kaons is obtained for momenta between 0.4 and 0.6 GeV/ c .

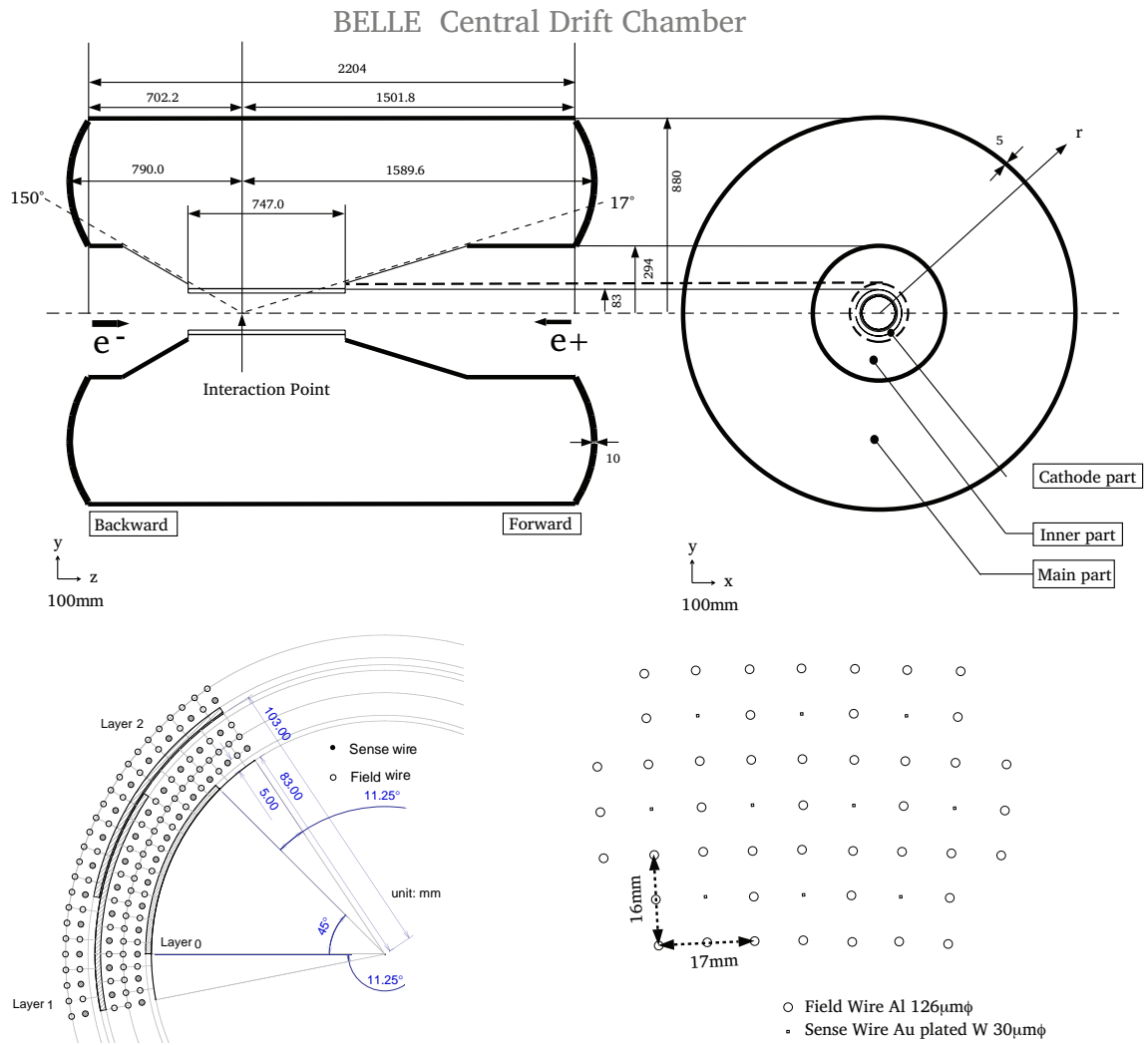


Figure 2.10: Top: general view of the CDC detector. Bottom: the CDC cell structure.

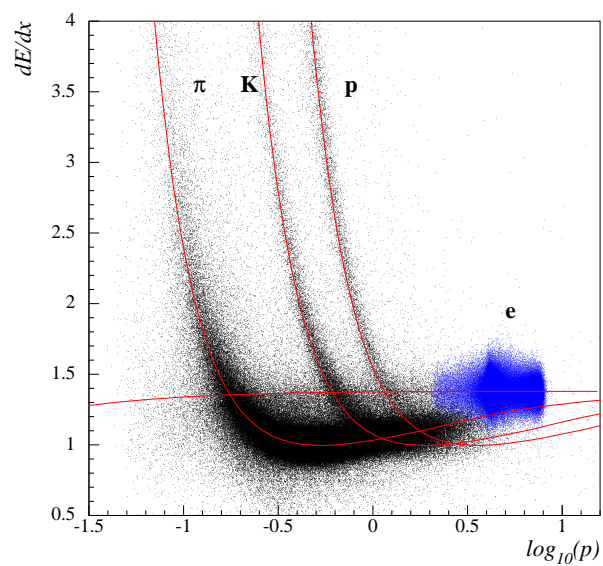


Figure 2.11: Particle identification performance for pions, kaons, protons and electrons based on the dE/dx measurement as a function of the momentum (p in GeV/c).

2.2.3 The aerogel Cherenkov counter (ACC)

Particle identification, specifically the ability to distinguish pions from kaons, plays a key role in Belle. An array of silica aerogel threshold Cherenkov counters has been selected as part of the particle identification system to extend the momentum coverage beyond the reach of dE/dx measurements by the CDC and time-of-flight measurements by the TOF.

The ACC is based on the Cherenkov principle. Cherenkov light is emitted when a particle passes through matter with a velocity v larger than the speed of light in that medium calculated as

$$v_{\text{light}} = c/n, \quad (2.8)$$

where n is the refractive index of the medium. The refractive indices of the ACC were chosen so that only pions with momenta between 1 and 4 GeV/ c produce light. Pions are indeed about three times lighter than kaons: for a given momentum, a pion travels faster than a kaon.

The ACC consists of 960 counter modules segmented into 60 cells in ϕ for the barrel part and 228 modules arranged in 5 concentric layers for the forward endcap. These modules are different for the barrel and the endcap, and have refractive indices between 1.01 and 1.03 depending on θ . The ACC structure and the modules are shown in Figure 2.12. ACC modules are made of five aerogel tiles stacked in an aluminium box with a size of about $12 \times 12 \times 12 \text{ cm}^3$. Photomultiplier tubes are attached to these boxes to collect the Cherenkov light.

2.2.4 The time-of-flight counters (TOF)

The time-of-flight system helps with particle identification and provides fast trigger signals. It consists of 128 TOF counters and 64 trigger scintillation counters (TSC) made of fast scintillators and fine-mesh photo-multiplier tubes. The TOF covers the angular region $33^\circ < \theta < 121^\circ$ and its configuration is shown in Figure 2.13.

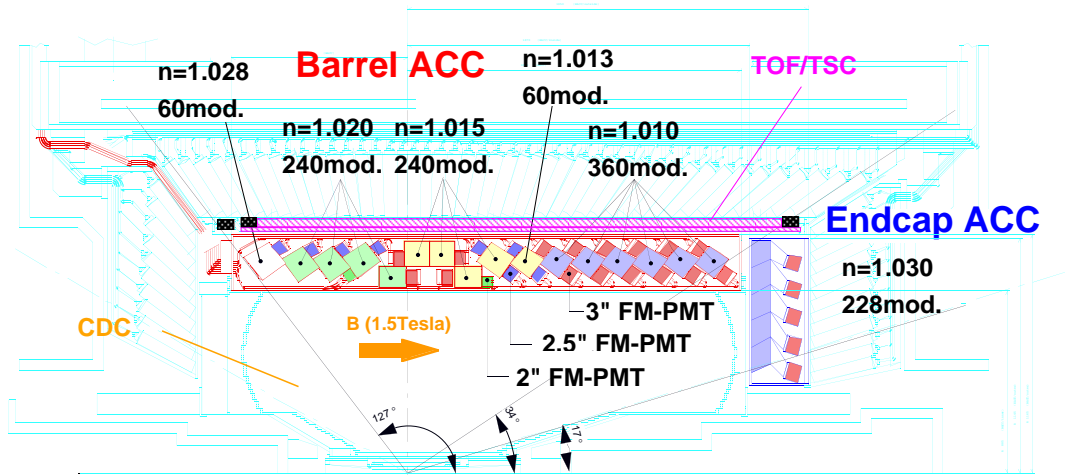
The signal of a particle crossing the TSC is used in coincidence with the two adjacent TOF counters to create a trigger signal.

The TOF measures the time interval T between a collision and the passage of a particle through a TOF module. The time resolution of the TOF is about 100 ps. The mass of the detected particle can be computed with

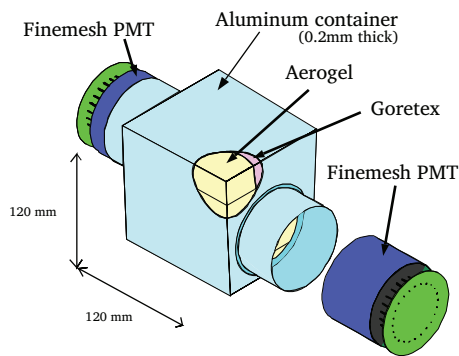
$$m = \frac{p}{c} \sqrt{\left(\frac{cT}{L}\right)^2 - 1}, \quad (2.9)$$

where p is the momentum obtained with the SVD and CDC and L is the distance travelled by the particle from the interaction point to the TOF module. The TOF distinguishes pions and kaons with momenta lower than 1.2 GeV/ c with more than 2 standard deviations, as shown in Figure 2.13.

The TOF is described in more detail in [104].



Barrel ACC Module



Endcap ACC Module

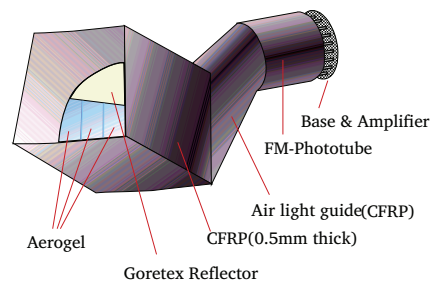


Figure 2.12: Top: transverse section of the Belle detector. Bottom: barrel ACC module (left) and endcap ACC module (right).

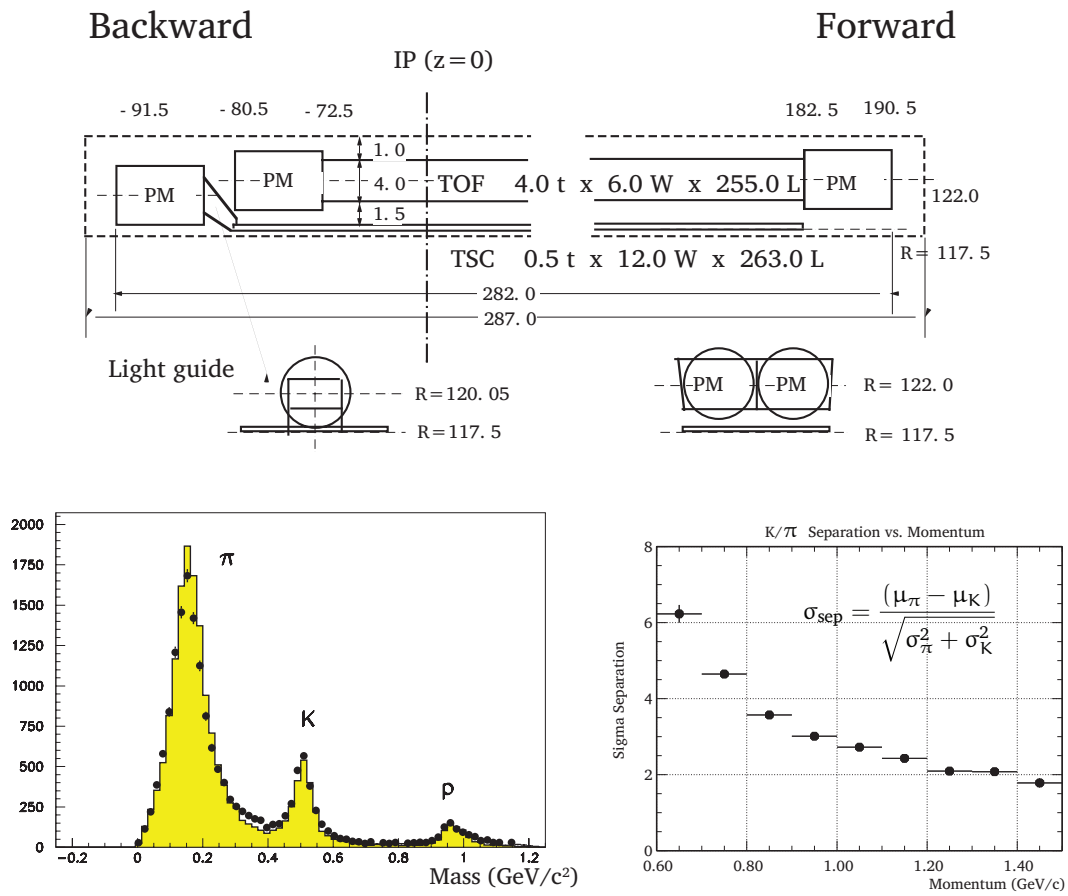


Figure 2.13: Top: the TOF configuration. Bottom left: mass measurement with clear peaks from pions, kaons and protons. Bottom right: separation, in standard deviations, between pions and kaons as a function of the momentum.

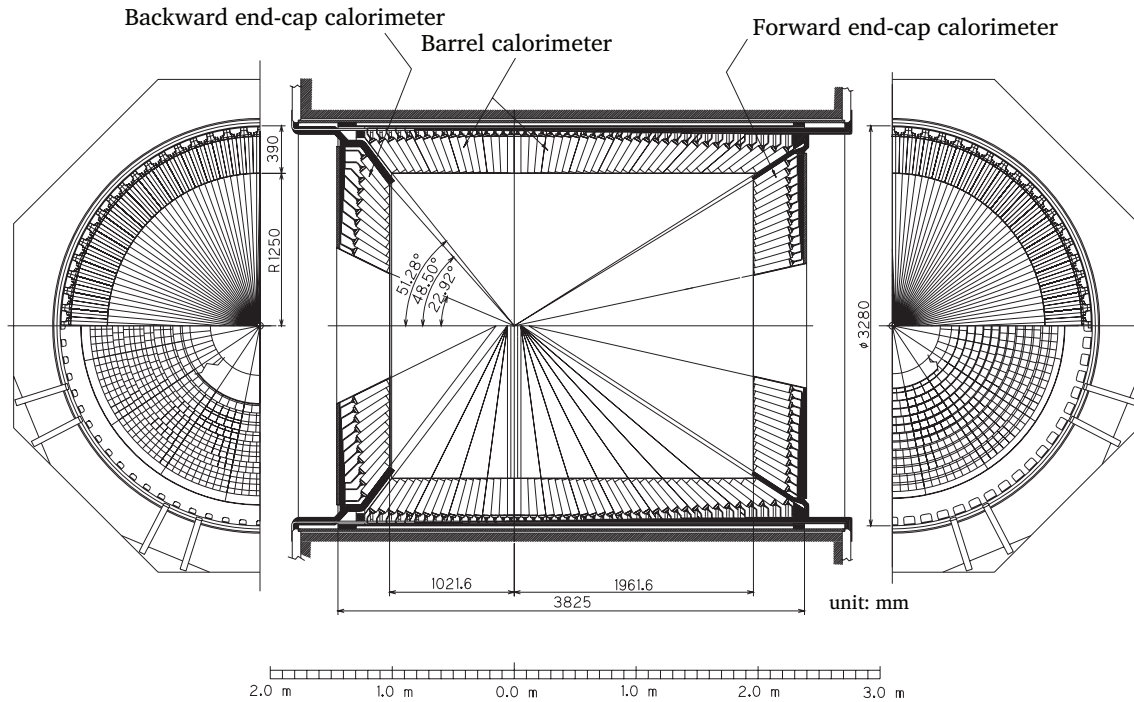


Figure 2.14: Configuration of the ECL.

2.2.5 The electromagnetic calorimeter (ECL)

The main purpose of the ECL is to detect and measure photons with high efficiency and good resolution in energy and position. Photons at Belle can come directly from the e^+e^- annihilation, from a B decay (eg. $B^0 \rightarrow K^*(892)^0\gamma$) or from the end products of decay chains (eg. $B^0 \rightarrow D^+D^-(K_S^0\pi^-\pi^0(\gamma\gamma))$), the ECL therefore has to cover a wide energy range. Furthermore, the ECL is the main system used for electron identification.

The ECL is an array of 8736 tower-shaped CsI(Tl) crystals. When a photon or an electron hits a crystal, it produces an electromagnetic shower by bremsstrahlung and pair creation. Other particles only deposit small amounts of energy via dE/dx ionization. Scintillation light is collected on each crystal by a pair of silicon PIN² photodiodes located at the rear of the crystals. Electron identification is based on the comparison of the energy deposited in the crystal and the momentum of a matched track.

The ECL consists of three parts, as shown in Figure 2.14:

- the forward endcap (1152 crystals) covers $12.4^\circ < \theta < 31.4^\circ$,
- the barrel (6624 crystals) covers $32.2^\circ < \theta < 128.7^\circ$,
- the backward endcap (960 crystals) covers $130.7^\circ < \theta < 155.1^\circ$.

The barrel region is 3.0 m long with an inner radius of 1.25 m and an outer radius of 1.64 m. The endcaps are located at $z = +2.0$ m and $z = -1.0$ m from the interaction point and are 0.4 m thick. The crystals are 30 cm long and have a cross section of about $6 \times$

²PIN is the acronym for positive-intrinsic-negative.

6 cm². Crystal size is a compromise between position determination and energy resolution. Crystals with smaller cross-sections would enhance the position determination at a cost on the energy resolution.

The position and energy resolutions as a function of the photon energy E (GeV) are given by

$$\frac{\sigma_E}{E} = \frac{0.066\%}{E} \oplus \frac{0.81\%}{E^{1/4}} \oplus 1.34\%, \quad (2.10)$$

$$\sigma_{\text{pos}} = \left(0.27 + \frac{3.4}{E^{1/2}} + \frac{1.8}{E^{1/4}} \right) \text{ mm}. \quad (2.11)$$

The ECL is described in more detail in [105].

2.2.6 The extreme forward calorimeter (EFC)

The EFC extends the angular coverage of the ECL: it covers the forward region $6.4^\circ < \theta < 11.5^\circ$ and the backward region $163.3^\circ < \theta < 171.2^\circ$ to detect electrons and photons very close to the beam pipe. It also serves as a beam mask to protect the CDC, as a beam monitor for KEKB and as a luminosity monitor for Belle. The luminosity measurement is described in Section 2.6.1. The EFC is generally not used in physics analysis to reconstruct photons and electrons.

Both parts of the EFC are composed of 160 BGO crystals, that are arranged in 5 θ and 32 ϕ segments as shown in Figure 2.15. The scintillation light is collected by photodiodes. The energy resolution measured with the HER and the LER is 7.3% at 8 GeV and 5.8% at 3.5 GeV.

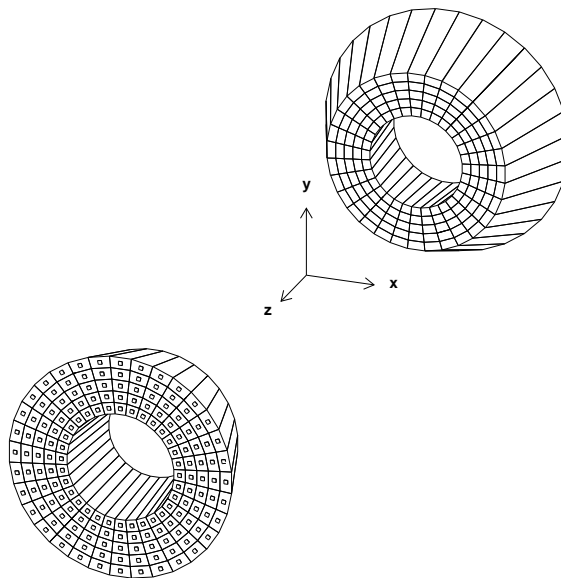


Figure 2.15: Arrangement of the crystals composing the EFC.

2.2.7 The K_L^0 and muon detector (KLM)

K_L^0 and muons are particles depositing only small amounts of energy in the above subdetectors. They live long enough to decay outside of the detector. The KLM is a very dense and massive detector consisting of layers of iron plates alternating with charged particle detectors (glass resistive-plate chambers, RPC). K_L^0 and muons create, in iron, ionizing particles that are detected by the RPCs.

The KLM consists of a barrel part and two endcaps. The barrel covers $45^\circ < \theta < 125^\circ$ and is made of 15 layers of RPCs and 14 cm thick iron plates. The forward and backward endcaps extend the angular coverage up to $20^\circ < \theta < 155^\circ$ and each endcap contains 14 layers of RPCs and 4.7 cm thick iron plates.

KLM layers are grouped in “super-layers”, as shown in Figure 2.16. A super-layer is made of θ and ϕ cathode strips surrounding two RPCs. Resistive-plate counters have two parallel-plate electrodes separated by a gas-filled gap. An ionizing particle traversing the gap initiates a streamer in the gas that results in a local discharge. This discharge creates a signal on the external cathode strips which can be used to record the location and time of the ionization.

The KLM iron provides about 3.9 interaction lengths of material. The shower induced by a K_L^0 is used to determine the K_L^0 direction assuming that it comes from the interaction point. No energy information can be derived from the shower.

Muons are clusters in the KLM that can be associated to a charged track. The muon identification is based on the length and dispersion of the shower. Indeed, muons travel much further and with smaller deflections in the KLM compared to other charged particles such as pions and kaons. For muons with momenta above $1.5 \text{ GeV}/c$, the identification efficiency is typically $\sim 90\%$ with a fake rate of $\sim 3\%$

The KLM detector is described in more detail in [106].

2.3 The trigger

The purpose of the trigger is to reject uninteresting events and to forward interesting ones to the Data Acquisition system, presented in the next section. Many events seen by the

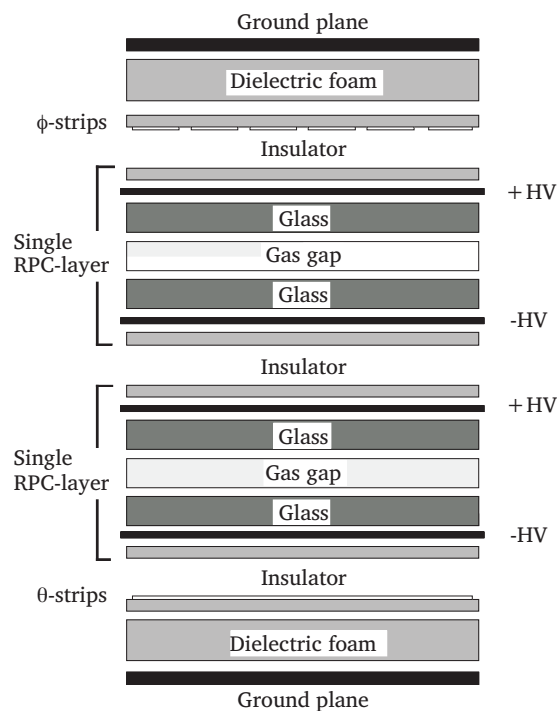


Figure 2.16: Cross-section of a super-layer of the KLM detector.

Table 2.3: Expected trigger rates from various sources at $\Upsilon(4S)$ and with a luminosity of $10^{34} \text{ cm}^{-2}\text{s}^{-1}$ [107].

Source	Rate (Hz)
$\Upsilon(4S) \rightarrow B\bar{B}$	12
Hadron production from continuum	28
$e^+e^- \rightarrow \mu^+\mu^-$ and $e^+e^- \rightarrow \tau^+\tau^-$	16
$e^+e^- \rightarrow e^+e^-$ and $e^+e^- \rightarrow \gamma\gamma$ (prescaled by 100)	5
Two-photon processes ($p_t > 0.3 \text{ GeV}/c$)	35
Beam background	$\mathcal{O}(100)$
Cosmic ray background	20

detector are not the result of a e^+e^- collision and should be ignored to save storage space and to reduce dead time:

- interactions between the beams and the residual gas,
- interactions in the beam pipe,
- synchrotron radiation,
- cosmic ray events.

At an instantaneous luminosity of $10^{34} \text{ cm}^{-2}\text{s}^{-1}$, the rate for events of physical interest is around 100 Hz and the total rate is about 220 Hz, as listed in Table 2.3. The rate of beam background events heavily depends on the accelerator condition. The trigger now operates at around 500 Hz and can handle a rate up to 1300 Hz with 5% occupancy [102].

The Belle trigger system consists of the Level-1 hardware trigger and the Level-3 and Level-4 software triggers. The signal delivered by the TOF to the SVD can be considered a Level-0 trigger. However, there is no Level-2 trigger. The overall trigger efficiency for hadronic events from e^+e^- collisions is more than 99.5%. An overview of the Belle trigger is shown in Figure 2.17.

2.3.1 The Level-1 trigger

A schematic layout of the Level-1 trigger is shown in Figure 2.18. This trigger consists of subdetector triggers governed by a central trigger system called Global Decision Logic (GDL), which issues the Level-1 decision.

The GDL receives subdetector triggers within $1.85 \mu\text{s}$ after the collision and issues a decision $2.2 \mu\text{s}$ after the collision. Subdetector triggers are based on track or energy information. The CDC and TOF trigger on charged particles. The ECL triggers on the deposited energy and the number and timing of ECL cluster hits. The KLM triggers on muon hits. The EFC triggers on Bhabha ($e^+e^- \rightarrow e^+e^-$) and two-photon ($e^+e^- \rightarrow \gamma\gamma$) events. The Level-1 trigger is described in more detail in [108].

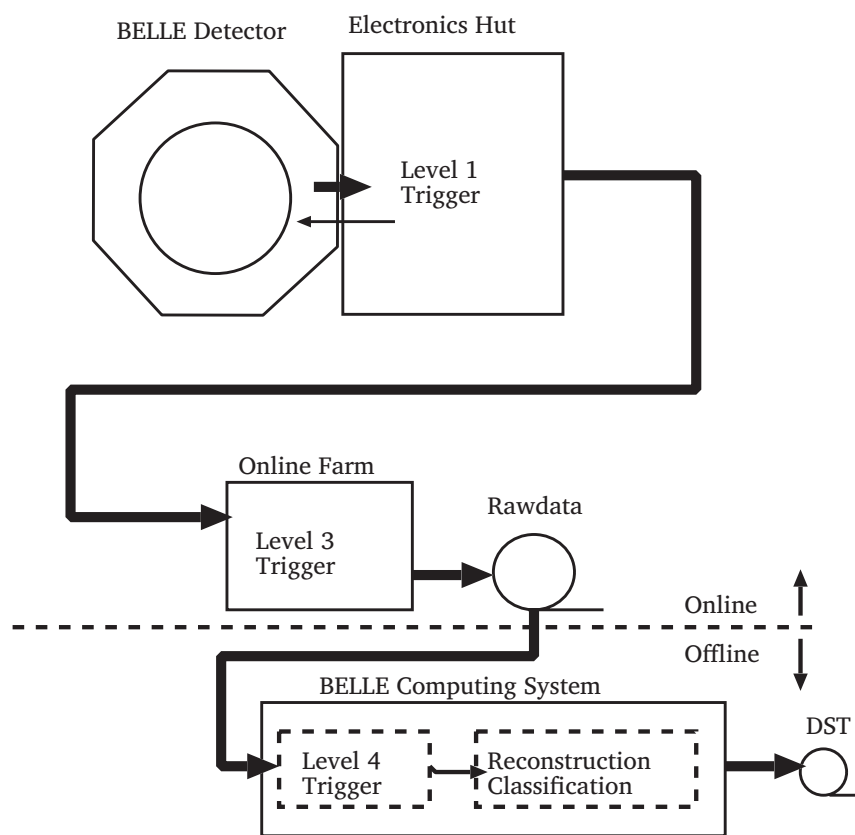


Figure 2.17: Overview of the Belle trigger. The DSTs are now produced online.

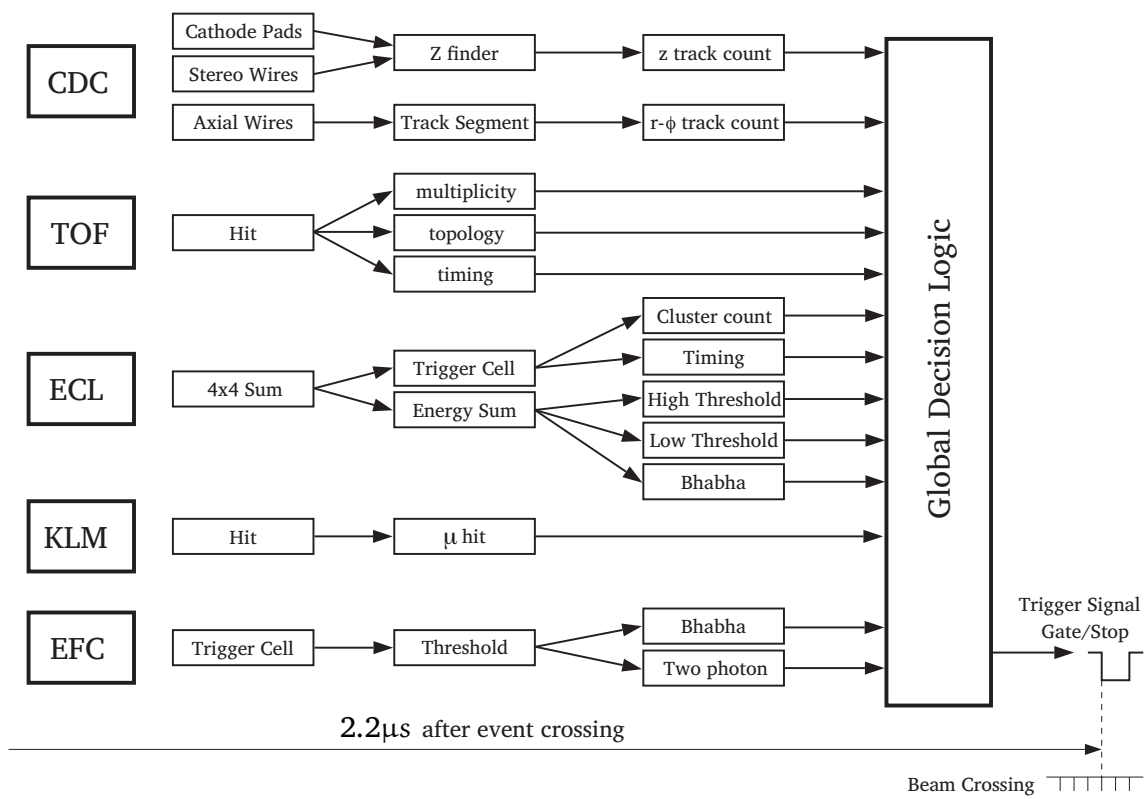


Figure 2.18: Overview of the Level-1 trigger.

The Level-1.5 hardware trigger is a trigger used in conjunction with SVD2. Its purpose is to reject beam-gas events characterized by vertices far away from the interaction point. This trigger uses SVD information available 25.6 μs after the collision, hence too late for the Level-1 decision. The purpose of this trigger is therefore to abort the readout system, which generally takes 50 μs . The Level-1.5 trigger can hence reduce dead time significantly. The Level-1.5 trigger is described in details in [109].

2.3.2 The Level-3 trigger

The Level-3 trigger system is a software trigger running on a Linux PC farm. It uses fast reconstruction and rejects events having no track with an impact parameter in z lower than 5 cm and events having less than 3 GeV deposited in the ECL. The event rate is reduced by about $\sim 50\%$.

2.3.3 The Data Acquisition system (DAQ)

For Level-1 triggered events, the Data Acquisition (DAQ) collects subdetector information. As shown in Figure 2.19, the DAQ is a system running in parallel segmented into 7 subsystems corresponding to the different subdetectors.

In most subdetectors, signals correspond to pulses proportional to the deposited energy in the detector. These pulses are converted to times by Q-to-T modules and these times are then digitized by time digital converters (TDC). For the KLM, only the timing information of the shower is recorded, hence a Q-to-T converter is not needed. For the SVD, the DSSDs are read out by on-board chips and passed to Flash Analog-to-Digital Converters (FADC).

After the sequence control (SEQ) has received a GDL signal, subdetector data are sent to the event builder, which combines parallel data from all subdetectors into event-by-event data. The event is then sent to the online PC farm, which performs the Level-3 trigger and writes to storage raw data, which contain all subdetector information. The size of a typical hadronic event is about 30 kB and about 15 MB/s have to be written to tape.

2.3.4 The Level-4 filter and Data Summary Tapes (DST) production

The Level-4 filter is now applied online on raw data by a PC farm and events passing this filter are converted from raw data to full reconstructed data, where, for example, particle tracks, photon candidates and likelihoods for particle identification are computed. The full reconstructed data are stored in DST files in the PANTHER [110] file format.

The Level-4 filter requires events with more than 4 GeV of energy deposited in the ECL and with at least one track with a transverse momentum larger than 300 MeV/ c and an impact parameter less than 1 cm in r and 4 cm in z .

DSTs files are reduced for specific physics purposes in a process called “skimming” and are stored in Mini-DST (MDST) files [111]. Both analyses presented in this document use the “HadronB” (“HadronBJ”) skims, obtained after loose requirements to select B meson events (B meson and J/ψ events) [112]. The “HadronBJ” skim is an update of the “HadronB” skim and is used for data collected after August 2002. Both the (M)DST pro-

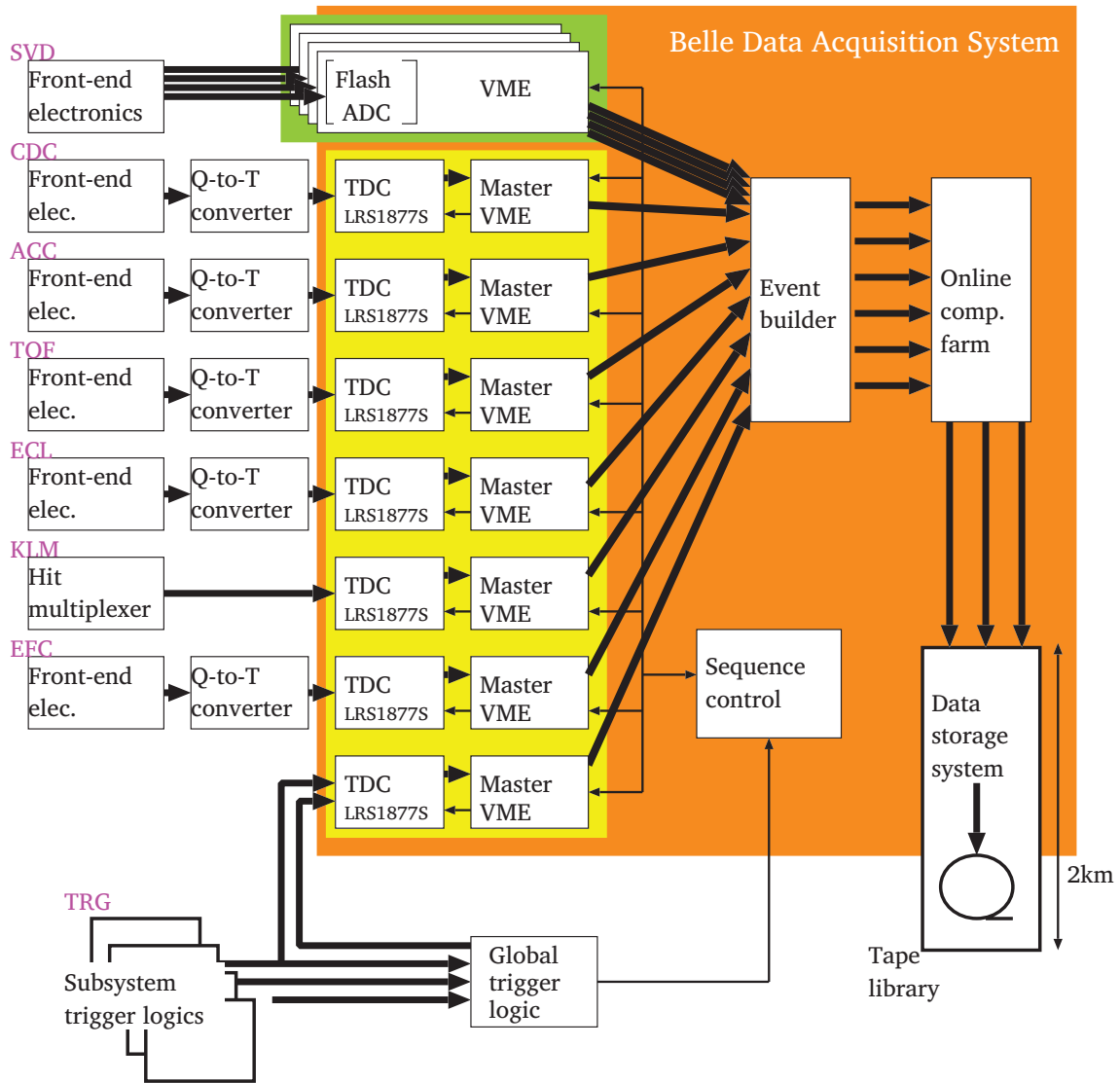


Figure 2.19: Overview of the Belle Data Acquisition system..

duction and the analyses are performed in a C++ framework called BASF [113] (Belle Analysis Framework).

2.4 The detector simulation

The detector is completely simulated using Monte Carlo techniques. Simulated events are produced in two steps: events are generated according to physics processes and then are reconstructed as real data using a complete simulation of the Belle detector. The first step is achieved with EvtGen [66], an event generator written by the *BABAR* collaboration. The second step involves GEANT 3 [114], the detector simulation software from CERN, and the same software used to reconstruct real data. Beam background, obtained from random triggered real data events, is embedded on each simulated event.

2.5 The flavor tagging

The flavor tagging is the identification of the flavor of the accompanying neutral B meson. This information is crucial in, for example, CP violation analyses where the flavor of the studied B decay mode cannot be derived from its decay final state, such as in $B^0(\bar{B}^0) \rightarrow J/\psi(l^+l^-)K_S^0(\pi^+\pi^-)$.

The flavor of the accompanying B meson can only be determined when that B decays into a flavor-specific mode, where the flavor can be derived from the charge of a decay particle. Belle uses the following modes where the flavor can be determined from these specific particles:

- high-momentum leptons from $B^0 \rightarrow Xl^+\nu$,
- kaons, since the majority of them originate from $B^0 \rightarrow K^+X$ decays through the cascade $\bar{b} \rightarrow \bar{c} \rightarrow \bar{s}$,
- intermediate-momentum leptons from $\bar{b} \rightarrow \bar{c} \rightarrow \bar{s}l^-\bar{\nu}$,
- high-momentum pions coming from $B^0 \rightarrow D^{(*)}\pi^+X$ decays,
- slow pions from $B^0 \rightarrow D^{*-}X, D^{*-} \rightarrow \bar{D}^0\pi^-$,
- $\bar{\Lambda}$ baryons from the cascade decays $\bar{b} \rightarrow \bar{c} \rightarrow \bar{s}$.

The flavor tagging tool of the Belle software requires as input the particles forming the B candidate (eg. the two pions and leptons for $B^0 \rightarrow J/\psi K_S^0$) and returns the value of two variables:

- f : the flavor of the accompanying B meson (+1 for B^+ and B^0 and -1 for B^- and \bar{B}^0),
- r : an expected flavor dilution factor that ranges from zero for no flavor information to one for unambiguous flavor assignment.

The f and r variables are computed by comparing the particles composing the rest of the event (and hence assumed to come from the accompanying B) with the “flavor candles” listed above. This computation involves multi-dimensional likelihoods built from MC events and is described in details in [115, 116].

2.6 Number of B meson pairs at the Υ resonances

2.6.1 The luminosity measurement

The instantaneous luminosity of a e^+e^- collider can be measured by counting Bhabha scattering events ($e^+e^- \rightarrow e^+e^-$). Bhabha events are electroweak processes and, therefore, their cross-section can be computed with a precision of $\sim 0.5\%$ using next-to-leading order radiative corrections [117]. The luminosity (\mathcal{L}) is measured with

$$\mathcal{L} = \frac{\mathcal{R}}{\sigma \times \epsilon}, \quad (2.12)$$

where \mathcal{R} is the rate of Bhabha events measured by a calorimeter, ϵ is the reconstruction efficiency and σ the theoretical Bhabha cross-section integrated over the calorimeter acceptance. At Belle, the luminosity is measured by both the EFC and the ECL; the Bhabha rate in the EFC is ~ 148 Hz at $\mathcal{L} = 10^{33} \text{ cm}^{-2}\text{s}^{-1}$. The uncertainty on the luminosity is about 1.4%.

2.6.2 The $b\bar{b}$ production cross-section

At both the $\Upsilon(4S)$ and $\Upsilon(5S)$ resonances, a hadronic event is either a $b\bar{b}$ event or a continuum event. The number of $b\bar{b}$ events has therefore to satisfy the obvious relation

$$N_{\Upsilon}^{b\bar{b}} = N_{\Upsilon}^{\text{had}} - N_{\Upsilon}^{\text{cont}}, \quad (2.13)$$

where $N_{\Upsilon}^{\text{had}}$ is the total number of hadronic events and $N_{\Upsilon}^{\text{cont}}$ the number of hadronic events from continuum.

We can estimate $N_{\Upsilon}^{\text{cont}}$ using continuum data samples recorded below the $\Upsilon(4S)$ resonance, where no B meson can be produced. The previous relation can therefore be written as

$$N_{\Upsilon}^{b\bar{b}} = \frac{1}{\epsilon_{\Upsilon}^{b\bar{b}}} \times \left(N_{\Upsilon}^{\text{had,meas}} - N_{\text{cont}}^{\text{had,meas}} \times \frac{\mathcal{L}_{\Upsilon}}{\mathcal{L}_{\text{cont}}} \times \frac{E_{\text{cont}}^2}{E_{\Upsilon}^2} \times \frac{\epsilon_{\Upsilon}^{\text{cont}}}{\epsilon_{\text{cont}}^{\text{cont}}} \right), \quad (2.14)$$

where $N_{\Upsilon}^{b\bar{b}}$ is the produced number of $b\bar{b}$ events, $N_{\Upsilon}^{\text{had,meas}}$ ($N_{\text{cont}}^{\text{had,meas}}$) is the measured number of hadronic events in the Υ (continuum) sample, \mathcal{L} are the luminosities of the two samples, E are the CM energies of the two samples to account for the energy dependence of the hadronic cross section and ϵ are the reconstruction efficiencies of the different event types in the two samples.

The $b\bar{b}$ production can then be evaluated with

$$\sigma_{b\bar{b}} = N_{\Upsilon}^{b\bar{b}} / \mathcal{L}_{\Upsilon}. \quad (2.15)$$

2.7 B_s^0 production at the $\Upsilon(5S)$ resonance

We discuss below how the $b\bar{b}$ cross-section and the fractions related to B_s^0 production were measured in [95, 58] with the first sample (1.86 fb^{-1}) recorded by Belle at the $\Upsilon(5S)$ resonance.

2.7.1 The $b\bar{b}$ production cross-section at the $\Upsilon(5S)$ resonance

Using a 3.76 fb^{-1} continuum sample recorded 60 MeV below the $\Upsilon(4S)$ resonance and the method detailed in Section 2.6, the number of $b\bar{b}$ events in the 1.86 fb^{-1} sample is determined to be $(5.61 \pm 0.29) \times 10^5$ [95]. The $b\bar{b}$ production cross-section at the $\Upsilon(5S)$ resonance is therefore

$$\sigma_{b\bar{b}}^{\Upsilon(5S)} = (0.302 \pm 0.015) \text{ nb}. \quad (2.16)$$

At the $\Upsilon(4S)$ resonance, the $b\bar{b}$ cross-section is about 1.1 nb, hence is more than three times larger.

2.7.2 The fraction f_s

The f_s fraction is the fraction of $b\bar{b}$ events containing a B_s^0 meson at the $\Upsilon(5S)$ resonance and is computed as the ratio of $B_s^{(*)}\bar{B}_s^{(*)}$ events among the $b\bar{b}$ events.

In a $b\bar{b}$ event at the $\Upsilon(5S)$ energy, a D meson is either the product of the decay of a B_s^0 meson or a B meson. Therefore, f_s can be extracted from the relations

$$\mathcal{B}(\Upsilon(5S) \rightarrow D_s X)/2 = f_s \times \mathcal{B}(B_s^0 \rightarrow D_s X) + (1 - f_s) \times \mathcal{B}(B \rightarrow D_s X), \quad (2.17)$$

$$\mathcal{B}(\Upsilon(5S) \rightarrow D^0 X)/2 = f_s \times \mathcal{B}(B_s^0 \rightarrow D^0 X) + (1 - f_s) \times \mathcal{B}(B \rightarrow D^0 X). \quad (2.18)$$

The inclusive branching fractions of the $\Upsilon(5S) \rightarrow \{D_s, D^0\}X$ decays are measured with a continuum subtraction method in the $x(D)$ variable. This variable is defined as $p(D)/p_{\max}(D)$ where $p(D)$ is the measured momentum of the D meson and $p_{\max}(D)$ is its momentum if it was produced in the process $e^+e^- \rightarrow DD$. Due to kinematics, the D mesons from the $\Upsilon(5S)$ decay contribute in the region $x(D) < 0.5$ while those from continuum events contribute in the region $x(D) > 0.5$, as shown in Figure 2.20.

The inclusive branching fractions of the $B \rightarrow \{D_s, D^0\}X$ decays have been measured elsewhere [2] and model-dependent theoretical predictions exist for the $B_s \rightarrow \{D_s, D^0\}X$ branching fractions [93]. Two measurements of f_s are obtained [95]

$$f_s(D_s) = (17.9 \pm 1.4 \pm 4.1)\%, \quad (2.19)$$

$$f_s(D^0) = (18.1 \pm 3.6 \pm 7.4)\%. \quad (2.20)$$

The Particle Data Group has computed the average of the two previous Belle measurements [95] and the CLEO measurement [118] and has obtained [2]:

$$f_s = (19.5^{+3.0}_{-2.3})\%. \quad (2.21)$$

In the total sample recorded by Belle at the $\Upsilon(5S)$ resonance (23.6 fb^{-1}), we can therefore evaluate the number of B_s^0 mesons with

$$N_{B_s^0} = 2 \times L_{\text{int}} \times \sigma_{b\bar{b}}^{\Upsilon(5S)} \times f_s = (2.8^{+0.5}_{-0.4}) \times 10^6. \quad (2.22)$$

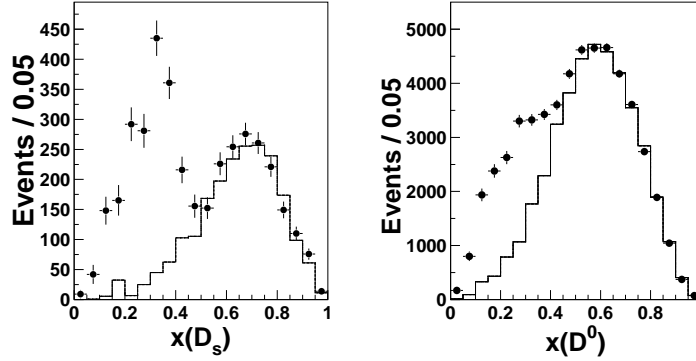


Figure 2.20: Normalized momentum distributions of D_s (left) and D^0 (right) mesons [95]. The points with error bars are the data recorded at the $\Upsilon(5S)$ resonance and the histograms are the continuum data, normalized to the same luminosity of 1.86 fb^{-1} .

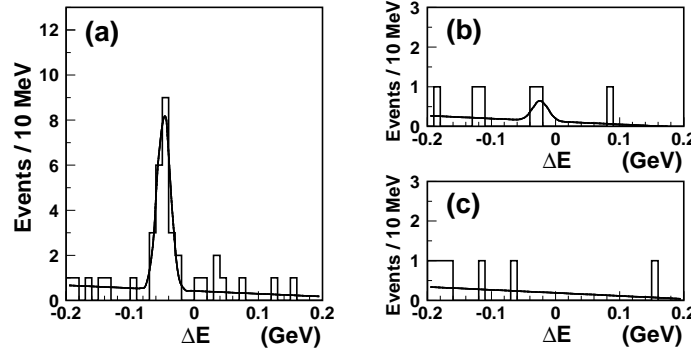


Figure 2.21: ΔE for six reconstructed B_s^0 decay modes [58] with M_{bc} in the $B_s^* \bar{B}_s^*$ region (a), in the $B_s^* \bar{B}_s^0$ region (b) and in the $B_s^0 \bar{B}_s^0$ region (c). A significant signal is seen in the $B_s^* \bar{B}_s^*$ region. The M_{bc} and ΔE variables are defined in Section 3.1.4.

2.7.3 The fraction $f_{B_s^* \bar{B}_s^*}$

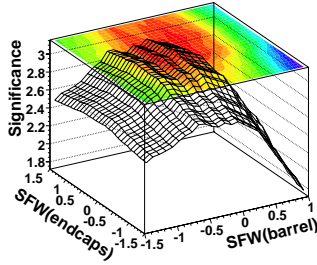
The $\Upsilon(5S)$ can decay to $B_s^* \bar{B}_s^*$, $B_s^* \bar{B}_s^0$ and $B_s^0 \bar{B}_s^0$. Due to low statistics, six B_s^0 decay modes are reconstructed and combined: $B_s^0 \rightarrow D_s^{(*)-} \pi^+$, $B_s^0 \rightarrow D_s^{(*)-} \rho^+$, $B_s^0 \rightarrow J/\psi \phi$ and $B_s^0 \rightarrow J/\psi \eta$. Figure 2.21 shows a dominant $B_s^* \bar{B}_s^*$ production compared to the $B_s^* \bar{B}_s^0$ and $B_s^0 \bar{B}_s^0$ productions. The fraction $f_{B_s^* \bar{B}_s^*}$ defined as the ratio of the $B_s^* \bar{B}_s^*$ events among $B_s^{(*)} \bar{B}_s^{(*)}$ events is measured to be [58]

$$f_{B_s^* \bar{B}_s^*} = (93_{-9}^{+7})\%. \quad (2.23)$$

The two other fractions ($f_{B_s^* \bar{B}_s^0}$ and $f_{B_s^0 \bar{B}_s^0}$) are small and not yet measured. Of course, the sum of the three fractions should equal 100%.

Chapter 3

Reconstruction



We describe the reconstruction of B mesons for the $B^+ \rightarrow K^+ h \rightarrow K^+ \gamma \gamma$, the $B_s^0 \rightarrow \phi \gamma$ and the $B_s^0 \rightarrow \gamma \gamma$ modes. Possible backgrounds are analyzed and their suppression studied. Large efforts are directed toward the rejection of the continuum background.

3.1 Signal reconstruction

WE describe below the reconstruction of signal candidates for the $B^+ \rightarrow K^+ h \rightarrow K^+ \gamma \gamma$, $B_s^0 \rightarrow \phi \gamma$ and $B_s^0 \rightarrow \gamma \gamma$ modes.

3.1.1 Charged tracks and kaons

Charged tracks are reconstructed using the SVD and CDC detectors and are required to originate from the nominal interaction point with the requirements

$$|dr| < 0.5 \text{ cm}, \quad (3.1)$$

$$|dz| < 3.0 \text{ cm}, \quad (3.2)$$

where dr and dz are the radial distance and the distance along the beam axis to the interaction point, respectively. Kaon candidates are then selected from the charged tracks with the requirement

$$\mathcal{L}_{K/\pi} \equiv \mathcal{L}_K / (\mathcal{L}_K + \mathcal{L}_\pi) > 0.6, \quad (3.3)$$

where \mathcal{L}_K (respectively \mathcal{L}_π) is the likelihood for a track to be a kaon (respectively a pion) based on the response of the ACC and on measurements from the CDC and TOF. Tracks with $\mathcal{L}_{K/\pi} < 0.6$ are assumed to be pions. The kaon identification efficiency depends on the kaon momentum and therefore depends on the reconstructed mode. We compute an average for each mode and we obtain the identification efficiency to be between 84% and 90% with 7% to 11% of pions misidentified as kaons.

Table 3.1: Nominal mass (GeV/c^2) of the reconstructed particles and definition of invariant mass windows (GeV/c^2) for photon pairs.

Particle	Mass	Wide $m_{\gamma\gamma}$ window	Tight $m_{\gamma\gamma}$ window
η	0.548	0.4–0.7	0.50–0.57
η'	0.958	0.8–1.1	0.90–0.98
η_c	2.980	2.5–3.2	2.82–3.05
$\eta_c(2S)$	3.637	3.2–3.8	3.44–3.70
χ_{c0}	3.415	3.0–3.5	3.25–3.50
χ_{c2}	3.556	3.0–3.8	3.40–3.62
J/ψ	3.097	2.5–3.2	2.92–3.15
$X(3872)$	3.872	3.0–4.1	3.72–3.95

3.1.2 Photons

Photons are identified as energy depositions in the ECL that cannot be matched to a charged track. We require their energies in the laboratory to be greater than 100 MeV and their shower shape in the ECL to be consistent with that of a photon to reject neutral hadrons such as neutrons and K_L^0 mesons, and merged photons from π^0 to two photons decays. For each ECL cluster, we compute $E_{9/25}$, the ratio of the energy deposited in the array of the central 3×3 calorimeter cells to that of 5×5 cells. For the reconstruction of $B_s^0 \rightarrow \phi\gamma$, $B_s^0 \rightarrow \gamma\gamma$ and $B^+ \rightarrow K^+h \rightarrow K^+\gamma\gamma$ with $h \equiv \eta_c, \eta_c(2S), \chi_{c0}, \chi_{c2}, J/\psi, X(3872)$, we require $E_{9/25} > 0.95$ for all candidate photons. For the reconstruction of $B^+ \rightarrow K^+h \rightarrow K^+\gamma\gamma$ with $h \equiv \eta, \eta'$, we require $E_{9/25} > 0.90$ for the photon with the lowest energy in the laboratory and $E_{9/25} > 0.95$ for the other photon. For the $B_s^0 \rightarrow \gamma\gamma$ mode, we select photons only¹ in the barrel part of the ECL corresponding to

$$33^\circ < \theta < 128^\circ. \quad (3.4)$$

3.1.3 Resonances: the h particles and ϕ mesons

For the $B^+ \rightarrow K^+h \rightarrow K^+\gamma\gamma$ analysis, pairs of photons are retained and associated with the corresponding h particle when their invariant mass ($m_{\gamma\gamma}$) is inside one of the wide mass windows defined in Table 3.1. A mass-constrained fit of the photon momenta is performed to match the nominal masses, listed in Table 3.1, with the constraint that the photons originate from the nominal interaction point. Figure 3.1 shows the $m_{\gamma\gamma}$ distribution for every $B^+ \rightarrow K^+h$ mode. One can notice that the $m_{\gamma\gamma}$ windows overlap for some modes, hence a specific mode can be reconstructed as another mode and therefore be a background for this other mode. This cross-feed effect is studied in Section 5.4 and is found to be negligible, except for the $B^+ \rightarrow K^+J/\psi$ mode, where a significant contribution from $B^+ \rightarrow K^+\eta_c$ is expected.

¹See Sections 3.2.2 and 4.2.

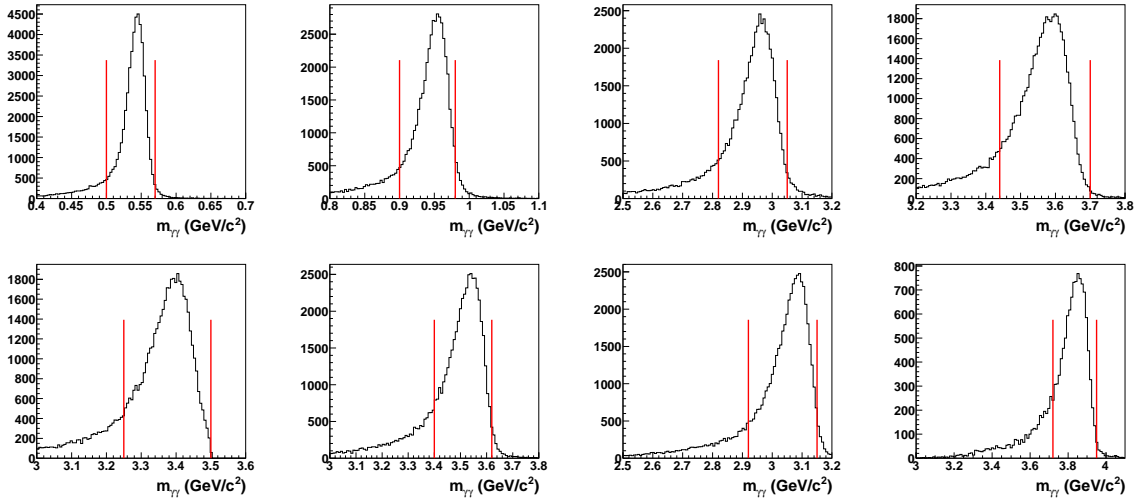


Figure 3.1: $m_{\gamma\gamma}$ signal distributions for the $B^+ \rightarrow K^+h \rightarrow K^+\gamma\gamma$ modes. Top from left to right: $B^+ \rightarrow K^+\eta$, $B^+ \rightarrow K^+\eta'$, $B^+ \rightarrow K^+\eta_c$ and $B^+ \rightarrow K^+\eta_c(2S)$. Bottom from left to right: $B^+ \rightarrow K^+\chi_{c0}$, $B^+ \rightarrow K^+\chi_{c2}$, $B^+ \rightarrow K^+J/\psi$, $B^+ \rightarrow K^+X(3872)$. Lines show the tight requirement on $m_{\gamma\gamma}$ discussed in Section 3.2.2.

For the $B_s^0 \rightarrow \phi\gamma$ analysis, we reconstruct ϕ mesons in the decay mode $\phi \rightarrow K^+K^-$ by combining oppositely charged kaons having an invariant mass within ± 12 MeV/ c^2 of the nominal ϕ mass of 1019.5 MeV/ c^2 [2]. With a resolution of about 4.6 MeV/ c^2 , the latter requirement corresponds to about ± 2.5 standard deviations.

3.1.4 B meson selections

In the $B^+ \rightarrow K^+h \rightarrow K^+\gamma\gamma$ analysis, B^+ mesons are formed by combining a kaon and a h particle. In the $B_s^0 \rightarrow \phi\gamma$ and $B_s^0 \rightarrow \gamma\gamma$ analyses, B_s^0 mesons are formed by combining a ϕ meson with a photon or by combining two photons, respectively. We select B mesons by means of the beam-energy constrained mass, M_{bc} , and an energy difference, ΔE , defined as

$$M_{bc} \equiv \sqrt{(E_{\text{beam}}^{\text{CM}})^2 - p_B^{\text{CM}}}, \quad (3.5)$$

$$\Delta E \equiv E_B^{\text{CM}} - E_{\text{beam}}^{\text{CM}}. \quad (3.6)$$

In these definitions, $E_{\text{beam}}^{\text{CM}} \equiv \sqrt{s}/2$ is the beam energy and p_B^{CM} and E_B^{CM} are the reconstructed momentum and energy of the B meson candidate, all variables being evaluated in the center-of-mass (CM) frame.

The $B^+ \rightarrow K^+h \rightarrow K^+\gamma\gamma$ signals peak at $M_{bc} = m_{B^+} \approx 5.28$ GeV/ c^2 and at $\Delta E \approx 0$ GeV. For the $B_s^0 \rightarrow \gamma\gamma$ and $B_s^0 \rightarrow \phi\gamma$ modes, we do not fully reconstruct the B_s^* meson due to the low energy, about 50 MeV, of the photon of the $B_s^* \rightarrow B_s^0\gamma$ decay. Therefore, the B_s^0 modes peak at different M_{bc} and ΔE positions depending on how the B_s^0 meson was produced [119]:

- $B_s^*\bar{B}_s^*$ production: the B_s^0 signal peaks at $M_{bc} = m_{B_s^*} \approx 5.41$ GeV/ c^2 and $\Delta E \approx m_{B_s^0} - m_{B_s^*} \approx -0.050$ GeV.

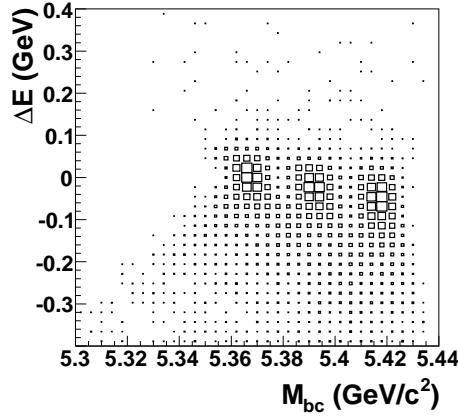


Figure 3.2: ΔE versus M_{bc} for the $B_s^0 \rightarrow \phi\gamma$ signal MC. Signals coming from $B_s^0\bar{B}_s^0$, $B_s^*\bar{B}_s^0$ and $B_s^*\bar{B}_s^*$ are arbitrarily normalized and appear from upper left to bottom right.

- $B_s^*\bar{B}_s^0$ and $B_s^*\bar{B}_s^*$ production: the B_s^0 signal peaks at $M_{bc} \approx (m_{B_s^*} + m_{B_s^0})/2 \approx 5.39 \text{ GeV}/c^2$ and $\Delta E \approx (m_{B_s^0} - m_{B_s^*})/2 \approx -0.025 \text{ GeV}$.
- $B_s^0\bar{B}_s^0$ production: the B_s^0 signal peaks at $M_{bc} = m_{B_s^0} \approx 5.37 \text{ GeV}/c^2$ and $\Delta E \approx 0 \text{ GeV}$.

The expected distribution of the different $B_s^0 \rightarrow \phi\gamma$ signals is shown in Figure 3.2. Signals overlap in ΔE but are well separated in M_{bc} .

For the $B^+ \rightarrow K^+h \rightarrow K^+\gamma\gamma$ analysis, we select B^+ meson candidates with $M_{bc} > 5.2 \text{ GeV}/c^2$ and $-0.3 \text{ GeV} < \Delta E < 0.3 \text{ GeV}$. For the $\Upsilon(5S)$ analysis, we select $B_s^0 \rightarrow \phi\gamma$ candidates with $M_{bc} > 5.3 \text{ GeV}/c^2$ and $-0.4 \text{ GeV} < \Delta E < 0.4 \text{ GeV}$, and $B_s^0 \rightarrow \gamma\gamma$ candidates with $M_{bc} > 5.3 \text{ GeV}/c^2$ and $-0.7 \text{ GeV} < \Delta E < 0.4 \text{ GeV}$. The latter regions are called “fit regions”.

The helicity angle in the $B_s^0 \rightarrow \phi\gamma$ mode

The helicity angle θ_{hel} is defined as the angle between the K^+ and the B_s^0 meson computed in the ϕ rest frame. For signal events, $\cos\theta_{\text{hel}}$ follows a $1 - \cos^2\theta_{\text{hel}}$ distribution, due to the longitudinal helicity of the ϕ meson, while for continuum events, $\cos\theta_{\text{hel}}$ has a flat distribution. No requirement is applied on the helicity angle but this quantity will be used in the fit presented in Chapter 4.1 to help separate signal and background. The helicity angle distributions for signal MC and sideband data is shown in Figure 4.5 on page 76.

Best candidate selection

In the $B^+ \rightarrow K^+h \rightarrow K^+\gamma\gamma$ analysis, we perform a best candidate selection when more than one candidate in an event is seen. For each h mode, we choose the photon pair with the smallest χ^2 of the mass fit, and if multiple kaons can be associated with this photon pair, the kaon with the highest probability to be a kaon ($\mathcal{L}_{K/\pi}$) is chosen.

Table 3.2: Signal windows for the $B^+ \rightarrow K^+ h \rightarrow K^+ \gamma \gamma$ modes. The M_{bc} signal windows are defined as $M_{bc} > 5.27 \text{ GeV}/c^2$ for all modes.

Particle	ΔE window (GeV)	Particle	ΔE window (GeV)
η	$-0.15 < \Delta E < 0.10$	η'	$-0.15 < \Delta E < 0.10$
η_c	$-0.10 < \Delta E < 0.10$	$\eta_c(2S)$	$-0.08 < \Delta E < 0.06$
χ_{c0}	$-0.10 < \Delta E < 0.10$	χ_{c2}	$-0.06 < \Delta E < 0.06$
J/ψ	$-0.09 < \Delta E < 0.09$	$X(3872)$	$-0.09 < \Delta E < 0.09$

In the $B_s^0 \rightarrow \phi \gamma$ and $B_s^0 \rightarrow \gamma \gamma$ analyses, after all requirements, all selected B_s^0 mesons originate from different events. Hence a best candidate selection is not needed.

3.1.5 Definition of the signal windows

For the $B^+ \rightarrow K^+ h \rightarrow K^+ \gamma \gamma$ analysis, the M_{bc} signal window is defined as $M_{bc} > 5.27 \text{ GeV}/c^2$ for all modes and the ΔE signal windows are different for each mode, as shown in Table 3.2.

For the analysis at the $\Upsilon(5S)$ resonance, we define signal windows corresponding to $B_s^* \bar{B}_s^*$ production since $\sim 90\%$ of the B_s^0 mesons are produced in this decay mode. For the $B_s^0 \rightarrow \phi \gamma$ mode, the signal window is defined as $M_{bc} > 5.4 \text{ GeV}/c^2$, $-0.2 \text{ GeV} < \Delta E < -0.02 \text{ GeV}$ and $|\cos \theta_{\text{hel}}| < 0.8$. For the $B_s^0 \rightarrow \gamma \gamma$ mode, it is defined as $M_{bc} > 5.4 \text{ GeV}/c^2$ and $-0.3 \text{ GeV} < \Delta E < 0.05 \text{ GeV}$.

Signal windows will be used to optimize the rejection of the continuum background and to obtain projection figures of the fits to the data presented in Chapters 4 and 5.

3.2 Background study

3.2.1 Continuum suppression variables

The main background in both analyses is due to continuum events, ie. events coming from light-quark pair production ($e^+ e^- \rightarrow u\bar{u}, d\bar{d}, s\bar{s}, c\bar{c}$ processes). This section describes the tools used to suppress this background and Section 3.2.2 describes how the rejection is optimized and achieved.

Four variables describing event topology are used to suppress the continuum background: the SFW, $|\cos \theta_B^{\text{CM}}|$ and Δz variables, and the flavor tagging variable. In addition, we also reject photons from π^0 and η decays to two photons to mainly reduce the continuum.

The SFW variable

The SFW (Super Fox-Wolfram) variable is a Fisher discriminant based on modified Fox-Wolfram moments. The Fox-Wolfram moments were introduced in [120] and the SFW variable used by Belle in many publications was employed for the first times in [121, 122]. SFW describes how the particles composing the event are distributed: the continuum

Table 3.3: α_l and β_l coefficients used to compute SFW.

Mode	α_2	α_4	β_1	β_2	β_3	β_4
$B^+ \rightarrow K^+\eta$	-4.485	-1.238	-2.071	0.282	1.653	1.705
$B^+ \rightarrow K^+\eta'$	-4.294	-1.248	-2.003	0.240	1.654	1.667
$B^+ \rightarrow K^+\eta_c$	-4.165	-0.734	-2.182	0.291	1.593	1.605
$B^+ \rightarrow K^+\eta_c(2S)$	-3.418	-1.028	-2.150	0.026	1.971	1.713
$B^+ \rightarrow K^+\chi_{c0}$	-3.756	-0.938	-2.178	0.114	1.877	1.660
$B^+ \rightarrow K^+\chi_{c2}$	-3.572	-0.982	-2.066	0.066	1.896	1.689
$B^+ \rightarrow K^+J/\psi$	-4.220	-0.759	-2.098	0.260	1.620	1.602
$B^+ \rightarrow K^+X(3872)$	-3.598	-0.903	-1.730	-0.104	0.626	1.498
$B_s^0 \rightarrow \phi\gamma$	-4.153	-1.603	-2.781	-0.032	1.473	1.788
$B_s^0 \rightarrow \gamma\gamma$	-4.026	-1.861	-3.415	0.132	1.242	1.580

events tend to have a jet-like signature while the $\Upsilon(4S)/\Upsilon(5S) \rightarrow BB$ events a spherical signature due to the fact that B mesons are produced almost at rest in the CM frame. The SFW variable is built from six Fox-Wolfram moments (h_l) and is computed as

$$\text{SFW} = \sum_{l=2,4} \alpha_l \frac{h_l^{\text{signal, other}}}{h_0^{\text{signal, other}}} + \sum_{l=1,2,3,4} \beta_l \frac{h_l^{\text{other, other}}}{h_0^{\text{other, other}}}, \quad (3.7)$$

$$h_l = \sum_{i,j} p_i^{\text{CM}} p_j^{\text{CM}} P_l(\cos \theta_{ij}^{\text{CM}}), \quad (3.8)$$

where P_l is the l^{th} -order Legendre polynomial function and p_i^{CM} and θ_{ij}^{CM} are the momentum of the i^{th} particle and the angle between the i^{th} and the j^{th} particles in the CM frame. The *signal, other* superscript of h_l means that i runs over the reconstructed particles forming the B signal candidate and j over all the other particles composing the event. The *other, other* superscript means that both i and j run over the “other” particles. The α_l and β_l parameters, optimized for each mode using signal and continuum MC events, are listed in Table 3.3. SFW distributions for signal and continuum are shown in Figure 3.3 on page 60 for the $B^+ \rightarrow K^+\eta$ mode and in Figure 3.5 on page 64 for the $B_s^0 \rightarrow \phi\gamma$ and $B_s^0 \rightarrow \gamma\gamma$ modes.

The $|\cos \theta_B^{\text{CM}}|$ variable ($B^+ \rightarrow K^+h \rightarrow K^+\gamma\gamma$ only)

The $|\cos \theta_B^{\text{CM}}|$ variable is defined as the absolute value of the cosine of the B production angle with respect to the beam computed in the CM frame. This variable can be used to suppress the continuum in analyses at the $\Upsilon(4S)$ resonance due to the fact that the $\Upsilon(4S)$, a particle with $J = 1$, decays to two $J = 0$ particles. Therefore, $|\cos \theta_B^{\text{CM}}|$ is distributed following a $1 - \cos^2$ function for signal events, while its distribution is found to be flat for continuum events. The $|\cos \theta_B^{\text{CM}}|$ distributions for signal and continuum are shown in Figure 3.3 on page 60.

The Δz variable ($B^+ \rightarrow K^+ h \rightarrow K^+ \gamma\gamma$ only)

The Δz variable is the flight length difference between the two B mesons along the beam axis. This variable is generally used in time-dependent analyses but it can be used to discriminate signal events from continuum events: the Δz distribution, while being centred at zero for both contributions, is wider for signal events than for continuum events. This is due to the fact that B mesons fly for a short distance, typically 0.2 mm, before decaying, while particles from continuum tend to originate directly from the interaction point. The Δz variable is computed as

$$\Delta z = z_{B^+ \rightarrow K^+ \gamma\gamma} - z_{B_{\text{other}}} , \quad (3.9)$$

where $z_{B^+ \rightarrow K^+ \gamma\gamma}$ is obtained by intersecting the kaon track with the beam profile, measured run by run mainly with Bhabha scattering events, and $z_{B_{\text{other}}}$ is obtained by performing a vertex fit with all the other tracks composing the event, except the tracks compatible with a $K_S^0 \rightarrow \pi^+ \pi^-$ decay. If the $\chi^2/\text{n.d.f.}$ of the vertex fit is larger than 20, the track with the largest χ^2 to the vertex is removed and the fit is performed again. This procedure is repeated until the fit yields a $\chi^2/\text{n.d.f.}$ smaller than 20 or until the number of track is reduced to one. In the latter case, the vertex fit fails. The Δz variable remains unknown when the kaon track does not intersect the beam profile or when the vertex fit fails. The Δz distributions for signal and continuum are found to be slightly different between the two configurations of the inner detector, and are shown in Figure 3.3 on page 60.

The likelihood ratio \mathcal{R}

In the $B^+ \rightarrow K^+ h \rightarrow K^+ \gamma\gamma$ analysis, the SFW, $|\cos \theta_B^{\text{CM}}|$ and Δz variables are combined into a single variable \mathcal{R}_h , a likelihood ratio defined as

$$\mathcal{R}(\text{SFW}, |\cos \theta_B^{\text{CM}}|, \Delta z) = \frac{L_{\text{signal}}}{L_{\text{signal}} + L_{\text{continuum}}} , \quad (3.10)$$

$$L_{\text{signal}}(\text{SFW}, |\cos \theta_B^{\text{CM}}|, \Delta z) = L_{\text{signal}}^{\text{SFW}} \times L_{\text{signal}}^{|\cos \theta_B^{\text{CM}}|} \times L_{\text{signal}}^{\Delta z} , \quad (3.11)$$

$$L_{\text{continuum}}(\text{SFW}, |\cos \theta_B^{\text{CM}}|, \Delta z) = L_{\text{continuum}}^{\text{SFW}} \times L_{\text{continuum}}^{|\cos \theta_B^{\text{CM}}|} \times L_{\text{continuum}}^{\Delta z} , \quad (3.12)$$

where L are probability density functions (PDFs), obtained from MC for each h mode, of their respective variables for signal and continuum events. The SFW and $|\cos \theta_B^{\text{CM}}|$ PDFs for both signal and continuum are modeled, respectively, with three Gaussian functions and a second order polynomial function. The Δz PDF for the signal is modeled with the convolution of a Gaussian function with an exponential decay function. The Δz PDF for the continuum is modeled with the convolution of two Gaussian functions with the sum of an exponential decay function and a Dirac function. We use two different PDFs to describe Δz measured by SVD1 and SVD2. The PDFs for the three variables are shown in Figure 3.3. When Δz is unknown, \mathcal{R} is computed without this variable, ie. we use $L_{\text{signal}}^{\Delta z} \equiv L_{\text{continuum}}^{\Delta z} \equiv 1$ in the above formulae. Signal and continuum distributions for \mathcal{R} are shown in Figure 3.4 for the $B^+ \rightarrow K^+ \eta$ mode.

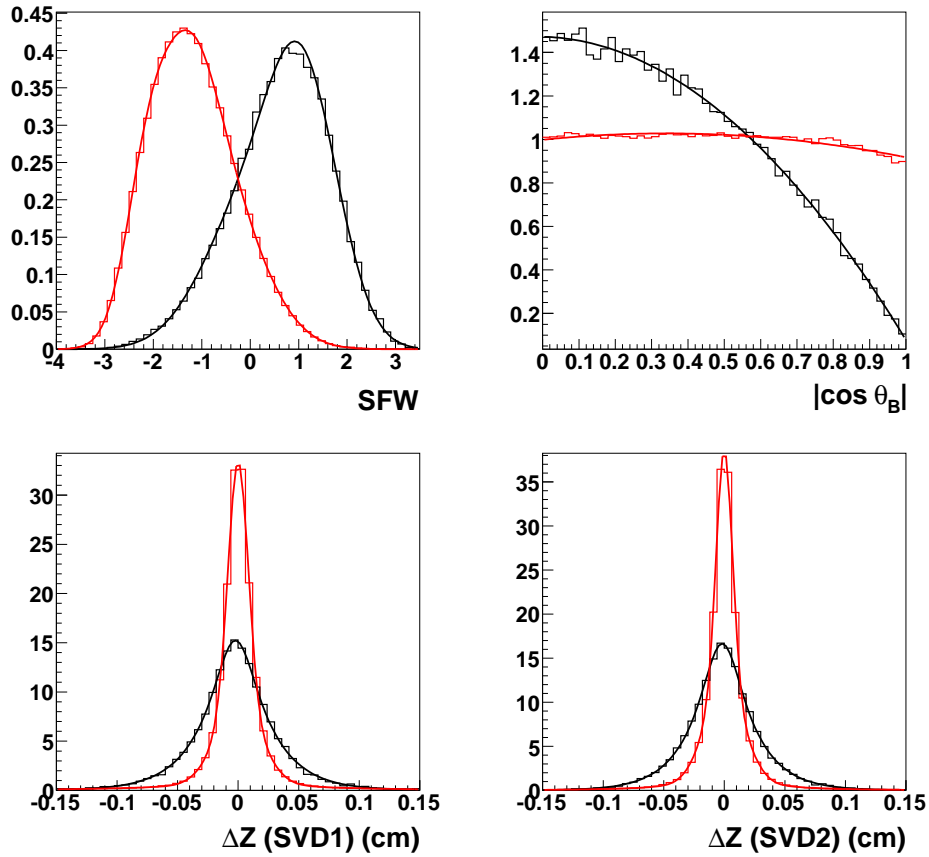


Figure 3.3: MC distributions of SFW (top left), $|\cos \theta_B^{\text{CM}}|$ (top right), Δz for SVD1 (bottom left) and Δz for SVD2 (bottom right) for signal (black) and continuum (red) for the $B^+ \rightarrow K^+ \eta$ mode. All distributions are arbitrarily normalized and are shown with fits used as PDFs to form the likelihood ratio \mathcal{R} . The distributions for the other $B^+ \rightarrow K^+ h \rightarrow K^+ \gamma \gamma$ modes are given in Appendix A on page 105.

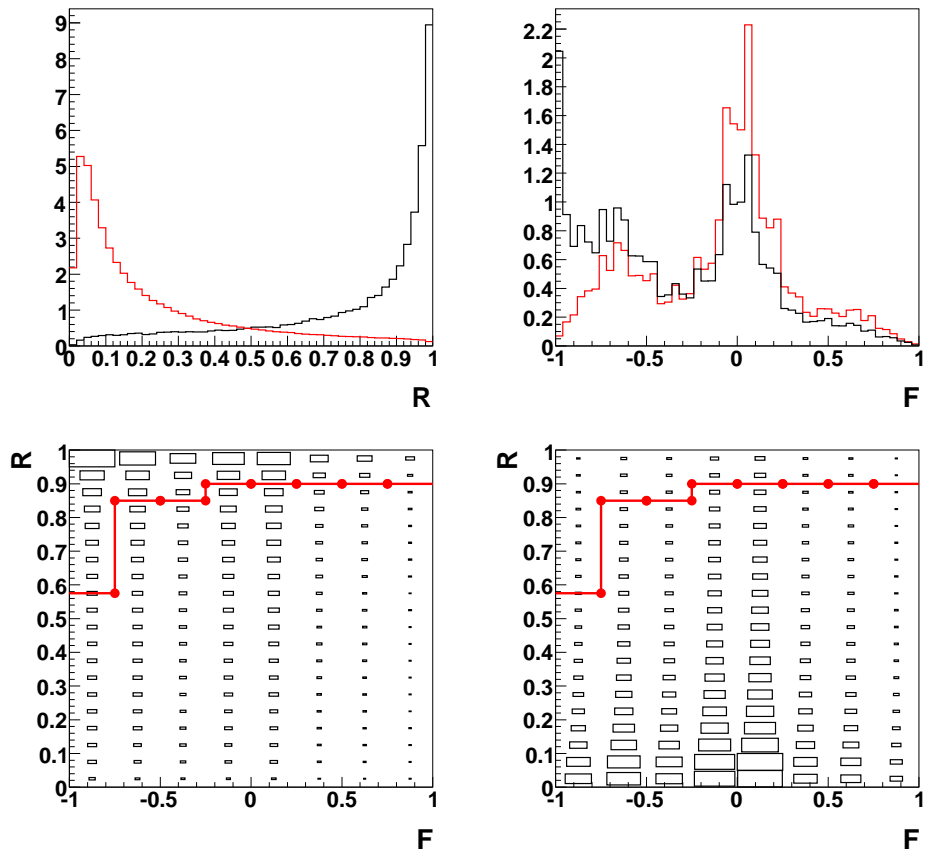


Figure 3.4: Top: MC distributions of \mathcal{R} (top left) and \mathcal{F} (top right) for signal (black) and continuum (red) for the $B^+ \rightarrow K^+\eta$ mode. Bottom: \mathcal{R} versus \mathcal{F} for signal (left) and continuum (right). The red lines show the requirements on \mathcal{R} optimized simultaneously in each bin in \mathcal{F} . The distributions for the other $B^+ \rightarrow K^+h \rightarrow K^+\gamma\gamma$ modes are given in Appendix A on page 105.

The flavor variable \mathcal{F}

The flavor tagging, discussed in Section 2.5, is generally used in CP violation analyses but its usual purpose can be diverted to reduce the contribution from the continuum background. We form a variable \mathcal{F} defined as

$$\mathcal{F} = q_{\text{kaon}} \times f_{B_{\text{other}}} \times r, \quad (3.13)$$

where q_{kaon} is the kaon charge of the $K^+\gamma\gamma$ candidate, $f_{B_{\text{other}}}$ is the flavor of the other B meson and r the flavor dilution factor. In a perfect world, \mathcal{F} should be equal to -1 for signal events: q_{kaon} and $f_{B_{\text{other}}}$ have opposite signs and r is one. For continuum events, \mathcal{F} should be equal to zero because the flavor should not be determined ($r \approx 0$). However, a large fraction of signal and continuum events are badly identified, as shown in Figure 3.4.

Rejection of photons from π^0 and η decays

The decay of η and especially π^0 to two photons is an important source of high energy photons that are important to veto when searching for radiative rare decays. Two different methods are used in the analyses at the $\Upsilon(4S)$ and $\Upsilon(5S)$ resonances.

In the $B^+ \rightarrow K^+h \rightarrow K^+\gamma\gamma$ analysis, we veto photons from π^0 in the following way: we reject pairs of photons having an invariant mass between $117.8 \text{ MeV}/c^2$ and $150.2 \text{ MeV}/c^2$. The latter requirement corresponds to about ± 2.5 standard deviations around the nominal π^0 mass ($m_{\pi^0} \approx 135 \text{ MeV}/c^2$ [2]).

In the $B_s^0 \rightarrow \phi\gamma$ and $B_s^0 \rightarrow \gamma\gamma$ analysis, we reject photons from π^0 and η decays to two photons using a likelihood based on the energy and polar angles of the photons in the laboratory frame and the invariant mass of the photon pair. For each candidate photon, we obtain the probabilities, P_{π^0} and P_{η} , that this photon originates from a π^0 or η decay. The requirements on P_{π^0} and P_{η} are discussed in Section 3.2.2 and their MC distributions are shown in Figure 3.5 on page 64. This π^0 and η rejection is described in more detail in [123].

Table 3.4 summarizes the different variables used in the two analyses to suppress the continuum background.

Table 3.4: Summary of the variables used to suppress the continuum background.

Variable	$B^+ \rightarrow K^+h \rightarrow K^+\gamma\gamma$	$B_s^0 \rightarrow \phi\gamma$ and $B_s^0 \rightarrow \gamma\gamma$
SFW	combined	✓
$ \cos \theta_B^{\text{CM}} $	into a	×
Δz	likelihood ratio \mathcal{R}	×
Flavor tagging \mathcal{F}	✓	×
$\pi^0 \rightarrow \gamma\gamma$ rejection	✓	✓
$\eta \rightarrow \gamma\gamma$ rejection	×	✓

3.2.2 Optimization of the continuum background suppression

Large MC samples are used to optimize the rejection of this background:

- $B_s^0 \rightarrow \gamma\gamma$ and $B_s^0 \rightarrow \phi\gamma$: 50'000 signal events for each mode and about three times the size of the studied data sample for continuum events,
- $B^+ \rightarrow K^+h \rightarrow K^+\gamma\gamma$: 100'000 signal events for each mode and about 1.5 times the size of the studied data sample for continuum events.

For the $B^+ \rightarrow K^+h \rightarrow K^+\gamma\gamma$ analysis, we apply a tighter requirement on $m_{\gamma\gamma}$ and different requirements on \mathcal{R} depending on \mathcal{F} . For the modes with $h = \eta, \eta'$, we use eight ranges on \mathcal{F} ($-1.00 \leq \mathcal{F} < -0.75$, $-0.75 \leq \mathcal{F} < -0.50$, ..., $0.75 \leq \mathcal{F} \leq 1.00$) and for the other modes, we use five ranges ($-1.00 \leq \mathcal{F} < -0.75$, $-0.75 \leq \mathcal{F} < -0.25$, $-0.25 \leq \mathcal{F} < 0.25$, $0.25 \leq \mathcal{F} < 0.75$ and $0.75 \leq \mathcal{F} \leq 1.00$). We optimize simultaneously the requirements on \mathcal{R} and $m_{\gamma\gamma}$ to maximize the figure of merit defined as $N_{\text{signal}}/\sqrt{N_{\text{signal}} + N_{\text{continuum}}}$ for the modes with $h = \eta, \eta'$ and defined as $\epsilon/\sqrt{N_{\text{continuum}}}$ for the other modes. In these definitions, ϵ is the signal efficiency and N_{signal} and $N_{\text{continuum}}$ are the expected number of signal and continuum events in the signal window normalized to the size of the studied data sample assuming the measured branching fractions, listed in Table 1.3. The second figure of merit does not depend on any branching fraction assumption and is therefore used for modes with large uncertainty on the branching fraction. Table 3.1 lists the tight $m_{\gamma\gamma}$ requirements. Figure 3.4 shows the requirement on \mathcal{R} as a function of \mathcal{F} for the $B^+ \rightarrow K^+\eta$ mode. About 95% of the continuum background is rejected by the requirement on \mathcal{R} while about 60% of the signal is kept. For the $B^+ \rightarrow K^+X(3872)$ mode where a looser requirement is applied, $\sim 84\%$ of the continuum is rejected and $\sim 81\%$ of the signal is kept.

For the $B_s^0 \rightarrow \phi\gamma$ analysis, we use a tighter requirement on SFW when the candidate photon is reconstructed outside the barrel part of the ECL. Indeed, the process $e^+e^- \rightarrow q\bar{q}\gamma$ is a source of high-energy photons with low polar angles and can thus be a background for radiative B decays. We optimize simultaneously the requirements on SFW and on the rejection of photons from π^0 and η decays to maximize $\mathcal{S} \equiv N_{\text{signal}}/\sqrt{N_{\text{signal}} + N_{\text{continuum}}}$. N_{signal} and $N_{\text{continuum}}$ are computed in the $B_s^0 \rightarrow \phi\gamma$ signal window corresponding to $B_s^*\bar{B}_s^*$ production and are normalized to the studied data sample assuming $\mathcal{B}(B_s^0 \rightarrow \phi\gamma) = 40 \times 10^{-6}$, $f_s = 19.5\%$ and $f_{B_s^*\bar{B}_s^*} = 93\%$. The optimization of the figure of merit is shown in Figure 3.6. We expect to reconstruct ~ 12.0 signal events on top of ~ 3.6 continuum events, corresponding to a significance of $\mathcal{S} \approx 3.0$, with the following requirements

$$\text{SFW}(\text{barrel}) > -0.1, \quad (3.14)$$

$$\text{SFW}(\text{endcaps}) > 0.5, \quad (3.15)$$

$$P_{\pi^0} < 0.75, \quad (3.16)$$

$$P_{\eta} < 0.65. \quad (3.17)$$

For the $B_s^0 \rightarrow \gamma\gamma$ mode, we use on both photon candidates the same π^0 and η rejection requirements as for the $B_s^0 \rightarrow \phi\gamma$ mode and, since we do not have the sensitivity to observe this decay, we optimize the requirements on SFW to minimize the limit at 90% CL on the $B_s^0 \rightarrow \gamma\gamma$ branching fraction. The limit is computed with the Feldman-Cousins

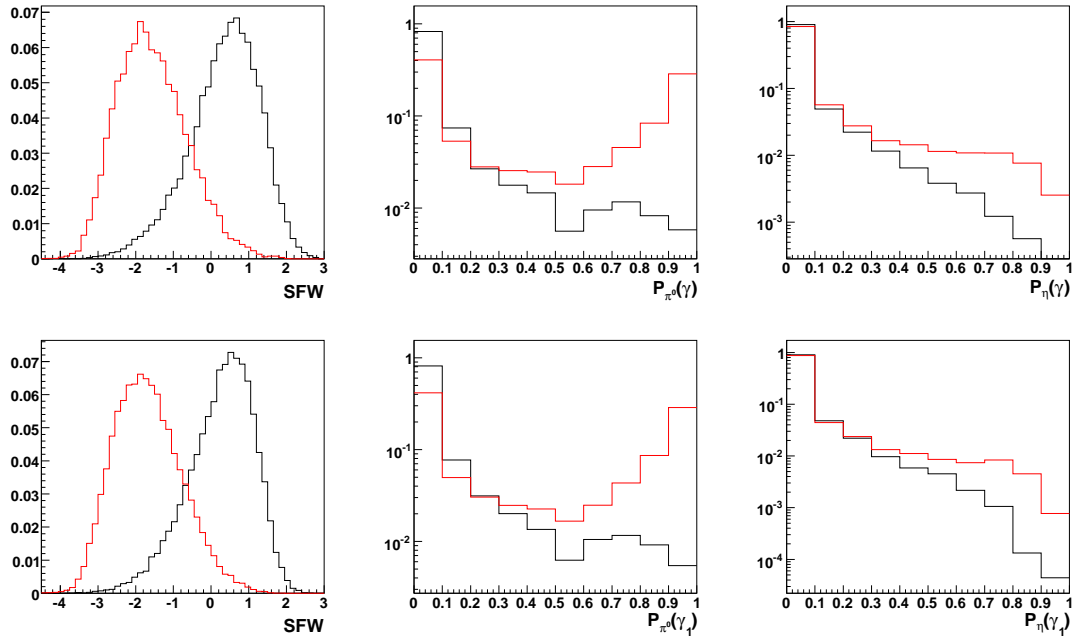


Figure 3.5: SFW, P_{π^0} and P_{η} MC distributions for signal (black) and continuum (red) for the $B_s^0 \rightarrow \phi\gamma$ mode (top) and the $B_s^0 \rightarrow \gamma\gamma$ mode (bottom). For the $B_s^0 \rightarrow \gamma\gamma$ mode, the P_{π^0} and P_{η} distributions are shown for the higher energy photon.

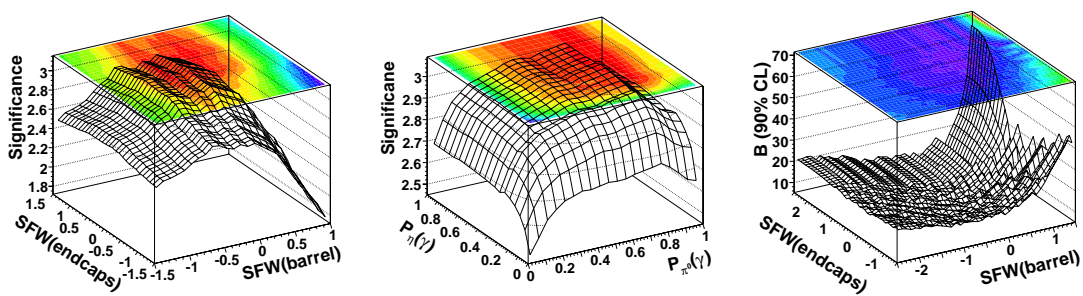


Figure 3.6: Optimization of the rejection of the continuum background. Left: $B_s^0 \rightarrow \phi\gamma$ signal significance as a function of the SFW requirement with the optimized requirements on P_{π^0} and P_{η} applied. Middle: $B_s^0 \rightarrow \phi\gamma$ signal significance as a function of the requirements on P_{π^0} and P_{η} with the optimized requirements on SFW applied. Right: expected upper limit at 90% CL on the $B_s^0 \rightarrow \gamma\gamma$ branching fraction (10^{-6}) as a function of the SFW requirements.

method [124]. Two inputs are required: the number of observed events (N_{obs}) and the number of expected background events (N_{bkg}). We assume $N_{\text{obs}} \equiv N_{\text{signal}} + N_{\text{continuum}}$ and $N_{\text{bkg}} \equiv N_{\text{continuum}}$. Figure 3.6 presents this minimization. Assuming $\mathcal{B}(B_s^0 \rightarrow \gamma\gamma) = 1.0 \times 10^{-6}$, we expect to obtain $\mathcal{B}(B_s^0 \rightarrow \gamma\gamma) < 8.6 \times 10^{-6}$ (90% CL) with

$$\text{SFW}(\text{barrel}) > 0.0, \quad (3.18)$$

$$\text{SFW}(\text{endcaps}) > 1.0, \quad (3.19)$$

where the SFW(barrel) requirement is applied when the two candidate photons lie in the barrel region of the ECL. The SFW(endcaps) requirement is applied otherwise. In fact, since the two photons of a $B_s^0 \rightarrow \gamma\gamma$ candidate are mostly back-to-back due to kinematics, it is very unlikely to have one photon in the barrel and one in an endcap. The SFW(endcaps) requirement was finally abandoned due to systematic uncertainties, as explained in Section 4.2. An optimization without the endcaps was not performed due to time constraints.

3.2.3 Background from B decays

Background from B decays are studied using large MC samples. At the $\Upsilon(4S)$ resonance, we use samples of charmed and charmless B decays about 1.5 and 36 times larger than the studied data sample, respectively. At the $\Upsilon(5S)$ resonance, we use a sample of mainly charmed $b\bar{b}$ decays having about the same size as the studied data sample and a sample of $B^{+/-} \rightarrow X_s\gamma$ decays about 10 times larger.

B background for the $B_s^0 \rightarrow \phi\gamma$ and $B_s^0 \rightarrow \gamma\gamma$ modes

For the $B_s^0 \rightarrow \gamma\gamma$ mode, no candidate is reconstructed in the fit region from both studied samples and we therefore assume that continuum is the only background for this mode. For the $B_s^0 \rightarrow \phi\gamma$ mode, backgrounds coming from the charmed B^+ and B^0 decays and the $B \rightarrow X_s\gamma$ decays are found to lie outside of the fit region. However, we have a potential background contribution from B_s^0 decays in the fit region: the $B_s^0 \rightarrow \phi\eta$ and $B_s^0 \rightarrow \phi\pi^0$ decays to the $K^+K^-\gamma\gamma$ final state are identified as possible sources of background and are studied using large MC samples. With reconstruction efficiencies estimated to be 5.8% and 2.8%, respectively, their branching fractions have to be about 1.6×10^{-5} and 1.3×10^{-5} to produce one background event in the fit region. The branching fraction of $B_s^0 \rightarrow \phi\pi^0$ can be estimated to be much lower than 10^{-5} because the gluons of the gluonic penguin $b \rightarrow s$ transition, shown in Figure 1.6 on page 15, cannot couple to the π^0 due to its isospin. Other diagrams are color-suppressed and Cabibbo-suppressed, hence can be estimated to have a few orders of magnitude lower branching fractions. The $B^0 \rightarrow K^*(892)^0\pi^0$ decay, the B^0 counterpart to $B_s^0 \rightarrow \phi\pi^0$, is constrained for the same reason and its branching fractions is measured to be less than 3.5×10^{-6} at 90% CL [2]. We conclude the $B_s^0 \rightarrow \phi\pi^0$ decay to be a negligible background. On the other hand, for the $B_s^0 \rightarrow \phi\eta$ mode, the gluonic transition is allowed and the branching fraction of its B^0 partner decay has been measured to be $\mathcal{B}(B^0 \rightarrow K^*(892)^0\eta) = (1.63 \pm 0.13) \times 10^{-5}$ [2]. Due to the large uncertainty on the $B_s^0 \rightarrow \phi\eta$ branching fraction, this background is treated as a source of systematic uncertainty assuming the $B^0 \rightarrow K^*(892)^0\eta$ branching fraction. The M_{bc} and ΔE distributions for this background are shown in Figure 4.6 on page 76.

B background for the $B^+ \rightarrow K^+ h \rightarrow K^+ \gamma\gamma$ modes

In the $B^+ \rightarrow K^+ \eta$ channel, 56% of this type of background is from $B \rightarrow K^*(892)\eta$ with the rest being composed of several small contributions, the largest ones being due to $B \rightarrow X_s \gamma$ and $B^+ \rightarrow \pi^+ \eta$. In the $B^+ \rightarrow K^+ \eta'$ channel, the dominant source (about 2/3) is $B \rightarrow X_s \gamma$, about half of which is from $B \rightarrow K^*(K\pi)\gamma$. For the other modes, about 95% of the charmless B decay contributions is due to $B \rightarrow X_s \gamma$. The final state with $K^+ \pi^0 \gamma$ is a significant background for modes with charmonia and with the $X(3872)$ resonance. It is suppressed with the requirement

$$m_{K\gamma_2} > 1.5 \text{ GeV}/c^2, \quad (3.20)$$

where $m_{K\gamma_2}$ is the invariant mass of the system formed by the kaon and the lowest energy photon (in the laboratory frame) forming the $K\gamma\gamma$ candidate. Figure 3.7 shows signal and background distributions for this variable for the $B^+ \rightarrow K^+ \eta_c$ and $B^+ \rightarrow K^+ X(3872)$ modes. For the $B^+ \rightarrow K^+ \eta_c$ channel, the $B \rightarrow K^*(892)\eta_c(\gamma\gamma)$ background is the most relevant contribution. All discussed B backgrounds produce a broad, compared to signal, peak in the M_{bc} signal region. The $B \rightarrow X_s \gamma$ background is flat in ΔE , $B^+ \rightarrow \pi^+ \eta$ peaks at $\Delta E \approx 0.05$ GeV due to the misidentification of the pion as a kaon and $B \rightarrow K^*(892)\eta$ and $B \rightarrow K^*(892)\eta_c$ peak at $\Delta E \approx -0.2$ GeV, where the pion from the $K^*(892)$ decay is missed in the reconstruction. Distributions of these backgrounds can be seen in Figures 5.4 and 5.5 on pages 95 and 96.

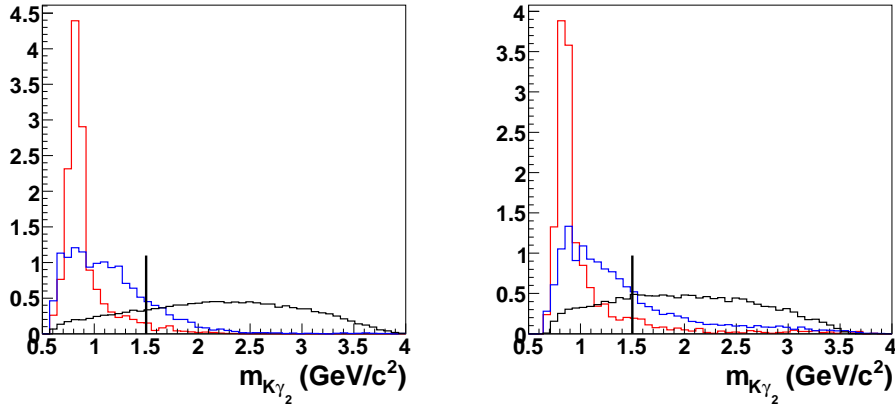


Figure 3.7: $m_{K\gamma_2}$ distributions for signal (black), $B \rightarrow K^*(892)\gamma$ (red) and $B \rightarrow X\gamma$ (blue) for the $B^+ \rightarrow K^+ \eta_c$ (left) and $B^+ \rightarrow K^+ X(3872)$ (right) modes, with arbitrary normalization. The line shows the requirement. The other modes have similar $m_{K\gamma_2}$ distributions.

3.2.4 The off-time QED background

Another source of background is produced by the overlap of a hadronic event with a previous QED interaction (mainly Bhabha scattering) that has left energy deposits in the calorimeter. This off-time background was seen for the first time in the $B^0 \rightarrow \gamma\gamma$ analysis [125] and is discussed in details in [126]. It can be removed with $\sim 100\%$ efficiency

by means of the timing information ($\text{tdc}(\text{TC})$) of the calorimeter clusters corresponding to each photon candidate. The requirement is

$$9000 \text{ ns} < \text{tdc}(\text{TC}) < 11000 \text{ ns}. \quad (3.21)$$

Though being saved in the raw data since the beginning of Belle data taking, this timing information was however only propagated to the reconstructed datasets available to Belle users for analysis after the off-time background was discovered. For the $\Upsilon(5S)$ data, this background can be vetoed in the entire studied dataset and is therefore not an issue. However, for the $B^+ \rightarrow K^+ h \rightarrow K^+ \gamma \gamma$ analysis, the off-time background can only be removed for the last $258 \times 10^6 B\bar{B}$ pairs. For the rest of the data, it is included in the fit described in Chapter 5, by modeling it with the distribution of the off-time background events rejected from the most recent data. In this fit, we will differentiate when one photon or both photons are off-time. These two contributions are slightly different but both are almost flat in ΔE and slightly peak at low M_{bc} , as shown in Figures 5.4 and 5.5 on pages 95 and 96 in Chapter 5. The importance of this background is proportional to the mass of h : the contribution from the off-time background is negligible for the $B^+ \rightarrow K^+ \eta$ and $B^+ \rightarrow K^+ \eta'$ modes but it is particularly important for $B^+ \rightarrow K^+ X(3872)$. For the latter mode, we apply a requirement on the center-of-mass momentum of the $X(3872)$ particle of

$$p_h^{\text{CM}} > 0.5 \text{ GeV}/c. \quad (3.22)$$

A large fraction of the “two-photons” off-time background is removed with this requirement, as shown in Figure 3.8. This is due to the fact that both photons were produced in a $e^+e^- \rightarrow \gamma\gamma$ process, hence the $\gamma\gamma$ system is mostly at rest in the CM frame.

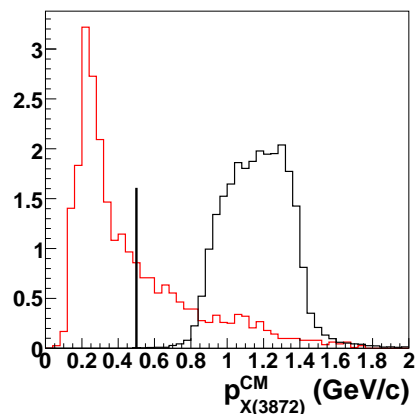


Figure 3.8: Center-of-mass momentum of the $X(3872)$ for signal MC (black) and data when two off-time photons are selected to reconstruct the $X(3872)$ candidate (red).

3.3 Summary of all requirements and expectations

Table 3.5 summarizes all requirements for the $B_s^0 \rightarrow \phi\gamma$ and $B_s^0 \rightarrow \gamma\gamma$ analysis and Table 3.6 for the $B^+ \rightarrow K^+h \rightarrow K^+\gamma\gamma$ analysis.

With these requirements, the B_s^0 signal reconstruction efficiencies evaluated with MC are

$$\epsilon_{B_s^0 \rightarrow \phi\gamma} = 24.7\% , \quad (3.23)$$

$$\epsilon_{B_s^0 \rightarrow \gamma\gamma} = 17.8\% . \quad (3.24)$$

For the $B_s^0 \rightarrow \phi\gamma$ mode, we expect to obtain a first evidence assuming $\mathcal{B}(B_s^0 \rightarrow \phi\gamma) = 40 \times 10^{-6}$: the MC study indicates that we will reconstruct about 12.0 signal events on top of 3.6 continuum events, thus corresponding to a significance of about 3. For the $B_s^0 \rightarrow \gamma\gamma$ mode, we don't expect to see any SM signal and expect to set a limit of $\mathcal{B}(B_s^0 \rightarrow \gamma\gamma) < 8.6 \times 10^{-6}$ (90% CL).

For the $B^+ \rightarrow K^+h \rightarrow K^+\gamma\gamma$ modes, the expectations are listed in Table 3.7. In summary, we expect to observe large signals for the $B^+ \rightarrow K^+\eta$ and $B^+ \rightarrow K^+\eta'$ modes and to obtain an evidence for $B^+ \rightarrow K^+\eta_c$. For the $B^+ \rightarrow K^+\chi_{c0}$ and $B^+ \rightarrow K^+\chi_{c2}$ modes, we don't expect to see any signal due to the very low branching fractions. The J/ψ meson is not allowed to decay into two photons, thus we don't expect to see $B^+ \rightarrow K^+J/\psi \rightarrow K^+\gamma\gamma$. As for the $B^+ \rightarrow K^+\eta_c(2S)$ and $B^+ \rightarrow K^+X(3872)$ modes, their respective branching fractions suffer from large uncertainties. Efficiencies listed in Table 3.7 are computed in the signal regions and are the averages of the efficiencies computed for the two configurations of the inner-detector. These efficiencies are listed in Table 5.1 on page 86.

Table 3.5: Selection requirements for the $B_s^0 \rightarrow \phi\gamma$ and $B_s^0 \rightarrow \gamma\gamma$ analysis. Signal windows are introduced in Section 3.1.5 on page 57.

Selection	Channel	Requirement	Comment
Kaons	$B_s^0 \rightarrow \phi\gamma$	$\mathcal{L}_{K/\pi} > 0.6$	
		$ dr < 0.5 \text{ cm}$	
		$ dz < 3.0 \text{ cm}$	
Photons	$B_s^0 \rightarrow \gamma\gamma$	$33^\circ < \theta < 128^\circ$	ECL barrel region
		$E_9/E_{25} > 0.95$	
	both	$P_{\pi^0}(\gamma) < 0.75$	π^0 rejection
		$P_\eta(\gamma) < 0.65$	η rejection
		$9000 < \text{tdc(TC)} < 11000 \text{ ns}$	off-time photons
ϕ	$B_s^0 \rightarrow \phi\gamma$	$ m_{K^+K^-} - m_\phi < 12 \text{ MeV}/c^2$	$\pm 2.5 \sigma$ window
B_s^0	both	$M_{bc} > 5.3 \text{ GeV}/c^2$	fit region
	$B_s^0 \rightarrow \phi\gamma$	$ \Delta E < 0.4 \text{ GeV}$	
	$B_s^0 \rightarrow \gamma\gamma$	$-0.7 < \Delta E \text{ (GeV)} < 0.4$	
Event	$B_s^0 \rightarrow \phi\gamma$	SFW(barrel) > -0.1	
		SFW(endcaps) > 0.5	
	$B_s^0 \rightarrow \gamma\gamma$	SFW(barrel) > 0.0	
		$E_{\text{tot}} < 12 \text{ GeV}$	
Signal windows	both	$M_{bc} > 5.4 \text{ GeV}/c^2$	
	$B_s^0 \rightarrow \phi\gamma$	$-0.2 < \Delta E \text{ (GeV)} < 0.02$	
		$ \cos \theta_{\text{hel}} < 0.8$	
$B_s^0 \rightarrow \gamma\gamma$	$-0.3 < \Delta E \text{ (GeV)} < 0.05$		

Table 3.6: Selection requirements for the $B^+ \rightarrow K^+ h \rightarrow K^+ \gamma \gamma$ analysis. Requirements applied after the best candidate selection (BCS) discussed in Section 3.1.4 on page 56 are shown with a \star symbol. Signal windows are introduced in Section 3.1.5 on page 57.

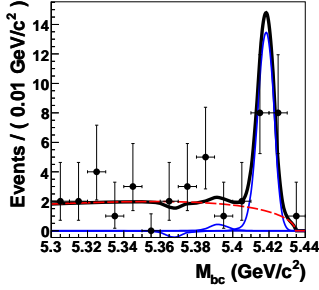
Selection	Particle h	Requirement	Comment	BCS
Kaons	all	$\mathcal{L}_{K/\pi} > 0.6$		
		$ dr < 0.5 \text{ cm}$		
		$ dz < 3.0 \text{ cm}$		
Photons	η, η'	$E_9/E_{25}(\gamma_1, \gamma_2) > 0.95, 0.90$	$E_{\gamma_1} > E_{\gamma_2}$	\star
	all exc. η, η'	$E_9/E_{25} > 0.95$		\star
	all	$ m_{\gamma\gamma} - m_{\pi^0} > 16 \text{ MeV}$	π^0 rejection	
		$ E_{\gamma_1} - E_{\gamma_2} /(E_{\gamma_1} + E_{\gamma_2}) > 0.9$		
		$9000 < \text{tdc(TC)} < 11000 \text{ ns}$	off-time photons	\star
h	all	tight $m_{\gamma\gamma}$ windows of Table 3.1		\star
	$X(3872)$	$p_h^{\text{CM}} > 0.5 \text{ GeV}/c$	off-time photons	\star
B^+	all	$M_{\text{bc}} > 5.2 \text{ GeV}/c^2$	fit region	
		$ \Delta E < 0.3 \text{ GeV}$		
Event	all	$\mathcal{R}(\mathcal{F})$ req.	continuum rejection	\star
	all exc. η, η'	$m_{K\gamma_2} > 1.5 \text{ GeV}/c^2$	$X_s\gamma$ rejection	\star
Signal windows	all	Table 3.2		

Table 3.7: Expectations for the $B^+ \rightarrow K^+ h \rightarrow K^+ \gamma \gamma$ modes assuming the $\mathcal{B}(B^+ \rightarrow K^+ h \rightarrow K^+ \gamma \gamma)$ listed in Table 1.3 on page 22. All values are computed in the signal windows listed in Table 3.2 on page 57. The last column is computed as $N_{\text{signal}}/\sqrt{N_{\text{signal}} + N_{\text{continuum}} + N_{B \text{ bkg}}}$ for the modes with $h = \eta, \eta', \eta_c$ and as $\epsilon/\sqrt{N_{\text{continuum}} + N_{B \text{ bkg}}}$ for the other modes.

Mode	Efficiency	N_{signal}	$N_{\text{continuum}}$	$N_{B \text{ bkg}}$	Figure of merit
$B^+ \rightarrow K^+ \eta$	15.6%	85	77	27	6.2
$B^+ \rightarrow K^+ \eta'$	14.9%	118	40	20	8.8
$B^+ \rightarrow K^+ \eta_c$	10.1%	13.5	4.7	2.5	3.0
$B^+ \rightarrow K^+ \eta_c(2S)$	10.9%	–	8.1	2.4	3.3%
$B^+ \rightarrow K^+ \chi_{c0}$	10.9%	~ 0	7.0	2.8	3.5%
$B^+ \rightarrow K^+ \chi_{c2}$	10.6%	~ 0	2.4	1.4	5.4%
$B^+ \rightarrow K^+ J/\psi$	9.5%	0	4.3	2.0	3.8%
$B^+ \rightarrow K^+ X(3872)$	14.0%	–	20.3	4.9	2.8%

Chapter 4

Fitting procedure and results for the $B_s^0 \rightarrow \phi\gamma$ and $B_s^0 \rightarrow \gamma\gamma$ analysis



This chapter describes, for the analysis of the radiative penguin $B_s^0 \rightarrow \phi\gamma$ and $B_s^0 \rightarrow \gamma\gamma$ decays, the probability density functions and the fitting procedure. Results and the study of systematic uncertainties are also presented.

4.1 Fitting procedure

FOR the $B_s^0 \rightarrow \phi\gamma$ ($B_s^0 \rightarrow \gamma\gamma$) mode, we perform a three-dimensional (two-dimensional) unbinned extended maximum likelihood fit to M_{bc} , ΔE and $\cos\theta_{\text{hel}}$ (M_{bc} and ΔE) of the selected B_s^0 candidates in the data using the probability density functions (PDF) described below. The likelihood is defined as

$$\mathcal{L} = e^{-\sum_j S_j} \times \prod_i \left(\sum_j S_j P_j^i \right), \quad (4.1)$$

where i runs over all selected B_s^0 meson candidates, j runs over the possible event categories (signals and backgrounds), S_j is the number of events in each category and P_j is the corresponding PDF.

4.1.1 Probability density functions for the signal

For both modes, the $B_s^* \bar{B}_s^*$, $B_s^* \bar{B}_s^0$ and $B_s^0 \bar{B}_s^0$ signal PDFs for M_{bc} and ΔE are modeled separately with two-dimensional smoothed histograms obtained from signal MC. The $B_s^* \bar{B}_s^*$ signal PDF is calibrated using control modes reconstructed in the data. We do not calibrate $B_s^* \bar{B}_s^0$ and $B_s^0 \bar{B}_s^0$ signal PDFs since their relative fractions are small ($f_{B_s^* \bar{B}_s^*} = 93\%$). Furthermore, these signals will not be used to measure the branching fraction.

Table 4.1: M_{bc} (MeV/ c^2) and ΔE (MeV) mean values of $B_s^0 \rightarrow D_s^- \pi^+$ in data and MC. The difference ($\delta\mu$) is used to adjust the $B_s^0 \rightarrow \phi\gamma$ and $B_s^0 \rightarrow \gamma\gamma$ signal MC.

Variable	μ_{MC}	μ_{data}	$\delta\mu$ (correction)
M_{bc}	5416.69 ± 0.04	5417.9 ± 0.4	1.2 ± 0.4
ΔE	-49.0 ± 0.1	-53.1 ± 1.6	-4.1 ± 1.6

To account for the uncertainty on the B_s^* meson mass and the uncertainty on the beam energy, we adjust the mean values of the M_{bc} and ΔE $B_s^* \bar{B}_s^*$ signal distributions of both modes using $B_s^0 \rightarrow D_s^- \pi^+$ events reconstructed in the same $\Upsilon(5S)$ data sample. These events are reconstructed as described in detail in [119]. To summarize the $B_s^0 \rightarrow D_s^- \pi^+$ selection, we reconstruct the D_s mesons in the three experimentally clean decay modes $\phi(K^+ K^-)\pi$, $K^*(892)^0(K\pi)K$ and $K_S^0(\pi\pi)K$ with the pions and kaons selected using the same criteria as in this analysis. Mass requirements are applied on the D_s , ϕ , $K^*(892)^0$ and K_S^0 candidates and B_s^0 mesons are selected using the M_{bc} and ΔE variables.

We perform a two-dimensional fit to M_{bc} and ΔE of the selected $B_s^0 \rightarrow D_s^- \pi^+$ candidates in data and in signal MC. The signal PDF is modeled with the product of two Gaussian functions (one for M_{bc} and one for ΔE) and, for the fit to the real data, the continuum with the product of an ARGUS function [127] for M_{bc} and a linear function for ΔE . The results of these fits are shown in Figure 4.1 and the obtained mean values for M_{bc} and ΔE are listed in Table 4.1. The difference between data and MC is used to adjust the mean values of the PDFs derived from the $B_s^0 \rightarrow \phi\gamma$ and $B_s^0 \rightarrow \gamma\gamma$ signal MC. The M_{bc} mean value of the $B_s^0 \rightarrow D_s^- \pi^+$ signal MC agrees with the Evtgen input value for the B_s^* mass and the M_{bc} mean value obtained in the data agrees with that of a previous Belle analysis [58]. The uncertainties on the corrections to the mean values will be propagated as systematic uncertainties.

We also calibrate the M_{bc} and ΔE resolutions of the $B_s^* \bar{B}_s^*$ signal. For the $B_s^0 \rightarrow \phi\gamma$ mode, we use $B^0 \rightarrow K^*(892)^0(K\pi)\gamma$ events reconstructed in a 112 fb^{-1} data sample recorded at the $\Upsilon(4S)$ resonance. The 21.7 fb^{-1} sample at the $\Upsilon(5S)$ resonance was collected during the latter $\Upsilon(4S)$ sample, hence, with similar experimental conditions. We apply the same requirements to reconstruct $B_s^0 \rightarrow \phi\gamma$ and $B^0 \rightarrow K^*(892)^0\gamma$, except that we require $0.845 \text{ GeV}/c^2 < m_{K\pi} < 0.941 \text{ GeV}/c^2$ to reconstruct the $K^*(892)^0$ resonance. We perform one-dimensional fits to M_{bc} with ΔE in signal region ($-0.15 \text{ GeV} < \Delta E < 0.100 \text{ GeV}$) and to ΔE with $M_{bc} > 5.27 \text{ GeV}/c^2$. The signal for both M_{bc} and ΔE is modeled with a Crystal Ball function [128]. The continuum is modeled with an ARGUS function for M_{bc} and with a linear function for ΔE . Fits results are shown in Figure 4.2 and the obtained resolutions are listed in Table 4.2. The M_{bc} resolution in data is compatible with the MC resolution. For ΔE , a small discrepancy at the $\sim 1\sigma$ level is seen. We decide not to correct the M_{bc} and ΔE resolutions of the signal $B_s^0 \rightarrow \phi\gamma$ MC sample but will include the result of this test as systematic uncertainty.

For the signal resolutions of the $B_s^0 \rightarrow \gamma\gamma$ mode, we use the same corrections computed for the $B^0 \rightarrow \gamma\gamma$ analysis [126]. These corrections were obtained with the study of $e^+e^- \rightarrow \gamma\gamma$ events where the photon momenta were smeared to reproduce in MC

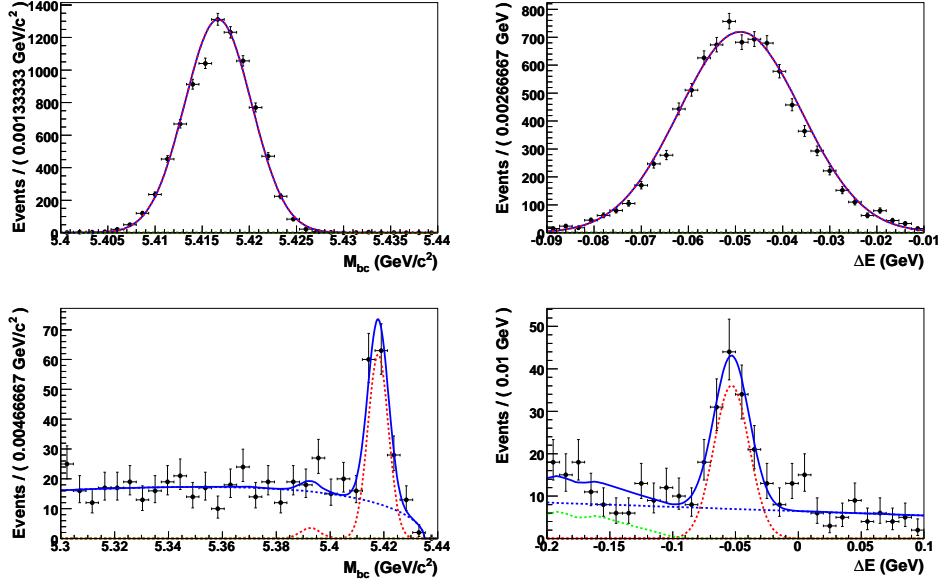


Figure 4.1: Top: Gaussian fits of the M_{bc} (left) and ΔE (right) distributions of $B_s^0 \rightarrow D_s^- \pi^+$ MC signal from $B_s^* \bar{B}_s^*$ events. Bottom: M_{bc} (left) and ΔE (right) projections in the $B_s^* \bar{B}_s^*$ region of the fit to the $B_s^0 \rightarrow D_s^- \pi^+$ signal seen in the data. The points with error bars represent data, the solid curves are the fit functions and the dotted curves represent the various signal and background components: $B_s^0 \rightarrow D_s^- \pi^+$ signal from $B_s^* \bar{B}_s^*$ at $M_{bc} \approx 5.42 \text{ GeV}/c^2$ and $\Delta E \approx -0.05 \text{ GeV}$, $B_s^0 \rightarrow D_s^- \pi^+$ signal from $B_s^* \bar{B}_s^0$ at $M_{bc} \approx 5.39 \text{ GeV}/c^2$, $B_s^0 \rightarrow D_s^{*-} \pi^+$ background at $\Delta E \approx -0.15 \text{ GeV}$, and continuum background in the whole M_{bc} and ΔE ranges.

Table 4.2: M_{bc} (MeV/ c^2) and ΔE (MeV) resolutions of $B^0 \rightarrow K^*(892)^0 \gamma$ in data and in signal MC.

Variable	σ_{MC}	σ_{data}
M_{bc}	3.02 ± 0.04	3.1 ± 0.2
ΔE	37.2 ± 0.4	41 ± 3

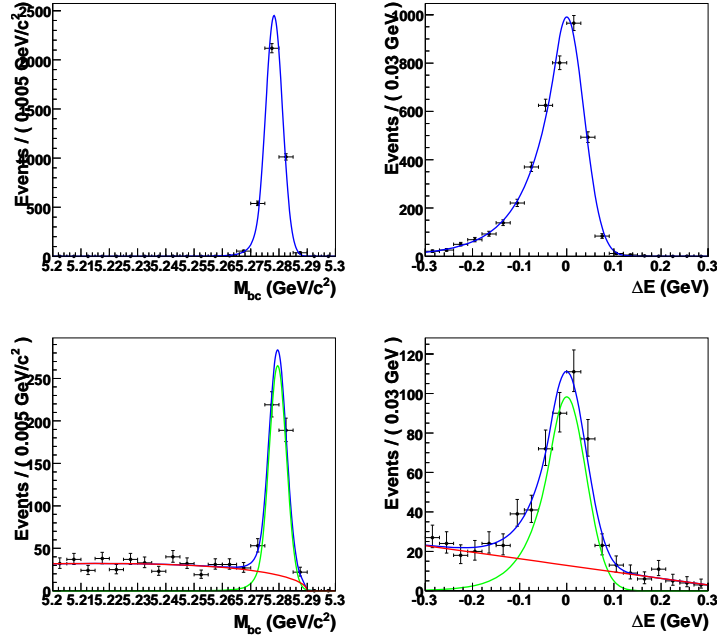


Figure 4.2: M_{bc} and ΔE distributions for $B^0 \rightarrow K^*(892)^0\gamma$. Top: MC signal fitted with Crystal Ball functions. Bottom: data and projections of the full fit in the signal window defined as $M_{bc} > 5.27 \text{ GeV}/c^2$ and $-0.15 \text{ GeV} < \Delta E < 0.100 \text{ GeV}$.

the measured 1.7% energy resolution of the ECL. This smearing has a negligible effect on M_{bc} but increases the ΔE resolution from 56 MeV to 70 MeV. We therefore apply a $\sqrt{70^2 - 56^2} \approx 42 \text{ MeV}$ smearing to the ΔE resolution of the $B_s^0 \rightarrow \gamma\gamma$ signal MC and we conservatively assume a 50% uncertainty on this correction.

Figures 4.3 and 4.4 show for both modes the corrected signal MC with the smoothed histograms used as PDFs in the final fit.

For the $B_s^0 \rightarrow \phi\gamma$ mode, we perform a fit to the $\cos\theta_{\text{hel}}$ distribution of signal MC after all selection requirements with a $1 + c_1 \cos\theta_{\text{hel}} + c_2 \cos^2\theta_{\text{hel}} + c_3 \cos^3\theta_{\text{hel}}$ function, shown in Figure 4.5. We obtain, in complete agreement with the expected $\sin^2\theta_{\text{hel}} \equiv 1 - \cos^2\theta_{\text{hel}}$ function,

$$c_1 = -0.004 \pm 0.022, \quad c_2 = -0.996 \pm 0.006, \quad c_3 = 0.007 \pm 0.026.$$

We therefore use the $1 - \cos^2\theta_{\text{hel}}$ function PDF to describe $\cos\theta_{\text{hel}}$ of signal in the fit.

The total PDF for the three variables is the product of the two-dimensional PDF for M_{bc} and ΔE and the $1 - \cos^2\theta_{\text{hel}}$ function for $\cos\theta_{\text{hel}}$.

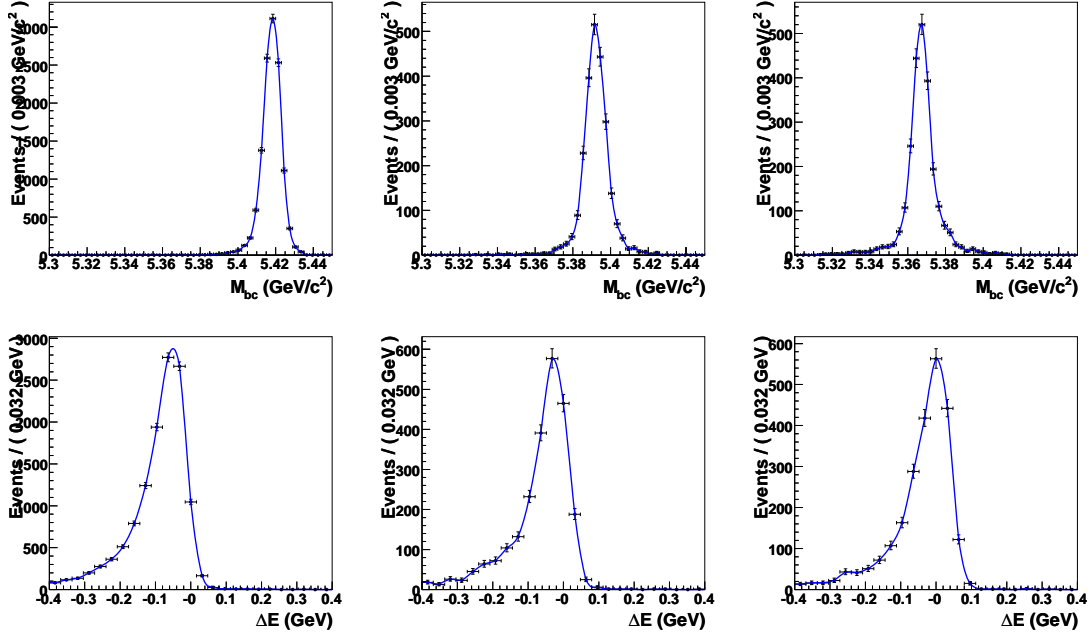


Figure 4.3: $B_s^0 \rightarrow \phi\gamma$ signal PDFs for M_{bc} (top) and ΔE (bottom) from $B_s^* \bar{B}_s^*$ events (left), $B_s^* \bar{B}_s^0$ events (middle) and $B_s^0 \bar{B}_s^0$ events (right).

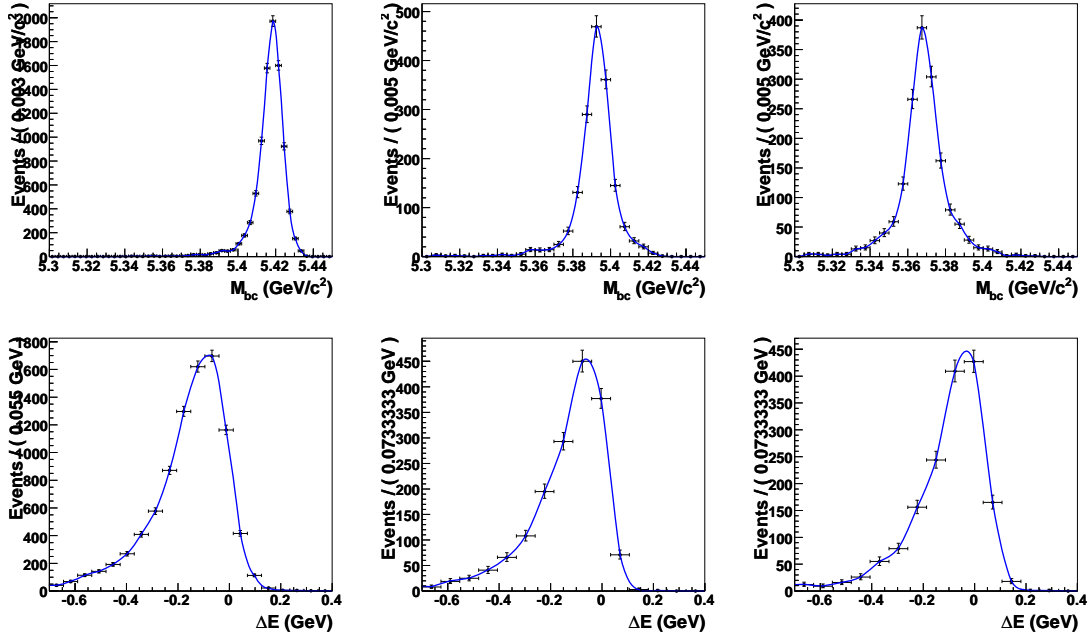


Figure 4.4: $B_s^0 \rightarrow \gamma\gamma$ signal PDFs for M_{bc} (top) and ΔE (bottom) from $B_s^* \bar{B}_s^*$ events (left), $B_s^* \bar{B}_s^0$ events (middle) and $B_s^0 \bar{B}_s^0$ events (right).

4.1.2 Probability density functions for the background

The continuum contribution is modeled with the product of an ARGUS function for M_{bc} and a linear function for ΔE .

For the $B_s^0 \rightarrow \phi\gamma$ mode, we perform a fit to the $\cos\theta_{\text{hel}}$ distribution of sideband data ($M_{bc} < 5.3 \text{ GeV}/c^2$) with a linear function ($1 + c_1 \cos\theta_{\text{hel}}$). We obtain $c_1 = 0.004 \pm 0.011$ in complete agreement with the expected flat distribution. The fit result is shown in Figure 4.5. In the final fit, we therefore use a flat function to describe $\cos\theta_{\text{hel}}$ for the continuum.

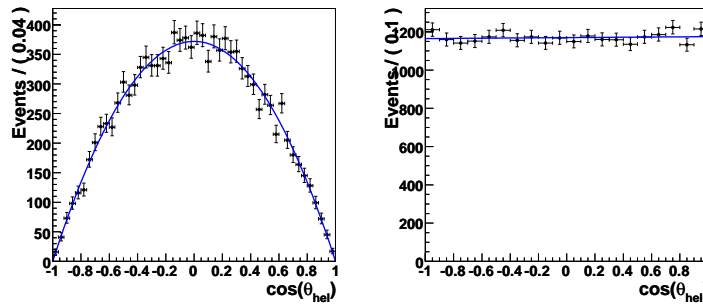


Figure 4.5: Left: $\cos\theta_{\text{hel}}$ distribution of signal MC fitted with a $1 + c_1 \cos\theta_{\text{hel}} + c_2 \cos^2\theta_{\text{hel}} + c_3 \cos^3\theta_{\text{hel}}$ function. Right: $\cos\theta_{\text{hel}}$ distribution of sideband data ($M_{bc} < 5.3 \text{ GeV}/c^2$) fitted with a linear function.

The $B_s^0 \rightarrow \phi\eta$ background PDFs in the $B_s^0 \rightarrow \phi\gamma$ fit is modeled with a two-dimensional smoothed histogram for M_{bc} and ΔE and a one-dimensional histogram for $\cos\theta_{\text{hel}}$. The $B_s^0 \rightarrow \phi\eta$ PDF is shown in Figure 4.6.

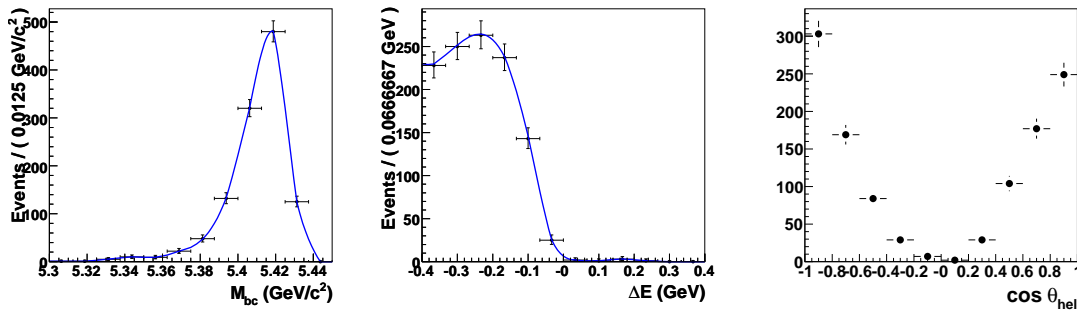


Figure 4.6: $B_s^0 \rightarrow \phi\eta$ PDF for M_{bc} , ΔE and $\cos\theta_{\text{hel}}$ used in the fit to the data.

4.1.3 Fit parameters

Both fits have six free variables: the yields for the $B_s^* \bar{B}_s^*$, $B_s^* \bar{B}_s^0$ and $B_s^0 \bar{B}_s^0$ signals ($S_{B_s^* \bar{B}_s^*}$, $S_{B_s^* \bar{B}_s^0}$ and $S_{B_s^0 \bar{B}_s^0}$), the continuum background normalization and PDF parameters (M_{bc} and ΔE slopes), except the ARGUS endpoint which is fixed to 5.435 GeV. The branching fractions $\mathcal{B}(B_s^0 \rightarrow \phi\gamma)$ and $\mathcal{B}(B_s^0 \rightarrow \gamma\gamma)$ are determined from the $B_s^* \bar{B}_s^*$ signal yields with

the relations

$$S_{B_s^* \bar{B}_s^*}^{B_s^0 \rightarrow \gamma\gamma} = \mathcal{B}(B_s^0 \rightarrow \gamma\gamma) \times \epsilon_{\gamma\gamma} \times N_{B_s^0} \times f_{B_s^* \bar{B}_s^*}, \quad (4.2)$$

$$S_{B_s^* \bar{B}_s^*}^{B_s^0 \rightarrow \phi\gamma} = \mathcal{B}(B_s^0 \rightarrow \phi\gamma) \times \mathcal{B}(\phi \rightarrow K^+ K^-) \times \epsilon_{\phi\gamma} \times N_{B_s^0} \times f_{B_s^* \bar{B}_s^*}, \quad (4.3)$$

where ϵ are the MC signal efficiencies listed in Table 4.6, $N_{B_s^0}$ is the number of B_s^0 mesons evaluated as $N_{B_s^0} = 2 \times L_{\text{int}} \times \sigma_{b\bar{b}}^{\Upsilon(5S)} \times f_s = (2.8_{-0.4}^{+0.5}) \times 10^6$ and $f_{B_s^* \bar{B}_s^*}$ is the fraction of $B_s^* \bar{B}_s^*$ events among $B_s^{(*)} \bar{B}_s^{(*)}$. The computation of the number of B_s^0 mesons is detailed in Section 2.7.

4.2 Systematic uncertainties

4.2.1 Uncertainty on the signal reconstruction efficiency

Uncertainty on the photon reconstruction efficiency

The uncertainty on the photon reconstruction efficiency has been studied with radiative Bhabha events [129] and has been evaluated to be 2.2% per photon.

Uncertainty on the tracking efficiency

The uncertainty on the tracking efficiency has been evaluated by comparing the yield ratio $r = N(\eta \rightarrow \pi^+ \pi^- \pi^0(\gamma\gamma))/N(\eta \rightarrow \gamma\gamma)$ between data and MC [130, 131]. Assuming that the tracking efficiency for the two pions are equal and assuming that the uncertainty on the photon reconstruction efficiency cancel in the ratio, they have obtained the tracking efficiency ratio between data and MC with

$$\epsilon_{\text{data}}/\epsilon_{\text{MC}} = \sqrt{r_{\text{data}}/r_{\text{MC}}} = 0.993 \pm 0.018. \quad (4.4)$$

The uncertainty on the tracking efficiency is assumed to be 1% per track.

Uncertainty on the kaon identification efficiency

This uncertainty has been studied with inclusive $D^{*+} \rightarrow D^0(K^- \pi^+) \pi^+$ decays [132]. Due to the momentum and polar angle dependence of the identification efficiency, the systematic uncertainty is computed as a weighted average for the kaons of the $B_s^0 \rightarrow \phi\gamma$ signal MC. We obtain an uncertainty of 1.1% per kaon.

Systematic uncertainty on the SFW requirement efficiency

This systematic uncertainty is studied with the same $B_s^0 \rightarrow D_s^- \pi^+$ sample used to calibrate the signal mean values of M_{bc} and ΔE . We study the efficiency discrepancy between MC and data when the SFW requirements are applied. A double ratio R is calculated as

$$R = \left(\frac{N_{\text{data}}(\text{with SFW req.})}{N_{\text{data}}(\text{without SFW req.})} \right) / \left(\frac{\epsilon_{\text{MC}}(\text{with SFW req.})}{\epsilon_{\text{MC}}(\text{without SFW req.})} \right), \quad (4.5)$$

Table 4.3: SFW systematic uncertainties. $B_s^0 \rightarrow D_s^- \pi^+$ MC reconstruction efficiency (including D_s branching fractions), signal yield measured in data for $B_s^0 \rightarrow D_s^- \pi^+$ events from $B_s^* \bar{B}_s^*$ events and computed double ratio R .

	Requirement	Efficiency (MC)	Yield (data)	Double ratio R
	No requirement	1.76%	126 ± 13	
$B_s^0 \rightarrow \phi\gamma$	Barrel: SFW > -0.1	1.23%	88 ± 10	1.01 ± 0.10
	Endcaps: SFW > 0.5	0.73%	53 ± 8	1.03 ± 0.09
$B_s^0 \rightarrow \gamma\gamma$	Barrel: SFW > 0.0	1.11%	79 ± 9	1.00 ± 0.10
	Endcaps: SFW > 1.0	0.26%	27 ± 5	1.47 ± 0.32

Table 4.4: Systematic uncertainty on the signal reconstruction efficiency for the $B_s^0 \rightarrow \phi\gamma$ and $B_s^0 \rightarrow \gamma\gamma$ channels.

Source	$B_s^0 \rightarrow \phi\gamma$	$B_s^0 \rightarrow \gamma\gamma$
Photon reconstruction	2.2%	$2 \times 2.2\%$
Kaon identification	$2 \times 1.1\%$	–
Tracking	$2 \times 1.0\%$	–
SFW cut	10%	10%
MC statistics	0.8%	1.1%
Total (quadratic sum)	10.7%	11.0%

where ϵ_{MC} is the $B_s^0 \rightarrow D_s^- \pi^+$ signal MC reconstruction efficiency and N is the $B_s^0 \rightarrow D_s^- \pi^+$ signal yield in the $B_s^* \bar{B}_s^*$ region obtained with the same fit prepared for the calibration of the mean values. Table 4.3 presents the result of this study. For the $B_s^0 \rightarrow \phi\gamma$ mode, we assign a systematic uncertainty of 10%. For the $B_s^0 \rightarrow \gamma\gamma$ mode, due to the large systematic uncertainty of the SFW requirement for the calorimeter endcaps, we select photons only in the barrel part; we also have 10% uncertainty.

Total uncertainty

The total systematic uncertainty on the signal reconstruction efficiency is computed as the quadratic sum of the previously mentioned systematic uncertainties. For the $B_s^0 \rightarrow \phi\gamma$ mode, we have a total uncertainty of 10.7% and, for the $B_s^0 \rightarrow \gamma\gamma$ mode, 11.0%. These systematic uncertainties are summarized in Table 4.4.

4.2.2 Uncertainty on the number of B_s^0 mesons

The relative uncertainties on the determination of the number of B_s^0 mesons are listed in Table 4.5. The fraction f_s introduces the largest uncertainty on the branching fraction measurement. The $f_{B_s^* \bar{B}_s^*}$ variable is also responsible for a large uncertainty of $^{+7.5}_{-9.7}\%$.

Table 4.5: Uncertainty on the determination of the number of B_s^0 mesons.

Source	Uncertainty
L_{int}	1.4%
$\sigma_{b\bar{b}}^{\Upsilon(5S)}$	5.0%
f_s	$^{+15}_{-12}\%$
$N_{B_s^0}$ (quadratic sum)	$^{+16}_{-13}\%$

4.3 Fit results

The two-dimensional distributions in the ΔE - M_{bc} plane of the $B_s^0 \rightarrow \phi\gamma$ and $B_s^0 \rightarrow \gamma\gamma$ candidates selected in the data sample are shown in Figure 4.7. These candidates are fitted as described in Section 4.1. The numerical values and errors of all fit parameters for each mode are given in Appendix B on page 109, while the final results are summarized in Table 4.6.

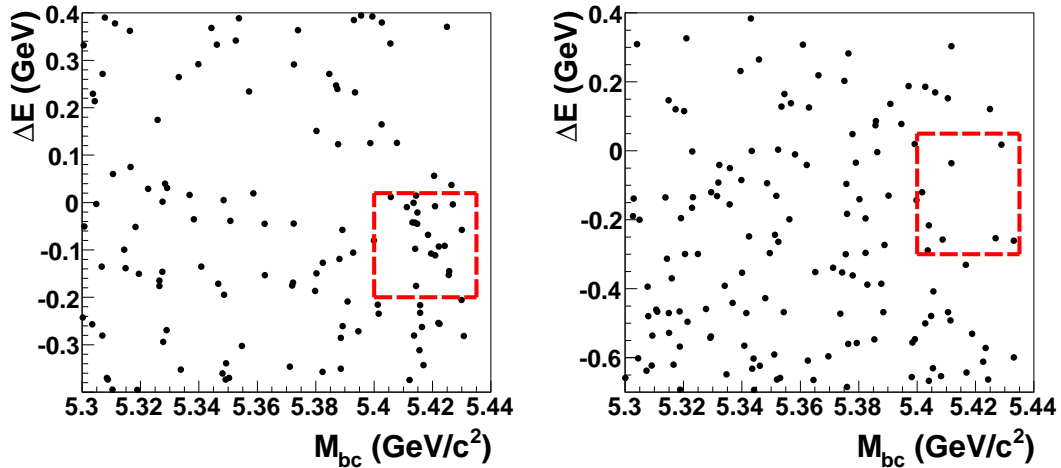


Figure 4.7: Distribution of ΔE versus M_{bc} for selected data events for the $B_s^0 \rightarrow \phi\gamma$ mode (left) and $B_s^0 \rightarrow \gamma\gamma$ mode (right). The dashed lines show the signal window.

Table 4.6: Efficiencies, signal yields, branching fractions and significances obtained from the fits described in the text. The first uncertainty is statistical and the second systematic. The upper limit is calculated at the 90% CL.

Mode	ϵ (%)	$S_{B_s^0 \bar{B}_s^0}$	$S_{B_s^* \bar{B}_s^0}$	$S_{B_s^* \bar{B}_s^*}$	\mathcal{B} (10^{-6})	Significance
$B_s^0 \rightarrow \phi\gamma$	24.7	$-0.7^{+2.5}_{-1.6}$	$0.5^{+2.9}_{-1.9}$	18_{-5}^{+6}	57_{-15}^{+18+12}	5.5
$B_s^0 \rightarrow \gamma\gamma$	17.8	$-4.7^{+3.9}_{-2.8}$	$-0.8^{+4.8}_{-3.8}$	$-7.3^{+2.4}_{-2.0}$	< 8.7	–

4.3.1 $B_s^0 \rightarrow \phi\gamma$

Figure 4.8 shows the data with the fit results. We observe 18_{-5}^{+6} $B_s^0 \rightarrow \phi\gamma$ signal events in the $B_s^* \bar{B}_s^*$ region and no significant signals in the two other regions. These signal yields are compatible with $f_{B_s^* \bar{B}_s^*} = 93_{-9}^{+7}\%$. We measure

$$\mathcal{B}(B_s^0 \rightarrow \phi\gamma) \times f_s \times f_{B_s^* \bar{B}_s^*} = (10.3_{-2.8}^{+3.2} \pm 1.3) \times 10^{-6}, \quad (4.6)$$

$$\mathcal{B}(B_s^0 \rightarrow \phi\gamma) = (57_{-15}^{+18+12}) \times 10^{-6}, \quad (4.7)$$

with a significance of 5.5 standard deviations, where the first uncertainty is statistical and the second is systematic. The computation of the significance and of the systematic uncertainty is detailed below.

The measured branching fraction is in agreement with the Standard Model expectations 39×10^{-6} [44] and 43×10^{-6} [45] and with the measurements of the B^+ and B^0 counterpart decays: $\mathcal{B}(B^0 \rightarrow K^*(892)^0 \gamma) = (40.1 \pm 2.0) \times 10^{-6}$ and $\mathcal{B}(B^+ \rightarrow K^*(892)^+ \gamma) = (40.3 \pm 2.6) \times 10^{-6}$ [2].

We compute the systematic uncertainty on the branching fraction by repeating the fit with each constant parameter successively varied by plus or minus one standard deviation around its central value. The positive (negative) systematic uncertainty is the quadratic sum of the positive (negative) branching fraction deviations with respect to the branching fraction obtained with the nominal fit. The uncertainty due the $B_s^0 \rightarrow \phi\gamma$ signal PDF modeling is introduced in this computation by building signal PDF with corrections modified by $\pm 1\sigma$. The uncertainty on the branching fraction due to signal modeling and the $B_s^0 \rightarrow \phi\eta$ background are evaluated to be $_{-4.2}^{+3.2}\%$ and $_{-1.2}^{+0.0}$, respectively.

The significance (\mathcal{S}) of the signal is computed as

$$\mathcal{S} = \sqrt{2(\ln \mathcal{L}_{\max} - \ln \mathcal{L}_0)}, \quad (4.8)$$

where \mathcal{L}_{\max} is the likelihood value returned by the nominal fit and \mathcal{L}_0 the likelihood value of a fit where the signal yield $S_{B_s^* \bar{B}_s^*}^{B_s^0 \rightarrow \phi\gamma}$ is set to zero. The significance without systematic uncertainties is 5.6 standard deviations. Systematic uncertainties are included by choosing the lowest significance value returned by the fits used to evaluate the systematic uncertainty. The parameter related to the $B_s^0 \rightarrow \phi\eta$ background is the only parameter having a non-negligible effect on the significance. The significance is reduced to 5.5.

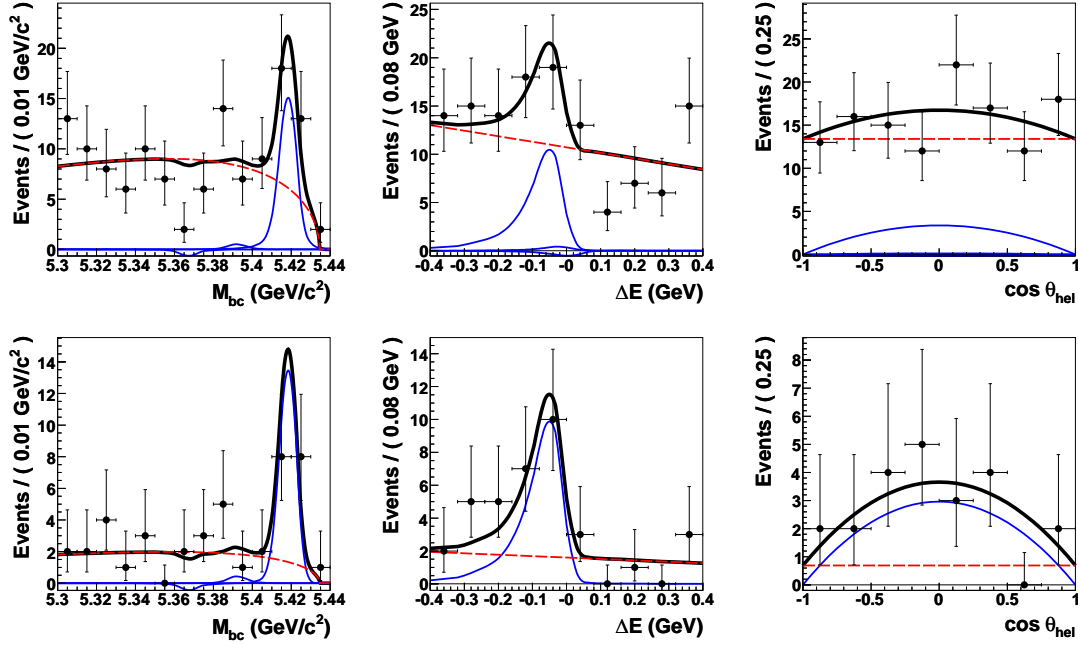


Figure 4.8: Top: M_{bc} , ΔE and $\cos\theta_{\text{hel}}$ data distributions together with fit results for the $B_s^0 \rightarrow \phi\gamma$ mode in the m_{K+K^-} signal region. Bottom: projections of the fit in the signal window. The points with error bars represent data, the thick solid curves are the fit functions, the thin solid curves are the signal functions and the dashed lines show the continuum contribution. On the M_{bc} plots, signals from $B_s^0\bar{B}_s^0$, $B_s^*\bar{B}_s^0$ and $B_s^*\bar{B}_s^*$ appear from left to right.

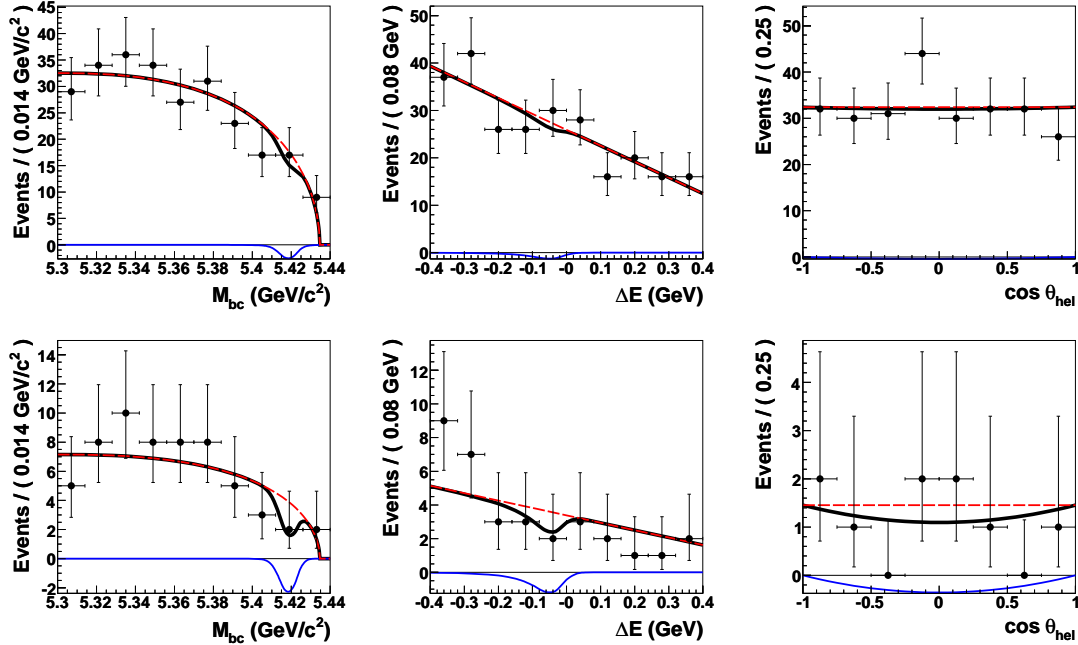


Figure 4.9: M_{bc} , ΔE and $\cos\theta_{\text{hel}}$ data distributions together with fit results for the $B_s^0 \rightarrow \phi\gamma$ mode in the m_{K+K^-} sideband. See above for a description of the plots and curves.

4.3.2 $B_s^0 \rightarrow \phi\gamma$ in the m_{K+K^-} sideband

As a check, we perform a fit to M_{bc} , ΔE and $\cos \theta_{\text{hel}}$ of the data in the region $1.1 \text{ GeV}/c^2 < m_{K+K^-} < 1.2 \text{ GeV}/c^2$, where no $B_s^0 \rightarrow \phi\gamma$ signal can contribute. This fit is simplified: we consider only continuum and signal from $B_s^* \bar{B}_s^*$ events using the same $B_s^0 \rightarrow \phi\gamma$ shape as for the fit in the m_{K+K^-} signal region. Figure 4.9 shows no evidence of signal and we obtain a signal yield of $-2.2_{-1.9}^{+2.9}$ compatible with zero.

4.3.3 $B_s^0 \rightarrow \gamma\gamma$

Figure 4.10 shows the data with the fit results. We do not observe any significant signal and we extract an upper limit at 90% CL including systematic uncertainties of

$$\mathcal{B}(B_s^0 \rightarrow \gamma\gamma) < 8.7 \times 10^{-6}. \quad (4.9)$$

The latter limit is about six times more restrictive than the previously published one, $\mathcal{B}(B_s^0 \rightarrow \gamma\gamma) < 53 \times 10^{-6}$ [58, 95]. The obtained limit is still about one order of magnitude larger than the SM expectations in the range $(0.5 - 1.0) \times 10^{-6}$ [55, 56, 57] and still above existing New Physics models predictions (up to $\sim 5 \times 10^{-6}$ [60, 61, 62]).

Computation of the upper limit

We obtain the upper limit at 90% confidence level on the branching fraction ($\mathcal{B}_{\text{limit}}$) using a Bayesian approach with a flat prior by integrating to 90% the likelihood of the fit according to

$$\int_0^{\mathcal{B}_{\text{limit}}} \mathcal{L}(\mathcal{B}) d\mathcal{B} = 0.9 \times \int_0^1 \mathcal{L}(\mathcal{B}) d\mathcal{B}. \quad (4.10)$$

We first include the signal shape uncertainty into a modified likelihood (\mathcal{L}_{mod}). This likelihood is the average of the likelihoods obtained by repeating 1000 times the fit with randomly chosen signal shapes according to the statistical error on the M_{bc} and ΔE mean values and resolutions corrections. Then, we obtain the upper limit at 90% confidence level by integrating to 90% the convolution of the modified likelihood with the normalized sensitivity (S/S_0) where

$$S = N_{B_s^0} \times f_{B_s^* \bar{B}_s^*} \times \epsilon \quad (4.11)$$

and S_0 is the nominal sensitivity.

We perform a MC integration: the 90% CL limit is the 90% percentile of the $\mathcal{B}(B_s^0 \rightarrow \gamma\gamma) \times S/S_0$ distribution formed by randomly choosing $\mathcal{B}(B_s^0 \rightarrow \gamma\gamma)$ and S according to their respective distributions. We model $\mathcal{L}_{\text{mod}}(\mathcal{B}(B_s^0 \rightarrow \gamma\gamma))$ with a spline and S with the product of Gaussian functions and bifurcated Gaussian functions for parameters having asymmetric uncertainties (for example, f_s). The different distributions used to obtain the limit are shown in Figure 4.11. We finally obtain $\mathcal{B}(B_s^0 \rightarrow \gamma\gamma) < 8.7 \times 10^{-6}$ (90% CL).

The latter limit can be checked by computing two other limits: the statistical limit (integration to 90% of the unmodified likelihood) is $\mathcal{B}(B_s^0 \rightarrow \gamma\gamma) < 8.1 \times 10^{-6}$ and a semi-systematic limit (integration to 90% of the convolution of the unmodified likelihood with the normalized sensitivity) is $\mathcal{B}(B_s^0 \rightarrow \gamma\gamma) < 8.5 \times 10^{-6}$. This is of course not a thorough check but this at least gives confidence in the numerical integration.

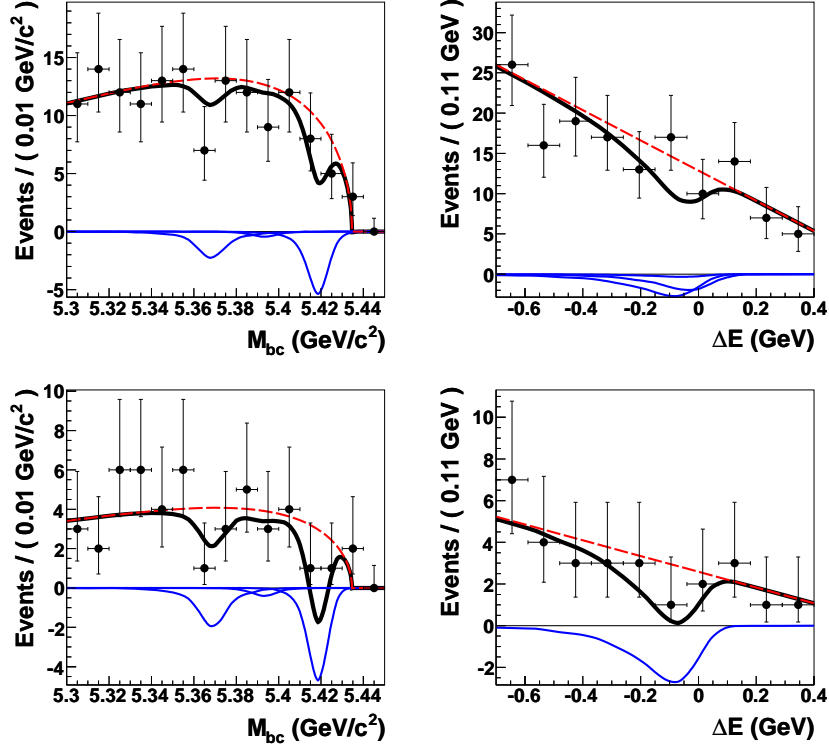


Figure 4.10: Top: M_{bc} and ΔE data distributions together with fit results for the $B_s^0 \rightarrow \gamma\gamma$ mode. Bottom: projections of the fit in the signal window. The points with error bars represent data, the thick solid curves are the fit functions, the thin solid curves are the signal functions and the dashed lines show the continuum contribution. On the M_{bc} plots, signals from $B_s^0 \bar{B}_s^0$, $B_s^* \bar{B}_s^0$ and $B_s^* \bar{B}_s^*$ appear from left to right.

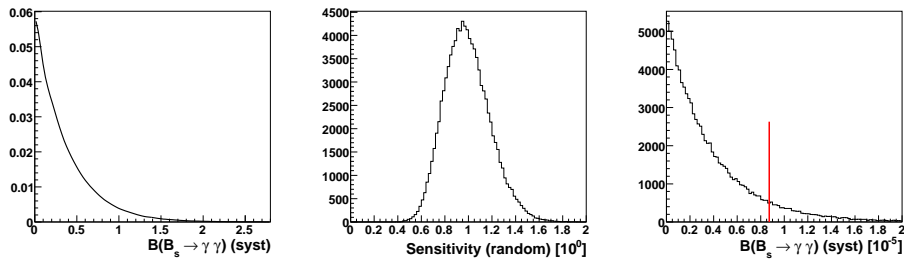
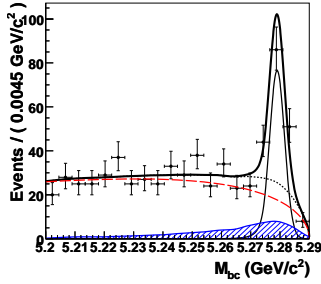


Figure 4.11: Left: modified likelihood of the $B_s^0 \rightarrow \gamma\gamma$ fit modeled with a spline. Middle: histogram of the randomly chosen normalized sensitivity values. Right: final histogram where all known systematic uncertainties have been absorbed. The line shows the 90% CL limit.

Chapter 5

Fitting procedure and results for the $B^+ \rightarrow K^+ h \rightarrow K^+ \gamma\gamma$ analysis



This chapter describes, for the analysis of the resonant $B^+ \rightarrow K^+ h \rightarrow K^+ \gamma\gamma$ decays, the data samples, the probability density functions and the fitting procedure. Results and the study of systematic uncertainties are also presented.

5.1 Fitting procedure

WE perform a two-dimensional unbinned extended maximum likelihood fit to M_{bc} and ΔE using the probability density functions (PDF) described in the following section. The likelihood is defined as

$$\mathcal{L} = e^{-\sum_j S_j} \times \prod_i \left(\sum_j S_j P_j^i \right), \quad (5.1)$$

where i runs over all selected B^+ meson candidates, j runs over the possible event categories (signal and backgrounds), S_j is the number of events in each category and P_j is the corresponding PDF.

5.1.1 Signal probability density functions and efficiencies

We obtain the signal PDFs using a two-dimensional unbinned maximum likelihood fit to signal Monte Carlo events. M_{bc} is modeled with a Crystal Ball [128] function and ΔE with the sum of three Gaussian functions. Figure 5.1 shows the fit to the signal MC for the $B^+ \rightarrow K^+ \eta$ mode. Plots for the other modes are shown in Appendix C on page 111.

Signal efficiencies are counted from the number of signal MC events that survive all requirements. Separate set of efficiencies are obtained for each of the two configurations of the inner detector. We check the signal shape modeling by performing a fit where

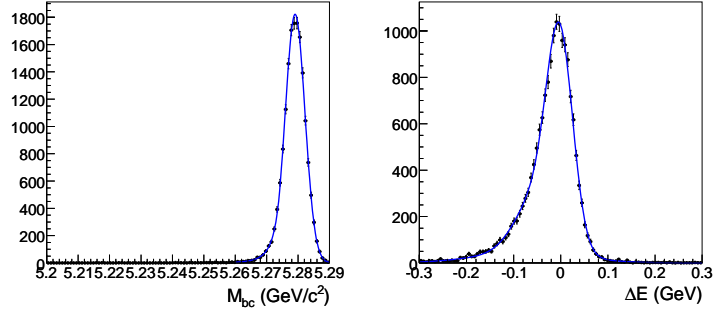


Figure 5.1: M_{bc} and ΔE distributions for the $B^+ \rightarrow K^+ \eta$ signal MC together with the fit functions used as PDFs.

Table 5.1: Signal efficiencies for the two configurations of the inner detector and efficiency corrections.

Channel	$\epsilon(\text{SVD1})$ (%)	$\epsilon(\text{SVD2})$ (%)	ϵ_{corr} (%)
$B^+ \rightarrow K^+ \eta$	16.0 ± 0.1	16.9 ± 0.1	98.5 ± 0.2
$B^+ \rightarrow K^+ \eta'$	14.9 ± 0.1	16.0 ± 0.1	98.3 ± 0.2
$B^+ \rightarrow K^+ \eta_c$	10.0 ± 0.1	10.9 ± 0.1	99.4 ± 0.2
$B^+ \rightarrow K^+ \eta_c(2S)$	11.0 ± 0.1	11.6 ± 0.1	98.7 ± 0.1
$B^+ \rightarrow K^+ \chi_{c0}$	11.1 ± 0.1	11.7 ± 0.1	98.9 ± 0.2
$B^+ \rightarrow K^+ \chi_{c2}$	10.6 ± 0.1	11.4 ± 0.1	98.7 ± 0.1
$B^+ \rightarrow K^+ J/\psi$	9.4 ± 0.1	10.0 ± 0.1	99.1 ± 0.2
$B^+ \rightarrow K^+ X(3872)$	14.1 ± 0.1	15.5 ± 0.1	96.9 ± 0.1

signal MC events are merged in toy continuum events generated assuming an ARGUS function [127] for M_{bc} and a first order polynomial function for ΔE . We compute an efficiency correction factor defined as $\epsilon_{\text{corr}} = n_{\text{fit}}/n_{\text{input}}$ where n_{fit} is the signal yield returned by the fit and n_{input} is the number of embedded signal MC events. This correction mainly accounts for the fact that we use a factorized signal shape to model signals: in fact, M_{bc} and ΔE are slightly correlated due to the two photons in the final state. Signal efficiencies and corrections are listed in Table 5.1.

We correct the M_{bc} and ΔE signal resolutions using a sample of $B^+ \rightarrow K^+ \pi^0$ events reconstructed in the same data sample. The $B^+ \rightarrow K^+ \pi^0$ mode decays to the same final state as the studied modes and its branching fraction is about ten times larger than the $B^+ \rightarrow K^+ \eta'$ one. We reconstruct approximately 1200 signal events. Figure 5.2 shows the results of the fit to the data. The resolution discrepancy between data and MC is mainly due to the imperfect description of the ECL energy resolution, hence we require the energies of the most energetic and least energetic photons of the $B^+ \rightarrow K^+ \pi^0$ decay to be within the ranges accessible to each $B^+ \rightarrow K^+ h$ mode. These requirements are listed in Table 5.2. We obtain the M_{bc} and ΔE resolutions listed in Table 5.3. The corrections

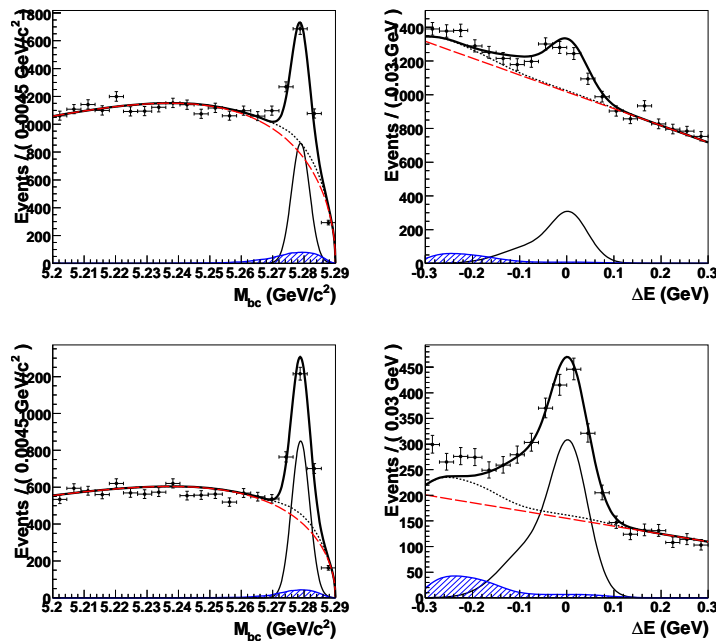


Figure 5.2: Top: M_{bc} and ΔE distributions together with fit results of the $B^+ \rightarrow K^+\pi^0$ control mode in the data. Bottom: fit projections in the signal region defined as $M_{bc} > 5.27 \text{ GeV}/c^2$ and $-0.2 \text{ GeV} < \Delta E < 0.1 \text{ GeV}$. The points with error bars represent data, the thick solid curves are the fit functions, the thin solid curves are the signal functions, the dashed curves are the contribution from the continuum background and the hashed areas are the contribution from B background.

$(\delta\sigma)$ are computed as $(\sigma_{\text{data}} - \sigma_{\text{MC}})/\sigma_{\text{MC}}$. We also compare the mean values of M_{bc} and ΔE between MC and data. The ΔE mean values and corrections are listed in Table 5.4. The mean values of M_{bc} are consistent between data and MC, and agree with the mass of the B^+ meson [2]. For ΔE , we only compare the mean values of the main Gaussian function which describes the ΔE peak. The obtained corrections are in agreement with other studies [133, 134, 135, 136].

5.1.2 Background PDFs

The continuum component is modeled with an ARGUS function for M_{bc} and a first order polynomial function for ΔE . The B and the off-time backgrounds are modeled with two-dimensional non-parametric KEYS¹ PDFs [137] built with MC events and with off-time data events, respectively. KEYS are computed directly out of unbinned $M_{bc}-\Delta E$ datasets and are therefore very handy to describe complicated distributions. One does not need to find fit functions and the resulting distribution is smooth, by construction.

We model separately B background contributions having different M_{bc} or ΔE distributions. For example, in the $B^+ \rightarrow K^+\eta$ fit, the $B \rightarrow K^*(892)\eta$ background, the $B^+ \rightarrow \pi^+\eta$

¹KEYS is an acronym for Kernel Estimating Your Shapes.

Table 5.2: Photon energy requirements on the $B^+ \rightarrow K^+ \pi^0$ sample to mimic the other modes. The requirement E_{γ_1} is applied on the higher energy photon. All values are in GeV.

Channel	E_{γ_1} win.	E_{γ_2} win.	Channel	E_{γ_1} win.	E_{γ_2} win.
$B^+ \rightarrow K^+ \eta$	0.9 – 3.5	0.1 – 2.0	$B^+ \rightarrow K^+ \chi_{c0}$	1.6 – 4.0	0.7 – 2.3
$B^+ \rightarrow K^+ \eta'$	1.0. – 3.5	0.1 – 2.0	$B^+ \rightarrow K^+ \chi_{c2}$	1.7 – 4.0	0.8 – 2.4
$B^+ \rightarrow K^+ \eta_c$	1.5 – 3.8	0.5 – 2.2	$B^+ \rightarrow K^+ J/\psi$	1.5 – 4.0	0.6 – 2.2
$B^+ \rightarrow K^+ \eta_c(2S)$	1.6 – 4.0	0.8 – 2.4	$B^+ \rightarrow K^+ X(3872)$	1.9 – 4.0	0.9 – 2.4

Table 5.3: Signal resolutions in MC and data, and corrections for M_{bc} and ΔE obtained with the $B^+ \rightarrow K^+ \pi^0$ control sample. Resolutions are in MeV/ c^2 for M_{bc} and MeV for ΔE .

h	$\sigma_{M_{bc}}$ (MC)	$\sigma_{M_{bc}}$ (data)	$\delta\sigma$ [%]	$\sigma_{\Delta E}$ (MC)	$\sigma_{\Delta E}$ (data)	$\delta\sigma$ [%]
π^0	3.38 ± 0.02	2.8 ± 0.1	-15 ± 3	34.7 ± 0.6	38.9 ± 2.1	12 ± 6
η	3.38 ± 0.02	2.8 ± 0.1	-16 ± 3	34.7 ± 0.6	39.3 ± 2.1	13 ± 6
η'	3.37 ± 0.02	2.8 ± 0.1	-16 ± 3	34.6 ± 0.6	39.1 ± 2.1	13 ± 6
η_c	3.32 ± 0.02	2.7 ± 0.1	-18 ± 3	33.2 ± 0.7	38.0 ± 2.7	14 ± 8
$\eta_c(2S)$	3.30 ± 0.03	2.8 ± 0.2	-16 ± 6	33.4 ± 0.9	37.8 ± 3.9	13 ± 12
χ_{c0}	3.30 ± 0.03	2.9 ± 0.2	-13 ± 6	33.7 ± 0.8	36.4 ± 3.4	8 ± 10
χ_{c2}	3.28 ± 0.03	2.7 ± 0.2	-17 ± 6	33.5 ± 1.0	37.0 ± 4.0	10 ± 12
J/ψ	3.31 ± 0.03	2.9 ± 0.2	-12 ± 6	33.3 ± 0.7	37.2 ± 2.8	12 ± 8
$X(3872)$	3.25 ± 0.04	2.7 ± 0.3	-18 ± 9	33.5 ± 1.5	38.9 ± 5.4	16 ± 16

Table 5.4: Mean values of ΔE in MC and data and corrections obtained with the $B^+ \rightarrow K^+ \pi^0$ control sample. All values are in MeV.

Channel	$\mu_{\Delta E}$ (MC)	$\mu_{\Delta E}$ (data)	$\delta\mu$
$B^+ \rightarrow K^+ \pi^0$	-2.8 ± 0.7	6.8 ± 2.4	10 ± 2
$B^+ \rightarrow K^+ \eta$	-2.9 ± 0.7	6.9 ± 2.4	10 ± 2
$B^+ \rightarrow K^+ \eta'$	-2.9 ± 0.7	7.0 ± 2.4	10 ± 2
$B^+ \rightarrow K^+ \eta_c$	-2.5 ± 0.8	6.3 ± 3.1	9 ± 3
$B^+ \rightarrow K^+ \eta_c(2S)$	-3.3 ± 1.1	9.2 ± 4.2	13 ± 4
$B^+ \rightarrow K^+ \chi_{c0}$	-3.4 ± 1.0	5.1 ± 3.7	8 ± 4
$B^+ \rightarrow K^+ \chi_{c2}$	-3.1 ± 1.1	9.1 ± 4.4	12 ± 4
$B^+ \rightarrow K^+ J/\psi$	-3.0 ± 0.9	7.4 ± 3.2	10 ± 3
$B^+ \rightarrow K^+ X(3872)$	-1.6 ± 1.5	9.8 ± 6.1	11 ± 6

background and the other contributions (mainly $B \rightarrow X_s \gamma$) are modeled with three independent PDFs and have independent normalization parameters.

A $B^+ \rightarrow K^+ \eta_c$ cross-feed is introduced in the $B^+ \rightarrow K^+ J/\psi$ fit as it will be explained in Section 5.4. This cross-feed is modeled with a Crystal Ball function for M_{bc} and three Gaussian functions for ΔE .

5.1.3 Fit description

For each channel, the fit is simultaneously performed on two or three sub-data samples defined by the following experimental conditions: SVD1 and SVD2 (efficiency discrepancy) and for experiments with or without timing information.

For the $B^+ \rightarrow K^+ \eta$ and $B^+ \rightarrow K^+ \eta'$ modes, we consider two sub-samples:

- SVD1 (exp. 7 to 27) containing 152×10^6 $B\bar{B}$ pairs.
- SVD2 (exp. 31 to 49) containing 383×10^6 $B\bar{B}$ pairs.

For the other modes, we consider three sub-samples:

- SVD1 (exp. 7 to 27) containing 152×10^6 $B\bar{B}$ pairs.
- SVD2 without timing information (exp. 31 to 37) containing 125×10^6 $B\bar{B}$ pairs.
- SVD2 with timing information (exp. 39 to 49) containing 258×10^6 $B\bar{B}$ pairs.

For each mode, the branching fraction (\mathcal{B}) is the only free parameter for the signal. The signal yield S^i in sub-sample i is then defined as

$$S^i = \mathcal{B} \times \epsilon^i \times \epsilon_{\text{corr}} \times N_{B\bar{B}}^i, \quad (5.2)$$

where $N_{B\bar{B}}^i$ is the number of $B\bar{B}$ pairs in sub-sample i , ϵ^i is the signal efficiency in sub-sample i and ϵ_{corr} is the correction applied to the signal efficiency.

The other free fit parameters are the continuum normalizations (one per sub-sample) and the continuum shape parameters, except the ARGUS endpoint which is fixed to 5.29 GeV/ c^2 . The continuum shape parameters in MC are found to be consistent between SVD1 and SVD2 and we therefore use the same parameters to describe all sub-samples.

5.2 Systematic uncertainties and results

For each mode, the fit contains by construction all known sources of systematic uncertainties, which can be studied by changing the values of fixed parameters:

1. uncertainties on the signal PDF parameters and corrections (signal shape modeling),
2. uncertainties on the signal reconstruction efficiency and on the efficiency correction,
3. uncertainties on the normalizations of the B and off-time backgrounds,
4. uncertainties on the number of $B\bar{B}$ events.

5.2.1 Uncertainty on the signal reconstruction efficiency

Uncertainty due to the $m_{\gamma\gamma}$ requirement

We compare the distribution of the two-photons invariant mass between data and Monte Carlo in the $B^+ \rightarrow K^+ \pi^0$ mode. We perform the fit in the data in bins of $m_{\gamma\gamma}$ and compare the signal yield obtained in each $m_{\gamma\gamma}$ bin with the $m_{\gamma\gamma}$ distribution of signal MC, as shown in Figure 5.3. We compute the efficiency of the tight $m_{\gamma\gamma}$ requirement. This efficiency is $\epsilon_{\text{data}} = (95.9 \pm 1.1)\%$ in the data and $\epsilon_{\text{MC}} = 93.6\%$ in the MC. We assign, for each mode, a 3.6% relative systematic uncertainty due to the $m_{\gamma\gamma}$ requirement, computed as $(|\epsilon_{\text{data}} - \epsilon_{\text{MC}}| + \sigma_{\epsilon_{\text{data}}})/\epsilon_{\text{MC}}$.

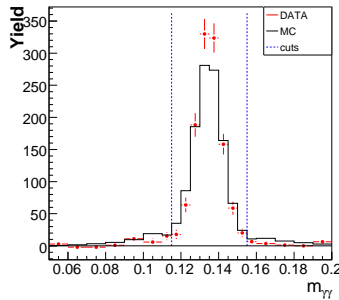


Figure 5.3: $m_{\gamma\gamma}$ comparison between data and MC for the $B^+ \rightarrow K^+ \pi^0$ channel used to estimate the systematic uncertainty on the $m_{\gamma\gamma}$ requirement.

Uncertainty due to the continuum rejection requirement

We compute the efficiency of the \mathcal{R} requirement using the $B^+ \rightarrow K^+ \pi^0$ control sample. This efficiency is evaluated as

$$\epsilon_{\mathcal{R}} = \frac{S_{\mathcal{R} > \mathcal{R}_{\text{cut}}}}{S_{\text{tot}}}, \quad (5.3)$$

where $S_{\mathcal{R} > \mathcal{R}_{\text{cut}}}$ is the number of $B^+ \rightarrow K^+ \pi^0$ signal events with the continuum rejection requirement applied and S_{tot} without it. The number of signal events are obtained in the data with a fit and in MC by counting. We obtain an efficiency of $\epsilon_{\text{MC}} = 54.6\%$ in MC and $\epsilon_{\text{data}} = (54.7 \pm 3.8)\%$ in the data, in perfect agreement with each other. In the data, we take into account the correlation between $S_{\mathcal{R} > \mathcal{R}_{\text{cut}}}$ and S_{tot} to have a better estimate of the efficiency uncertainty. We assign, for each mode, a 6.9% relative systematic uncertainty due to the \mathcal{R} requirement for all modes, computed as $\sigma_{\epsilon_{\text{data}}}/\epsilon_{\text{MC}}$.

Total uncertainty on the signal reconstruction efficiency

We consider a 2.2% uncertainty per photon for the photon reconstruction efficiency, 1% per track for the tracking efficiency, 2% for kaon identification efficiency, 3.6% for the $m_{\gamma\gamma}$ requirement efficiency and 6.9% for the \mathcal{R} requirement efficiency. The first three uncertainties are the same as those used in the $B_s^0 \rightarrow \phi\gamma$ and $B_s^0 \rightarrow \gamma\gamma$ analyses and are described

Table 5.5: Uncertainty on the signal reconstruction efficiency.

Source	Uncertainty (%)
Photon reconstruction efficiency	2×2.2
Tracking efficiency	1×1
Kaon identification efficiency	2.0
$m_{\gamma\gamma}$ cut efficiency	3.6
\mathcal{R} cut efficiency	6.9
MC statistics	1.0
Total	9.3

in Section 4.2 on page 77. These uncertainties are summed in quadrature and listed in Table 5.5.

5.2.2 Likelihood including systematic uncertainties

The likelihood of the fit depends on free parameters (\mathcal{B} , α_i) and on many constant parameters (β_i) that are only known to some extent

$$\mathcal{L} \equiv \mathcal{L}(\mathcal{B}, \alpha_1, \dots, \alpha_m, \beta_1, \dots, \beta_n). \quad (5.4)$$

These β_i parameters, listed in Tables D.10-D.18 in Appendix D on page 113, are often called nuisance parameters in the literature [138]. Their uncertainties are sources of systematic uncertainty on the parameters that we want to measure, ie. \mathcal{B} and α_i . We compute a likelihood including the systematic uncertainties by convolving the likelihood function with the distributions of the β_i parameters

$$\mathcal{L}_{\text{conv}}(\mathcal{B}, \alpha_1, \dots, \alpha_m) = \int \mathcal{L}(\mathcal{B}, \alpha_1, \dots, \alpha_m, \beta'_1, \dots, \beta'_n) g_1(\beta'_1 - \beta_1) \dots g_n(\beta'_n - \beta_n) d\beta'_1 \dots d\beta'_n, \quad (5.5)$$

where we assume no correlation between all the β_i parameters and we assume that their distributions can be described with Gaussian functions. A likelihood including systematic uncertainties ($\mathcal{L}_{\text{syst}}$) depending on \mathcal{B} only is then computed by maximizing $\mathcal{L}_{\text{conv}}$ for each value of \mathcal{B} according to

$$\mathcal{L}_{\text{syst}}(\mathcal{B}) = \max_{\alpha_1, \dots, \alpha_m} \mathcal{L}_{\text{conv}}(\mathcal{B}, \alpha_1, \dots, \alpha_m). \quad (5.6)$$

An analytical integration is impossible to perform. We choose to do a Monte Carlo integration

$$\mathcal{L}_{\text{syst}}(\mathcal{B}) = \frac{1}{N} \sum_{i=1}^N \max_{\alpha_1, \dots, \alpha_m} \mathcal{L}(\mathcal{B}, \alpha_1, \dots, \alpha_m, \beta_1^i, \dots, \beta_n^i), \quad (5.7)$$

where $\max_{\alpha_1, \dots, \alpha_m} \mathcal{L}(\mathcal{B}, \alpha_1, \dots, \alpha_m, \beta_1^i, \dots, \beta_n^i)$ is the maximum value of the likelihood of a fit of the α_j parameters where \mathcal{B} is fixed and the β_j^i parameters randomly chosen according

to their distributions. A large number ($N = 500$) of fits has to be performed in order to obtain a good estimate of the integral.

We then extract the final results from this likelihood, which include, by construction, all known systematic uncertainties. We report the central value of \mathcal{B} (\mathcal{B}_0) as the maximum of $\mathcal{L}_{\text{syst}}$ and we compute the total uncertainties ($\delta_{\text{tot}}^{\pm}$) on the branching fraction with

$$\int_{\mathcal{B}_0 + \delta_{\text{tot}}^-}^{\mathcal{B}_0 + \delta_{\text{tot}}^+} \mathcal{L}_{\text{syst}} d\mathcal{B} = 68.3\% \times \int_0^1 \mathcal{L}_{\text{syst}} d\mathcal{B}, \quad (5.8)$$

$$\mathcal{L}_{\text{syst}}(\mathcal{B}_0 + \delta_{\text{tot}}^-) = \mathcal{L}_{\text{syst}}(\mathcal{B}_0 + \delta_{\text{tot}}^+). \quad (5.9)$$

Systematic uncertainties ($\delta_{\text{syst}}^{\pm}$) are then computed with

$$\delta_{\text{syst}}^{\pm} = \sqrt{\delta_{\text{tot}}^{\pm 2} - \delta_{\text{stat}}^{\pm 2}}, \quad (5.10)$$

where the statistical uncertainties ($\delta_{\text{stat}}^{\pm}$) are obtained from the nominal fit likelihood (\mathcal{L}) as in Equation 5.8. We compute limits on the \mathcal{B} at 90% confidence level ($\mathcal{B}_{\text{limit}}$) with

$$\int_0^{\mathcal{B}_{\text{limit}}} \mathcal{L}_{\text{syst}} d\mathcal{B} = 90\% \times \int_0^1 \mathcal{L}_{\text{syst}} d\mathcal{B}. \quad (5.11)$$

And finally, we compute the significance (S) with

$$S = \sqrt{2(\ln \mathcal{L}_{\text{syst}}(\mathcal{B} \equiv \mathcal{B}_0) - \ln \mathcal{L}_{\text{syst}}(\mathcal{B} \equiv 0))}. \quad (5.12)$$

5.3 Fit results

Figures 5.4 and 5.5 show the data with the fit results. The numerical values and errors for all fit parameters for each mode are given in Appendix D on page 113, while the main final results are summarized in Tables 5.6, 5.7 and 5.9.

We observe signals in the $B^+ \rightarrow K^+ \eta$ and the $B^+ \rightarrow K^+ \eta'$ modes and obtain an evidence for a signal in the $B^+ \rightarrow K^+ \eta_c$ channel. We report the first measurements of $B^+ \rightarrow K^+ \eta'$ and $B^+ \rightarrow K^+ \eta_c$ channels in the $K^+ \gamma \gamma$ final state. We measure

$$\mathcal{B}(B^+ \rightarrow K^+ \eta \rightarrow K^+ \gamma \gamma) = (0.87_{-0.15}^{+0.16}(\text{stat})_{-0.07}^{+0.10}(\text{syst})) \times 10^{-6}, \quad (5.13)$$

in agreement with Belle's measurement of this mode with the same dataset [139], and

$$\mathcal{B}(B^+ \rightarrow K^+ \eta' \rightarrow K^+ \gamma \gamma) = (1.40_{-0.15}^{+0.16}(\text{stat})_{-0.12}^{+0.15}(\text{syst})) \times 10^{-6}, \quad (5.14)$$

$$\mathcal{B}(B^+ \rightarrow K^+ \eta_c \rightarrow K^+ \gamma \gamma) = (0.22_{-0.07}^{+0.09}(\text{stat})_{-0.02}^{+0.04}(\text{syst})) \times 10^{-6}, \quad (5.15)$$

where the first uncertainty is statistical and the second systematic. All measured branching fractions agree with the values shown in the third column of Table 1.3 on page 22.

We see no significant signal in the other modes, and we extract the following 90% CL upper limits

$$\mathcal{B}(B^+ \rightarrow K^+ \eta_c(2S) \rightarrow K^+ \gamma \gamma) < 0.18 \times 10^{-6}, \quad (5.16)$$

$$\mathcal{B}(B^+ \rightarrow K^+ \chi_{c0} \rightarrow K^+ \gamma \gamma) < 0.11 \times 10^{-6}, \quad (5.17)$$

$$\mathcal{B}(B^+ \rightarrow K^+ \chi_{c2} \rightarrow K^+ \gamma \gamma) < 0.09 \times 10^{-6}, \quad (5.18)$$

$$\mathcal{B}(B^+ \rightarrow K^+ J/\psi \rightarrow K^+ \gamma \gamma) < 0.16 \times 10^{-6}, \quad (5.19)$$

$$\mathcal{B}(B^+ \rightarrow K^+ X(3872) \rightarrow K^+ \gamma \gamma) < 0.24 \times 10^{-6}. \quad (5.20)$$

Table 5.6: Total signal yields, branching fractions and significance results for $B^+ \rightarrow K^+ h \rightarrow K^+ \gamma \gamma$. The first uncertainty is statistical, the second one is systematic.

Channel	Signal yield	\mathcal{B} (10^{-6})	\mathcal{B} significance
$B^+ \rightarrow K^+ \eta$	76_{-13}^{+14}	$0.87_{-0.15-0.07}^{+0.16+0.10}$	7.3
$B^+ \rightarrow K^+ \eta'$	114 ± 13	$1.40_{-0.15-0.12}^{+0.16+0.15}$	13.8
$B^+ \rightarrow K^+ \eta_c$	$13.3_{-4.1}^{+4.8}$	$0.22_{-0.07-0.02}^{+0.09+0.04}$	4.1
$B^+ \rightarrow K^+ \eta_c(2S)$	$4.0_{-3.0}^{+3.9}$	$0.07_{-0.05}^{+0.06}$	1.4
$B^+ \rightarrow K^+ \chi_{c0}$	$0.7_{-1.7}^{+2.5}$	$0.01_{-0.03}^{+0.04}$	0.21
$B^+ \rightarrow K^+ \chi_{c2}$	$-0.3_{-1.9}^{+2.6}$	$0.00_{-0.03}^{+0.04}$	–
$B^+ \rightarrow K^+ J/\psi$	$3.4_{-2.0}^{+2.8}$	$0.06_{-0.04}^{+0.05}$	2.0
$B^+ \rightarrow K^+ X(3872)$	$-0.9_{-1.4}^{+2.2}$	$-0.01_{-0.02}^{+0.03}$	–

Table 5.7: 90% CL upper limits on the branching fractions for the $B^+ \rightarrow K^+ h \rightarrow K^+ \gamma \gamma$ decays including systematic uncertainties.

Resonance h	\mathcal{B} limit at 90% CL (10^{-6})
$\eta_c(2S)$	0.18
χ_{c0}	0.11
χ_{c2}	0.09
J/ψ	0.16
$X(3872)$	0.24

Table 5.8: Estimation of the $\mathcal{B}(B^+ \rightarrow K^+ X(3872))$ branching fractions. Note that $\mathcal{B}(B^+ \rightarrow K^+ X(3872)) \times \mathcal{B}(X(3872) \rightarrow J/\psi \pi^+ \pi^- \pi^0)$ is known as $\mathcal{B}(B^+ \rightarrow K^+ X(3872)) \times \mathcal{B}(X(3872) \rightarrow J/\psi \pi^+ \pi^-) \times (1.0 \pm 0.5)$ [81].

Channel	Value
$\mathcal{B}(B^+ \rightarrow K^+ X(3872)) \times \mathcal{B}(X(3872) \rightarrow J/\psi \pi^+ \pi^-)$	$(11.4 \pm 2.0) \times 10^{-6}$ [2]
$\mathcal{B}(B^+ \rightarrow K^+ X(3872)) \times \mathcal{B}(X(3872) \rightarrow J/\psi \pi^+ \pi^- \pi^0)$	$(11.4 \pm 6.0) \times 10^{-6}$ [81]
$\mathcal{B}(B^+ \rightarrow K^+ X(3872)) \times \mathcal{B}(X(3872) \rightarrow J/\psi \gamma)$	$(3.3 \pm 1.0) \times 10^{-6}$ [82]
$\mathcal{B}(B^+ \rightarrow K^+ X(3872))$	$(26.1 \pm 7.0) \times 10^{-6}$

The likelihoods used to obtain all above results are shown in Figure 5.6 for all modes.

Whenever the branching fraction of $B^+ \rightarrow K^+ h$ has been measured elsewhere, we also perform the fit by constraining $\mathcal{B}(B^+ \rightarrow K^+ h)$ to the measured value [2], thus extracting a measurement or an upper limit on $\mathcal{B}(h \rightarrow \gamma \gamma)$. The uncertainty on $\mathcal{B}(B^+ \rightarrow K^+ h)$ is included as a source of systematic uncertainty. We obtain

$$\mathcal{B}(\chi_{c0} \rightarrow \gamma \gamma) < 9.5 \times 10^{-4}, \quad (5.21)$$

$$\mathcal{B}(\eta_c(2S) \rightarrow \gamma \gamma) < 8.2 \times 10^{-4}, \quad (5.22)$$

$$\mathcal{B}(J/\psi \rightarrow \gamma \gamma) < 1.6 \times 10^{-4}, \quad (5.23)$$

at 90% CL. Similarly, for the three modes where we have an evidence of signal, we determine

$$\mathcal{B}(\eta' \rightarrow \gamma \gamma) = (2.01_{-0.22}^{+0.23+0.23})\%, \quad (5.24)$$

$$\mathcal{B}(\eta_c \rightarrow \gamma \gamma) = (2.4_{-0.8}^{+0.9+0.7}) \times 10^{-4}, \quad (5.25)$$

where the first uncertainty is statistical and the second systematic.

The absolute branching fraction $\mathcal{B}(B^+ \rightarrow K^+ X(3872))$ has not yet been measured. However, there are measurements of the product of this quantity and the branching fractions of different decays of the $X(3872)$. Assuming that the $X(3872)$ partial widths to $J/\psi \pi^+ \pi^-$, $J/\psi \pi^+ \pi^- \pi^0$ and $J/\psi \gamma$ saturate the total decay width of the $X(3872)$ and taking the values of the corresponding products listed in Table 5.8, we can estimate $\mathcal{B}(B^+ \rightarrow K^+ X(3872))$ and derive the upper limit

$$\mathcal{B}(X(3872) \rightarrow \gamma \gamma) < 1.1\% \quad (5.26)$$

at 90% CL. The latter limit is conservative: if a new decay mode of the $X(3872)$ particle is discovered, the branching fraction $\mathcal{B}(B^+ \rightarrow K^+ X(3872))$ would increase thus reducing $\mathcal{B}(X(3872) \rightarrow \gamma \gamma)$, which is equal to $\mathcal{B}(B^+ \rightarrow K^+ X(3872) \rightarrow K^+ \gamma \gamma) / \mathcal{B}(B^+ \rightarrow K^+ X(3872))$.

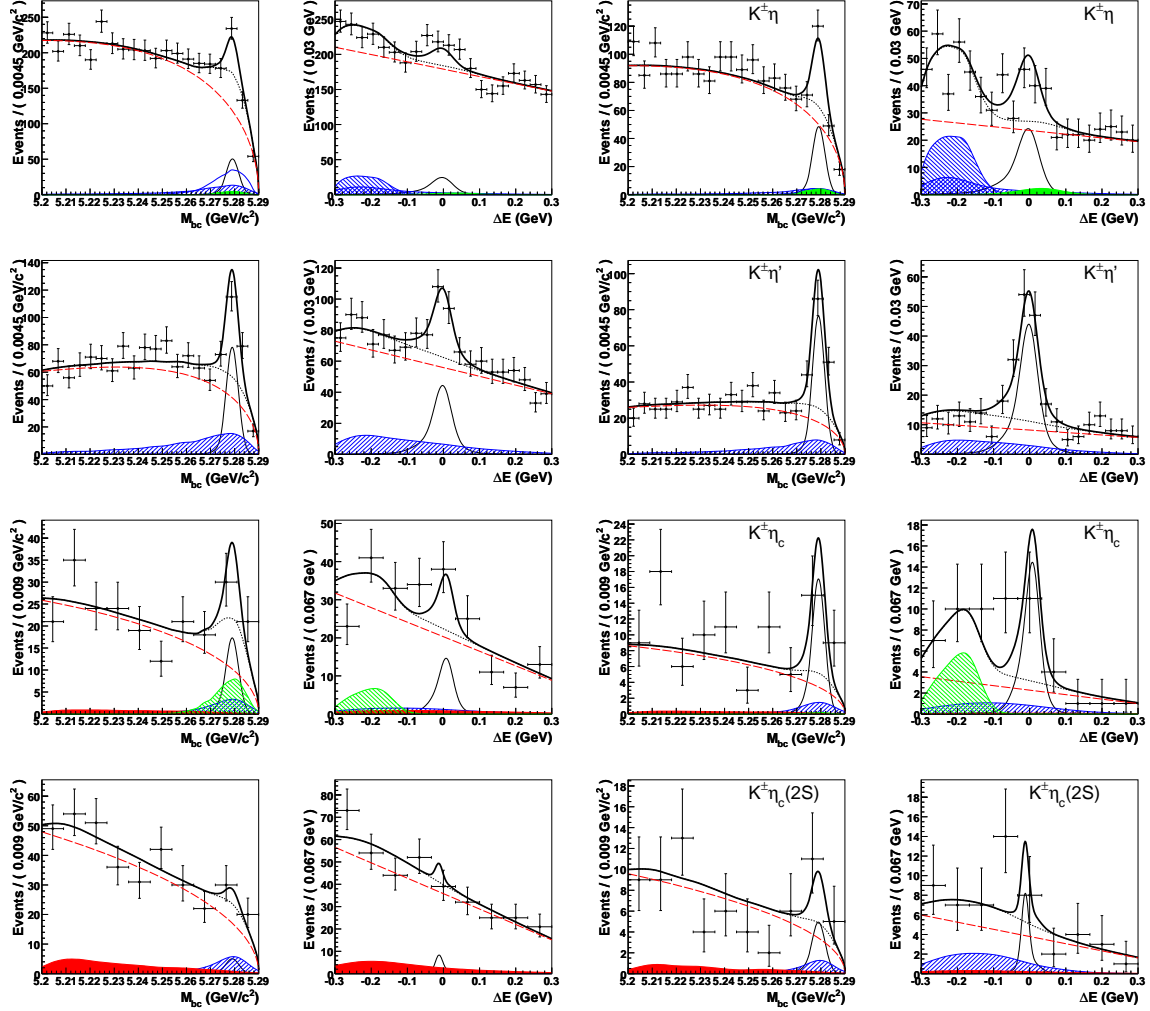


Figure 5.4: M_{bc} and ΔE distributions together with fit results for the modes $B^+ \rightarrow K^+\eta$ (first row), $B^+ \rightarrow K^+\eta'$ (second row), $B^+ \rightarrow K^+\eta_c$ (third row) and $B^+ \rightarrow K^+\eta_c(2S)$ (fourth row). In each row, the two left plots show the full fit region while the two right plots are the projections of the fit in the signal region. The points with error bars represent data, the thick solid curves are the fit functions, the thin solid curves are the signal functions, the dashed lines show the continuum contribution and the dotted lines show the sum of all background contributions. The hatched area present in the whole ΔE region is the contribution from charmless B decays. The hatched area around $\Delta E = -0.2$ GeV in the $B^+ \rightarrow K^+\eta$ ($B^+ \rightarrow K^+\eta_c$) case shows the contribution from $B \rightarrow K^*(892)\eta$ ($B \rightarrow K^*(892)\eta_c$) decays. The filled area around $\Delta E = 0.05$ GeV in the $B^+ \rightarrow K^+\eta$ case is the contribution from $B^+ \rightarrow \pi^+\eta$ decays. The filled area in the $B^+ \rightarrow K^+\eta_c$ and $B^+ \rightarrow K^+\eta_c(2S)$ cases is the contribution from the off-time background.

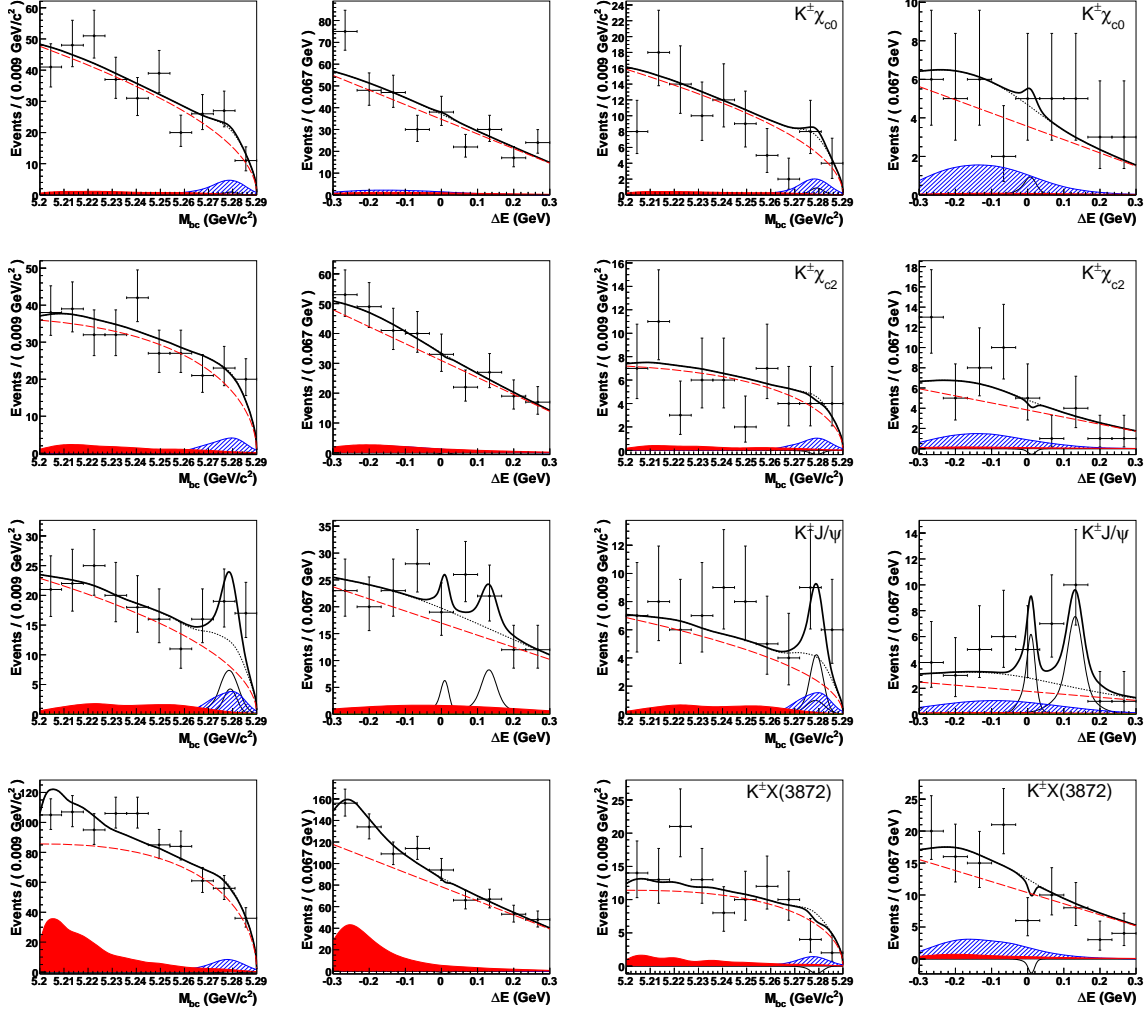


Figure 5.5: M_{bc} and ΔE distributions together with fit results for the modes $B^+ \rightarrow K^+ \chi_{c0}$ (first row), $B^+ \rightarrow K^+ \chi_{c2}$ (second row), $B^+ \rightarrow K^+ J/\psi$ (third row) and $B^+ \rightarrow K^+ X(3872)$ (fourth row). In each row, the two left plots show the full fit region, while the two right plots are the projections of the fit in the signal region. The points with error bars represent data, the thick solid curves are the fit functions, the thin solid curves are the signal functions, the dashed lines show the continuum contribution, the dotted lines show the sum of all background contributions, the hatched area is the contribution from charmless B decays and the filled areas the contribution from the off-time background. In the $B^+ \rightarrow K^+ J/\psi$ plots, the $B^+ \rightarrow K^+ \eta_c$ cross-feed is visible in thin solid curves as a small peaking background in M_{bc} while it is peaking around 120 MeV in ΔE .

Table 5.9: Measurements of the $\mathcal{B}(h \rightarrow \gamma\gamma)$ branching fractions. Second uncertainties are systematic. Limits are computed at the 90% CL and include systematic uncertainties. The assumed $B^+ \rightarrow K^+h$ branching fractions are taken from Table 5.8 for $h = X(3872)$ and Table 1.3 on page 22 for the other modes.

Decay	Assumed $\mathcal{B}(B^+ \rightarrow K^+h)$	$\mathcal{B}(h \rightarrow \gamma\gamma)$
$\eta' \rightarrow \gamma\gamma$	$(69.7 \pm 2.8) \times 10^{-6}$	$(2.01^{+0.23+0.23}_{-0.22-0.19})\%$
$\eta_c \rightarrow \gamma\gamma$	$(9.1 \pm 1.3) \times 10^{-4}$	$(2.4^{+0.9+0.7}_{-0.8-0.4}) \times 10^{-4}$
$\eta_c(2S) \rightarrow \gamma\gamma$	$(3.4 \pm 1.8) \times 10^{-4}$	$< 8.2 \times 10^{-4}$
$\chi_{c0} \rightarrow \gamma\gamma$	$(1.40^{+0.23}_{-0.19}) \times 10^{-4}$	$< 9.5 \times 10^{-4}$
$J/\psi \rightarrow \gamma\gamma$	$(10.07 \pm 0.35) \times 10^{-4}$	$< 1.6 \times 10^{-4}$
$X(3872) \rightarrow \gamma\gamma$	$(26.1 \pm 7.0) \times 10^{-6}$	$< 1.1 \times 10^{-4}$

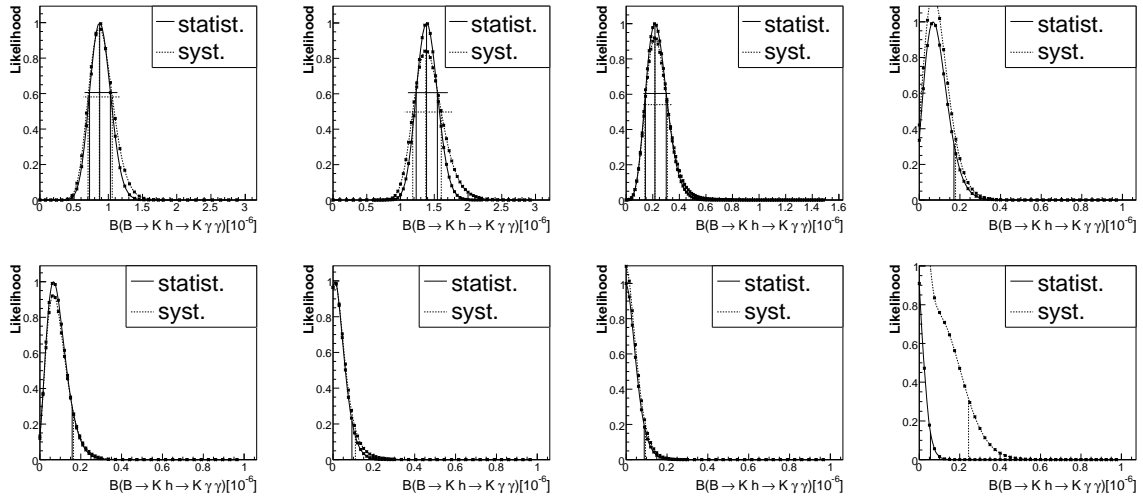


Figure 5.6: Likelihoods as a function of $\mathcal{B}(B^+ \rightarrow K^+h \rightarrow K^+\gamma\gamma)$ used to extract results. Top: $B^+ \rightarrow K^+\eta$, $B^+ \rightarrow K^+\eta'$, $B^+ \rightarrow K^+\eta_c$ and $B^+ \rightarrow K^+\eta_c(2S)$. Bottom: $B^+ \rightarrow K^+J/\psi$, $B^+ \rightarrow K^+\chi_{c0}$, $B^+ \rightarrow K^+\chi_{c2}$ and $B^+ \rightarrow K^+X(3872)$. In the $B^+ \rightarrow K^+\eta$, $B^+ \rightarrow K^+\eta'$ and $B^+ \rightarrow K^+\eta_c$ figures, the lines show the $\pm 1\sigma$ uncertainties. In the remaining figures, the line shows the 90% CL limit on the branching fraction.

5.3.1 Fit in bins of the $m_{\gamma\gamma}$ mass

For the modes where we observe a signal, we scan the invariant mass of the two photons by repeating the fit in several $m_{\gamma\gamma}$ bins. We then compare the signal yields obtained by these fits with the MC signal shape. A good agreement between data and MC is obtained, as shown in Figure 5.7.

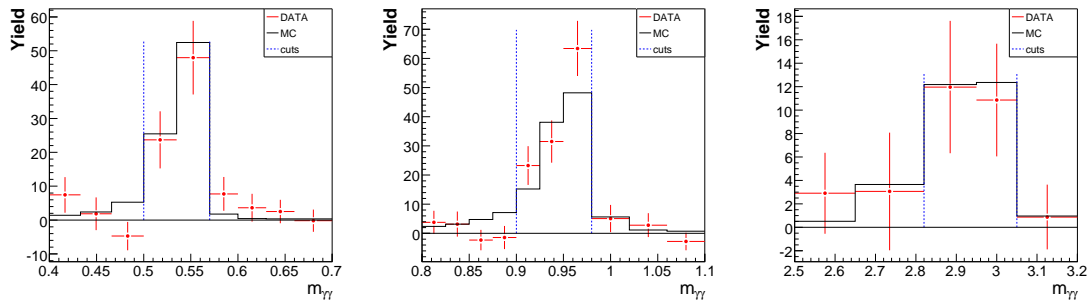


Figure 5.7: Scan of $m_{\gamma\gamma}$ (GeV/c^2) for $B^+ \rightarrow K^+\eta$ (left), $B^+ \rightarrow K^+\eta'$ (middle) and $B^+ \rightarrow K^+\eta_c$ (right). The points with error bars represent the signal yield fitted in data and the histograms represent the signal MC shapes. The blue lines show the tight $m_{\gamma\gamma}$ windows.

5.4 Study of the cross-feeds between the h resonances

The tight $m_{\gamma\gamma}$ selections listed in Table 3.1 on page 54 overlap for the $B^+ \rightarrow K^+\eta_c$ and $B^+ \rightarrow K^+J/\psi$ modes and for the $B^+ \rightarrow K^+\chi_{c0}$, $B^+ \rightarrow K^+\chi_{c2}$ and $B^+ \rightarrow K^+\eta_c(2S)$ modes. When we reconstruct one mode, we also reconstruct the other one(s) with a shift on ΔE equal to the mass difference between the two resonances due to the mass-constrained fit. As a check, we study the effect of this overlap by performing two simultaneous fits, described below, where cross-feed PDFs are introduced and are used to measure the respective branching fractions. This study has proved that the results previously discussed in Section 5.3 are reliable and can be considered final results.

Independent datasets are required to perform these simultaneous fits. This is achieved by modifying the $m_{\gamma\gamma}$ selection, as listed in Table 5.10. Efficiencies then have to be computed again and are listed in Table 5.11 for the simultaneous fit of the $B^+ \rightarrow K^+\eta_c$ and $B^+ \rightarrow K^+J/\psi$ modes and in Table 5.12 for the $B^+ \rightarrow K^+\chi_{c0}$, $B^+ \rightarrow K^+\chi_{c2}$ and $B^+ \rightarrow K^+\eta_c(2S)$ modes, including cross-feed efficiencies.

Table 5.10: Definitions of the tight invariant mass windows (GeV/c^2) for photon pairs.

Particle	Tight $m_{\gamma\gamma}$ window	Non-overlapping tight $m_{\gamma\gamma}$ window
η_c	2.82–3.05	2.82–3.05
J/ψ	2.92–3.15	3.05–3.15
χ_{c0}	3.25–3.50	3.25–3.45
χ_{c2}	3.40–3.62	3.45–3.57
$\eta_c(2S)$	3.44–3.70	3.57–3.70

Table 5.11: Signal reconstruction efficiencies (%) for the nominal fit and for the simultaneous fit of the $B^+ \rightarrow K^+\eta_c$ and $B^+ \rightarrow K^+J/\psi$ modes. Note that there is no $B^+ \rightarrow K^+\eta_c$ signal reconstructed in the $m_{\gamma\gamma}$ region of the J/ψ .

	Nominal efficiencies		Updated efficiencies			
	SVD1	SVD2	SVD1	SVD2	SVD1	SVD2
			True η_c		True J/ψ	
reconstructed as η_c	10.0	10.9	10.0	10.9	4.8	4.8
reconstructed as J/ψ	9.4	9.7	–	–	5.8	6.3

For both fits, the signal fit variables are the branching fractions. The signal yields $S_i^j(k)$, for mode k , are computed from the branching fraction $\mathcal{B}(k)$ with the relations

$$S_i^j(k) = \mathcal{B}(k) \times \epsilon_i^j(k) \times N_{B\bar{B}}^j, \quad (5.27)$$

where i runs over the simultaneously reconstructed and fitted resonances and j over the different sub-samples.

Table 5.12: Signal reconstruction efficiencies (%) for the nominal fit and for the simultaneous fit of the $B^+ \rightarrow K^+ \chi_{c0}$, $B^+ \rightarrow K^+ \chi_{c2}$ and $B^+ \rightarrow K^+ \eta_c(2S)$ modes. Note that there is no $B^+ \rightarrow K^+ \chi_{c0}$ signal reconstructed in the $m_{\gamma\gamma}$ region of the $\eta_c(2S)$.

	Nominal efficiencies		Updated efficiencies					
	SVD1	SVD2	SVD1	SVD2	SVD1	SVD2	SVD1	SVD2
			True χ_{c0}		True χ_{c2}		True $\eta_c(2S)$	
recon. as χ_{c0}	11.0	11.6	10.0	10.4	2.9	2.9	1.8	1.8
recon. as χ_{c2}	10.4	11.3	1.3	1.5	7.2	7.7	4.9	5.1
recon. as $\eta_c(2S)$	10.9	11.4	–	–	2.1	2.5	5.9	6.3

Table 5.13: Signal yields and branching fractions results for the simultaneous combined fits with cross-feeds. The uncertainties are statistical. Limits are calculated at 90% confidence level and include systematic uncertainties.

Resonance	Signal yield	$\mathcal{B}(B^+ \rightarrow K^+ h \rightarrow K^+ \gamma \gamma)$ (10^{-6})
η_c	$12.7^{+4.8}_{-4.1}$	$0.22^{+0.08}_{-0.07}$
J/ψ	$-1.1^{+2.1}_{-1.6}$	< 0.13
χ_{c0}	$1.1^{+2.5}_{-1.7}$	< 0.11
χ_{c2}	$-1.6^{+1.6}_{-1.1}$	< 0.07
$\eta_c(2S)$	$2.9^{+2.2}_{-1.8}$	< 0.20

The results of the simultaneous fits are shown in Table 5.13 and in Figures 5.8 and 5.9. They are globally consistent with the results from the nominal fits. In particular, the limits vary by very small amounts. However, some of the cross-feed components go negative, which is difficult to interpret on statistical grounds. Therefore, we decide to keep the nominal fits as our final results.

For each of the $B^+ \rightarrow K^+ \chi_{c0}$, $B^+ \rightarrow K^+ \chi_{c2}$ and $B^+ \rightarrow K^+ \eta_c(2S)$ modes, we try another fit where cross-feed branching fractions are set equal to the limits presented in Table 5.7 on page 93. The fit results are listed in Table 5.14. We obtain the same or slightly smaller limits. We conclude that the limits presented in Table 5.7 for these three modes are reliable and conservative.

For the $B^+ \rightarrow K^+ \eta_c$, we do not try another fit with non-zero fixed $B^+ \rightarrow K^+ J/\psi$ cross-feed, which is a forbidden background. However, note that we have introduced in the nominal $B^+ \rightarrow K^+ J/\psi$ fit a $B^+ \rightarrow K^+ \eta_c$ background component using our measured $B^+ \rightarrow K^+ \eta_c$ branching fraction.

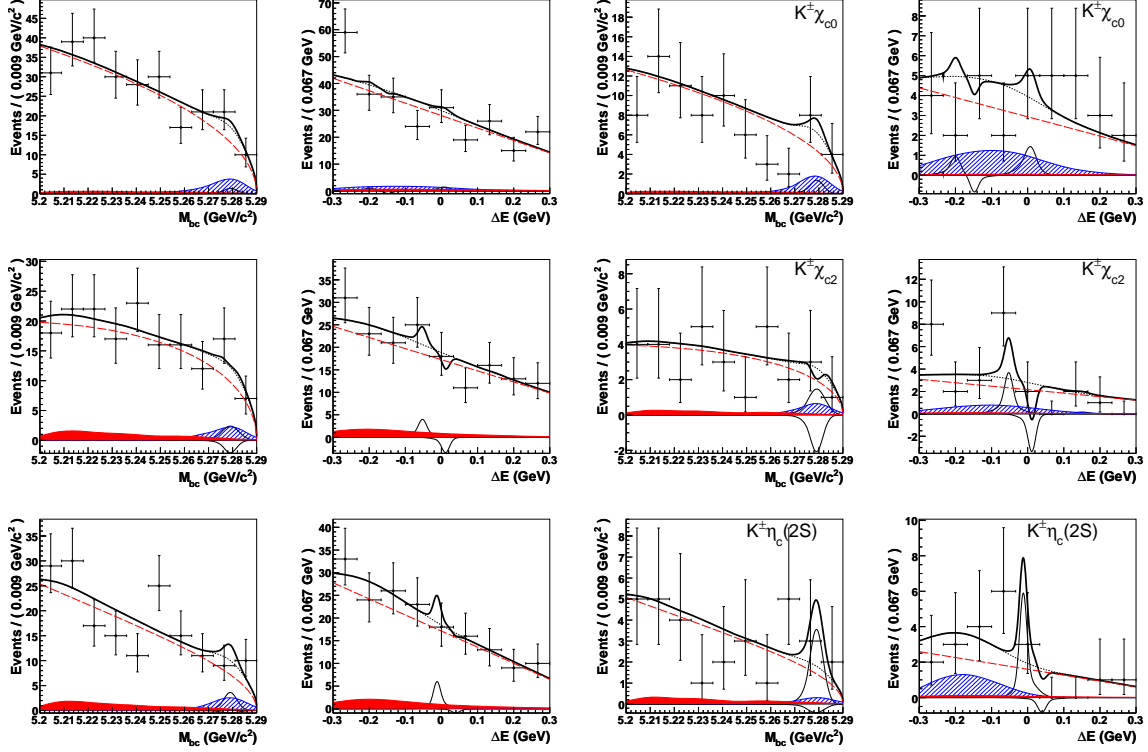


Figure 5.8: Results for the simultaneous combined fit of the modes $B^+ \rightarrow K^+ \chi_{c0}$ (first row), $B^+ \rightarrow K^+ \chi_{c2}$ (second row) and $B^+ \rightarrow K^+ \eta_c(2S)$ (third row). For each row, the two left plots show the full fit region, while the two right plots show the projection of the fit in the signal window. Fit curves are described in Figures 5.4 and 5.5 on pages 95 and 96.

Table 5.14: $B^+ \rightarrow K^+ h \rightarrow K^+ \gamma \gamma$ branching fractions results for the fit with cross-feeds fixed to the upper limits of Table 5.7 on page 93. The uncertainty is statistical. Limits are calculated at 90% confidence level and include systematic uncertainties.

Resonance	Signal yield	$\mathcal{B}(B^+ \rightarrow K^+ h \rightarrow K^+ \gamma \gamma)$ (10^{-6})
χ_{c0}	$0.7^{+2.5}_{-1.7}$	< 0.10
χ_{c2}	$-1.2^{+2.5}_{-1.7}$	< 0.09
$\eta_c(2S)$	$2.9^{+3.6}_{-2.7}$	< 0.18

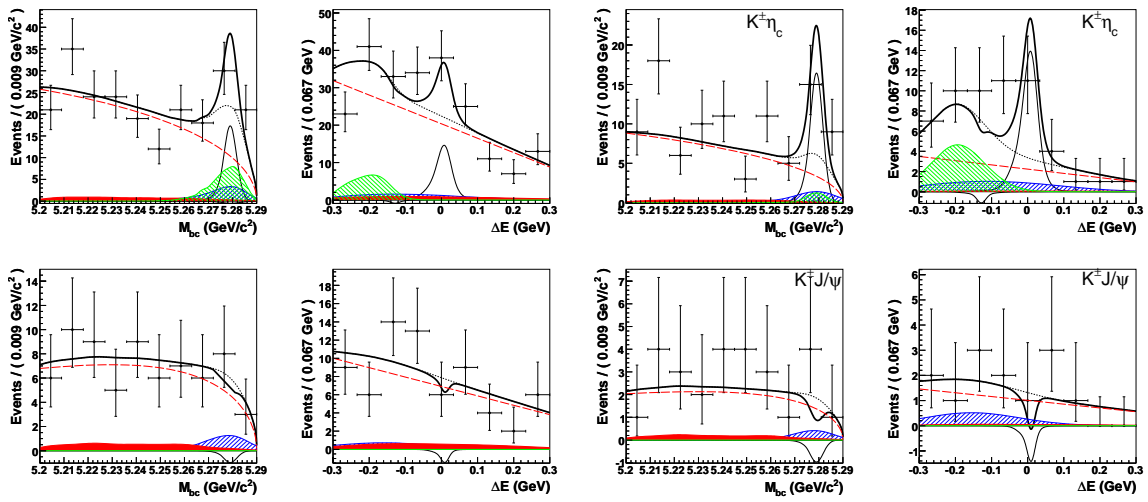


Figure 5.9: Results for the simultaneous combined fit of the $B^+ \rightarrow K^+ \eta_c$ mode (first row) and $B^+ \rightarrow K^+ J/\psi$ (second row). For each row, the two left plots show the full fit region, while the two right plots show the projection of the fit in the signal window. Fit curves are described in Figures 5.4 and 5.5 on pages 95 and 96.

Conclusion

WE have studied the $B_s^0 \rightarrow \phi\gamma$ and $B_s^0 \rightarrow \gamma\gamma$ radiative penguin decays in a 23.6 fb^{-1} sample containing 2.8 million B_s^0 mesons recorded at the $\Upsilon(5S)$ resonance with the Belle detector at KEKB, an electron-positron collider located in Tsukuba, Japan. We have obtained the first observation of a radiative penguin decay of the B_s^0 meson in the $B_s^0 \rightarrow \phi\gamma$ mode with a significance of 5.5 standard deviations, and we have measured

$$\mathcal{B}(B_s^0 \rightarrow \phi\gamma) = (57_{-15}^{+18}(\text{stat})_{-11}^{+12}(\text{syst})) \times 10^{-6}$$

in agreement with the Standard Model expectation [44, 45].

We have not observed any significant $B_s^0 \rightarrow \gamma\gamma$ signal and computed an upper limit at the 90% confidence level on its branching fraction of

$$\mathcal{B}(B_s^0 \rightarrow \gamma\gamma) < 8.7 \times 10^{-6}.$$

This limit is about six times more stringent than the previously published one [58]. It is only about one order of magnitude larger than the expectation from the Standard Model [55, 56, 57] leaving good hope for a Super B -factory [83, 84, 85] to observe this decay in the future. Its observation would provide an important test of the Standard Model [60, 61, 62].

We have studied the resonant $B^+ \rightarrow K^+h \rightarrow K^+\gamma\gamma$ decays, where the h particle can be a η , η' , η_c , $\eta_c(2S)$, χ_{c0} , χ_{c2} or a J/ψ meson, or the $X(3872)$ particle. We have searched for these decays in a 492 fb^{-1} sample containing about 535 millions $B\bar{B}$ pairs recorded at the $\Upsilon(4S)$ resonance.

We have observed the modes with $h = \eta$ and η' , and we have obtained an evidence of the mode with $h = \eta_c$. We have measured

$$\begin{aligned} \mathcal{B}(B^+ \rightarrow K^+\eta \rightarrow K^+\gamma\gamma) &= (0.87_{-0.15}^{+0.16}(\text{stat})_{-0.07}^{+0.10}(\text{syst})) \times 10^{-6}, \\ \mathcal{B}(B^+ \rightarrow K^+\eta' \rightarrow K^+\gamma\gamma) &= (1.40_{-0.15}^{+0.16}(\text{stat})_{-0.12}^{+0.15}(\text{syst})) \times 10^{-6}, \\ \mathcal{B}(B^+ \rightarrow K^+\eta_c \rightarrow K^+\gamma\gamma) &= (0.22_{-0.07}^{+0.09}(\text{stat})_{-0.02}^{+0.04}(\text{syst})) \times 10^{-6}, \end{aligned}$$

with significances of 7.3, 13.8 and 4.1, respectively. This is the first time that a $B^+ \rightarrow K^+\eta_c$ signal is seen in the $K\gamma\gamma$ final state. This evidence provides hope to test the Standard Model by measuring, at a future Super B -factory, the photon polarization of the $b \rightarrow s\gamma$ transition [70].

For the other $B^+ \rightarrow K^+h \rightarrow K^+\gamma\gamma$ modes, we have computed upper limits on their branching fractions. We have also measured or set limits at the 90% confidence level on the branching fractions of the $h \rightarrow \gamma\gamma$ decays, whenever $\mathcal{B}(B^+ \rightarrow K^+h)$ had been

measured elsewhere. We have set, for the first time, an upper limit on the branching fraction of the decay of the $X(3872)$ particle into two photons of

$$\mathcal{B}(X(3872) \rightarrow \gamma\gamma) < 1.1\% .$$

Appendix A

Continuum suppression figures for $B^+ \rightarrow K^+ h \rightarrow K^+ \gamma \gamma$

We present in this appendix continuum suppression figures for all $B^+ \rightarrow K^+ h \rightarrow K^+ \gamma \gamma$ modes, except those for $B^+ \rightarrow K^+ \eta$ which are shown in Figures 3.3 and 3.4 on pages 60 and 61.

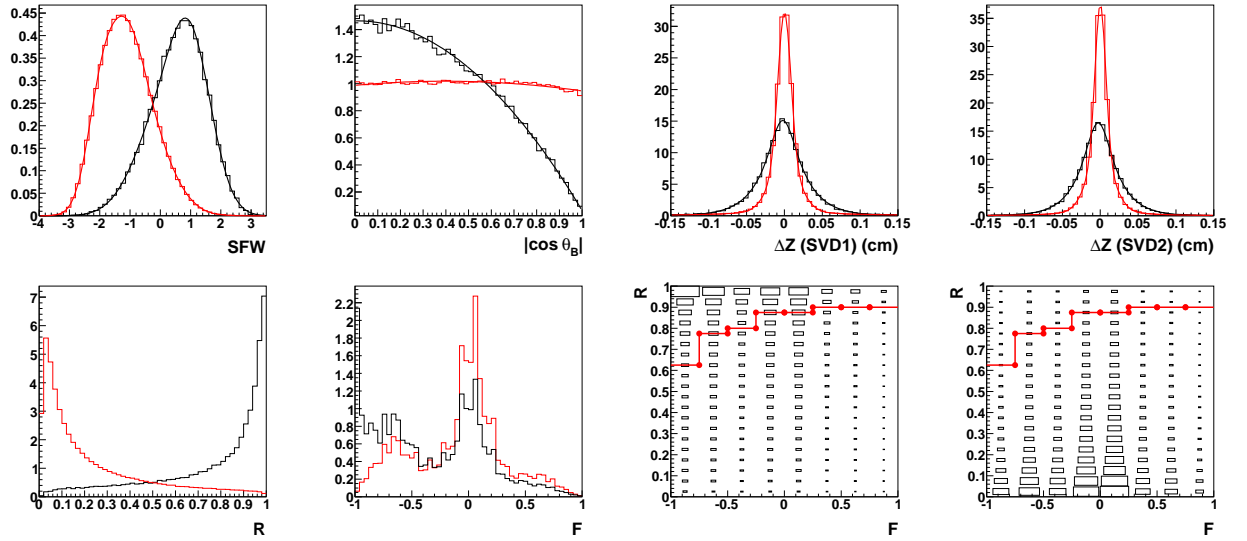


Figure A.1: MC distributions for the $B^+ \rightarrow K^+ \eta'$ mode. Top: SFW, $|\cos \theta_B^{\text{CM}}|$, Δz for SVD1 and Δz for SVD2 distributions for signal (black) and continuum (red). Bottom: \mathcal{R} , \mathcal{F} , and \mathcal{R} versus \mathcal{F} for signal and continuum.

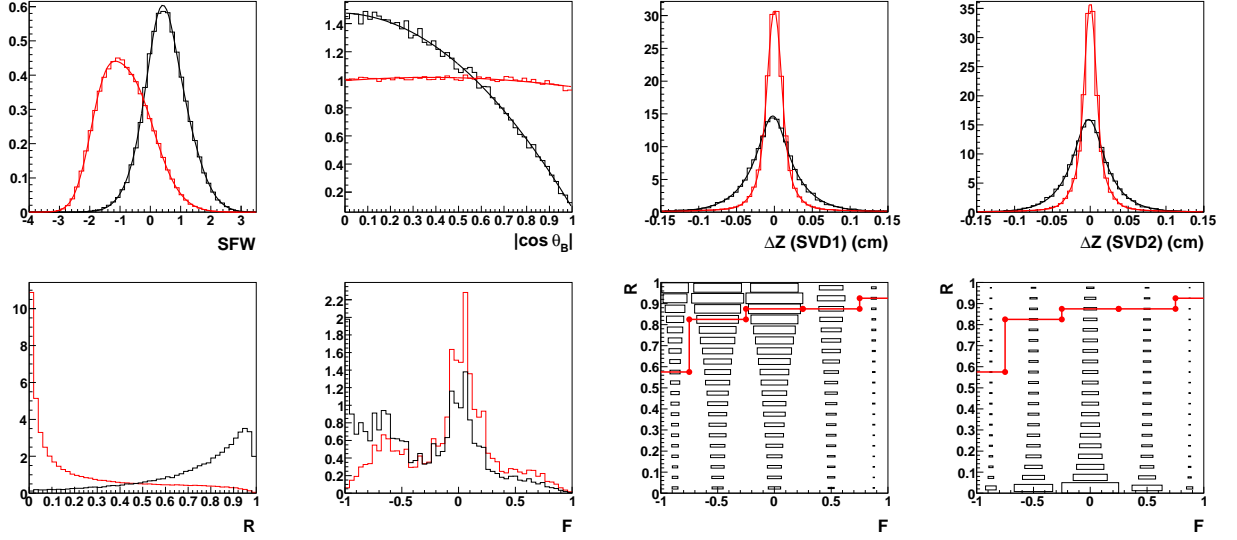


Figure A.2: MC distributions for the $B^+ \rightarrow K^+ \eta_c$ mode. Top: SFW, $|\cos \theta_B^{\text{CM}}|$, Δz for SVD1 and Δz for SVD2 distributions for signal (black) and continuum (red). Bottom: \mathcal{R} , \mathcal{F} , and \mathcal{R} versus \mathcal{F} for signal and continuum.

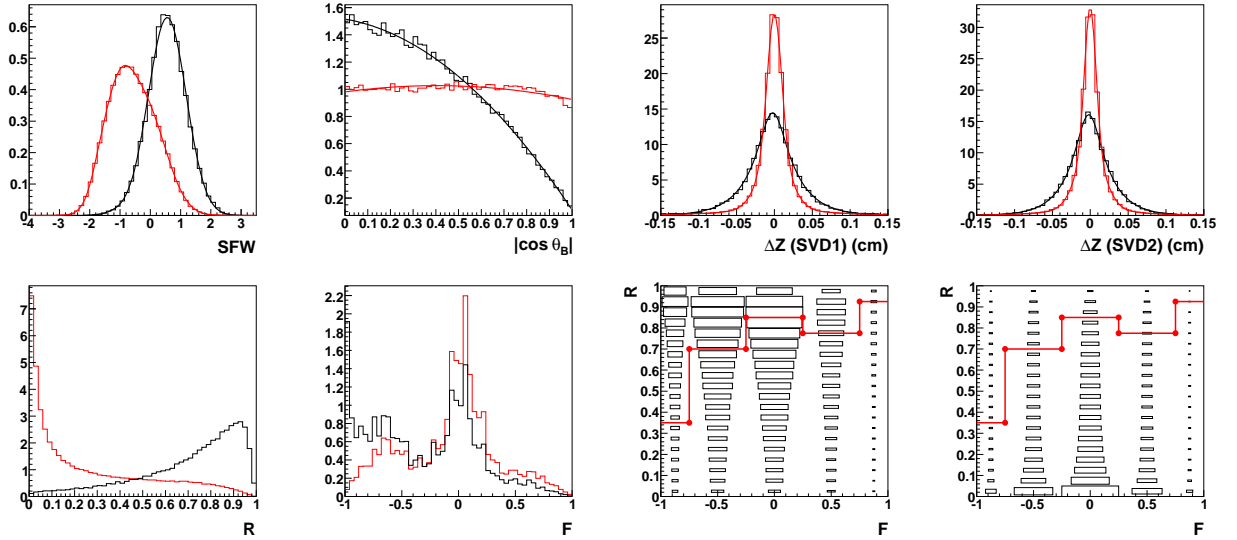


Figure A.3: MC distributions for the $B^+ \rightarrow K^+ \eta_c(2S)$ mode. Top: SFW, $|\cos \theta_B^{\text{CM}}|$, Δz for SVD1 and Δz for SVD2 distributions for signal (black) and continuum (red). Bottom: \mathcal{R} , \mathcal{F} , and \mathcal{R} versus \mathcal{F} for signal and continuum.

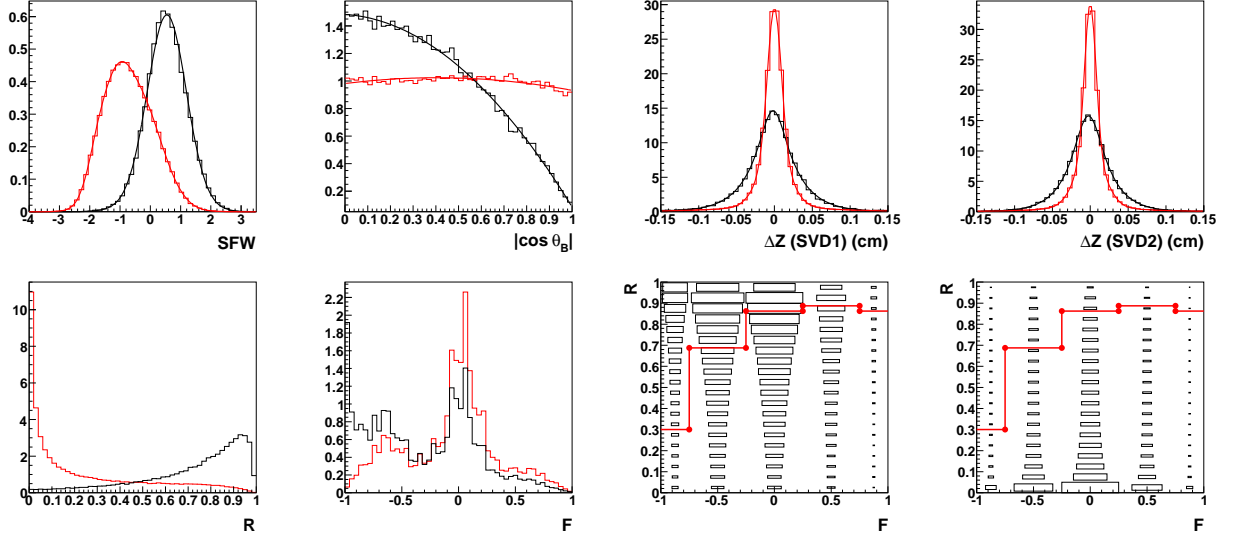


Figure A.4: MC distributions for the $B^+ \rightarrow K^+ \chi_{c0}$ mode. Top: SFW, $|\cos \theta_B^{\text{CM}}|$, Δz for SVD1 and Δz for SVD2 distributions for signal (black) and continuum (red). Bottom: \mathcal{R} , \mathcal{F} , and \mathcal{R} versus \mathcal{F} for signal and continuum.

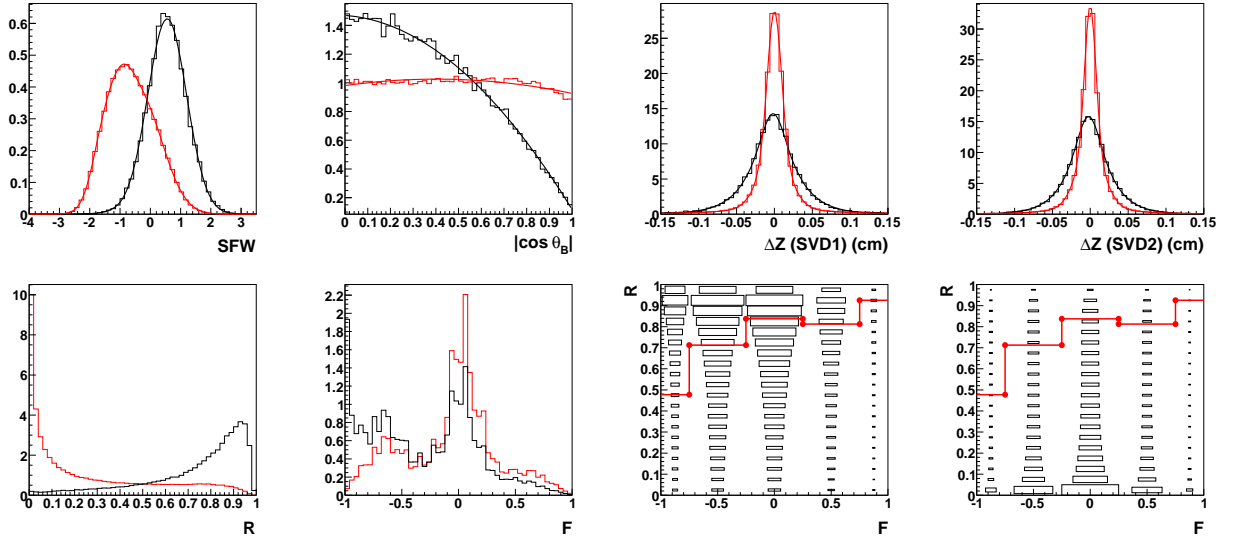


Figure A.5: MC distributions for the $B^+ \rightarrow K^+ \chi_{c2}$ mode. Top: SFW, $|\cos \theta_B^{\text{CM}}|$, Δz for SVD1 and Δz for SVD2 distributions for signal (black) and continuum (red). Bottom: \mathcal{R} , \mathcal{F} , and \mathcal{R} versus \mathcal{F} for signal and continuum.

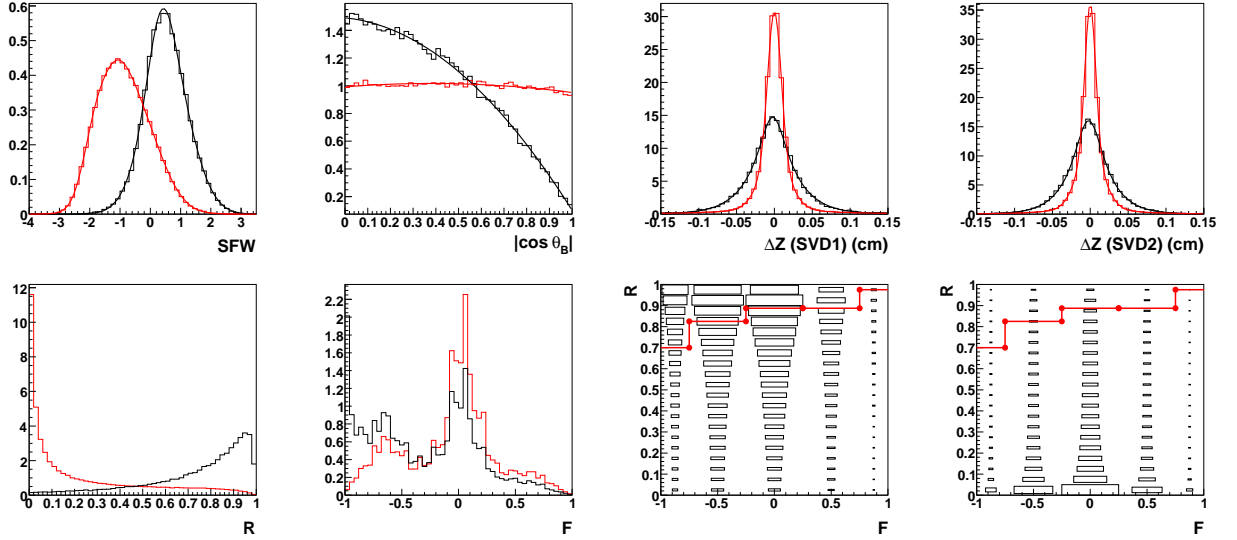


Figure A.6: MC distributions for the $B^+ \rightarrow K^+ J/\psi$ mode. Top: SFW, $|\cos \theta_B^{\text{CM}}|$, Δz for SVD1 and Δz for SVD2 distributions for signal (black) and continuum (red). Bottom: \mathcal{R} , \mathcal{F} , and \mathcal{R} versus \mathcal{F} for signal and continuum.

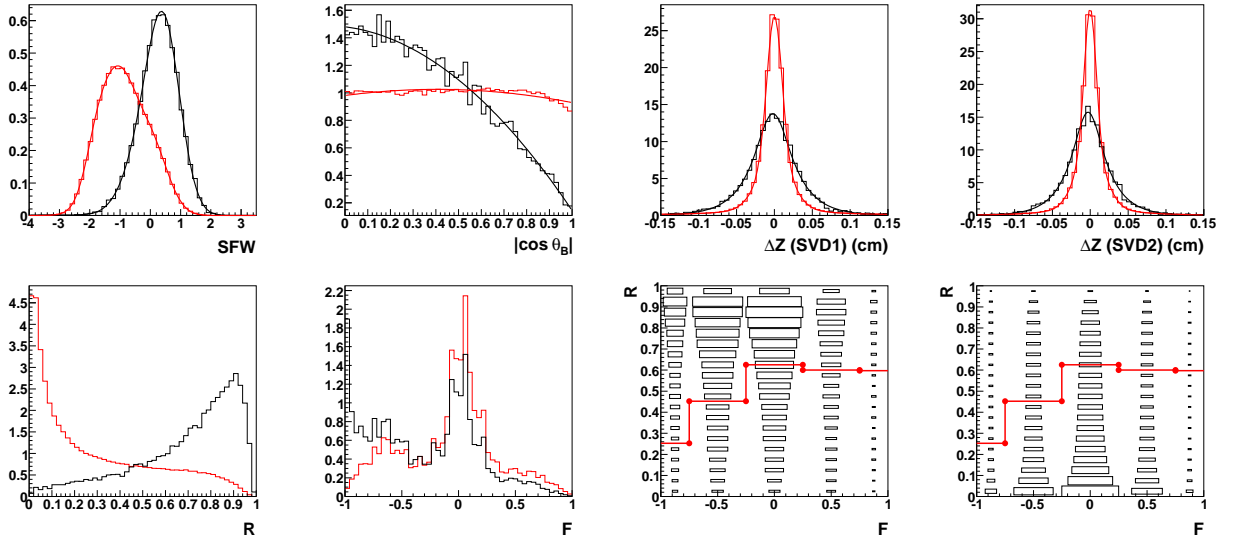


Figure A.7: MC distributions for the $B^+ \rightarrow K^+ X(3872)$ mode. Top: SFW, $|\cos \theta_B^{\text{CM}}|$, Δz for SVD1 and Δz for SVD2 distributions for signal (black) and continuum (red). Bottom: \mathcal{R} , \mathcal{F} , and \mathcal{R} versus \mathcal{F} for signal and continuum.

Appendix B

Fit Parameters for $B_s^0 \rightarrow \phi\gamma$ and $B_s^0 \rightarrow \gamma\gamma$

We give in this appendix parameters of the nominal fits described in Chapter 4. For the $B_s^0 \rightarrow \phi\gamma$ fit, floating (constant) parameters are listed in Table B.1 (Table B.2). For the $B_s^0 \rightarrow \gamma\gamma$ fit, floating (constant) parameters are listed in Table B.3 (Table B.4).

Table B.1: Floating parameters of the $B_s^0 \rightarrow \phi\gamma$ fit.

Parameter	Value
$\mathcal{B}(B_s^0 \rightarrow \phi\gamma)$	$(5.702_{-1.543}^{+1.786}) \times 10^{-5}$
deltae_udsc_a1	$-0.21436_{-0.1519}^{+0.1590}$
mbc_udsc_arguspar	$-16.9142_{-8.231}^{+8.417}$
$N_{\text{continuum}}$	$107.15_{-11.02}^{+11.85}$
$S_{B_s^0 \bar{B}_s^0}$	$-0.7049 \pm_{-1.605}^{+2.455}$
$S_{B_s^* \bar{B}_s^0}$	$0.539 \pm_{-1.869}^{+2.937}$

Table B.2: Constant parameters of the $B_s^0 \rightarrow \phi\gamma$ fit.

Parameter	Value
$\mathcal{B}(B_s^0 \rightarrow \phi\eta)$	$(0.00_{-0.00}^{+1.63}) \times 10^{-5}$
$\mathcal{B}(\eta \rightarrow \gamma\gamma)$	$(39.39 \pm 0.24)\%$
$\mathcal{B}(\phi \rightarrow K^+K^-)$	$(49.3 \pm 0.6)\%$
$\sigma_{bb}^{\Upsilon(5S)}$	$(0.302 \pm 0.015) \text{ nb}$
$E_{\text{beam}}^{\text{CM}}$	5.4346
$\epsilon_{B_s^0 \rightarrow \phi\gamma}$	$(24.7 \pm 0.2)\%$
$\epsilon_{B_s^0 \rightarrow \phi\eta}$	$(5.8 \pm 0.2)\%$
$f_{B_s^* \bar{B}_s^*}$	$(93_{-9}^{+7})\%$
f_s	$(19.5_{-2.3}^{+3.0})\%$
intlum_e43	$(1.857 \pm 0.026) \text{ fb}^{-1}$
intlum_e53	$(21.744 \pm 0.304) \text{ fb}^{-1}$
systemerror	1.000 ± 0.107

Table B.3: Floating parameters of the $B_s^0 \rightarrow \gamma\gamma$ fit.

Parameter	Value
$\mathcal{B}(B_s^0 \rightarrow \gamma\gamma)$	$(-1.72135_{-0.4486}^{+0.5345}) \times 10^{-5}$
deltae_udsc_a1	$-0.65611_{-0.1246}^{+0.1360}$
mbc_udsc_arguspar	$-21.4750_{-6.679}^{+6.772}$
$N_{\text{continuum}}$	$157.76_{-14.12}^{+14.99}$
$S_{B_s^0 \bar{B}_s^0}$	$-4.4830_{-2.675}^{+3.831}$
$S_{B_s^* \bar{B}_s^0}$	$-1.3665_{-3.565}^{+4.537}$

Table B.4: Constant parameters of the $B_s^0 \rightarrow \gamma\gamma$ fit.

Parameter	Value
$\sigma_{bb}^{\Upsilon(5S)}$	$(0.302 \pm 0.015) \text{ nb}$
$E_{\text{beam}}^{\text{CM}}$	5.4346
$\epsilon_{B_s^0 \rightarrow \gamma\gamma}$	$(17.8 \pm 0.2)\%$
$f_{B_s^* \bar{B}_s^*}$	$(93_{-9}^{+7})\%$
f_s	$(19.5_{-2.3}^{+3.0})\%$
intlum_e43	$(1.857 \pm 0.026) \text{ fb}^{-1}$
intlum_e53	$(21.744 \pm 0.304) \text{ fb}^{-1}$
systemerror	1.000 ± 0.109

Appendix C

Signal probability density functions for $B^+ \rightarrow K^+ h \rightarrow K^+ \gamma\gamma$

We present in this appendix the signal probability density functions for the $B^+ \rightarrow K^+ h \rightarrow K^+ \gamma\gamma$ modes, except those for $B^+ \rightarrow K^+ \eta$ which are shown in Figure 5.1 on page 86.

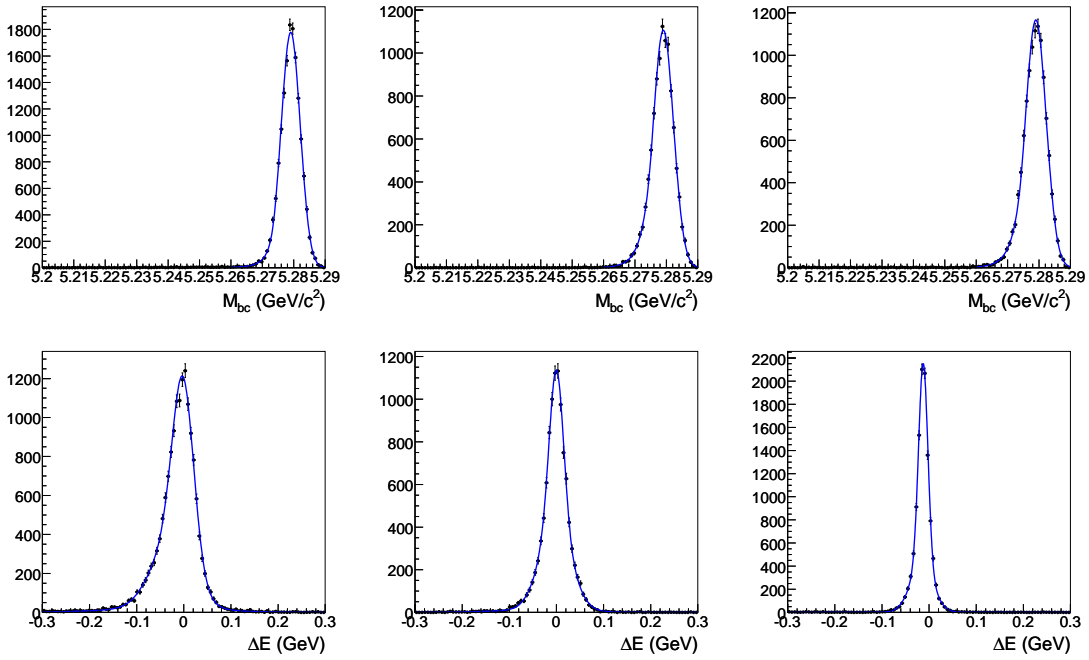


Figure C.1: M_{bc} and ΔE distributions for the $B^+ \rightarrow K^+ \eta'$ (first column), $B^+ \rightarrow K^+ \eta_c$ (second column) and $B^+ \rightarrow K^+ \eta_c(2S)$ (third column) signal MC together with the fit functions used as PDFs.

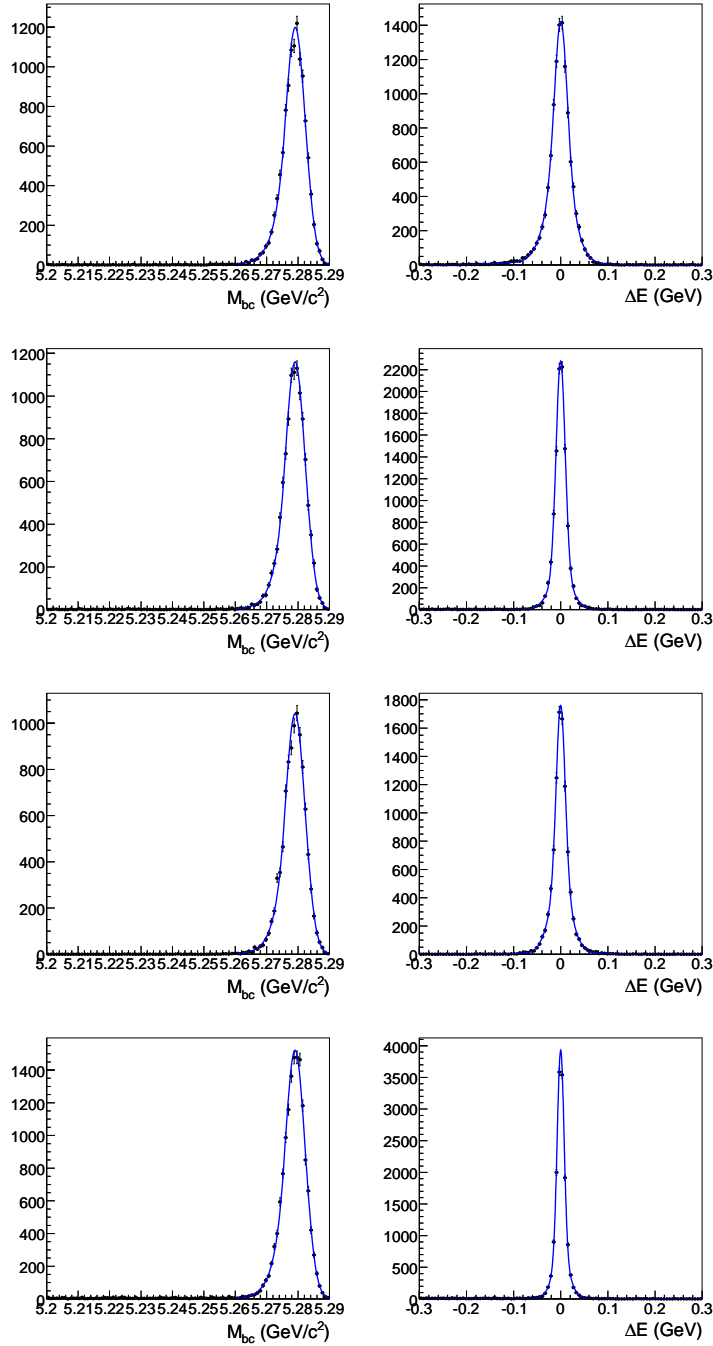


Figure C.2: M_{bc} and ΔE distributions for the $B^+ \rightarrow K^+ \chi_{c0}$ (first row), $B^+ \rightarrow K^+ \chi_{c2}$ (second row), $B^+ \rightarrow K^+ J/\psi$ (third row) and $B^+ \rightarrow K^+ X(3872)$ (fourth row) signal MC together with the fit functions used as PDFs.

Appendix D

Fit Parameters for

$$B^+ \rightarrow K^+ h \rightarrow K^+ \gamma \gamma$$

We give in this appendix parameters of the nominal fits described in Chapter 5. Table D.1 links to tables containing the fit parameters for all studied modes.

Table D.1: This table links to tables containing constant and floating parameters.

Mode	floating	constant
$B^+ \rightarrow K^+ \eta$	D.2	D.10
$B^+ \rightarrow K^+ \eta'$	D.3	D.11
$B^+ \rightarrow K^+ \eta_c$	D.4	D.12
$B^+ \rightarrow K^+ \eta_c(2S)$	D.5	D.13
$B^+ \rightarrow K^+ \chi_{c0}$	D.6	D.14
$B^+ \rightarrow K^+ \chi_{c2}$	D.7	D.15
$B^+ \rightarrow K^+ J/\psi$	D.8	D.16 and D.17
$B^+ \rightarrow K^+ X(3872)$	D.9	D.18

Table D.2: Floating parameters of the $B^+ \rightarrow K^+ \eta$ fit.

Parameter	Value
$\mathcal{B}(B^+ \rightarrow K^+ \eta \rightarrow K^+ \gamma \gamma)$	$(0.872_{-0.148}^{+0.157}) \times 10^{-6}$
$N_{\text{continuum}}^{e31to49}$	2565_{-52}^{+53}
$N_{\text{continuum}}^{e7to27}$	1022 ± 33
qq_deltae_p2_a0	$-0.175_{-0.030}^{+0.029}$
qq_mbc_argus_par	-14.4 ± 2.0

Table D.3: Floating parameters of the $B^+ \rightarrow K^+ \eta'$ fit.

Parameter	Value
$\mathcal{B}(B^+ \rightarrow K^+ \eta' \rightarrow K^+ \gamma \gamma)$	$(1.379_{-0.152}^{+0.161}) \times 10^{-6}$
$N_{\text{continuum}}^{e31to49}$	840 ± 31
$N_{\text{continuum}}^{e7to27}$	282_{-17}^{+18}
qq_deltae_p2_a0	$-0.303_{-0.052}^{+0.053}$
qq_mbc_argus_par	$-21.95_{-3.63}^{+3.65}$

Table D.4: Floating parameters of the $B^+ \rightarrow K^+ \eta_c$ fit.

Parameter	Value
$\mathcal{B}(B^+ \rightarrow K^+ \eta_c \rightarrow K^+ \gamma \gamma)$	$(0.235_{-0.073}^{+0.086}) \times 10^{-6}$
$N_{\text{continuum}}^{e31to37}$	$45.9_{-6.9}^{+7.6}$
$N_{\text{continuum}}^{e39to49}$	$95.2_{-10.0}^{+10.6}$
$N_{\text{continuum}}^{e7to27}$	$40.4_{-6.6}^{+7.4}$
qq_deltae_p2_a0	$-0.565_{-0.115}^{+0.126}$
qq_mbc_argus_par	$-3.55_{-9.67}^{+9.91}$

Table D.5: Floating parameters of the $B^+ \rightarrow K^+ \eta_c(2S)$ fit.

Parameter	Value
$\mathcal{B}(B^+ \rightarrow K^+ \eta_c(2S) \rightarrow K^+ \gamma \gamma)$	$(0.067_{-0.050}^{+0.064}) \times 10^{-6}$
$N_{\text{continuum}}^{e31to37}$	$76.6_{-9.3}^{+9.9}$
$N_{\text{continuum}}^{e39to49}$	$158.6_{-12.5}^{+13.2}$
$N_{\text{continuum}}^{e7to27}$	$86.1_{-9.9}^{+10.5}$
qq_deltae_p2_a0	$-0.578_{-0.083}^{+0.088}$
qq_mbc_argus_par	$-0.032_{-6.98}^{+7.08}$

Table D.6: Floating parameters of the $B^+ \rightarrow K^+ \chi_{c0}$ fit.

Parameter	Value
$\mathcal{B}(B^+ \rightarrow K^+ \chi_{c0} \rightarrow K^+ \gamma \gamma)$	$(0.012^{+0.041}_{-0.027}) \times 10^{-6}$
$N_{\text{continuum}}^{e31to37}$	$74.5^{+9.3}_{-8.7}$
$N_{\text{continuum}}^{e39to49}$	162 ± 13
$N_{\text{continuum}}^{e7to27}$	$76.1^{+9.4}_{-8.8}$
qq_deltae_p2_a0	$-0.581^{+0.083}_{-0.078}$
qq_mbc_argus_par	$1.95^{+6.85}_{-6.77}$

Table D.7: Floating parameters of the $B^+ \rightarrow K^+ \chi_{c2}$ fit.

Parameter	Value
$\mathcal{B}(B^+ \rightarrow K^+ \chi_{c2} \rightarrow K^+ \gamma \gamma)$	$(-0.005^{+0.044}_{-0.032}) \times 10^{-6}$
$N_{\text{continuum}}^{e31to37}$	$63.9^{+8.8}_{-8.2}$
$N_{\text{continuum}}^{e39to49}$	144 ± 12
$N_{\text{continuum}}^{e7to27}$	$69.8^{+9.4}_{-8.7}$
qq_deltae_p2_a0	$-0.550^{+0.094}_{-0.089}$
qq_mbc_argus_par	$-10.1^{+7.3}_{-7.2}$

Table D.8: Floating parameters of the $B^+ \rightarrow K^+ J/\psi$ fit.

Parameter	Value
$\mathcal{B}(B^+ \rightarrow K^+ J/\psi \rightarrow K^+ \gamma \gamma)$	$(0.065^{+0.053}_{-0.039}) \times 10^{-6}$
$N_{\text{continuum}}^{e31to37}$	$37.5^{+7.1}_{-6.5}$
$N_{\text{continuum}}^{e39to49}$	$72.7^{+9.2}_{-8.6}$
$N_{\text{continuum}}^{e7to27}$	$38.9^{+7.3}_{-6.6}$
qq_deltae_p2_a0_jpsi	$-0.398^{+0.150}_{-0.143}$
qq_mbc_argus_par_jpsi	$0.6^{+10.9}_{-10.6}$

Table D.9: Floating parameters of the $B^+ \rightarrow K^+ X(3872)$ fit.

Parameter	Value
$\mathcal{B}(B^+ \rightarrow K^+ X(3872) \rightarrow K^+ \gamma\gamma)$	$-0.012^{+0.028}_{-0.018} \times 10^{-6}$
$N_{\text{continuum}}^{e31to37}$	$160.9^{+14.6}_{-13.9}$
$N_{\text{continuum}}^{e39to49}$	396^{+21}_{-20}
$N_{\text{continuum}}^{e7to27}$	$161.4^{+14.8}_{-14.1}$
qq_deltae_p2_a0	$-0.500^{+0.063}_{-0.061}$
qq_mbc_argus_par	$-14.6^{+4.5}_{-4.4}$

Table D.10: Constant parameters of the $B^+ \rightarrow K^+ \eta$ fit.

Parameter	Value
$N_{B\bar{B}}^{e31to49}$	$(382.6 \pm 5.8) \times 10^6$
$N_{B\bar{B}}^{e7to27}$	$(152.0 \pm 1.2) \times 10^6$
$N_{B \rightarrow K^*(892)\eta}^{e31to49}$ bkg.	92.1 ± 1.3
$N_{B \rightarrow K^*(892)\eta}^{e7to27}$ bkg.	36.6 ± 0.5
$N_{\text{charmless B}}^{e31to49}$ bkg.	59.0 ± 1.1
$N_{\text{charmless B}}^{e7to27}$ bkg.	23.5 ± 0.4
$N_{B^+ \rightarrow \pi^+ \eta}^{e31to49}$ bkg.	9.3 ± 2.3
$N_{B^+ \rightarrow \pi^+ \eta}^{e7to27}$ bkg.	3.7 ± 0.9
qq_mbc_argus_m0	$5.29 \text{ GeV}/c^2$
sigcorr_deltae_g1_m	0.010 ± 0.002
sigcorr_deltae_g1_s	1.13 ± 0.06
sigcorr_mbc_m	0.0
sigcorr_mbc_s	0.84 ± 0.03
$\epsilon_{\text{corr.}}$	0.980 ± 0.002
$\epsilon(\text{SVD1})$	0.1598 ± 0.0008
$\epsilon(\text{SVD2})$	0.1689 ± 0.0008
sigmc_deltae_g1_f	0.704 ± 0.047
sigmc_deltae_g1_m	$(-0.0485 \pm 0.0052) \text{ GeV}$
sigmc_deltae_g1_s	$(0.0452 \pm 0.0030) \text{ GeV}$
sigmc_deltae_g2_f	0.400 ± 0.036
sigmc_deltae_g2_m	$(-0.0713 \pm 0.0045) \text{ GeV}$
sigmc_deltae_g2_s	$(0.1046 \pm 0.0062) \text{ GeV}$
sigmc_deltae_g3_m	$(-0.00197 \pm 0.00095) \text{ GeV}$
sigmc_deltae_g3_s	$(0.02771 \pm 0.00074) \text{ GeV}$
sigmc_mbc_cb_a	5.638
sigmc_mbc_cb_m	$5.27910 \pm 0.00003 \text{ GeV}/c^2$
sigmc_mbc_cb_n	1.5594
sigmc_mbc_cb_s	$0.00313 \pm 0.00002 \text{ GeV}/c^2$
systemerror	1.00000 ± 0.09430

Table D.11: Constant parameters of the $B^+ \rightarrow K^+ \eta'$ fit.

Parameter	Value
$N_{BB}^{e31to49}$	$(382.6 \pm 5.9) \times 10^6$
N_{BB}^{e7to27}	$(152.0 \pm 1.2) \times 10^6$
$N_{\text{charmless B bkg.}}^{e31to49}$	91.3 ± 1.3
$N_{\text{charmless B bkg.}}^{e7to27}$	36.3 ± 0.5
qq_mbc_argus_m0	$5.29 \text{ GeV}/c^2$
sigcorr_deltae_g1_m	0.010 ± 0.002
sigcorr_deltae_g1_s	1.13 ± 0.06
sigcorr_mbc_m	0.0
sigcorr_mbc_s	0.84 ± 0.03
$\epsilon_{\text{corr.}}$	0.9832 ± 0.0015
$\epsilon(\text{SVD1})$	0.14868 ± 0.00079
$\epsilon(\text{SVD2})$	0.15990 ± 0.00082
sigmc_deltae_g1_f	0.865 ± 0.018
sigmc_deltae_g1_m	$(-0.0265 \pm 0.0017) \text{ GeV}$
sigmc_deltae_g1_s	$(0.0427 \pm 0.0013) \text{ GeV}$
sigmc_deltae_g2_f	0.448 ± 0.028
sigmc_deltae_g2_m	$(-0.0478 \pm 0.0056) \text{ GeV}$
sigmc_deltae_g2_s	$(0.1175 \pm 0.0073) \text{ GeV}$
sigmc_deltae_g3_m	$(-0.00143 \pm 0.00059) \text{ GeV}$
sigmc_deltae_g3_s	$(0.02242 \pm 0.00058) \text{ GeV}$
sigmc_mbc_cb_a	4.697
sigmc_mbc_cb_m	$5.27900 \pm 0.00003 \text{ GeV}/c^2$
sigmc_mbc_cb_n	1.765
sigmc_mbc_cb_s	$0.003026 \pm 0.000024 \text{ GeV}/c^2$
systemerror	1.000 ± 0.094

Table D.12: Constant parameters of the $B^+ \rightarrow K^+ \eta_c$ fit.

Parameter	Value
$N_{BB}^{e31to37}$	$(124.7 \pm 1.9) \times 10^6$
$N_{BB}^{e39to49}$	$(258.0 \pm 3.4) \times 10^6$
N_{BB}^{e7to27}	$(152.0 \pm 1.2) \times 10^6$
$N_{B \rightarrow K^*(892)\eta_c}^{e31to37}$ bkg.	3.2 ± 0.8
$N_{B \rightarrow K^*(892)\eta_c}^{e39to49}$ bkg.	6.7 ± 1.6
$N_{B \rightarrow K^*(892)\eta_c}^{e7to27}$ bkg.	3.9 ± 1.0
$N_{\text{off-time 1}}^{e31to37}$	1.9 ± 1.0
$N_{\text{off-time 1}}^{e39to49}$	0.0
$N_{\text{off-time 1}}^{e7to27}$	2.4 ± 1.2
$N_{\text{off-time 2}}^{e31to37}$	1.0 ± 0.7
$N_{\text{off-time 2}}^{e39to49}$	0.0
$N_{\text{off-time 2}}^{e7to27}$	1.2 ± 0.8
$N_{\text{charmless B bkg.}}^{e31to37}$	2.0 ± 0.1
$N_{\text{charmless B bkg.}}^{e39to49}$	4.1 ± 0.2
$N_{\text{charmless B bkg.}}^{e7to27}$	2.4 ± 0.1
qq_mbc_argus_m0	5.29 GeV/ c^2
sigcorr_deltae_g1_m	0.009 ± 0.003
sigcorr_deltae_g1_s	1.14 ± 0.08
sigcorr_mbc_m	0.0
sigcorr_mbc_s	0.82 ± 0.03
$\epsilon_{\text{corr.}}$	0.9944 ± 0.0015
$\epsilon(\text{SVD1})$	0.09991 ± 0.00067
$\epsilon(\text{SVD2})$	0.10915 ± 0.00070
sigmc_deltae_g1_f	0.915 ± 0.018
sigmc_deltae_g1_m	(0.00007 ± 0.00041) GeV
sigmc_deltae_g1_s	(0.01499 ± 0.00070) GeV
sigmc_deltae_g2_f	0.477 ± 0.037
sigmc_deltae_g2_m	(-0.0400 ± 0.0063) GeV
sigmc_deltae_g2_s	(0.0903 ± 0.0058) GeV
sigmc_deltae_g3_m	(-0.00238 ± 0.00071) GeV
sigmc_deltae_g3_s	(0.0327 ± 0.0011) GeV
sigmc_mbc_cb_a	99.97
sigmc_mbc_cb_m	5.27900 ± 0.00004 GeV/ c^2
sigmc_mbc_cb_n	1.1954
sigmc_mbc_cb_s	0.003229 ± 0.000036 GeV/ c^2
systemerror	1.000 ± 0.094

Table D.13: Constant parameters of the $B^+ \rightarrow K^+ \eta_c(2S)$ fit.

Parameter	Value
$N_{BB}^{e31to37}$	$(124.7 \pm 1.9) \times 10^6$
$N_{BB}^{e39to49}$	$(258.0 \pm 3.4) \times 10^6$
N_{BB}^{e7to27}	$(152.0 \pm 1.2) \times 10^6$
$N_{\text{off-time 1}}^{e31to37}$	0.5 ± 0.5
$N_{\text{off-time 1}}^{e39to49}$	0.0
$N_{\text{off-time 1}}^{e7to27}$	0.6 ± 0.6
$N_{\text{off-time 2}}^{e31to37}$	11.1 ± 2.3
$N_{\text{off-time 2}}^{e39to49}$	0.0
$N_{\text{off-time 2}}^{e7to27}$	13.5 ± 2.8
$N_{\text{charmless B bkg.}}^{e31to37}$	3.0 ± 0.1
$N_{\text{charmless B bkg.}}^{e39to49}$	6.2 ± 0.3
$N_{\text{charmless B bkg.}}^{e7to27}$	3.6 ± 0.2
qq_mbc_argus_m0	5.29 GeV/ c^2
sigcorr_deltae_g1_m	0.013 ± 0.004
sigcorr_deltae_g1_s	1.13 ± 0.12
sigcorr_mbc_m	0.0
sigcorr_mbc_s	0.84 ± 0.06
$\epsilon_{\text{corr.}}$	0.9870 ± 0.0015
$\epsilon(\text{SVD1})$	0.1100 ± 0.0007
$\epsilon(\text{SVD2})$	0.1159 ± 0.0007
sigmc_deltae_g1_f	0.9698 ± 0.0046
sigmc_deltae_g1_m	(-0.0158 ± 0.0005) GeV
sigmc_deltae_g1_s	(0.0237 ± 0.0007) GeV
sigmc_deltae_g2_f	0.365 ± 0.02
sigmc_deltae_g2_m	(-0.027 ± 0.014) GeV
sigmc_deltae_g2_s	(0.137 ± 0.018) GeV
sigmc_deltae_g3_m	(-0.0123 ± 0.0002) GeV
sigmc_deltae_g3_s	(0.00981 ± 0.00026) GeV
sigmc_mbc_cb_a	18.06
sigmc_mbc_cb_m	5.27900 ± 0.00005 GeV/ c^2
sigmc_mbc_cb_n	1.259
sigmc_mbc_cb_s	0.003297 ± 0.000038 GeV/ c^2
systemerror	1.000 ± 0.094

Table D.14: Constant parameters of the $B^+ \rightarrow K^+ \chi_{c0}$ fit.

Parameter	Value
$N_{BB}^{e31to37}$	$(124.7 \pm 1.9) \times 10^6$
$N_{BB}^{e39to49}$	$(258.0 \pm 3.4) \times 10^6$
N_{BB}^{e7to27}	$(152.0 \pm 1.2) \times 10^6$
$N_{\text{off-time 1}}^{e31to37}$	1.9 ± 1.0
$N_{\text{off-time 1}}^{e39to49}$	0.0
$N_{\text{off-time 1}}^{e7to27}$	2.4 ± 1.2
$N_{\text{off-time 2}}^{e31to37}$	1.4 ± 0.8
$N_{\text{off-time 2}}^{e39to49}$	0.0
$N_{\text{off-time 2}}^{e7to27}$	1.78 ± 1.02
$N_{\text{charmless B bkg.}}^{e31to37}$	2.5 ± 0.1
$N_{\text{charmless B bkg.}}^{e39to49}$	5.2 ± 0.3
$N_{\text{charmless B bkg.}}^{e7to27}$	3.1 ± 0.2
qq_mbc_argus_m0	$5.29 \text{ GeV}/c^2$
sigcorr_deltae_g1_m	0.008 ± 0.004
sigcorr_deltae_g1_s	1.08 ± 0.10
sigcorr_mbc_m	0.0
sigcorr_mbc_s	0.87 ± 0.06
$\epsilon_{\text{corr.}}$	0.9897 ± 0.0015
$\epsilon(\text{SVD1})$	0.11134 ± 0.00070
$\epsilon(\text{SVD2})$	0.11714 ± 0.00072
sigmc_deltae_g1_f	0.894 ± 0.021
sigmc_deltae_g1_m	$(0.00034 \pm 0.00035) \text{ GeV}$
sigmc_deltae_g1_s	$(0.01332 \pm 0.00070) \text{ GeV}$
sigmc_deltae_g2_f	0.515 ± 0.045
sigmc_deltae_g2_m	$(-0.0405 \pm 0.0046) \text{ GeV}$
sigmc_deltae_g2_s	$(0.0804 \pm 0.0041) \text{ GeV}$
sigmc_deltae_g3_m	$(-0.0020 \pm 0.0008) \text{ GeV}$
sigmc_deltae_g3_s	$(0.0287 \pm 0.0013) \text{ GeV}$
sigmc_mbc_cb_a	100.0
sigmc_mbc_cb_m	$5.27910 \pm 0.00005 \text{ GeV}/c^2$
sigmc_mbc_cb_n	1.0841
sigmc_mbc_cb_s	$0.003189 \pm 0.000037 \text{ GeV}/c^2$

Table D.15: Constant parameters of the $B^+ \rightarrow K^+ \chi_{c2}$ fit.

Parameter	Value
$N_{BB}^{e31to37}$	$(124.7 \pm 1.9) \times 10^6$
$N_{BB}^{e39to49}$	$(258.0 \pm 3.4) \times 10^6$
N_{BB}^{e7to27}	$(152.0 \pm 1.2) \times 10^6$
$N_{\text{off-time 1}}^{e31to37}$	1.0 ± 0.7
$N_{\text{off-time 1}}^{e39to49}$	0.0
$N_{\text{off-time 1}}^{e7to27}$	1.2 ± 0.8
$N_{\text{off-time 2}}^{e31to37}$	4.8 ± 1.5
$N_{\text{off-time 2}}^{e39to49}$	0.0
$N_{\text{off-time 2}}^{e7to27}$	5.9 ± 1.9
$N_{\text{charmless B bkg.}}^{e31to37}$	2.3 ± 0.1
$N_{\text{charmless B bkg.}}^{e39to49}$	4.9 ± 0.3
$N_{\text{charmless B bkg.}}^{e7to27}$	2.9 ± 0.1
qq_mbc_argus_m0	5.29 GeV/ c^2
sigcorr_deltae_g1_m	0.012 ± 0.004
sigcorr_deltae_g1_s	1.10 ± 0.12
sigcorr_mbc_m	0.0
sigcorr_mbc_s	0.83 ± 0.06
$\epsilon_{\text{corr.}}$	0.9874 ± 0.0015
$\epsilon(\text{SVD1})$	0.10562 ± 0.00069
$\epsilon(\text{SVD2})$	0.11418 ± 0.00071
sigmc_deltae_g1_f	0.9862 ± 0.0025
sigmc_deltae_g1_m	(-0.00027 ± 0.00015) GeV
sigmc_deltae_g1_s	(0.00960 ± 0.00023) GeV
sigmc_deltae_g2_f	0.731 ± 0.024
sigmc_deltae_g2_m	(-0.033 ± 0.018) GeV
sigmc_deltae_g2_s	(0.144 ± 0.020) GeV
sigmc_deltae_g3_m	(-0.00063 ± 0.00053) GeV
sigmc_deltae_g3_s	(0.02328 ± 0.00086) GeV
sigmc_mbc_cb_a	100.0
sigmc_mbc_cb_m	5.279000 ± 0.000044 GeV/ c^2
sigmc_mbc_cb_n	1.152
sigmc_mbc_cb_s	0.003201 ± 0.000036 GeV/ c^2
systemerror	1.000 ± 0.094

Table D.16: Constant parameters of the $B^+ \rightarrow K^+ J/\psi$ fit. See also Table D.17 for more parameters.

Parameter	Value
$\mathcal{B}(B^+ \rightarrow K^+ \eta_c \rightarrow K^+ \gamma \gamma)$	$(0.22 \pm 0.09) \times 10^{-6}$
$\epsilon(\text{SVD1})_{B^+ \rightarrow K^+ \eta_c}$	0.0669 ± 0.0012
$\epsilon(\text{SVD2})_{B^+ \rightarrow K^+ \eta_c}$	0.0755
$N_{B\bar{B}}^{e31to37}$	$(124.7 \pm 1.9) \times 10^6$
$N_{B\bar{B}}^{e39to49}$	$(258.0 \pm 3.4) \times 10^6$
$N_{B\bar{B}}^{e7to27}$	$(152.0 \pm 1.2) \times 10^6$
$N_{\text{off-time 1}}^{e31to37}$	4.4 ± 1.5
$N_{\text{off-time 1}}^{e39to49}$	0.0
$N_{\text{off-time 1}}^{e7to27}$	5.3 ± 1.8
$N_{\text{off-time 2}}^{e31to37}$	1.0 ± 0.7
$N_{\text{off-time 2}}^{e39to49}$	0.0
$N_{\text{off-time 2}}^{e7to27}$	1.2 ± 0.8
$N_{\text{charmless B bkg.}}^{e31to37}$	1.9 ± 0.1
$N_{\text{charmless B bkg.}}^{e39to49}$	3.8 ± 0.2
$N_{\text{charmless B bkg.}}^{e7to27}$	2.3 ± 0.1
qq_mbc_argus_m0_jpsi	5.29 GeV/ c^2

Table D.17: Constant parameters of the $B^+ \rightarrow K^+ J/\psi$ fit. See also Table D.16 for more parameters.

Parameter	Value
sigcorr_deltae_g1_m_jpsi	0.010 ± 0.003
sigcorr_deltae_g1_s_jpsi	1.12 ± 0.08
sigcorr_mbc_m_jpsi	0.0
sigcorr_mbc_s_jpsi	0.88 ± 0.06
sigeff_corr_jpsi	0.9917 ± 0.0015
$\epsilon(\text{SVD1})_{B^+ \rightarrow K^+ J/\psi}$	0.09434 ± 0.00065
$\epsilon(\text{SVD2})_{B^+ \rightarrow K^+ J/\psi}$	0.10044 ± 0.00067
sigmc_deltae_g1_f_jpsi	0.546 ± 0.041
sigmc_deltae_g1_m_jpsi	(-0.00011 ± 0.00022) GeV
sigmc_deltae_g1_s_jpsi	(0.00943 ± 0.00044) GeV
sigmc_deltae_g2_f_jpsi	0.9551 ± 0.0094
sigmc_deltae_g2_m_jpsi	(-0.001020 ± 0.00046) GeV
sigmc_deltae_g2_s_jpsi	(0.0223 ± 0.0012) GeV
sigmc_deltae_g3_m_jpsi	(0.0045 ± 0.0036) GeV
sigmc_deltae_g3_s_jpsi	(0.0627 ± 0.0044) GeV
sigmc_etac_jpsi_deltae_g1_f	0.84 ± 0.01
sigmc_etac_jpsi_deltae_g1_m	(0.1266 ± 0.001) GeV
sigmc_etac_jpsi_deltae_g1_s	(0.0466 ± 0.001) GeV
sigmc_etac_jpsi_deltae_g2_f	0.4904 ± 0.022
sigmc_etac_jpsi_deltae_g2_m	(0.0859 ± 0.005) GeV
sigmc_etac_jpsi_deltae_g2_s	(0.1309 ± 0.004) GeV
sigmc_etac_jpsi_deltae_g3_m	0.1318 GeV
sigmc_etac_jpsi_deltae_g3_s	0.0197 GeV
sigmc_etac_jpsi_mbc_cb_a	4.3964
sigmc_etac_jpsi_mbc_cb_m	$5.2785 \text{ GeV}/c^2$
sigmc_etac_jpsi_mbc_cb_n	1.2006
sigmc_etac_jpsi_mbc_cb_s	$0.0039 \text{ GeV}/c^2$
sigmc_mbc_cb_a_jpsi	99.999
sigmc_mbc_cb_m_jpsi	$5.27900 \pm 0.00004 \text{ GeV}/c^2$
sigmc_mbc_cb_n_jpsi	1.1582
sigmc_mbc_cb_s_jpsi	$0.003180 \pm 0.000036 \text{ GeV}/c^2$
systemerror	1.000 ± 0.092

Table D.18: Constant parameters of the $B^+ \rightarrow K^+ X(3872)$ fit.

Parameter	Value
$N_{BB}^{e31to37}$	$(124.7 \pm 1.9) \times 10^6$
$N_{BB}^{e39to49}$	$(258.0 \pm 3.4) \times 10^6$
N_{BB}^{e7to27}	$(152.0 \pm 1.1) \times 10^6$
$N_{\text{off-time 1}}^{e31to37}$	3.9 ± 1.4
$N_{\text{off-time 1}}^{e39to49}$	0.0
$N_{\text{off-time 1}}^{e7to27}$	4.7 ± 1.7
$N_{\text{off-time 2}}^{e31to37}$	49.3 ± 4.9
$N_{\text{off-time 2}}^{e39to49}$	0.0
$N_{\text{off-time 2}}^{e7to27}$	60.1 ± 6.0
$N_{\text{charmless B bkg.}}^{e31to37}$	5.4 ± 0.2
$N_{\text{charmless B bkg.}}^{e39to49}$	11.2 ± 0.4
$N_{\text{charmless B bkg.}}^{e7to27}$	6.6 ± 0.2
qq_mbc_argus_m0	$5.29 \text{ GeV}/c^2$
sigcorr_deltae_g1_m	0.011 ± 0.006
sigcorr_deltae_g1_s	1.16 ± 0.16
sigcorr_mbc_m	0.0
sigcorr_mbc_s	0.82 ± 0.09
$\epsilon_{\text{corr.}}$	0.9694 ± 0.0015
$\epsilon(\text{SVD1})$	0.1410 ± 0.0008
$\epsilon(\text{SVD2})$	0.1547 ± 0.0008
sigmc_deltae_g1_f	0.9724 ± 0.0029
sigmc_deltae_g1_m	$(-0.00022 \pm 0.00010) \text{ GeV}$
sigmc_deltae_g1_s	$(0.00722 \pm 0.00017) \text{ GeV}$
sigmc_deltae_g2_f	0.688 ± 0.024
sigmc_deltae_g2_m	$(-0.0427 \pm 0.0097) \text{ GeV}$
sigmc_deltae_g2_s	$(0.1300 \pm 0.0094) \text{ GeV}$
sigmc_deltae_g3_m	$(0.0004 \pm 0.0003) \text{ GeV}$
sigmc_deltae_g3_s	$(0.01714 \pm 0.00056) \text{ GeV}$
sigmc_mbc_cb_a	100.0
sigmc_mbc_cb_m	$5.2790 \pm 0.00004 \text{ GeV}/c^2$
sigmc_mbc_cb_n	1.1396
sigmc_mbc_cb_s	$0.003224 \pm 0.000032 \text{ GeV}/c^2$
systemerror	1.000 ± 0.094

Bibliography

- [1] A. PICH. The Standard Model of Electroweak Interactions. *arXiv:0705.4264*, 2007.
- [2] Particle Data Group, W.-M. YAO ET AL. Review of particle physics. *J. Phys. G*, 33:1, 2006, and 2007 partial update for the 2008 edition. See also <http://pdglive.lbl.gov>.
- [3] Tevatron Electroweak Working Group. A Combination of CDF and DØ Results on the Mass of the Top Quark. *arXiv:hep-ex/0703034*, 2007.
- [4] A. GOOBAR, S. HANNESTAD, E. MÖRTSELL, AND H. TU. The neutrino mass bound from WMAP 3 year data, the baryon acoustic peak, the SNLS supernovae and the Lyman- α forest. *J. Cosm. Astrophys. Phys.*, 0606:019, 2006.
- [5] The ALEPH, DELPHI, L3, OPAL, SLD Collaborations, the LEP Electroweak Working Group, the SLD Electroweak and Heavy Flavour Groups. Precision Electroweak Measurements on the Z Resonance. *Phys. Rept.*, 427:257, 2006.
- [6] The ALEPH, DELPHI, L3, OPAL, SLD Collaborations, the LEP Electroweak Working Group, the SLD Electroweak and Heavy Flavour Groups. Precision Electroweak Measurements on the Z Resonance. *arXiv:hep-ex/0612034*, 2007, see also <http://lepewwg.web.cern.ch/LEPEWWG/>.
- [7] C.S. WU ET AL. Experimental Test of Parity Conservation in Beta Decay. *Phys. Rev.*, 105:1413, 1957.
- [8] J.H. CHRISTENSON, J.W. CRONIN, V.L. FITCH, AND R. TURLAY. Evidence for the 2π Decay of the K_2^0 Meson. *Phys. Rev. Lett.*, 13:138, 1964.
- [9] Belle Collaboration, K. ABE ET AL. Observation of Large CP Violation in the Neutral B Meson System. *Phys. Rev. Lett.*, 87:091802, 2001.
- [10] BABAR Collaboration, B. AUBERT ET AL. Observation of CP Violation in the B^0 Meson System. *Phys. Rev. Lett.*, 87:091801, 2001.
- [11] A.D. SAKHAROV. Violation of CP invariance, C asymmetry, and baryon asymmetry of the Universe. *J. Exp. Theor. Phys. Lett.*, 5:24, 1967.
- [12] G. LÜDERS. Proof of the TCP theorem. *Ann. Phys.*, 2:1, 1957.

- [13] S.L. GLASHOW, J. ILIOPOULOS, AND L. MAIANI. Weak Interactions with Lepton-Hadron Symmetry. *Phys. Rev. D*, 2:1285, 1970.
- [14] N. CABIBBO. Unitary Symmetry and Leptonic Decays. *Phys. Rev. Lett.*, 10:531, 1963.
- [15] M. KOBAYASHI AND T. MASKAWA. CP -Violation in the Renormalizable Theory of Weak Interaction. *Prog. Theor. Phys.*, 49:652, 1973.
- [16] L. WOLFENSTEIN. Parametrization of the Kobayashi-Maskawa Matrix. *Phys. Rev. Lett.*, 51:1945, 1983.
- [17] A.J. BURAS, M. E. LAUTENBACHER, AND G. OSTERMAIER. Waiting for the Top Quark Mass, $K^+ \rightarrow \pi^+ \nu \bar{\nu}$, $B_s^0 - \bar{B}_s^0$ Mixing and CP Asymmetries in B -Decays. *Phys. Rev. D*, 50:3433, 1994.
- [18] C. JARLSKOG. Commutator of the Quark Mass Matrices in the Standard Electroweak Model and a Measure of Maximal CP Nonconservation. *Phys. Rev. Lett.*, 55:1039, 1985.
- [19] CKMfitter Group, J. CHARLES ET AL. CP Violation and the CKM Matrix: Assessing the Impact of the Asymmetric B Factories. *Eur. Phys. J. C*, 41:1, 2005, updated results and plots available at <http://ckmfitter.in2p3.fr>.
- [20] UTfit Collaboration, M. BONA ET AL. Model-independent constraints on $\Delta F = 2$ operators and the scale of New Physics. *arXiv:0707.0636*, 2007, see also <http://www.utfit.org>.
- [21] CDF Collaboration, A. ABULENCIA ET AL. Observation of $B_s^0 - \bar{B}_s^0$ Oscillations. *Phys. Rev. Lett.*, 97:242003, 2006.
- [22] A.B. CARTER AND A.I. SANDA. CP Nonconservation in Cascade Decays of B Mesons. *Phys. Rev. Lett.*, 45:952, 1980.
- [23] A.B. CARTER AND A.I. SANDA. CP violation in B -meson decays. *Phys. Rev. D*, 23:1567, 1981.
- [24] I.I. BIGI AND A.I. SANDA. Notes on the observability of CP violations in B decays. *Nucl. Phys. B*, 193:85, 1981.
- [25] Belle Collaboration, A. POLUEKTOV ET AL. Measurement of ϕ_3 with Dalitz Plot Analysis of $B \rightarrow D^{(*)}K$ Decay. *Phys. Rev. D*, 70:072003, 2004.
- [26] A. GIRI, Y. GROSSMAN, A. SOFFER, AND J. ZUPAN. Determining γ using $B^\pm \rightarrow DK^\pm$ with multibody D decays. *Phys. Rev. Lett.*, 68:054018, 2003.
- [27] D. ATWOOD, I. DUNIETZ, AND A. SONI. Improved methods for observing CP violation in $B^\pm \rightarrow KD$ and measuring the CKM phase γ . *Phys. Rev. D*, 63:036005, 2001, and cited articles from the same authors.
- [28] M. GRONAU. Improving bounds on γ in $B^\pm \rightarrow DK^\pm$ and $B^{\pm,0} \rightarrow DX_s^{\pm,0}$. *Phys. Lett. B*, 557:198, 2003, and cited articles from the same author.

- [29] R. DAVIS, D.S. HARMER, AND K.C. HOFFMAN. Search for Neutrinos from the Sun. *Phys. Rev. Lett.*, 20:1205, 1968.
- [30] Super-Kamiokande Collaboration, Y. FUKUDA ET AL. Evidence for Oscillation of Atmospheric Neutrinos. *Phys. Rev. Lett.*, 81:1562, 1998.
- [31] SNO Collaboration, Q.R. AHMAD ET AL. Direct Evidence for Neutrino Flavor Transformation from Neutral-Current Interactions in the Sudbury Neutrino Observatory. *Phys. Rev. Lett.*, 89:011301, 2002.
- [32] J.R. BROWNSTEIN AND J.W. MOFFAT. Galaxy Rotation Curves Without Non-Baryonic Dark Matter. *Astrophys. J.*, 636:721, 2006.
- [33] D. CLOWE, M. BRADAC, A.H. GONZALEZ, M. MARKEVITCH, S.W. RANDALL, C. JONES, AND D. ZARITSKY. A direct empirical proof of the existence of dark matter. *Astrophys. J.*, 648:L109, 2006.
- [34] WMAP Collaboration, D.N. SPERGEL ET AL. Wilkinson Microwave Anisotropy Probe (WMAP) three year results: implications for cosmology. *Astrophys. J. Suppl.*, 170:377, 2007.
- [35] V. SPRINGEL ET AL. Simulating the joint evolution of quasars, galaxies and their large-scale distribution. *Nature*, 435:629, 2005.
- [36] J. ELLIS, M.K. GAILLARD, D. NANOPOULOUS, AND S. RUDAZ. The phenomenology of the next left-handed quarks. *Nucl. Phys. B*, 131:285, 1977.
- [37] A.I. VAINSHTEIN, V.I. ZAKHAROV, AND M.A. SHIFMAN. A Possible mechanism for the $\Delta T = 1/2$ rule in nonleptonic decays of strange particles. *J. Exp. Theor. Phys. Lett.*, 22:55, 1975.
- [38] K. LINGEL, T. SKWARNICKI, AND J.G. SMITH. Penguin decays of B mesons. *Ann. Rev. Nucl. Part. Sci.*, 48:253, 1998.
- [39] S. KUROKAWA AND E. KIKUTANI. Overview of the KEKB accelerators. *Nucl. Instr. Meth. A*, 499:1, 2003.
- [40] Belle Collaboration, J. WICHT ET AL. Observation of $B_s^0 \rightarrow \phi\gamma$ and Search for $B_s^0 \rightarrow \gamma\gamma$ Decays at Belle. *arXiv:0712.2659*, 2007, accepted for publication in *Phys. Rev. Lett.*.
- [41] J. WICHT. Radiative penguin B_s^0 decays at Belle. *arXiv:0711.0271*, 2007, On behalf of the Belle Collaboration. Proceedings of the International Europhysics Conference on High Energy Physics (EPS-HEP2007), Manchester, England, 19-25 July 2007. To appear in *JoP: Conference Series*.
- [42] J. WICHT. Search for $B_s^0 \rightarrow \phi\gamma$ and $B_s^0 \rightarrow \gamma\gamma$. Belle Note 1009.
- [43] CLEO Collaboration, R. AMMAR ET AL. Evidence for penguin-diagram decays: First observation of $B \rightarrow K^*(892)\gamma$. *Phys. Rev. Lett.*, 71:674, 1993.

- [44] P. BALL, G.W. JONES, AND R. ZWICKY. $B \rightarrow V\gamma$ beyond QCD factorization. *Phys. Rev. D*, 75:054004, 2007.
- [45] A. ALI, B.D. PECJAK, AND C. GREUB. $B \rightarrow V\gamma$ Decays at NNLO in SCET. *arXiv:0709.4422*, 2007, submitted to *Eur. Phys. J. C*.
- [46] CDF Collaboration, D. ACOSTA ET AL. Search for radiative b -hadron decays in $p\bar{p}$ collisions at $\sqrt{s} = 1.8$ TeV. *Phys. Rev. D*, 66:112002, 2002.
- [47] A. ALI AND A.YA. PARKHOMENKO. Branching ratios for $B \rightarrow K^*\gamma$ and $B \rightarrow \rho\gamma$ decays in next-to-leading order in the Large Energy Effective Theory. *Eur. Phys. J. C*, 23:89, 2002.
- [48] M. MISIAK ET AL. Estimate of $\mathcal{B}(B \rightarrow X_s\gamma)$ at $\mathcal{O}(\alpha_s^2)$. *Phys. Rev. Lett.*, 98:022002, 2007.
- [49] T. HURTH AND T. MANNEL. Direct CP violation in radiative B decays. *AIP Conf. Proc.*, 602:212, 2001.
- [50] D. ATWOOD, M. GRONAU, AND A. SONI. Mixing induced CP asymmetries in radiative B decays in and beyond the standard model. *Phys. Rev. Lett.*, 79:185, 1997.
- [51] D. ATWOOD, T. GERSHON, M. HAZUMI, AND A. SONI. Mixing-induced CP violation in $B \rightarrow P_1P_2\gamma$ in search of clean new physics signals. *Phys. Rev. D*, 71:076003, 2005.
- [52] K. KIERS, A. SONI, AND G.-H. WU. Direct CP violation in radiative b decays in and beyond the standard model. *Phys. Rev. D*, 62:116004, 2000.
- [53] A. LENZ AND U. NIERSTE. Theoretical update of B_s^0 - \bar{B}_s^0 mixing. *JHEP*, 0706:072, 2007.
- [54] F. MUHEIM, Y. XIE, AND R. ZWICKY. Exploiting the width difference in $B_s^0 \rightarrow \phi\gamma$. *arXiv:0802.0876*, 2008.
- [55] C.-H.V. CHANG, G.-L. LIN, AND Y.P. YAO. QCD corrections to $b \rightarrow s\gamma\gamma$ and exclusive $B_s^0 \rightarrow \gamma\gamma$ decay. *Phys. Lett. B*, 415:395, 1997.
- [56] L. REINA, G. RICCIARDI, AND A. SONI. QCD corrections to $b \rightarrow s\gamma\gamma$ induced decays: $B \rightarrow X_s\gamma\gamma$ and $B_s^0 \rightarrow \gamma\gamma$. *Phys. Rev. D*, 56:5805, 1997.
- [57] S.W. BOSCH AND G. BUCHALLA. The Double Radiative Decays $B \rightarrow \gamma\gamma$ in the Heavy Quark Limit. *JHEP*, 0208:054, 2002.
- [58] Belle Collaboration, A. DRUTSKOY ET AL. Exclusive B_s^0 decays at $\Upsilon(5S)$. *Phys. Rev. D*, 76:012002, 2007.
- [59] S. BERTOLINI AND J. MATIAS. $b \rightarrow s\gamma\gamma$ transition in softly broken supersymmetry. *Phys. Rev. D*, 57:4197, 1998.
- [60] A. GEMINTERN, S. BAR-SHALOM, AND G. EILAM. $B \rightarrow X_s\gamma\gamma$ and $B_s^0 \rightarrow \gamma\gamma$ in supersymmetry with broken R parity. *Phys. Rev. D*, 70:035008, 2004.

- [61] W.J. HUO, C.D. LU, AND Z.J. XIAO. $B_{s,d} \rightarrow \gamma\gamma$ Decay with the Fourth Generation. *arXiv:hep-ph/0302177*, 2003.
- [62] T.M. ALIEV AND E.O. ILTAN. $B_s^0 \rightarrow \gamma\gamma$ decay in the two Higgs doublet model with flavor changing neutral currents. *Phys. Rev. D*, 58:095014, 1998.
- [63] ALEPH Collaboration, R. BARATE ET AL. A Measurement of the inclusive $b \rightarrow s\gamma$ branching ratio. *Phys. Lett. B*, 429:169, 1998.
- [64] S.R. CHOUDHURY, G.C. JOSHI, N. MAHAJAN, AND B.H.J. MCKELLAR. Study of the flavor changing neutral current decay mode $B \rightarrow K\gamma\gamma$. *Phys. Rev. D*, 67:074016, 2003, erratum: *Phys. Rev. D*, 72:119906, 2005.
- [65] J. WICHT. Caractérisation de la désintégration $B \rightarrow K\gamma\gamma$ et perspectives pour une mesure avec le détecteur Belle. Master thesis, École Polytechnique Fédérale de Lausanne, Switzerland, 2004.
- [66] D. J. LANGE. The EvtGen particle decay simulation package. *Nucl. Instr. Meth. A*, 462:152, 2001.
- [67] M. KNECHT. Aspects théoriques de la désintégration $B \rightarrow K\gamma\gamma$ et implications pour sa simulation dans le cadre de l'expérience Belle. Master thesis, École Polytechnique Fédérale de Lausanne, Switzerland, 2004.
- [68] S.R. CHOUDHURY, G.C. JOSHI, N. MAHAJAN, AND B.H.J. MCKELLAR. Erratum: Study of the flavor changing neutral current decay mode $B \rightarrow K\gamma\gamma$. *Phys. Rev. D*, 72:119906, 2005.
- [69] G. HILLER AND A.S. SAFIR. Predictions for $B \rightarrow K\gamma\gamma$ decays. *JHEP*, 0502:011, 2005.
- [70] M. KNECHT AND T. SCHIETINGER. Probing photon helicity in radiative B decays via charmonium resonance interference. *Phys. Lett. B*, 634:403, 2006.
- [71] Belle Collaboration, S.-K. CHOI, S.L. OLSEN, ET AL. Observation of a Narrow Charmonium like State in Exclusive $B^\pm \rightarrow K^\pm \pi^+ \pi^- J/\psi$ Decays. *Phys. Rev. Lett.*, 91:262001, 2003.
- [72] CDF Collaboration, D. ACOSTA ET AL. Observation of the Narrow State $X(3872) \rightarrow J/\psi \pi^+ \pi^-$ in $p\bar{p}$ Collisions at $\sqrt{s} = 1.96$ TeV. *Phys. Rev. Lett.*, 93:072001, 2004.
- [73] DØ Collaboration, V.M. ABAZOV ET AL. Observation and Properties of the $X(3872)$ Decaying to $J/\psi \pi^+ \pi^-$ in $p\bar{p}$ Collisions at $\sqrt{s} = 1.96$ TeV. *Phys. Rev. Lett.*, 93:162002, 2004.
- [74] BABAR Collaboration, B. AUBERT ET AL. Study of the $B^- \rightarrow J/\psi K^- \pi^+ \pi^-$ decay and measurement of the $B^- \rightarrow X(3872) K^-$ branching fraction. *Phys. Rev. D*, 71:071103, 2005.
- [75] C.N. YANG. Selection Rules for the Dematerialization of a Particle into Two Photons. *Phys. Rev.*, 77:242, 1950, See also: L.D. Landau, *Dokl. Akad. Nauk USSR* **60**, 207 (1948) and *Phys. Abstracts* A52, 125 (1949).

- [76] Belle Collaboration, K. ABE ET AL. Experimental constraints on the possible J^{PC} quantum numbers of the $X(3872)$. *arXiv:hep-ex/0505038*, 2005.
- [77] Belle Collaboration, G. GOKHROO, G. MAJUMDER, ET AL. Observation of a Near-Threshold $D^0\bar{D}^0\pi^0$ Enhancement in $B \rightarrow D^0\bar{D}^0\pi^0 K$ Decay. *Phys. Rev. Lett.*, 97:162002, 2006.
- [78] CDF Collaboration, A. ABULENCIA ET AL. Analysis of the Quantum Numbers J^{PC} of the $X(3872)$ Particle. *Phys. Rev. Lett.*, 98:132002, 2007.
- [79] BABAR Collaboration, B. AUBERT ET AL. Study of Resonances in Exclusive B Decays to $\bar{D}^{(*)}D^{(*)}K$. *arXiv:0708.1565*, 2007.
- [80] CDF Collaboration, A. ABULENCIA ET AL. Measurement of the Dipion Mass Spectrum in $X(3872) \rightarrow J/\psi\pi^+\pi^-$ Decays. *Phys. Rev. Lett.*, 96:102002, 2006.
- [81] Belle Collaboration, K. ABE ET AL. Evidence for $X(3872) \rightarrow \gamma J/\psi$ and the sub-threshold decay $X(3872) \rightarrow \omega J/\psi$. *arXiv:hep-ex/0505037*, 2005.
- [82] BABAR Collaboration, B. AUBERT ET AL. Search for $B^+ \rightarrow X(3872)K^+$, $X(3872) \rightarrow J/\psi\gamma$. *Phys. Rev. D*, 74:071101, 2006.
- [83] K. ABE ET AL. SuperKEKB Letter of Intent. *KEK Report 04-4*, 2004.
- [84] A.G. AKEROYD ET AL. Physics at Super B Factory. *arXiv:hep-ex/0406071*, 2004.
- [85] M BONA ET AL. SuperB: A High-Luminosity Asymmetric e^+e^- Super Flavor Factory. Conceptual Design Report. *arXiv:0709.0451*, 2007, INFN/AE - 07/2, SLAC-R-856, LAL 07-15.
- [86] Belle Collaboration, J. WICHT ET AL. Search for Resonant $B^\pm \rightarrow K^\pm h \rightarrow K^\pm\gamma\gamma$ Decays at Belle. *arXiv:hep-ex/0608037*, 2007, accepted for publication in *Phys. Lett. B*.
- [87] J. WICHT. Search for Resonant $B^+ \rightarrow K^+ h \rightarrow K^+\gamma\gamma$. Belle Note 936.
- [88] DASP Collaboration, R. BRANDELIK ET AL. Results from DASP on e^+e^- annihilation between 3.1 and 5.2 GeV. *Z. Phys. C*, 1:233, 1979.
- [89] CFS Collaboration, S.W. HERB ET AL. Observation of a Dimuon Resonance at 9.5 GeV in 400-GeV Proton-Nucleus Collisions. *Phys. Rev. Lett.*, 39:252, 1977.
- [90] CLEO Collaboration, B. BARISH ET AL. Measurement of the B Semileptonic Branching Fraction with Lepton Tags. *Phys. Rev. Lett.*, 76:1570, 1996.
- [91] Heavy Flavour Averaging Group, E. BARBERIO ET AL. Averages of b -hadron properties at the end of 2006. *arXiv:0704.3575*, 2007.
- [92] CLEO Collaboration, D. BESSON ET AL. Observation of New Structure in the e^+e^- Cross Section above the $\Upsilon(4S)$. *Phys. Rev. Lett.*, 54:381, 1985.

- [93] CLEO Collaboration, M. ARTUSO ET AL. Evidence for $B_s^{(*)}\bar{B}_s^{(*)}$ Production at the $\Upsilon(5S)$ Resonance. *Phys. Rev. Lett.*, 95:261801, 2005.
- [94] T.E. BROWDER AND K. HONSCHIED. B mesons. *Prog. Part. Nucl. Phys.*, 35:81, 1995.
- [95] Belle Collaboration, A. DRUTSKOY ET AL. Measurement of Inclusive D_s , D^0 , and J/ψ Rates and Determination of the $B_s^{(*)}\bar{B}_s^{(*)}$ Production Fraction in $b\bar{b}$ Events at the $\Upsilon(5S)$. *Phys. Rev. Lett.*, 98:052001, 2007.
- [96] Tristan Project Group. Tristan electron - positron colliding beam project. *KEK Report 86-14*, 1987.
- [97] Belle Collaboration, O. TAJIMA, H. HAYASHII, M. HAZUMI, K. INAMI, Y. IWASAKI, S. UEHARA, ET AL. Search for Invisible Decay of the $\Upsilon(1S)$. *Phys. Rev. Lett.*, 98:132001, 2007.
- [98] Belle Collaboration, A. ABASHIAN ET AL. The Belle detector. *Nucl. Instr. Meth. A*, 479:117, 2002.
- [99] C. JACOBY. Measurements of the rare radiative B meson decays $B \rightarrow \phi K\gamma$ and $B \rightarrow \omega K\gamma$ at the Belle experiment and contribution to software development at the LHCb experiment. PhD thesis, Ecole Polytechnique Fédérale de Lausanne, Switzerland, 2007.
- [100] F. RONGA. $B^0\bar{B}^0$ mixing measurement at Belle using dilepton events tagged with a soft pion. PhD thesis, Université de Lausanne, Switzerland, 2003.
- [101] G. TAYLOR. The Belle silicon vertex detector: present performance and upgrade plan. *Nucl. Instr. Meth. A*, 501:22, 2003.
- [102] Belle SVD2 Group, Z. NATKANIEC ET AL. Status of the Belle silicon vertex detector. *Nucl. Instr. Meth. A*, 560:1, 2006.
- [103] Y. OHNISHI. Track Parametrization. Belle Note 148.
- [104] H. KICHIMI ET AL. The BELLE TOF system. *Nucl. Instr. Meth. A*, 453:315, 2000.
- [105] K. MIYABAYASHI. Belle electromagnetic calorimeter. *Nucl. Instr. Meth. A*, 494:298, 2002.
- [106] A. ABASHIAN ET AL. The K_L^0/μ detector subsystem for the BELLE experiment at the KEK B -factory. *Nucl. Instr. Meth. A*, 449:112, 2000.
- [107] T. TSUBOYAMA. The silicon vertex detector for BELLE. *Nucl. Instr. Meth. A*, 447:26, 2000.
- [108] Y. USHIRODA ET AL. Development of the central trigger system for the BELLE detector at the KEK B -factory. *Nucl. Instr. Meth. A*, 438:460, 1999.
- [109] T. ZIEGLER ET AL. The Belle trigger system with the new silicon vertex detector SVD2. *IEEE Trans. Nucl. Sci.*, 51:1852, 2004.

- [110] S. NAGAYAMA. PANTHER - User's manual, reference manual and primer. Belle Note 130, Belle Note 131 and Belle Note 132.
- [111] H. OZAKI. Mini-DST Tables V0.0. Belle Note 146.
- [112] B. CASEY. HadronB. Belle Note 390.
- [113] R. ITOH. BASF User's Manual. Belle Note 161.
- [114] R. BRUN ET AL. GEANT 3.21: the detector response simulator. *CERN Report DD/EE/84-1*, 1984.
- [115] H. KAKUNO ET AL. Neutral B flavor tagging for the measurement of mixing-induced CP violation at Belle. *Nucl. Instr. Meth. A*, 533:516, 2004.
- [116] H. KAKUNO. Flavor tagging by Multidimensional likelihood method. Belle Note 384.
- [117] C.M. CARLONI CALAME, C. LUNARDINI, G. MONTAGNA, O. NICROSINI, AND F. PICCININI. Large-angle Bhabha scattering and luminosity at flavour factories. *Nucl. Phys. B*, 584:459, 2000.
- [118] CLEO Collaboration, G.S. HUANG ET AL. Measurement of $\mathcal{B}(\Upsilon(5S) \rightarrow B_s^{(*)}\bar{B}_s^{(*)})$ Using ϕ Mesons. *Phys. Rev. D*, 75:012002, 2007.
- [119] R. LOUVOT, J. WICHT, AND T. AUSHEV. Study of the decay $B_s^0 \rightarrow D_s^- \pi^+$ and Search for $B_s^0 \rightarrow D_s K$ at the $\Upsilon(5S)$. Belle Note 1036.
- [120] G.C. FOX AND S. WOLFRAM. Observables for the Analysis of Event Shapes in e^+e^- Annihilation and Other Processes. *Phys. Rev. Lett.*, 41:1581, 1978.
- [121] Belle Collaboration, K. ABE ET AL. Measurement of Branching Fractions for $B \rightarrow \pi\pi$, $K\pi$, and KK Decays. *Phys. Rev. Lett.*, 87:101801, 2001.
- [122] Belle Collaboration, K. ABE ET AL. A measurement of the branching fraction for the inclusive $B \rightarrow X_s \gamma$ decays with the Belle detector. *Phys. Lett. B*, 511:151, 2001.
- [123] P. KOPPENBURG. An improved π^0 and η veto. Belle Note 665.
- [124] G.J. FELDMAN AND R.D. COUSINS. Unified approach to the classical statistical analysis of small signals. *Phys. Rev. D*, 57:3873, 1998.
- [125] Belle Collaboration, S. VILLA ET AL. Search for the decay $B^0 \rightarrow \gamma\gamma$. *Phys. Rev. D*, 73:051107, 2006.
- [126] S. VILLA. Search for the decay $B^0 \rightarrow \gamma\gamma$. Belle Note 831.
- [127] ARGUS Collaboration, H. ALBRECHT ET AL. Reconstruction of B mesons. *Phys. Lett. B*, 185:218, 1987.
- [128] T. SKWARNICKI. Ph.D. Thesis, Institute for Nuclear Physics, Krakow 1986; DESY Internal Report, DESY F31-86-02 (1986).

- [129] H.W. KIM. Study of High Energy Photon Detection Efficiency Using Radiative Bhabha. Belle Note 499.
- [130] TRACKING GROUP. Charged Particle Tracking in Belle. Belle Note 327.
- [131] M. NAKAO. Study of Radiative Decay $B \rightarrow K^* \gamma$ with Belle. Belle Note 333.
- [132] S. NISHIDA. Study of kaon and pion identification using inclusive D^* sample. Belle Note 779.
- [133] P. CHANG. Measurement of Branching Fraction and CP Asymmetry in $B \rightarrow \eta h$ Decays. Belle Note 729.
- [134] J.Z. ZHANG. Search for $B^+ \rightarrow \rho^+ \pi^0$. Belle Note 688.
- [135] J. DRAGIC. Search for $B^0 \rightarrow \rho^0 \pi^0$. Belle Note 689.
- [136] Y. CHAO. Updated study on $B^0 \rightarrow \pi^0 \pi^0$ study at Belle. Belle Note 759.
- [137] K.S. CRANMER. Kernel Estimation in High-Energy Physics. *Comput. Phys. Commun.*, 136:198, 2001.
- [138] J.O. BERGER, B. LISEO, AND R.L. WOLPERT. Integrated likelihood methods for eliminating nuisance parameters. *Statist. Sci.*, 14:1, 1999.
- [139] Belle Collaboration, P. CHANG ET AL. Improved measurements of branching fractions and CP asymmetries in $B \rightarrow \eta h$ decays. *Phys. Rev. D*, 75:071104, 2007.

Jean Wicht

Physicist

Chemin de la Maula 6
1680 Romont
Switzerland

E-mail: jean.wicht@a3.epfl.ch

Date of birth 26.11.1978
Nationality Swiss
Marital status single



Education and degrees

April 2008	Ph.D. thesis in High-Energy Physics at the Laboratoire de Physique des Hautes Énergies (LPHE), École Polytechnique Fédérale de Lausanne (EPFL), Switzerland
February 2007	CERN-CLAF School of High-Energy Physics in Viña del Mar, Chile
Since April 2004	Member of the Belle Collaboration, Tsukuba, Japan
April 2004 - April 2008	Ph.D. studies in High-Energy Physics at LPHE, EPFL
March 2004	Master thesis in Physics (dipl. d'ingénieur physicien EPFL)
August 2001 - May 2002	Exchange student, École Polytechnique, Montréal, Canada
October 1998 - March 2004	Physics studies, EPFL

Publications

- J. Wicht et al. (Belle Collaboration), “Observation of $B_s^0 \rightarrow \phi\gamma$ and Search for $B_s^0 \rightarrow \gamma\gamma$ Decays at Belle”, accepted for publication in Physics Review Letters, arXiv:0712.2659 (2008).
- J. Wicht et al. (Belle Collaboration), “Search for Resonant $B^+ \rightarrow K^+h \rightarrow K^+\gamma\gamma$ Decays at Belle”, accepted for publication in Physics Letters B, arXiv:hep-ex/0608037 (2008).
- J. Wicht for the Belle Collaboration, “Radiative penguin B_s^0 decays at Belle”, to appear in Journal of Physics: Conference Series, arXiv:0711.0271 (2007).